Relativistic Phases in Condensed Matter

Thibaud Louvet

To cite this version:

Thibaud Louvet. Relativistic Phases in Condensed Matter. Condensed Matter [cond-mat]. Université de Lyon, 2018. English. NNT : 2018LYSEN025 . tel-01900468

HAL Id: tel-01900468
https://theses.hal.science/tel-01900468

Submitted on 22 Oct 2018

Numéro national de thèse : 2018LYSEN025

Thèse de doctorat de l'Université de Lyon
opéréé par
l'Ecole Normale Supérieure de Lyon

Ecole Doctorale N°52
Ecole Doctorale de Physique et Astrophysique de Lyon

Discipline: Physique

Soutenue publiquement le 12/07/2018, par :
Thibaud LOUVET

Phases relativistes en matière condensée
Relativistic phases in condensed matter

Devant le jury composé de:

Julia Meyer, professeure à l'Université Grenoble Alpes	Rapporteure
Mark O. Goerbig, directeur de recherche au LPS Orsay	Rapporteur
Bernard Plaçais, directeur de recherche au LPA	Examinateur
Denis Basko, directeur de recherche au LPMMC	Examinateur
David Carpentier, directeur de recherche au LP ENS de Lyon	Directeur de thèse
Andreï Fedorenko, chargé de recherche au LP ENS de Lyon	Co-encadrant de thèse

Remerciements

Les travaux qui sont présentés dans ce manuscrit sont le résultat d'un travail de thèse qui a débuté par un stage de recherche en mars 2014 et s'est poursuivi jusqu'en juillet 2018 sous la direction de David Carpentier et Anreï Fedorenko, au laboratoire de Physique Ens de Lyon. Je tiens à remercier tous les membres du Laboratoire de Physique Ens de Lyon et en particulier son directeur Thierry Dauxois pour m'avoir accueilli et pour ces quatre années au laboratoire. Merci aux secrétaires, en particulier Laurence Mauduit, pour leur aide précieuse.

Je remercie amicalement Julia Meyer et Mark Goerbig qui ont accepté d'être rapporteurs de ma thèse, ainsi que Denis Basko et Bernard Plaçais qui ont formé le jury lors de la soutenance.

Je voudrais spécialement remercier David Carpentier et Andreï Fedorenko qui m'ont fait confiance et m'ont encadré au cours de cette thèse. J'ai beaucoup appris à leur contact. Merci pour leur disponibilité, leur patience, pour m'avoir transmis leur enthousiasme et leur curiosité pour la science en général. Une partie des travaux de la thèse est le fruit de collaborations avec Pierre Delplace, une autre partie avec Manuel Houzet, et je les remercie ici. Un merci particulier à Pierre pour les discussions, scientifiques ou informelles, qui m'ont marqué au cours de ma première année au laboratoire.

Merci aux doctorants du laboratoire avec qui j'ai pu partager une pause, un repas ou un verre au cours de ces années. Enfin, je voudrais dire merci aux copains, copines et aux proches qui ont été là: à ma famille, à Anaïs, Julien, Ella, Basile pour le 73, Jordan, Ernesto, Yannick et Pauline au labo, aux anciens: Rudy, Aurélien, Hervé, Joris, Gabriel, Clément et les autres que je n'oublie pas et qui se reconnaîtront.

Abstract

This thesis adresses the study of crystals called relativistic semi-metals, in which electrons behave like massless relativistic particles. The first historical example of such a material is graphene. In this planar arrangement of carbon atoms, electronic valence and conduction bands touch at two distincts points in the reciprocal lattice. Thus, graphene is a zero-gap semiconductor, a semi-metal. The dynamics of electrons close to the Fermi level is relativistic, described by a Dirac equation, although their velocity is a hunder times lower than the velocity of light in vacuum. Analogous semi-metallic phases have recently been identified: 3D Weyl and Dirac semimetals, as well as more exotic phases described by crossings with more than two bands. This variety of relativistic materials raises the question of their common properties. A first part of this thesis presents work related to the study of the stability of these phases, i.e. of the electronic band crossing. We have investigated this stability first by relating it to topological properties, then by evaluating the effect of disorder, such as the presence of impurities in the material. In the second part, we focus on the manifestation of the relativistic nature of these electrons in transport. In a first study, we examine the condition of existence of a finite conductivity exactly at the band crossing, due to the contribution of evanescent states. A second study concerns the anomalous transport under a magnetic field in Weyl semi-metals, as a manifestation of the chiral anomaly, a unique property of massless relativistic fermions.

Résumé

Cette thèse porte sur l'étude des cristaux appelés semi-métaux relativistes dans lesquels les électrons se comportent comme des particules relativistes sans masse. Le premier exemple historique d'un tel matériau est le graphène. Dans cet assemblage planaire d'atomes de carbone, les bandes électroniques de valence et de conduction se touchent en deux points distincts du réseau réciproque: il s'agit d'un conducteur de gap nul, un semi-métal. Les électrons proches du niveau de Fermi ont une dynamique relativiste décrite par une équation de Dirac, bien que leur vitesse soit cent fois inférieure à celle de la lumière dans le vide. Des semi-métaux analogues ont récemment été identifiés : les semi-métaux de Weyl et de Dirac à 3D, et des phases plus exotiques décrites par des croisements à plus de deux bandes. Cette diversité de matériaux relativistes pose la question de leurs propriétés communes. Une première partie de la thèse présente les travaux reliés à l'étude de la stabilité de ces phases, c'est à dire du croisement de bandes électroniques. Nous avons étudié cette stabilité d'abord en la reliant à des propriétés topologiques, puis en évaluant l'effet du désordre, tel que des impuretés dans le matériau. Dans la deuxième partie, nous nous intéressons à la manifestation dans le transport de la nature relativiste de ces électrons. Dans une première étude, nous étudions la condition d'existence d'une conductivité finie exactement au croisement des bandes, due à une contribution d'états évanescents. Une deuxième étude porte sur le transport anormal sous champ magnétique dans les semi-métaux de Weyl, comme manifestation de l'anomalie chirale, propriété unique de fermions relativistes.

Contents

Chapter 1

General Introduction

This thesis concerns condensed matter systems, and how relativistic and topological properties come into play in some crystals. Understanding and classifying the material reality and the matter that surrounds us is at the core of physical sciences. From Aristotle's four elements of the terrestrial sphere in Ancient Greece, or other religious or philosophical representations of the cosmos, to Mendeleev's periodic table of elements in the nineteenth century and then the standard model of particle physics still accepted in the twenty first century, elaborating new classifications helps us grasp the fundamental distinctions and common properties between the objects that surround us, and eventually address their underlying constituents and the laws that drive them. Condensed matter physics aims at understanding the physical properties and structure of solid state matter. In 1897 Thomson discovered the existence of the electron, the elementary particle carrying electrical current. This breakthrough changed profoundly the way physicists thought about solids. In 1900, the Drude model offered an explanation for the behavior of electrons in metals, and linked the observation of a macroscopic current to the microscopic electrons trajectories. The advent of quantum mechanics marked another milestone. Physicists discovered that the laws of physics change radically at small scales, compared to macroscopic scales. They learned that they should also consider the wave-like nature of electrons. In particular, electrons, like waves, can interfere. Electrons statistics are restricted by the Pauli exclusion principle, which forbids two electrons to occupy the same state. Moreover, the interaction between the moving electrons and the fixed ions creates a periodic potential in which electrons move and modulates the electronic wavefunction according to Bloch's theorem. Thus, electronic states can only have certain energies depending on the solid's crystalline structure: the energy spectrum is divided between allowed energy bands and forbidden energy gaps, and is filled up to the chemical potential or Fermi energy. The formalism of electronic band theory and the Bloch theorem allowed physicists to achieve a classification of crystals that proved to be successful in accounting for their electronic properties and thus predict measurable physical characteristics as electric, thermal, mechanical, optical properties. In particular the electronic band theory of solids allowed to predict which material could be insulator and which one could carry current, based on their atomic content and crystalline structure.

Electronic band theory allowed to classify solids into metals, insulators and semiconductors. The development of the semiconductor industry over the last decades has considerably changed our everyday life. Recently, the discovery of semimetals, zero-gap semiconductors with band crossing, opened a whole new area of research in solid state physics. Semimetals have been known for a long time, a famous example being bismuth, but in 2004 Graphene was successfully synthesized and was something like no physicist had observed before. In this two-dimensional material, electrons behave as relativistic particles. Although electrons in graphene travel at speeds well below the velocity of light, their low-energy behaviour near the band crossing is relativistic, described by a massless Dirac equation. The relativistic behaviour of electrons in graphene has amazing consequences such as the absence of backscattering, an anomalous Quantum Hall Effect and the existence of a finite conductivity exactly at the band crossing. The discovery of graphene raised naturally the question of whether analogous materials can be found, and specifically whether 3D analogs of graphene existed. In 2013 and 2015 respectively, the three-dimensional Dirac and Weyl semimetals were discovered. These new materials shared with graphene a number of properties like the presence of a linear spectrum with band crossing, characteristic of relativistic semimetals. Moreover, it was found that 3D Semimetals have unique properties. In particular, Weyl semimetals were predicted to host robust surface states, protected against continuous deformations of the electronic band structure. The existence of these topologically protected surface states was later probed by ARPES. In addition to these 3D cousins of graphene, the existence of 2D massless Dirac fermions has been predicted to exist and probed in other two-dimensional materials than graphene. The surface states of so-called 3D topological insulators are of the same nature as electrons in graphene. Conversely, graphene can be seen as a critical phase between a topological and a trivial insulator, stabilized by symmetries. The stability of relativistic semimetals is related to the topological characterization of the band crossing. These nodal points can be characterized by the winding of a geometrical phase, such as 2D Berry windings in graphene, or protected by a topological invariant such as the Chern number for Weyl semimetals in 3D.

The classification and characterization of semimetals with a band crossing based on their intrinsic properties and physical observables is the object of this thesis. The introduction gives a general view of semimetallic phases with relativistic excitations, with a presentation of some existing materials and properties.

1.1 Electrons, solids, semimetals

1.1.1 Electronic band theory

The speed of conduction electrons in a typical metal is of the order of 10^6m.s^{-1}, 300 times less than the velocity of light in vacuum c. Their behaviour is non-relativistic in the sense that it differs qualitatively from the behaviour of an electron in the vacuum propagating at speeds close to c. Compared to free electrons, the behaviour of electrons in solids is affected by the surrounding atomic nuclei. Their energy landscape is organized into energy bands filled from the lowest energy following Pauli's principle. The study of these electronic bands is a powerful method to characterize the electronic transport properties of solids.

A successful description of the quantum mechanics of a single, non-interacting electron in a crystal is given by Bloch theorem. The Bloch theorem is the starting point of the band theory of crystals, which enabled physicists to classify solid state matter based on electric transport properties, into metals and insulators. It states that no matter how strong the attractive potential binding electrons to the atomic cores, it only gives a modulation of the plane waves states describing free electrons [Simon, 2013]. Just as a standing wave in a box can only resonate at a discrete set of frequencies, for electrons in crystals some energy ranges are allowed, the energy bands, while some are forbidden, the energy gaps. Within a band, the energy landscape is given by the dispersion relation between the energy of electronic states and their quasi-momentum $\vec{k}$, a conserved quantum quantity associated with the set of discrete translation symmetries of the crystal.

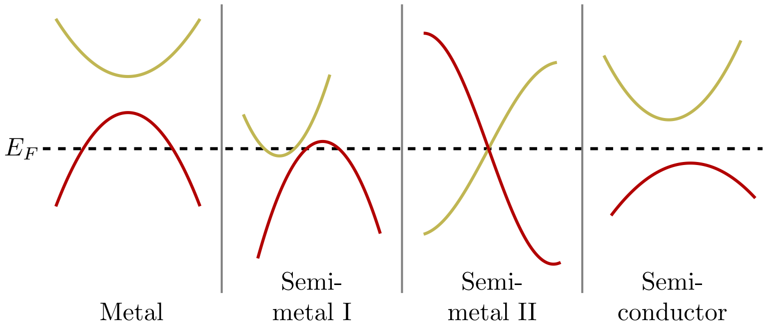

Figure 1.1: Classification of crystals depending on their band structure. In metals, the Fermi level lies within a band. In semimetals, valence and conduction bands slightly overlap at the Fermi level, without (I) or with (II) a band crossing occurring at the Fermi level. In semiconductors (and insulators) the Fermi level lies within an energy gap.

Because electrons are fermions, Pauli's principle states that two electrons can not occupy the same state. Energy bands are filled starting from the lowest energies up to the so-called Fermi energy at $T = 0$ or chemical potential at $T \neq 0$. Thus, the Fermi energy is the upper bound for energies of occupied electronic states at $T = 0$; it depends on the total number of electrons. Whether it lies within a band or within a gap determines whether an electronic state is available to excite an electron by adding an infinitesimal amount of energy to the system. When the Fermi energy lies within a band, this last occupied band is only partially filled and there are empty electronic states directly above the Fermi level. Any infinitesimal perturbation can promote an electron to an excited state and contribute to electric conduction in the presence of a potential drop. Hence, the material is conducting: it is a metal. On the contrary, if the Fermi energy lies within a gap, i.e. if the last occupied band is totally filled, there is no empty electronic state available directly above the Fermi level. An infinitesimal perturbation can not make an electron available for conduction. Hence, the material is insulating.

Thus, the location of the Fermi energy within a band or within a gap tells us whether the crystal is a metal or an insulator. One of the great merits of band theory was to allow for a classification of solid matter based on this simple criterion. An introduction to the electronic band theory of crystals can be found in a number of textbooks [Singleton, 2001, Kittel, 2004, Simon, 2013].

Along the same lines, a more refined classification of solids can be established. One can distinguish between insulators, semiconductors, metals and semimetals, see Fig. 1.1. In both insulators and semiconductors the Fermi energy lies within an energy gap: in an insulator the gap is large, typically $\Delta E > 4$ eV. The amount of energy necessary to excite an electron into the conduction band would then destroy the solid phase. In contrast in semiconductors the gap is small enough that one could get a reasonable concentration of electrons excited in the conduction band around $T = 300$ K ($k_B T \simeq 25$ meV) [Ashcroft and Mermin, 1976].

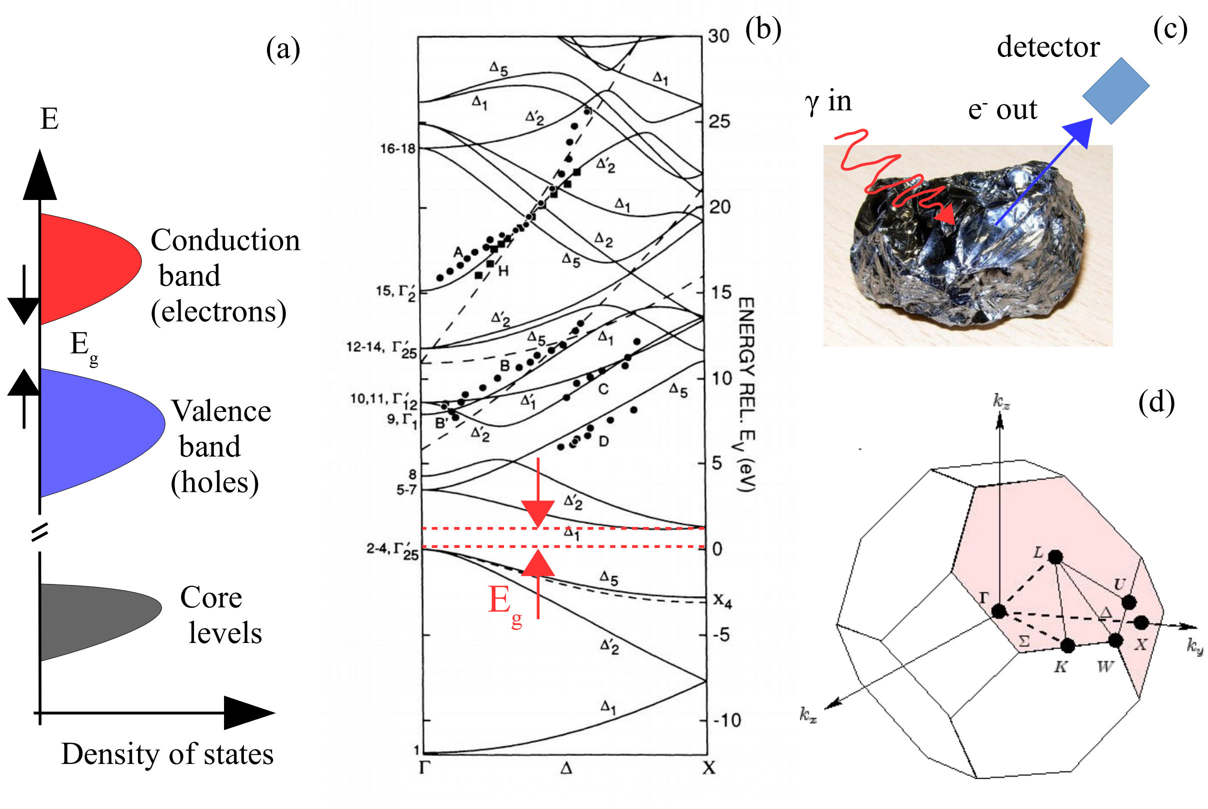

Figure 1.2: (a) Schematic view of the energy bands in a semiconductor: core electrons occupy the lowest energy states. They are localized around the atomic nucleus. Valence electrons can be shared between neighboring atoms. In the fundamental state, the valence band is completely filled, while above the energy gap E_g the conduction band is empty. Electrons excited into the conduction band are free to move around and can give rise to an electric current. A hole current can be obtained by removing an electron from the valence band. (b) Band structure of semiconductor Si from calculations (filled lines) and ARPES (dots). Taken from [Johansson et al., 1990]. (c) Description of an ARPES experiment: the Si sample is bombed with collimated energetic photons. An electron detector counts electrons from photoelectric emission at a given angle. Counting electrons at different angles and photon energy, one maps the energy landscape of the crystal in momentum space. (d) Brillouin zone (allowed values of quasi-momentum) of Si.

1.1.2 Semiconductors

Semiconductors are materials of great interest. They can be made insulating or conducting by tuning the Fermi level: this is called doping. Contrary to metals, their resistivity drops when the temperature increases. The physics of interest happens near the energy gap, in the two bands surrounding it: the valence or hole band below and the conduction or electron band above the gap, see Fig.1.2(a) and 1.2(b). Information on the band structure can be obtained experimentally, for example using angle-resolved photoemission spectroscopy (ARPES). A comparison between experimental ARPES results and calculations for the band structure of silicon (Si) is displayed in Fig. 1.2(b). The ARPES technique, presented in Fig.1.2(c), is based on detecting electrons emitted by a crystal when hit by an energetic photon from which one reconstructs the dispersion relation . Fig. 1.2(d) shows the Brillouin zone of silicon. The Brillouin zone is the primitive cell of the crystal's reciprocal lattice; it corresponds to the allowed values of quasi-momentum. By varying the incident angle and energy of the incident photon, and measuring the momentum and energy of the extracted electron, ARPES allows one to map the electronic band structure in the Brillouin zone.

To make semiconductors conducting, one can either excite electrons by heating the material or tune the Fermi level location by changing the chemical composition. This last method is called chemical doping: the Fermi level is brought into the conduction band (respectively the valence band) by adding (respectively subtracting) electrons to (from) the system. A simple way of doping is by adding foreign atoms to the crystal, which act as donors or acceptors of electrons [Simon, 2013, Alloul, 2010]. For example in Si, doping can be achieved by adding aluminum (Al) or phosphorus (P) atoms to the system. These species are located on the left (Al) or on the right (P) of Si in the periodic table, i.e. they have an extra electron or hole. Phosphorus has an extra proton and an extra electron compared to silicon, thus replacing one Si atom with a P atom in a silicon crystal will add an electron to the conduction band. When a donor is added, there are extra electrons in the semiconductor, it is *n*-doped. When an acceptor is added, there are fewer electrons or extra holes (see below): the semiconductor is *p*-doped.

Parabolic dispersion relation: the effective mass

Near the bottom of the conduction band or the top of the valence band, the dispersion relation of electrons is approximately parabolic. Assuming an isotropic dispersion for simplicity, it reads

$$E - E^* = \frac{\hbar^2(\mathbf{k} - \mathbf{K}^*)^2}{2m^*}, \tag{1.1}$$

where the bottom of the band is located at $\mathbf{K}^*$, $E(\mathbf{K}^*) = E^*$. The effective mass m^* is not the real electron mass but is related to the band curvature. Note that m^* has a different sign for the valence and conduction band, as in Fig.1.2(b) for Si. m^* enters the equation of motion of the electrons when they are submitted to an external force $\mathbf{f}$:

$$m^* \frac{d\mathbf{v}}{dt} = \mathbf{f}, \tag{1.2}$$

where $\mathbf{v} = 1/\hbar \; dE/d\mathbf{k}$ is the electronic velocity. The negative effective mass of valence band electrons means that they move the "wrong way" when submitted to a given force.

Holes

In doped semiconductors, the Fermi level often lies near a band extremum. At first sight, it might seem trickier to describe an almost full band with many electronic states than to describe an almost empty band with only a few occupied states. The description of an almost filled band is made easier by introducing the notion of "holes". Instead of describing the occupied states, we will describe the empty states. Completely filled bands carry no current, therefore the current carried by the almost filled valence band is equal to the current one would get from filling the band from the top down to the Fermi level with positively charged particles. Such particles with positive charge ($+e$) and positive mass ($-m^*$) are called holes. Removing an electron from the band amounts to adding a hole. The excitation energy of the hole is counted from the top of the valence band, see Fig. 1.3a. The lower the energy of the electron removed, the higher the energy of the hole: $E_h = -E_e$ (where E_e is negative, counted from the top of the valence band). When in reality current in the valence band is created by electrons moving e.g. to the left, as shown in Fig. 1.3b it is more accurate to think of it as coming from positively charged holes moving to the right.

Experimentally, the first measures of the Hall effect in semiconductors confirmed this point of view. When a (quasi-)two-dimensional electron gas is submitted to a magnetic field, charges are deviated by the Lorentz force, giving rise to charge accumulation and thus a voltage transverse to the electric current. The

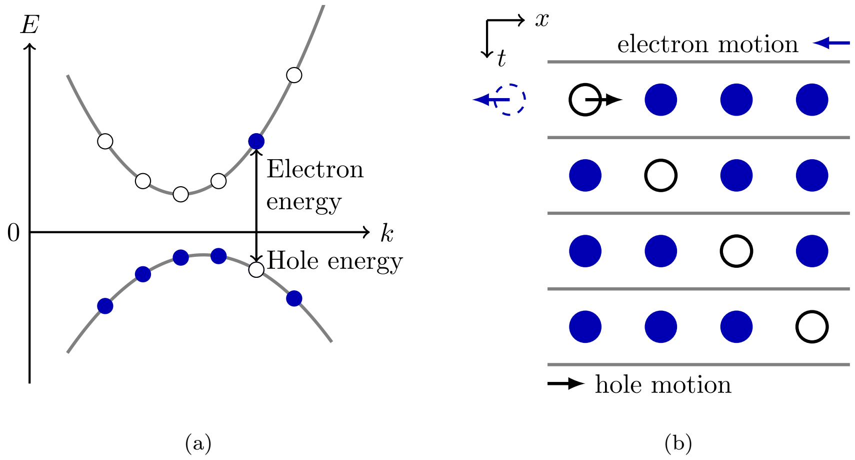

(a) (b)

Figure 1.3: (a) Energy band diagram of a semiconductor with one excited electron in the conduction band and one corresponding hole in the valence band. (b) Illustration of the motion of holes on a 1D tube. As electrons move left in the tube, the hole moves right.

sign of the voltage and the transverse resistivity depend on the carriers' charge. Hall effect experiments in p-type semiconductors showed that the current is carried by positively charged particles, holes.

The tunability of semiconductors and the combination of different charge carriers for transport triggered great developments in electronics, for making transistors and other information processing compounds.

1.1.3 Metals and semimetals

Metals are conductors even at zero temperature. Because they have partially filled bands, any electron from the Fermi surface -the set of electrons at Fermi energy- can be excited into an empty state above the Fermi energy even for an infinitesimal excitation energy. This excited electron can then contribute to the electric conduction. Thus, even the smallest potential difference applied to a metal creates an electric current.

In semimetals the valence band overlaps in energy with the conduction band so that there is no energy gap [Kittel, 2004, Burns, 2016]. The Fermi surface of a semimetal is made of tiny electrons and hole pockets. They are bad conductors: their carrier concentration is several orders of magnitude below 10^{22} electrons per cm^3, the concentration for a typical metal. To understand their band structure and electronic properties, it is instructive to think of semimetals as gapless semiconductors. The physics of interest also happens in the vicinity of the gap, and the Fermi surface is small.

Semi-metals I: with zero indirect gap

Semi-metals are zero gap semiconductors. We must distinguish between two classes of semimetals, named I and II on the diagram of Fig. 1.1. Semimetals from class I are not new: band structures of tin, bismuth, or graphite have been laid down in early days of band theory. In these materials, the bottom of the conduction band is located at a different quasi-momentum than the top of the valence band. The valence and conduction bands overlap because the top of the valence band is higher in energy than the bottom of the conduction band. The Fermi Surface consists of degenerate electron and hole pockets: both electrons and holes are present at the Fermi level in the absence of doping.

Semi-metals II: with band crossing

A new kind of semimetal came along with the discovery of graphene [Novoselov et al., 2004]. In these semimetals, valence and conduction bands are degenerate at a few points in the Brillouin Zone. The band crossing can occur because of symmetry constraints, or as a consequence of a band inversion driven by an external parameter. The bands can be degenerate either at isolated points as in graphene, or along lines or closed loops as we will see in some examples below. Note that the crossing can occur between more than two bands.

Interestingly, the dispersion relation around the crossing can be linear: it then resemble the dispersion of ultrarelativistic massless particles like photons for which $E = \hbar c k$.

In the following, we shall first consider the seminal example of graphene. In graphene, electrons near the band crossing not only have a relativistic-like spectrum but are described by the Dirac equation. Their intrinsic relativistic nature confers them fantastic properties. We will then describe the analogs of graphene in 3D, Dirac and Weyl semimetals, which turn out to be at least as fascinating as graphene. In the 3D so-called Weyl materials, a new particle emerges for the first time, the Weyl fermion, whose existence was conjectured by Hermann Weyl in 1929. Other, more exotic semimetallic phases with band crossings exist beyond Dirac and Weyl particles. Relativistic electronic wavefunctions in semimetals can have non trivial topological properties. In fact, the existence of relativistic phases is in deep connection with topological phase transitions between band insulators of different topological nature, i.e. insulators which can not be continuously deformed one into another without closing the gap. These topological properties open the perspective of an intrinsic characterization and classification of semimetals with band crossing.

1.2 Historical example of a relativistic semimetal: graphene

In graphene, valence and conduction bands cross linearly at two distinct points on the edge of the Brillouin Zone. The Fermi surface is a set of isolated points and the carrier concentration is exactly zero at the Fermi level. Amazingly, the physics of excitations close to the Fermi level is described by the Dirac equation for 2D massless fermions. The manifestation of relativistic physics in this 2D allotrope of carbon has opened fantastic perspectives for applications and offered a great tool for fundamental physicists: a pocket high-energy physics laboratory. Later on, it was found that 2D massless Dirac fermions emerge as surface states of another new and very intriguing class of solids, Topological Insulators.

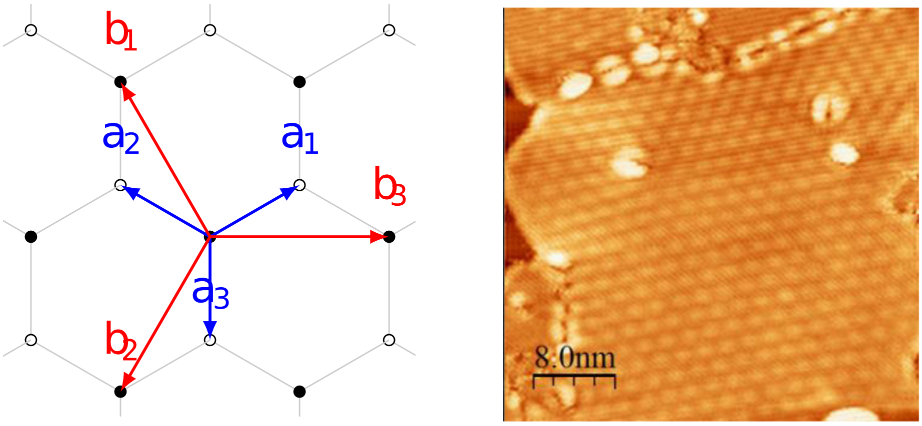

(a) (b)

Figure 1.4: (a) Honeycomb lattice of graphene with sublattices A (black circles) and B (open circles). $\mathbf{b_i}$ are vectors of the triangular Bravais lattice. (b) Scanning tunneling microscope (STM) image of a graphene flake grown on a Pt substrate using molecular beam epitaxy (MBE). Taken from [Hernández-Rodríguez et al., 2015].

1.2.1 Band structure: zero-gap semiconductor with two-band crossing

Graphene is an allotrope of carbon, made of a single layer of carbon atoms that form hexagonal rings. Geim and Novoselov were awarded the 2010 Nobel Prize in Physics for having isolated graphene from graphite and characterized this new material in 2004. Carbon is a very common element, the basis of organic matter. It has many allotropes, from $0-d$ fullerenes to $1-d$ carbon nanotubes to $3-d$ diamond or graphite. The first study of graphene is attributed to [Wallace, 1947]. However it has long been considered as only a theoretical object. Indeed, a two-dimensional crystal was deemed fundamentally unstable because of the Mermin-Wagner theorem that prohibits long range order in two dimensions. It has been a long time before the first monolayer flake of graphene was successfully exfoliated and observed on top of a SiO_2 substrate [Novoselov et al., 2004]. The honeycomb lattice is obtained from the triangular Bravais lattice with two atoms per unit cell, A and B, see Fig.1.4. The reciprocal lattice describing the momentum space of the crystal is also hexagonal. Carbon atoms possess four valence electrons: two $2s$ and two $2p$ electrons. In graphene, each atom is bounded through covalence between three sp^2 hybridized valence electrons, resulting in the honeycomb lattice with three nearest neighbors per site separated by $a = 1.42$ Å. The three sp^2 electrons form the deep valence σ-band. Symmetry arguments impose that

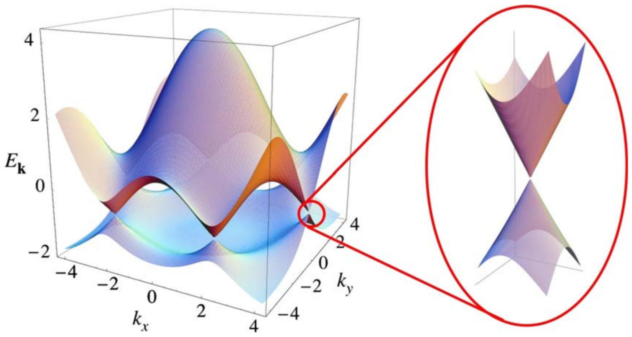

Figure 1.5: Energy bands of graphene in the Brillouin zone and zoom in around a Dirac cone. Taken from [Castro Neto et al., 2009]..

the p_z orbital does not overlap with the s or the p_x and p_y orbitals. Therefore the remaining electron on the p_z orbital can be treated independently. In this approximation, called the $\pi-$band approximation, the A and B atoms are defined by a single orbital $p_z(\mathbf{r} - \mathbf{r}_A)$ (resp. $p_z(\mathbf{r} - \mathbf{r}_B)$), where $\mathbf{r_A}$ (resp. $\mathbf{r_B}$) is the position vector of atomic site A (resp. B) [Katsnelson, 2012]. The electronic hopping amplitude $t \simeq 2.9$ eV between nearest neighbor sites A and B corresponds to the amplitude of the overlap between the p_z orbitals of the two sites. The symmetry of the hexagonal lattice between A and B sites confers graphene with an extra degree of freedom analogous to a spin for Dirac fermions, the pseudospin. It corresponds to the relative weight of the electronic wavefunction between A and B sublattices. Fig.1.5 shows the valence π and conduction π^* bands of graphene in the Brillouin Zone. The spectrum shows $E \to -E$ symmetry at low energies coming from sublattice symetry. It is broken at higher energies due to second nearest neighbour hoppings. The energy spectrum exhibits two linear band crossing points at opposite corners of the Brillouin zone $\mathbf{K}$ and $\mathbf{K'}$. Around the $\mathbf{K}$ point, the electronic excitations are described by the following Hamiltonian in the A, B basis:

$$H_{\mathbf{K}/\mathbf{K'}}(\mathbf{q}) = \hbar v_F \left(\pm q_x \sigma_x + q_y \sigma_y\right), \tag{1.3}$$

with σ_i the Pauli matrices, and the Fermi velocity $v_F = \frac{3at}{2} \simeq 10^6 \mathrm{m.s}^{-1}$, more than 150 times the velocity of electrons in silicon but 300 times less than the velocity of light c.

1.2.2 Relativistic spectrum

The low-energy spectrum of graphene is given by the eigenvalues of Hamiltonian (1.3). It is shown in the inset of Fig. 1.5. In contrast with conventional electronic spectrums (1.1), it is linear in momentum:

$$E_\pm(\mathbf{K} + \mathbf{q}) = \hbar v_F q. \tag{1.4}$$

This dispersion relation is characteristic of massless ultrarelativistic particles like photons. Consider the energy-momentum relation as established by Einstein's theory of special relativity for a relativistic particle:

$$E^2 = p^2 c^2 + m^2 c^4, \tag{1.5}$$

where m is the rest mass of the particle, p its momentum, E its energy and c the speed of light. For massless particles the relation becomes linear

$$E = pc. \tag{1.6}$$

In contrast, for massive non-relativistic particles the energy momentum relation is quadratic:

$$E = \frac{p^2}{2m} + \mathcal{O}\left((\frac{p}{mc})^4\right). \tag{1.7}$$

A high-energy particle traveling round the CERN particle accelerator would be described in good approximation by the energy-momentum relation (1.6). A low-energy particle whose speed is several orders of magnitudes smaller than c is well described by (1.7).

In graphene as in any other solid, the electrons are not free but feel the periodic potential of the atomic lattice. As a result, they move at speeds several orders of magnitude smaller than the velocity of light. Electrons in conventional solids have a quadratic dispersion (1.1), analog of (1.7) with the effective mass substituted for the particle's mass. In contrast, in graphene the dispersion relation (1.4) corresponds to the massless relativistic case (1.6) with the Fermi velocity v_F playing the role of c. It turns out that this analogy with relativistic particles goes beyond the spectrum, as the physics of low energy electrons in graphene is described by the Dirac equation for massless relativistic fermions.

1.2.3 Relativistic particles: Dirac equation for 2D massless fermions

Dirac famously established the wave equation that describes the quantum behavior of relativistic fermions [Dirac, 1928]. For a free fermion with mass m in dimension d, it reads:

$$i\hbar\partial_t\psi = \boldsymbol{\alpha}\cdot\mathbf{p}c\psi + mc^2\beta\psi, \tag{1.8}$$

where $\mathbf{p}$ is the particle's momentum and c the velocity of light in vacuum. The $\alpha_i,\ i=1,...,d$ and β matrices are $N\times N$ matrices that form a Clifford algebra for the Kronecker-delta δ_{ij} metric, i.e.:

$$\{\alpha_i,\alpha_j\} = 2\delta_{ij}I_N, \tag{1.9a}$$

$$\{\beta,\alpha_k\} = 0, \tag{1.9b}$$

$$\beta^2 = I_N. \tag{1.9c}$$

Relations (1.9) imply that N must be even. In dimension $d=2$ necessarily $N=2$. One finds $\alpha_i=\sigma_i$ for $i=x,y,z$, where σ_i are the Pauli matrices satisfying (1.9). The 2D Dirac equation takes the form

$$i\hbar\partial_t\psi = (\sigma_x p_x + \sigma_y p_y)c\psi + mc^2\sigma_z\psi, \tag{1.10}$$

where $\psi =^t (\psi_1,\psi_2)$. In the massless case $m=0$, the Dirac Hamiltonian (1.10) corresponds to the low-energy Hamiltonian near the crossing in graphene (1.3). Thus electrons in graphene behave like 2D massless Dirac fermions moving at the velocity of $v_F = 10^6\text{m.s}^{-1}$ – 300 times less than the velocity of light. Physical perturbations breaking the sublattice A/B symmetry can play the role of a mass term and turn graphene into a semiconductor with a finite gap. The dispersion relation for massive and massless 2D Dirac fermions is sketched in Fig. 1.6.

Electrons in graphene are relativistic massless Dirac fermions. Their relativistic nature should manifest itself in the material's physical properties.

1.2.4 Relativistic electronic properties

The relativistic nature of electrons in graphene has consequences on the material's electronic properties which can be probed experimentally. In particular, electronic transport in graphene is highly unconventional. It is characterized by the absence of backscattering which manifests in the so-called Klein paradox, a unique dispersion of landau levels giving a half-integer quantized Hall conductance and the existence of a finite conductivity at the Dirac point. Moreover, electrons in graphene do not necessarily localize in the presence of disorder, in contrast with conventional diffusive metals.

Klein tunneling

The low-energy spectrum, often referred to as the Dirac cone of graphene, displays particle-antiparticle type symmetry. This symmetry is broken at higher energies by second nearest neighbor hoppings – typical value for second-neighbor transfer integral is $0.1-0.2\gamma_0$. In this material, the notion of electrons and holes with positive mass and negative or positive charge is thus completed with the notion of Dirac particle and antiparticle, with positive or negative energy. An electron can be a particle or antiparticle depending on

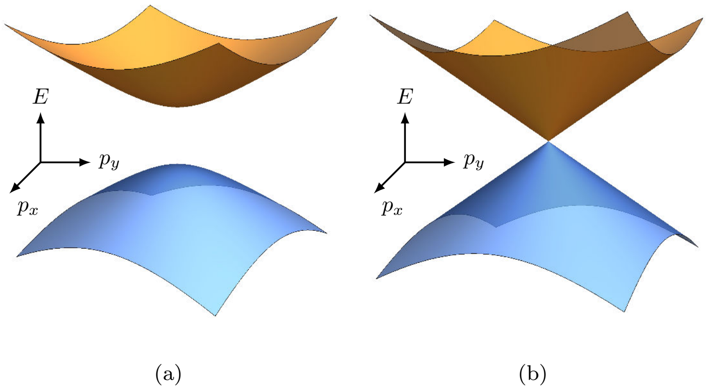

Figure 1.6: (a) Energy spectrum as a function of momenta for 2D massive Dirac fermions. (b) Energy spectrum of massless 2D Dirac fermions.

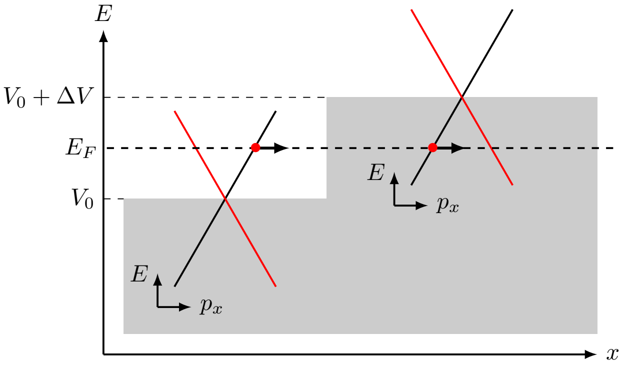

Figure 1.7: The Klein paradox: because of their relativistic nature, electrons in graphene can propagate through a potential barrier. Excitations in the upper Dirac cone, Dirac "particles", are transmitted as "antiparticles" (lower Dirac cone). Schematic depiction of the dispersion relation. The x-axis represents momentum while the y-axis represents energy. The group velocity is assumed to be along x; the black and red lines correspond respectively to positive and negative group velocity. The arrows show direction of velocity.

its location with respect to the band crossing energy; whether it is in the upper or lower Dirac cone, see Fig.1.5.

A striking property of electrons in graphene is the Klein paradox. In non-relativistic quantum mechanics, an electron incident on a potential step is either reflected or tunnels through the step as an evanescent wave. In contrast, low-energy electrons of graphene can propagate below a potential step, because of their Dirac nature: excitations with positive energy (particles, lying in the upper part of the cone) get transmitted through the potential step as propagating antiparticles (lower part of the Dirac cone) with the group velocity oriented in the same direction but opposite momentum (see Figure 1.7). At normal incidence the transmission is always perfect, irrespective of the height of the barrier [Katsnelson, 2012]. This peculiarity of the Dirac equation was discovered in 1929 by O. Klein, and observed in graphene in 2006 [Katsnelson et al., 2006]. Generalizing to transport in two dimensions, we see that backscattering is forbidden in graphene: a scattering center can not reflect electrons back to the incident direction. This absence of backscattering is related to a unique property of electronic states, a quantized Berry winding, which is defined and studied in Chapter 2.

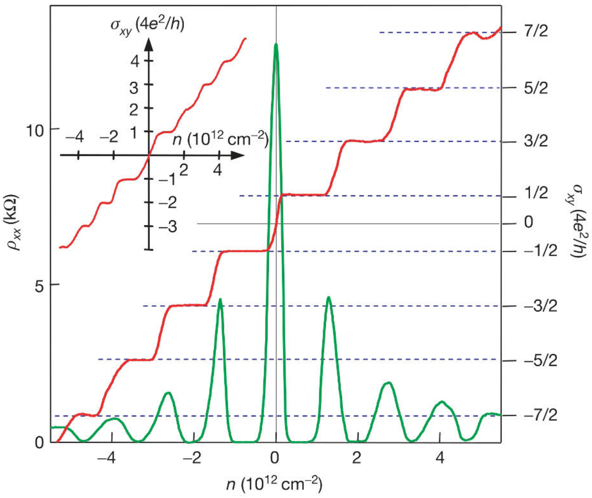

Figure 1.8: Observation of the Anomalous Quantum Hall Effect in Graphene. Hall conductivity σ_{xy} (red) and longitudinal resistivity ρ_{xx} (green) plotted against carrier concentration (negative n corresponds to hole transport) at $B = 14$ T, $T = 4$ K. Taken from [Novoselov et al., 2005].

Relativistic Landau levels

The experiment that convinced physicists of the relativistic nature of low energy electrons in graphene was the observation of a unique relativistic Quantum Hall Effect in a magnetic field [Novoselov et al., 2005, Zhang et al., 2005]. In the presence of a magnetic field, the conductivity tensor is anisotropic. The transverse conductivity shows conductivity plateaux at $\sigma_{xy} = (n + \frac{1}{2})4e^2/h$, while the longitudinal conductivity vanishes everywhere except when there is a change of plateau, see Fig. 1.8. When exposed to a high magnetic field at low temperature electrons in solids circulate along closed cyclotron orbits with quantized energy: the continuous energy bands collapse into Landau Levels. This results in quantization of the transverse conductivity, the famous Quantum Hall Effect. The integer n describing the quantization of σ_{xy} counts the number of filled Landau Levels. The plateaux of transverse conductivity σ_{xy} correspond to the gaps between Landau Levels. Everytime the chemical potential crosses a Landau Level, there is a peak in the longitudinal conductivity and n increases by 1. In graphene, Landau Levels have a characteristic $\propto \sqrt{B}$ dispersion coming from the linear spectrum at $B = 0$. The quantization of relativistic Landau Levels is shifted by $\frac{1}{2}$ compared to conventional Landau Levels; in particular, there is an anomalous Landau Level at zero energy.

Minimal conductivity

Another peculiar feature of graphene electronics is the existence of a finite minimal conductivity at the Fermi energy, where the Fermi surface reduces to a point and the charge carrier concentration vanishes.

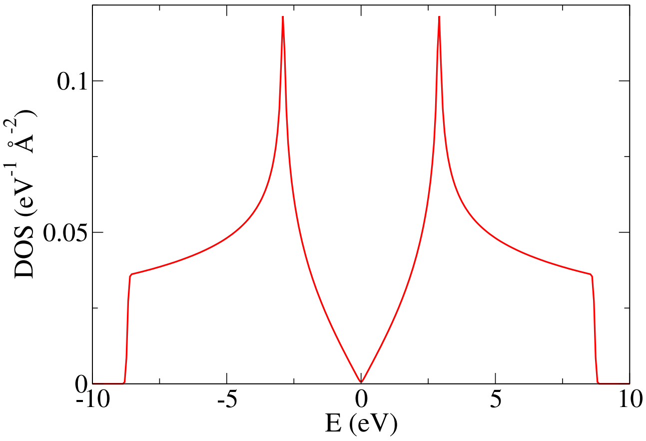

Figure 1.9: Electronic density of states in graphene, showing linear behavior near the band touching point. Exactly at the band touching point the density of states vanishes.

Figure 1.9 shows the density of states for graphene in the absence of disorder: the Fermi level is at $E_F = 0$, where we see that the density of states vanishes. When studying low-energy transport in graphene, it was discovered [Novoselov et al., 2005, Zhang et al., 2005] that, when the chemical potential is set to lie exactly at the Dirac point the conductivity remains finite and is of the order of the quantum of conductance e^2/h. Figure 1.10 shows the experimental observation of a conductivity plateau at the crossing which triggered the investigation of the existence of this finite conductivity. Although it turned out that the presence of electron and hole puddles in real graphene samples makes it complicated to fine tune the chemical potential exactly at the Dirac point, a finite minimal conductivity was predicted in the ballistic regime [Tworzydło et al., 2006, Katsnelson et al., 2006]. The existence of a finite conductivity in an ideal crystal, in the ballistic regime where no scattering process occurs, is a very puzzling result. In the semi-classical picture – the Drude-Boltzmann model, electrons propagate ballistically until they bounce off a scattering center. These collision processes tend to drive the system towards local equilibrium; one can define a corresponding momentum relaxation time, τ. In this approximation, the DC conductivity is given by the Drude formula $\sigma = \frac{ne^2\tau}{m}$ [Ashcroft and Mermin, 1976]. If the limit of zero disorder $\tau \to \infty$ is taken while keeping the electronic density n finite, one gets $\sigma \to \infty$: it is the so-called Drude peak, corresponding to a situation where an infinitesimal electric field will induce a collective motion of electrons in the same direction. On the other hand, if the electronic density – which is proportional to the chemical potential in the case of graphene – is set to zero prior to any other limit, the conductivity vanishes. In previous literature, the existence of a finite minimal conductivity at the charge neutrality point in pristine graphene has been linked to a special kind of interferences called Zitterbewegung, between plane wave states from the upper and lower Dirac cone. We have investigated this issue in semimetals beyond graphene, and we have shown that the occurrence of transport at the charge neutrality point is related to the nature of the evanescent states in connection with the robustness of the Berry phase [Louvet et al., 2015]. We report about this study in chapter 4.

Disordered graphene

Real crystals are affected by various kinds of disorder. Lattice deformations, grain boundaries, impurities or vacancies... can strongly modify electronic properties. In conventional materials scattering processes caused by disorder will eventually localize electrons when the disorder is strong. In striking contrast, low energy electrons in graphene do not undergo localization in the presence of long range disorder. If the disorder is short range correlated it will allow for coupling between the different valleys $\mathbf{K}$ and $\mathbf{K}'$ and electrons localize. On the other hand, any valley-independent disorder preserving the symmetries of clean graphene, such as a random chemical potential, will not open a gap. Such a disorder term models e.g. smooth gate voltage fluctuations from ripples. It will allow plane-wave states at the Dirac point, leading to a finite DOS and an increase in the conductivity [Bardarson et al., 2007, Nomura et al., 2007]. Scalar disorder in graphene has the highly non standard effect of improving electronic conduction; it does so by populating the Dirac point. Away from the Dirac point electrons behave as in a standard diffusive metal and the conductivity decreases with increasing disorder strength.

During this thesis we have studied the effect of disorder on 3D relativistic Weyl and Dirac semimetals.

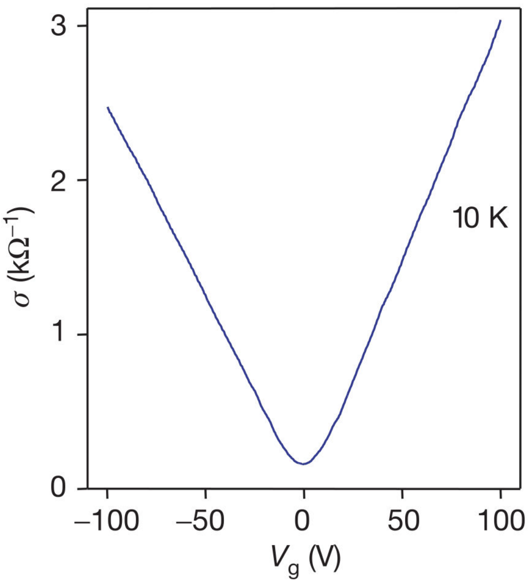

Figure 1.10: Variation of longitudinal conductivity in graphene with chemical potential (gate voltage), showing a finite minimum of conductivity at the band crossing $V_g = 0$. Taken from [Novoselov et al., 2005].

These semimetals are also protected against localization in the absence of intervalley scattering. However, contrary to graphene weak disorder does not qualitatively affect Weyl and Dirac points: disorder is irrelevant in 3D relativistic semimetals. In chapter 3 we report on the characterization of the phase transition which occurs between a weakly disordered semimetallic phase and a strong disordered, diffusive metal phase.

1.2.5 Dirac matter beyond graphene

We have seen some of the remarkable properties of the low energy relativistic electrons in graphene. The characterization of graphene naturally triggered the search for materials sharing similar properties. A variety of relativistic semimetals have been identified since graphene and we shall introduce a number of them in the following. Let us mention first that other occurrences of Dirac fermions have been identified in two dimensions. A remarkable example of 2D Dirac matter beyond graphene is the presence of 2D massless Dirac fermions on the surface of 3D Topological Insulators [Hasan and Kane, 2010]. In the context of the Quantum Hall Effect, it had already been established that graphene is a transition phase between a trivial insulator and a topological Chern insulator [Haldane, 1988]. In a Chern insulator, an Anomalous Quantum Hall Effect could be realized in the absence of magnetic field. This property is related to a non trivial topological invariant of the ensemble of Bloch eigenstates on the Brillouin Zone, the Chern number. We will come back to these notions in section 1.5.4 and chapter 2.

1.3 Beyond graphene: 3D Dirac and Weyl semimetals

Relativistic semimetals analog to graphene can be found in bulk materials. Although they share a number of properties with Graphene, such as their linear dispersion, they also have unique features.

The natural extension of Graphene to 3D, a 3D relativistic semimetal with two-band crossing, is called a Weyl semimetal. In 2D graphene symmetries forbid the Dirac mass term and guarantee the band degeneracy at the Dirac point. In contrary in three dimensions, a two band crossing can occur in the absence of any symmetry [Herring, 1937]. The low-energy Bloch Hamiltonian corresponds to the so called Weyl fermions, that will be described below in more details. Weyl fermions are massless and chiral: they are characterized by an internal degree of freedom analog to a spin which winds around the crossing. The sign of the winding defines the chirality of the Weyl fermion: left or right-handed. Weyl points come by pair of left and right-handed Weyls, and they can only be created or annihilated by pairs of opposite chirality. Because of an underlying robustness, an external perturbation can only shift Weyl points in

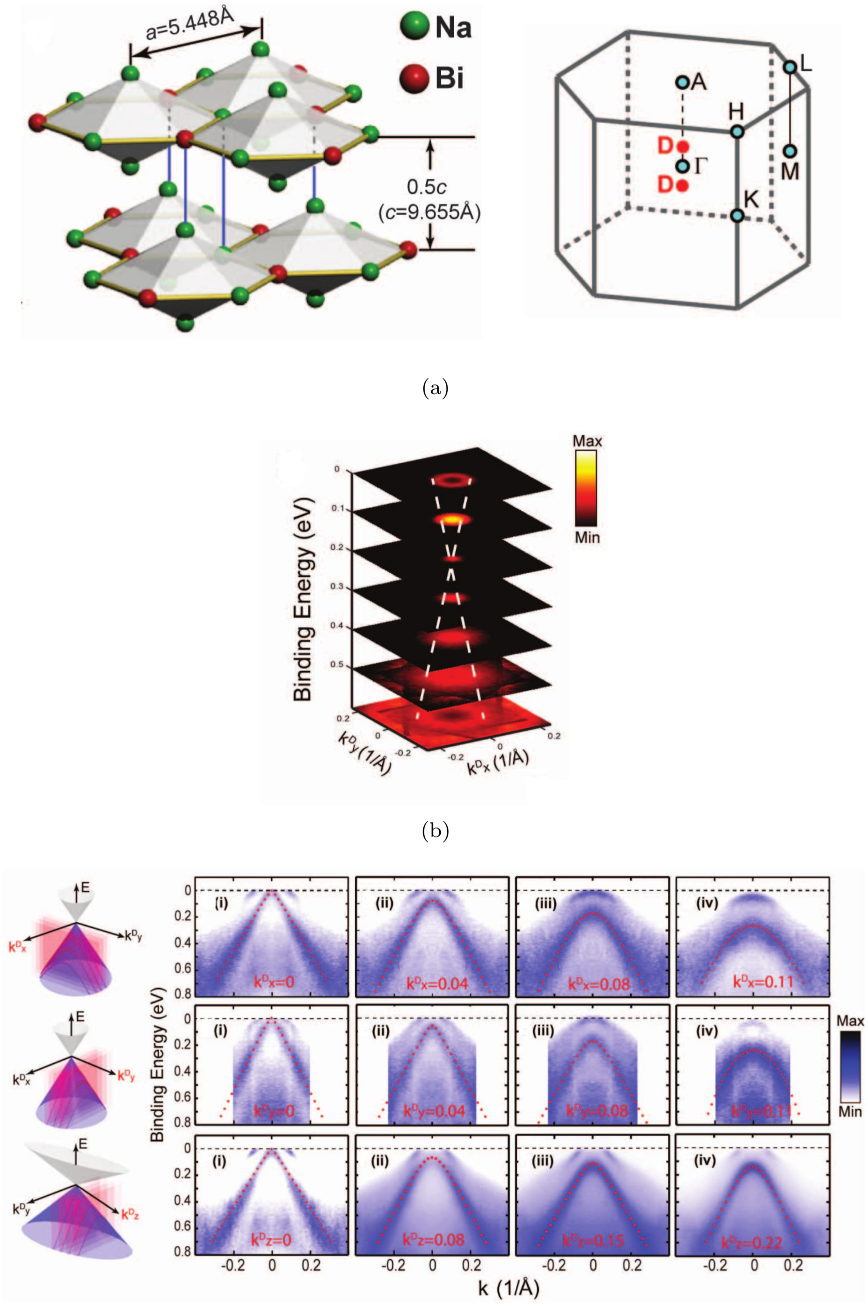

(a)

(b)

(c)

Figure 1.11: Dirac Semimetal Na_3Bi. (a) Crystal structure (left) and Brillouin Zone (right) of Na_3Bi. BZ high symmetry points are indicated in cyan and the two Dirac cones on the high symmetry axis near Γ are in red. (b) Constant energy contour plots in (k_x, k_y) plane for different binding energies showing the lower and upper Dirac cone after the Fermi energy has been tuned by surface doping. (c) Dispersion along the three directions of momentum space. in the absence of doping, the Fermi energy lies at the Dirac point. Schematics on the left show the slices through the Dirac cone at different momentum locations. Fitted and measured dispersions at different k_x^D, k_y^D or k_z^D show either linear or hyperbolic shape, depending on whether the measurement cuts through the nodal point. Adapted from [Liu et al., 2014]

momentum space but a single Weyl point can not be gapped.

In two dimensions, electrons near a two-band crossing behave like Dirac particles. In three dimensions, we have seen that low energy electrons near a two band crossing are Weyl particles. Dirac particles do occur in three dimensions, near four band crossings. The corresponding Hamiltonian is given by the 4×4 3D Dirac matrices. For a four-band crossing to be stable in three dimension, it has to be protected by a combination of non-spatial and crystalline symmetries against gap opening. When it is the case, it corresponds to a 3D massless Dirac fermion.

In the next section, we present the relativistic Weyl and Dirac equation that describes the low-energy physics in these 3D semimetals. We will see that these two particles are related in the sense that a 3D Dirac fermion is composed of two Weyl fermions with opposite chiralities. These semimetals share a number of properties with graphene as the Klein tunneling or the existence of a finite conductance at the band crossing. But we will see that Weyl semimetals have a number of unique features: in particular the existence of a winding around Weyl points has dramatic physical consequences related to the notion of topology. Finally, the impact of disorder depends on the dimensionality of electronic materials: whereas in 2D graphene any amount of disorder drives the system into a diffusive phase, in 3D semimetals a quantum phase transition occurs at a finite disorder strength between a clean semimetal phase and a diffusive metal phase.

1.3.1 3D relativistic particles: Weyl and Dirac equations

Contrary to the 2D case, there are more to 3D relativistic particles than just Dirac fermions. Soon after Dirac established his famous equation for relativistic quantum fermions, Hermann Weyl found that massless Dirac fermions can be described as a superposition of two chiral massless particles obeying the chiral two by two Weyl equation. In condensed matter also, a Dirac point is the superposition of pairs of Weyl points of opposite chirality.

Recall the Dirac equation (1.8)

$$i\hbar\partial_t\psi = \boldsymbol{\alpha}\cdot\mathbf{p}c\psi + mc^2\beta\psi, \tag{1.11}$$

where $\mathbf{p}$ is the particle's momentum and c the velocity of light in the vacuum. The $\alpha_i,\ i = 1, ..., d$ and β matrices are $N \times N$ matrices that form a Clifford algebra (1.9). In $d = 3$ $N \leq 4$. For $N = 4$, a possible representation of the Dirac matrices is:

$$\vec{\alpha} = \begin{pmatrix} \vec{\sigma} & 0 \\ 0 & -\vec{\sigma} \end{pmatrix}, \beta = \begin{pmatrix} 0 & \mathbb{1} \\ \mathbb{1} & 0 \end{pmatrix}. \tag{1.12}$$

This representation is known as the Weyl representation. Note that the α_i matrices are block diagonal. Therefore, in the massless case $m = 0$ the Dirac equation (1.11) is purely block-diagonal: the upper and lower components of ψ, χ_R and χ_L, are independent. Solving separately for each block, we get

$$i\hbar\partial_t\chi_{R/L} = \pm\boldsymbol{\sigma}\cdot\mathbf{p}c\ \chi_{R/L}. \tag{1.13}$$

This is the Weyl equation [Weyl, 1929]. Because all three Pauli matrices are assigned to the three component of momentum, no mass term is allowed: Weyl fermions are massless. They are also chiral, coming in left- and right-handed versions, corresponding to the ± sign in (1.13). The chirality describes whether the pseudospin associated with the Pauli matrices winds clockwise or anti-clockwise when the momentum circles around the origin $\mathbf{p} = \mathbf{0}$. Originally neutrinos were thought to be Weyl fermions but they turned out to be massive particles. Weyl fermions remained a purely theoretical entity until their discovery as quasiparticles in condensed matter systems. Thus, Dirac and Weyl particles are intimately related. We have seen that a massless Dirac fermion in 3D is the superposition of two Weyl fermions with opposite chirality:

$$\psi = \begin{pmatrix} \chi_R \\ \chi_L \end{pmatrix}. \tag{1.14}$$

Note that Weyl and Dirac equations presented here describe free particles propagating in the vacuum. In particular they propagate isotropically with velocity tensor c in any direction of space. For relativistic semimetals, the underlying crystalline structure is not necessarily isotropic and one should consider the full velocity tensor $v_{ij}, i = x, y, z$. However, for pedagogical reasons we assume isotropic dispersion in the following, unless it is explicitly stated.

1.3.2 Materials

Dirac semimetals correspond to a four band crossing described by Dirac matrices (1.12). They share with their Weyl counterpart a linear dispersion of electronic excitations near the Fermi-level, the particle-antiparticle symmetry and a diverging Fermi wavelength near the band crossing, which make these materials promising for electronics or spintronics applications. Stable Dirac semimetals protected by crystalline symmetries have been predicted [Young et al., 2012, Wang et al., 2012, Wang et al., 2013b] and realized in Na_3Bi [Liu et al., 2014], Cd_3As_2 [Neupane et al., 2014]. Fig. 1.11 shows the crystal structure and ARPES observations of the Dirac cone in Na_3Bi. When the Fermi level is varied through the Dirac cone by doping, the Fermi surface reduces to a point (Fig. 1.11b). The dispersion relation is linear in all three directions of momentum near the cone (Fig. 1.11c).

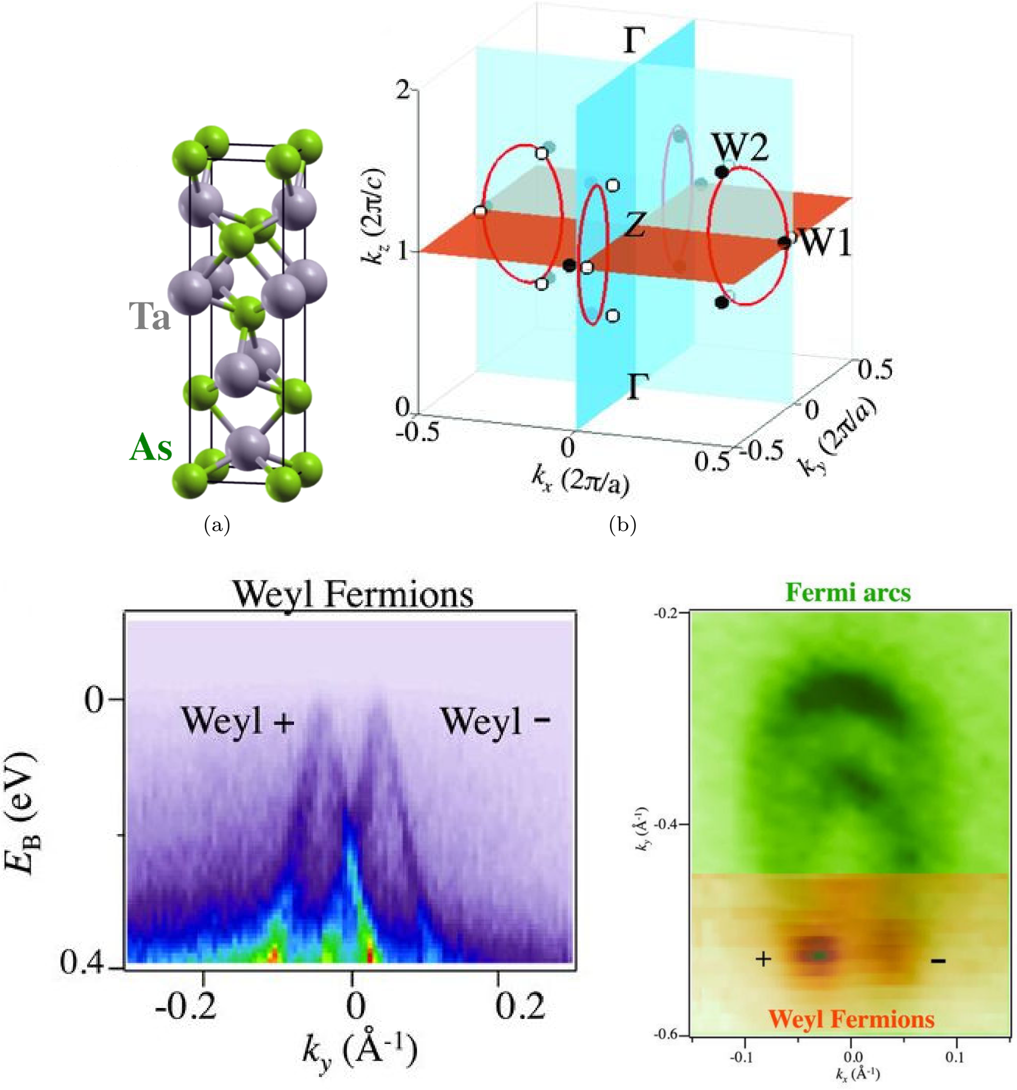

(a) (b)

(c) (d)

Figure 1.12: Weyl Semimetal TaAs. (a) Crystal structure of TaAs. (b) Brillouin Zone and Weyl points (black and white dots). (c) Observation of Weyl points by ARPES. (d) ARPES observation of Fermi arcs connecting the surface projections of Weyl points of opposite chiralities. From [Xu et al., 2015].

The stability of Weyl points is not related to a crystalline symmetry: although two band crossings are accidental, once they exist they are robust [Herring, 1937]. We will present the origin of this remarkable stability in the following. Meanwhile, note that as a consequence Weyl points are not so rare as one could think. For example, a search for Weyl degeneracies in a common material such as bcc Fe has revealed a number of them [Gosálbez-Martínez et al., 2015]. Nevertheless, the presence of Weyl points in this material has no practical consequence because they are located far away from the Fermi level. For the Weyl physics to be observable, the Fermi surface must reduce to the Weyl points i.e. the bands must cross at or very close to the Fermi level and the spectrum must be gapped away from the nodal points. Weyl fermions have recently been discovered, first in photonic lattices [Lu et al., 2015b], but shortly after in the non-centrosymmetric TaAs material class [Lv et al., 2015, Xu et al., 2015], see Fig. 1.12a. Fig. 1.12b shows the location of the six pairs of Weyl points in the Brillouin Zone of TaAs. The ARPES spectrum of a pair of Weyl cones is shown in Fig. 1.12c, displaying conical dispersion. The first proposal for materials containing Weyl cones near the Fermi level was in pyrochlore irridates $A_2Ir_2O_7$ [Wan et al., 2011]. Other early proposals included layered quantum anomalous hall insulators lattice models [Delplace et al., 2012] or magnetically doped topological insulator - trivial insulator heterostructures [Burkov and Balents, 2011]. Note that claims for the existence of a Weyl phase in Anti Ferromagnetic Half-Heusler compounds GdPtBi and NdPtBi under magnetic field have been made recently [Hirschberger et al., 2016, Suzuki et al., 2016, Shekhar et al., 2016]. An interesting review on Weyl materials progress can be found in [Yan and Felser, 2017].

1.3.3 Spectroscopic signature of Weyl points: Fermi arcs

The existence of robust surface states is a unique signature of the presence of Weyl points in the bulk. Between Weyl points of different chiralities open Fermi Arcs have been observed in the surface BZ of Weyl materials [Lv et al., 2015, Xu et al., 2015]. Contrary to ordinary 2D Fermi surfaces, Fermi arcs are open: they terminate at the two Weyl cones. The presence of these surface states with open Fermi surface is a surface manifestation of the presence of Weyl points in the bulk, see Fig. 1.12d. Fermi arc surface states are robust, they can only be gapped out when the Weyl points annihilate.

1.3.4 A signature of Weyl points in transport? The chiral anomaly

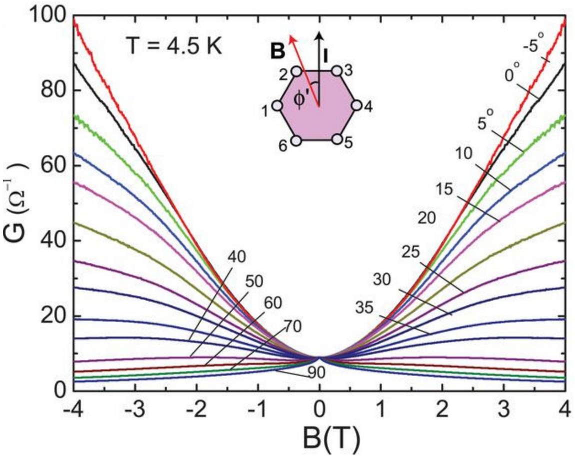

Figure 1.13: Magnetotransport in Dirac Semimetal Na_3Bi. Under a magnetic field, a Dirac cone splits into two Weyl cones of opposite chirality. A positive linear magnetoconcuctance is found when the electric field is applied parallel to the magnetic field, which might originate from the chiral anomaly. From [Xiong et al., 2015].

In the picture of an isolated Weyl cone, Weyl fermions have a well-defined chirality χ. In (1.13) it corresponds to the sign of the right-hand side term. In the general case of a single Weyl Hamiltonian $H = v_i p_i \sigma_i \ \chi$ is given by the sign of the product of velocities along the three directions of space $\chi = \text{sign}(v_x v_y v_z)$. Weyl points come by pairs of opposite chirality, as shown in Fig. 1.12c. However, the number of Weyl fermions of a given chirality is not a conserved quantity of the complete field theory. This is called the chiral anomaly: the chiral symmetry of the Hamiltonian is not conserved by the field theory. As a result, in Weyl materials a chiral current can occur between two Weyl cones in the absence of any explicit intercone coupling term. This manifests as an anomalous electromagnetic response of Weyl semimetals. in the presence of a magnetic field, Landau levels disperse along the field and a parallel electric field can create a chiral current from one cone to another. This chiral current is related to the lowest Landau level which is chiral, i.e. it disperses along the field for a given chirality and in the opposite direction for the other chirality. In a linear response regime, it is expected to give a positive quadratic longitudinal magnetoconductivity: $\sigma_{xx} \propto B^2$. Several experiments have observed this behavior for the magnetoconductivity, as illustrated in Fig.1.13. However, there is ongoing debate whether it can be considered as a smoking gun signature of the chiral anomaly, since other effects like current inhomogeneities might account for this behaviour. We have proposed to investigate the chiral anomaly in a mesoscopic transport setup [Louvet et al., 2017b]. Our study in ballistic Weyl junctions predict that the chiral current can be directly observed, since this setup is intrinsically out of equilibrium and exhibits a direct correspondence between chemical potential in the leads and at the Weyl cones of different chiralities. More details on this work and the chiral anomaly in Weyl materials can be found in Chapter 5. Other manifestations of Weyl physics have been reviewed recently in [Armitage et al., 2018].

1.3.5 Type-II Weyl semimetals

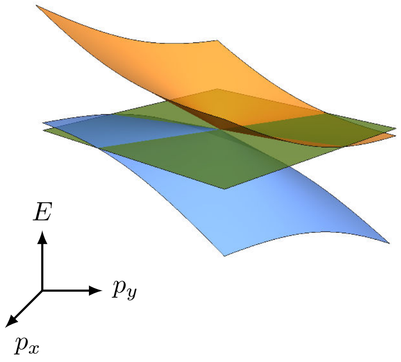

Figure 1.14: Energy spectrum of a Type-II Weyl semimetal at $k_z = 0$. A type II Weyl point contacts the electron and hole Fermi pocket. The Fermi level is highlighted in green for clarity.

Contrary to real relativistic particles, Weyl quasiparticles in solids are not constrained by Lorentz invariance, allowing for tilted Weyl cones. When the tilting is strong enough the Fermi Surface at the crossing is not pointlike anymore but is formed by an electron and a hole pocket contacted at the crossing, see Fig. 1.14. This new type of Weyl phases, called Type-II Weyl Semimetals, have been predicted to exist in materials WTe_2 and $MoTe_2$ [Soluyanov et al., 2015, Sun et al., 2015]. Several properties of overtilted Type-II Weyl semimetals are expected to differ from regular Type-I Weyl semimetals. In particular, whereas the chiral anomaly occurs for any direction of the magnetic field in Type-I Weyl, for Type-II Weyl it occurs only if the magnetic field is within a cone around the tilt axis.

1.3.6 Stability of Weyl and Dirac against disorder: a new quantum phase transition

In conventional materials the only quantum transition caused by the presence of disorder is the Anderson localization transition. Similar to graphene, in the presence of disorder Weyl and Dirac fermions do not necessarily localize. In graphene, disorder drives the system to a diffusive metal phase instead. 3D Weyl and Dirac semimetals are robust in the presence of weak disorder and then undergo a phase transition for a critical disorder strength, towards a diffusive metal phase characterized by a finite density of states at the nodal point [Fradkin, 1986a, Fradkin, 1986b]. Understanding the behavior of disordered Weyl and Dirac semimetals is not only relevant for experiments but now offers entirely new perspectives with the characterization of this novel quantum phase transition. It has triggered a number of studies in the recent years. We have proposed a simple renormalization group (RG) approach to study the transition based on the mapping of the problem to a model from high-energy physics describing Weyl fermions in a random imaginary potential near 4 dimensions [Louvet et al., 2016]. Furthermore, we have predicted a new quantum phase transition when the disorder is spatially correlated [Louvet et al., 2017a]. These studies and the problem of disordered Weyl fermions is adressed in Chapter 3.

1.4 Semimetals beyond Dirac and Weyl

Electrons in graphene, on the surface of topological insulators, in 3D Weyl and Dirac semimetals, share a conical dispersion relation characteristic of massless ultrarelativistic particles and a $E \to -E$ symmetry (with the exception of Type-II WSM, see section 1.3). Another property Weyl and Dirac particles share is their spin (or pseudospin) $S = 1/2$. Beyond these phases, a variety of more exotic semimetals with band crossing exist, carrying either a (pseudo-)spin $S \neq 1/2$ or no definite (pseudo-)spin. In this section, we give a non exhaustive overview of semimetals beyond Dirac and Weyl. Semimetals with three-bands crossing are a natural extension of graphene in 3D. In Chapter 4 we investigate the condition of existence of a finite conductivity at the crossing based on a study of lattice models with three-bands crossing. We find a correlation between the existence of a finite minimal conductivity and a quantized Berry winding around the band crossing. Crossings with locally quadratic or cubic dispersion in some directions can result from the merging of Dirac or Weyl points under given conditions. These so-called multi-Weyl or Semi-Dirac share some of the properties of their linear counterparts. Finally, bands can be degenerate along a line or a closed loop instead of isolated points. This diversity of semimetals with band crossing naturally raises the question of their common properties and characterization. In Chapter 2 we consider the stability of these crossings from the point of view of their topological characterization: we address the question whether a unifying scheme can be applied to describe the stability of a band crossing.

1.4.1 Semimetals with different number of bands

A natural extension of graphene to consider are Semimetals with linear three-bands crossing. Such phases have been realized in 2D and 3D [Wang et al., 2013a, Li et al., 2014, Orlita et al., 2014]. In these materials, the spectrum has $E \to -E$ symmetry, at least locally. As a consequence, the third band is constrained to be locally flat. The dispersion relation near the band crossing thus resembles a Dirac cone, but with an additional flat band, see Fig. 1.15b.

Massless Kane fermions characterized by a 3-band crossing with a locally flat band have been observed in critical HgCdTe [Orlita et al., 2014]. HgTe and CdTe are semiconductors with reverse band ordering; in HgTe the valence and conduction band are inverted with respect to the conventional ordering of bands according to their symmetries. In CdTe, bands are ordered following the conventional order, similar to atomic orbitals. A band inversion therefore occurs for a finite cadmium content, where the gap closes. Beyond the band inversion point, the system is a topological insulator that is characterized by robust edge states [Bernevig et al., 2006]. At the critical point, two conical-like bands are degenerate together with a nearly-flat heavy hole band. The energy band gap has been estimated to $E_g = 4meV$ in [Orlita et al., 2014]. Low-energy excitations, named Kane fermions [Orlita et al., 2014], are relativistic-like with linear dispersion and particle-antiparticle symmetry. Under a magnetic field, Landau levels from the dispersing bands have the characteristic $\propto \sqrt{B}$ dependence originating from the linear dispersion. Magneto-absorption measurements have confirmed this characteristic dependence, while the flat band manifests through new allowed transitions not present for Dirac and Weyl materials [Orlita et al., 2014]. However Kane fermions have no definite pseudospin and lack symmetry or topological protection: they require fine tuning of the system parameters (cadmium content) to be observed. Claims have been made that electronic excitations in the intermediate energy range in Cd_3As_2 are Kane fermions [Akrap et al., 2016].

In 2D, a three-band crossing has been observed in a MoS_2 allotrope [Li et al., 2014]. Low energy electrons at the crossing behave like Spin-1 particles. The simplest lattice realization of such Spin-1 quasiparticles is realized in the so-called dice or $\mathcal{T}_3$ lattice, an hexagonal lattice with an extra atomic site in the hexagon center, see Figure 1.15. The dice lattice has three sublattices (A_1, A_2, B): hub sites B are connected with 6 nearest neighbors from the two rim sublattices A_1, A_2. For rim sites, they only connect with three nearest neighbors from the hub sublattice. The symmetry between the two rim sublattices enforces a $E \to -E$ symmetry of the spectrum and the flatness of the third band. On the edges of the Brillouin zone, the three bands are degenerate with spin-1 excitations near the crossing. A proposal for the realization of this model in photonic lattices has been made [Bercioux et al., 2009], and a modified version of the $\mathcal{T}_3$ model, the so-called $\alpha - \mathcal{T}_3$ model, allows for continuous interpolation between $S = 1/2$ and $S = 1$ quasiparticles [Raoux et al., 2014]. An electronic realization of the Lieb lattice on a copper surface has been proposed [Slot et al., 2017]. The Lieb lattice is a tight-binding model based on a modified square lattice with three sublattices, two of them located on the x and y-oriented edges and one on the squares' corners. The symmetry between edge sublattices enforces a $E \to -E$ symmetry of the spectrum, hence the flat band. The two dispersing bands touch linearly at the center of the Brillouin Zone, where Spin-1 excitations emerge.

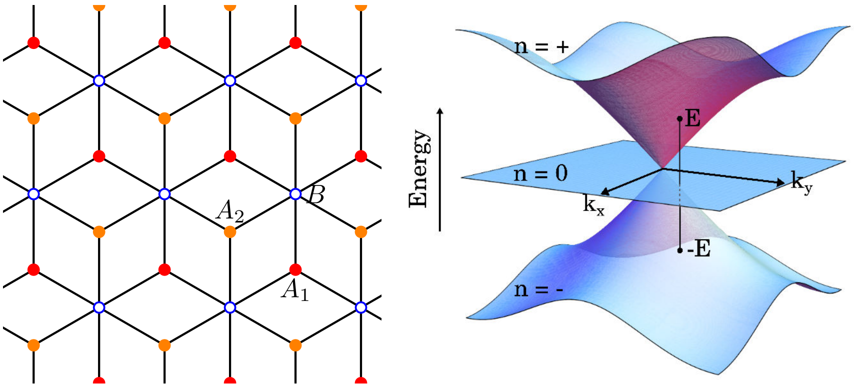

(a) (b)

Figure 1.15: The dice, or $\mathcal{T}_3$, lattice. (a) Lattice structure. (b) Conical dispersion relation with a flat band near the band crossing.

Three-band semimetals with a flat band have been among the first phases discovered beyond Dirac or Weyl semimetals in 2D or 3D. They either emerged “accidentally“, from experience, or were first designed theoretically, as toy models, and then specific tailor-made materials were designed to observe these phases. Later, a thorough investigation of non-symmorphic dual space groups revealed that other threefold, sixfold, fourfold and eightfold band crossings can be found in bulk materials [Bradlyn et al., 2016]. In particular spin-1 quasiparticles and spin-3/2 quasiparticles are predicted to emerge, respectively around three-bands and four-bands crossings.

Planar lattice models with three-band crossing offer the simplest extension of graphene. We have used them as an investigation ground to unveil the condition of existence of a finite conductivity at a band crossing. This allowed us to gain a deeper understanding of the origin of minimal conductivity in graphene, as detailed in Chapter 4.

The variety of different phases with linear band crossings with different number of bands and different dimensionality offers a wealth of possibility to observe interesting physical phenomena. In planar materials, the chemical potential can be tuned easily with a gate voltage using a capacitive effect. In bulk materials, the Landau levels states under a strong magnetic field disperse along the direction of the magnetic field. Quantities like the density of states also scale differently depending on the dimension. Materials with different number of bands will show different interband optical transitions, for instance. Hence the possibility to observe relativistic electronic phenomena in different dimensions and different materials is promising for conceptual studies as well as for applications.

1.4.2 Merging cones: semi-Dirac, multi-Weyl

When two band crossings are brought together at the same point in momentum space, either a gap can open or a different band crossing with specific properties results from the merging. In particular, the dispersion can become quadratic or cubic along some directions of momentum space. The merging of cones in graphene can in theory be realized by applying a strain. In this strained graphene, when the two Dirac cones from opposite valleys merge there is a transition towards an insulator. Exactly at the critical point where the merging occurs, there a critical phase with no band gap and anisotropic dispersion. The dispersion at the critical point is quadratic along the direction of the merging and linear in the orthogonal direction [Hasegawa et al., 2006, Dietl et al., 2008]. This hybrid band crossing is referred to as a semi-Dirac cone, and has been realized for example in artificial graphene made from an optical honeycomb lattice [Tarruell et al., 2012]. When 2D Dirac cones of the same valley are sent onto one another as in bilayer graphene, the band degeneracy remains but with now quadratic dispersion. As graphene, bilayer graphene has no band gap, however its electronic excitations are not massless Dirac fermions but massive quasiparticles with parabolic dispersion. As a consequence, Landau level dispersion and Quantum Hall Effect in bilayer graphene is distinct from monolayer graphene [McCann and Fal’ko, 2006].

In 3D, Weyl cones carry a monopole charge analogous to the charge of an electromagnetic monopole. This charge is related to the winding of the pseudospin around the Weyl point. As a result, Weyl cones can only annihilate by pairs of opposite charge. When two Weyl cones with opposite charge merge, a

Dirac cone appears as a critical phase between the Weyl semimetal phase and the insulating phase. The fusion of two or three Weyl cones with the same charge gives two-band crossings with double or triple topological charge and an anisotropic dispersion relation. Double Weyl nodes are two-band crossings formed by the fusion of two Weyl nodes. They show quadratic dispersion along two directions and linear dispersion in the third. Triple Weyl nodes, two-band crossings originating from three Weyl nodes with the same charge, show cubic dispersion along two directions and linear dispersion in the third one. Multi-Weyl cones have been proposed to occur along rotation symmetry axis [Fang et al., 2012]. Breaking the rotation symmetry splits the Multi-Weyl nodes into several (two or three) Weyl nodes, the global topological charge being conserved. The ferromagnetic compound $HgCr_2Se_4$ has been predicted to host a Double Weyl node [Xu et al., 2011].

1.4.3 Line node semimetals

So far, we have mentioned semimetals in which the conduction and valence bands touch at isolated points in the Brillouin Zone. Band degeneracies can also occur along extended lines or loops in the Brillouin Zone. They are protected by crystal symmetries, either mirror symmetry or the combination of time reversal and inversion [Chiu et al., 2016]. Line nodes in bulk materials can carry a topological charge corresponding to a phase winding for Bloch eigenstates circulating around the line. As a consequence of this bulk topological charge, 3D line node semimetals show protected surface states [Burkov et al., 2011]. Several material realizations of line node semimetals have been reported [Chiu et al., 2016] A 2D line node semimetal with 1D Fermi Surface has also been realized in monolayer Cu_2Si [Feng et al., 2017].

There is a large number of semimetals with band crossing beyond the historical examples of Graphene, Dirac and Weyl semimetals. This presentation is not exhaustive and yet other semimetals remain to be identified. Are they all unique or do they share some common trends? We have given this overview as a motivation to search for unifying properties and a universal method to characterize these materials.

1.5 Characterization of relativistic semimetals via topology

Why are band crossings stable? We have seen with the two examples of Graphene and Weyl semimetals that this question can have different answers. In Graphene the stability is related to the presence of crystalline symmetries while a Weyl point is robust in the absence of any symmetry. The stability of Weyl cones is related to a winding of the pseudospin around the node. This winding is associated with a charge analog to the charge of a magnetic monopole. As we will see below, this charge has a topological origin.

As we have already mentioned, the physics of band crossings can be related with topological properties of the manifold of electronic states indexed by momenta on the Brillouin Zone. The band touching point is analogous to a topological defect such as a vortex in 2D around which the phase of electronic states winds non trivially. This is the case in graphene and Weyl semimetals. In this section, we introduce the notion of topological properties of semimetals through the examples of graphene and Weyl semimetals. These notions will be further studied in the next chapter.

1.5.1 Topological semimetals: Weyl semimetals

Stability of the Weyl points

In Weyl semimetals, low energy excitations are described by the Weyl equation (1.13) involving the three Pauli matrices. Since the Pauli matrices together with the identity matrix form a basis of 2×2 matrices, no extra matrix can be found to add a mass term to the equation. Weyl fermions are massless, their dispersion is linear and cannot be gapped through a local perturbation. Any perturbation will only shift the Weyl point in momentum space. This stability of Weyl nodes, in the absence of any symmetry, guarantees that if a two band crossing occurs in three dimensions, it is stable. However, note that the energy of the Weyl point does not a priori coincide with the Fermi energy: therefore, all materials with Weyl nodes in their band structure are not Weyl semimetals.

At the origin of the Stability: a topological Charge

This robustness of two-band crossings in three dimensions of space has a topological origin: they carry a topological charge, embodied by a topological invariant, the Chern number. This property is associated with a geometric quantity in momentum space analogous to a magnetic field, the Berry curvature. Weyl points act as magnetic monopoles in momentum space, see Fig. 1.16: they are sources or sinks of Berry

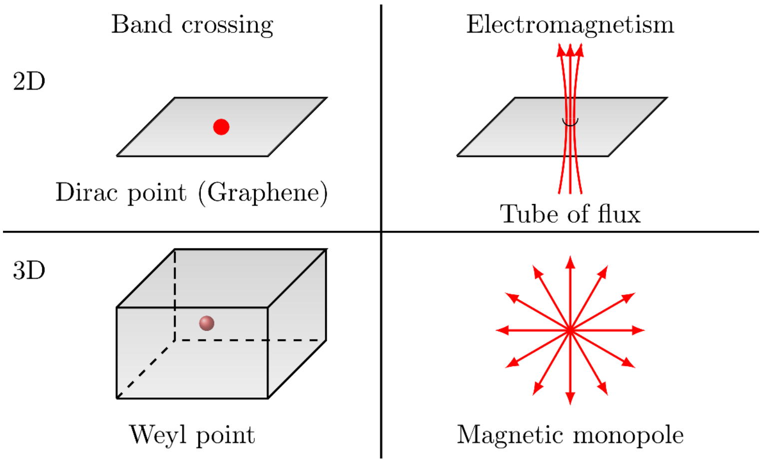

Figure 1.16: Analogy between band crossings and electromagnetics. A 2D Dirac point in graphene is analogous to a magnetic tube of flux: when circling the Dirac point electronic states acquire an finite additional phase, the so-called Berry phase. In 3D, a Weyl point is analogous to a magnetic monopole: it is a source of Berry flux, a quantity defined in momentum space analogous to a magnetic flux.

flux [Berry, 1985]. The charge of this Berry monopole is related to the chirality of the Weyl point (1.13). A dramatic consequence is that Weyl points can only be created or annihilated by pairs of opposite chirality. Besides their robustness, the topological charge associated with Weyl fermions is expected to give rise to an anomalous Quantum Hall Effect, the existence of protected Fermi arc surface states and anomalous responses related to the chiral anomaly, i.e. the non-conservation of the number of left and right-Weyl particles.

Manifestation of the topological charge: robust surface states

The most characteristic feature of topological matter, from the Quantum Hall Effect to Topological Insulators is the existence of robust surface states. In Weyl semimetals as well we have seen that Fermi Arc surface states have been observed, see Fig. 1.12d. To understand the origin of these Fermi Arcs Surface States, consider the low-energy case: the bulk Fermi surface consists of two well separated Fermi pockets surrounding the two Weyl points of opposite chiralities. Any 2D slice of the 3D BZ that is contained in between the Weyl points is a non trivial topological insulator: it is gapped, and the Berry flux connecting the two Weyl points goes through the slice. Hence, this insulator is topologically non trivial, characterized by a Chern number. As we shall see in the next chapter, topological insulators posses protected edge states. In fact, the existence of protected edge states is the signature of a topological charge of the bulk material. Fermi Arcs surface states can be seen as the collection of the edge states of the 2D topological insulators located between the Weyl nodes [Wan et al., 2011].

Manifestation of the topological Charge: quantum anomalous Hall effect

Consider the minimal example of a WSM with 2 Weyl nodes. Each 2D plane contained between the Weyl points is a 2D topological Chern insulator. A 2D Chern insulator with Chern number C_1 is characterized by a quantized transverse conductance $\sigma_{xy} = C_1 \frac{e^2}{h}$. This quantization of the conductance is the Quantum Hall Effect, see next Chapter. Here $C_1 = 1$, hence any 2D slice between the two Weyl cones will contribute to the Hall conductance by a quantum $\frac{e^2}{h}$. The number of such 2D topological insulators depends on the separation between the Weyl nodes. Thus, the WSM gives an anomalous Hall effect characterized by a Hall conductance proportional to the cones separation in momentum space. The momentum separation between cones plays a role analogous to an intrinsic magnetic field.

Weyl points and topological insulators: topological phase transition

We have seen that Weyl points carry a topological charge associated with a Berry flux. As a consequence, a Weyl node can only be gapped out by merging pairwise with a Weyl node of opposite charge. Furthermore, any 2D slice of the Brillouin Zone that is located between the nodes is threaded by a non zero Berry flux: it is a non trivial 2D topological insulator. Now imagine as a gedanken experiment that we want to gap out this Weyl phase with two Weyl points. To do so, we must merge the Weyl points. Exactly at the merging point, the two cones superpose and form a Dirac node, which is unstable in the absence of symmetry: therefore, any perturbation will then gap the system. We will see in the following that for symmetry reasons Weyl cones can only merge at time-reversal invariant momenta $\mathbf{k} = -\mathbf{k}$. Hence, there are two ways of merging the Weyl cones: either merge the Weyl cones in the center of the Brillouin Zone or on the edge of the Brillouin Zone. In the first case, the zone threaded by a non zero Berry flux is shrinked and vanishes when the Weyl cones come to coincide. The gapped phase thus obtained contains no net Berry flux, it is topologically trivial. On the contrary, in the second case where the Weyl cones come to coincide on a BZ edge the non-trivial topological region expands to the whole BZ. The gapped phase obtained after the cones have annihilated is threaded by a non zero Berry flux: it is topologically non trivial and possesses protected surface states.

This thought experiment demonstrates that a Weyl phase can be seen as a critical phase between two insulating phases of distinct topological nature. In reality things are a bit more complex as we shall see in the next chapter. Nonetheless, the line of thought is similar.

The Weyl semimetal is the first example of a gapless topological semimetal. Weyl points carry a topological charge described by a Chern number, which manifests in the presence of protected Fermi arcs surface states and a quantized transverse conductance in the absence of magnetic field: a Quantum Anomalous Hall Effect.

1.5.2 Symmetry protected semimetal: graphene

Contrary to Weyl points, the stability of Dirac points in Graphene is guaranteed by crystalline symmetries. Still, low energy electrons in graphene carry a pseudospin which winds when electrons circulate around the Dirac point. We will see below that this quantized winding is related to a Berry phase. Graphene is a good pedagogical example to illustrate the topological characterization of band crossings.

Stability and symmetries

The two energy bands of graphene cross linearly at two points $\mathbf{K}$ and $\mathbf{K}'$ in the Brillouin Zone. The low-energy Hamiltonian in these valleys is gapless and linear: it corresponds to the 2D massless Dirac Hamiltonian (1.10). In graphene the stability of the gapless points requires the presence of extra symmetries to kill the mass term in (1.10). The two valleys are related by time-reversal $\mathcal{T}$ and inversion $\mathcal{P}$ symmetries. The stability of Dirac points is guaranteed by the presence of these two symmetries: only a perturbation that breaks inversion symmetry or time-reversal symmetry will open a gap at the conical points. As we already mentioned, the inversion symmetry is related to the equivalence between sublattices A and B, both occupied by carbon atoms. When for example graphene is put on top of hexagonal boron-nitride h-BN, where one sublattice is filled with a boron atom and the other with a nitrogen atom, the inversion symmetry is broken and a gap opens [Castro Neto et al., 2009].

Topological characterization: quantized Berry phase

The protection of the Dirac point with respect to symmetry-preserving perturbations is associated with a peculiar geometric property of Dirac eigenstates, a π-quantized Berry phase. When winding around the nodal point $\mathbf{K}$, the Bloch eigenstates acquire a phase of $\pm\pi$, depending on whether it belongs to the upper or lower Dirac cone. This winding signals that there is a singularity at the crossing, analogous to a tube of flux threading the 2D Brillouin Zone, as described in Fig. 1.16. In the opposite valley $\mathbf{K}'$, the Bloch states' phase winds the opposite way: the Berry phase in the upper Dirac cone is $-\pi$. As a result, the total Berry phase in the Brillouin Zone sums up to zero.

Edge states

As a consequence of the topological Berry phase, metallic edge states can appear in graphene ribbons, depending on the orientation of the ribbon. The presence or absence of edge states is related to the integral of the Berry phase along the 1D Brillouin Zone of the ribbon, the so-called Zak phase. They appear for orientations for which the Zak phase takes non trivial values [Delplace et al., 2011].

Relativistic quantum Hall effect and topological Berry phase

Another manifestation of the topological Berry phase is the Relativistic Quantum Hall Effect in the presence of a magnetic field. In a strong magnetic field, energy bands of graphene collapse into Landau Levels, see Fig. 1.8. The presence of Landau Levels manifest through transverse conductance plateaux when the chemical potential lies between Landau Levels: in graphene the Hall conductance reads $\sigma_{xy} = 4(n+1/2)\frac{e^2}{h}$, where n is an integer (which can be negative) indexing Landau Levels. In contrast, in a conventional 2D electron system with parabolic dispersion the Hall conductance reads $\sigma_{xy} = ne^2/h$. The 1/2 shift of Landau Levels is characteristic of relativistic electrons in graphene. From a semiclassical description of the cyclotron orbits of electrons in the presence of the magnetic field, one can show that the $\frac{1}{2}$ shift originates from the π-quantized Berry phase [Goerbig, 2011].

Dirac model as a topological critical model

Consider the massive Dirac Hamiltonian:

$$H = k_x\sigma_x + k_y\sigma_y + m\sigma_z. \tag{1.15}$$

The low-energy Hamiltonian of graphene (1.3) is recovered from (1.15) when $m = 0$. Thus, the Dirac Hamiltonian of the $\mathbf{K}$ valley in graphene can be seen as a critical phase between two gapped phases described by (1.15) with $m > 0$ and $m < 0$. One can compute the Berry flux threading the valence band on each side of the transition, see next chapter, and find that the closing of the gap at $m = 0$ is associated with a change of Chern number $\Delta C_1 = 1$ when m changes sign. Thus, the emergence of 2D massless Dirac fermions at $m = 0$ is associated with a phase transition between two insulating phases of distinct topological nature. The first proposal for the study of this transition [Haldane, 1988] marked a milestone in the understanding of topological insulators.

1.5.3 From 3D Dirac to Weyl semimetals

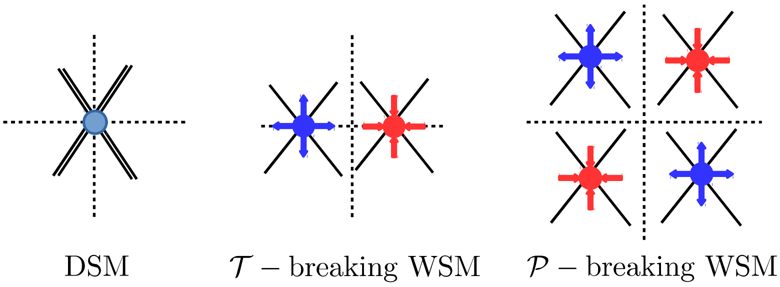

Figure 1.17: In a Dirac Semimetal (DSM) bands are doubly degenerate whereas in a Weyl Semimetal (WSM) the degeneracy is lifted due to time-reversal symmetry breaking or inversion (parity) symmetry breaking. Weyl points act as magnetic monopoles in momentum space and hence they can only be created or annihilated by pairs. On the contrary, Dirac points need to be stabilized by crystalline symmetries.

The three-dimensional massless Dirac cone consists of two Weyl points of opposite chiralities. As a result, the topological charge associated with a 3D Dirac point is zero: the charges of the Weyl points cancel each other. Thus the Dirac point is unstable in the absence of extra symmetries. In particular, it requires time-reversal ($\mathcal{T}$) and spatial inversion ($\mathcal{P}$) symmetry. Time-reversal acts following $\mathcal{T} : t \to -t$. Time-reversal symmetry is broken in the presence of an external magnetic field or in magnetic materials. Spatial inversion $\mathcal{P} : \mathbf{r} \to \mathbf{r}$ is related to the crystalline structure. Inversion symmetry is broken in non-centrosymmetric lattices or under lattice strains. When both $\mathcal{T}$ and $\mathcal{P}$ are present, the bands are doubly degenerate everywhere in the Brillouin zone due to Kramers theorem, and Weyl points (WP) of opposite chirality are sent onto one another at momenta that are even under inversion $\mathbf{k} = -\mathbf{k}$. When either the inversion or time-reversal invariance is lost, a Dirac point will split into a pair of Weyl points with opposite chiralities, see Fig. 1.17. Weyl fermions must therefore be sought in materials where either inversion or time-reversal symmetry is broken. Spatial inversion relates Weyl points with opposite chiralities: hence, the minimal number of Weyl points in $\mathcal{T}$-breaking materials (magnetic Weyl SM) is two, at opposite momenta. Time reversal sends a Weyl point onto another point with the same chirality:

therefore a non-centrosymmetric Weyl SM will contain at least four Weyl points in the Brillouin Zone, e.g. two WP with positive charge at $\pm\mathbf{k_1}$ and two WP with negative charge at $\pm\mathbf{k_2}$.

1.5.4 General argument for the stability of two-band crossings

We have introduced the notion of stability of band crossings in relation with topological properties, based on the examples of Graphene and Weyl semimetals. We have seen that some band crossings are naturally stable, while other require extra symmetries or fine tuning to exist. In order to understand the mechanisms at work behind the stability of band crossings, we present here a general argument to predict the possibility and the stability of a two band crossing, depending on the dimensionality of the system and the number of symmetry constraints.

Band crossings are typically avoided crossings because of level repulsion but sometimes a symmetry enforces the crossing. The possibility and stability of band degeneracies has been investigated already in the early days of band theory as a general problem [Herring, 1937], and in the context of graphene and graphite in [Wallace, 1947].

In the following, we assume for simplicity that the two bands are well separated in energy from the rest of the spectrum, and focus on the effective Hilbert space spanned by the two crossing states.

Two-band crossing in 1D

Take a one-dimensional crystal - a chain of atomic sites - with two orbitals per site, giving two bands. Suppose the bands touch at some point K of the Brillouin zone. For simplicity, we assume the contact occurs at zero energy: $H(K) = 0$. A Taylor expansion of the Hamiltonian near K reads

$$H(K+q) = \hbar v_i \sigma_i q + \hbar v_0 q \ \mathbb{1} + \mathcal{O}(q^2), \tag{1.16}$$

where σ_i are the Pauli matrices and $\mathbb{1}$ the 2×2 identity matrix. We can always chose the basis (rotate the pseudospin) such as to recover

$$H(K+q) = \hbar v_z \sigma_z q + \hbar v_0 q \ \mathbb{1}. \tag{1.17}$$

The low-energy dispersion relation reads:

$$\varepsilon_\pm(q) = \hbar v_z q \pm \hbar v_0 q \tag{1.18}$$

The spectrum is linear as expected, except when the crossing is also a local energy extremum,in which case $v_0 = v_z = 0$. Note that in 1D the two bands are either degenerate at isolated points only, or in the whole Brillouin zone. More importantly, note that in the absence of specific symmetries any perturbation can add a term non vanishing at point K, proportional to σ_x or σ_y, and so lift the degeneracy. Hence, band degeneracies are not stable in general in 1D. They need to be enforced by extra symmetries.

Two-band crossing in 2D

Going to two dimensions, the Bloch Hamiltonian in the vicinity of the crossing can be cast under the general form via the appropriate choice of pseudospin orientation:

$$H(\vec{K}+\vec{q}) = \hbar v_x q_x \sigma_x + \hbar v_y q_y \sigma_y + (a_x q_x + a_y q_y)\mathbb{1}, \tag{1.19}$$

where v_i and a_i, $i = x, y$ are real coefficients. The crossing occurs at an isolated point provided $v_i \neq 0$. The spectrum is linear:

$$\varepsilon_\pm(\mathbf{q}) = a_x q_x + a_y q_y \pm \sqrt{\hbar^2 v_x^2 q_x^2 + \hbar^2 v_y^2 q_y^2}. \tag{1.20}$$

The first term gives a tilt of the conical dispersion. An external perturbation can add a mass term proportional to σ_z in (1.19) and gap the spectrum. Hence band crossings in two dimensions must be protected by a symmetry. In graphene a mirror symmetry protects the 2-band crossings on the edge of the Brillouin zone. The low-energy excitations are described by Hamiltonian (1.19) with no tilting $a_i = 0$ and isotropic dispersion $|v_x| = |v_y| \simeq 10^6 \text{m.s}^{-1}$. In graphene the two band crossings come with different chirality: the chirality is given by the respective sign of the coefficients v_i which encodes how the Bloch states' pseudo-spin rotates with momentum around the node. Spatial inversion exchanges the two valleys and the chirality. When inversion and time-reversal symmetry are broken, it is possible to open a gap only in one of the valleys [Haldane, 1988].

Two-band crossing in 3D

Consider a two-band crossing point $\vec{K}$ in a three-dimensional momentum space. The low-energy 2×2 Hamiltonian can be cast into the form:

$$H(\mathbf{K}+\mathbf{q}) = (\hbar v_x q_x \sigma_x + \hbar v_y q_y \sigma_y + \hbar v_z q_z \sigma_z) + (a_x q_x + a_y q_y + a_z q_z)\mathbb{1}. \tag{1.21}$$

The dispersion relation reads:

$$\varepsilon_\pm(\mathbf{q}) = a_x q_x + a_y q_y + a_z q_z \pm \sqrt{\hbar^2 v_x^2 q_x^2 + \hbar^2 v_y^2 q_y^2 + \hbar^2 v_z^2 q_z^2}. \tag{1.22}$$

Adding a perturbation to the Hamiltonian (1.21) would only shift the crossing point in momentum space. This is because any perturbation term can be written in terms of the Pauli matrices and the identity, which form a basis of 2×2 hermitian matrices. Therefore a two-bands crossing in three-dimension momentum space, when it exists, is robust. The low-energy Hamiltonian describes a Weyl cone (1.21). The chirality χ of the Weyl cone depends on the respective signs of the v_i coefficients which encodes the orientation of (pseudo-)spin-momentum locking: $\chi = \text{sign}(v_x v_y v_z)$. The a_i coefficients correspond to a tilting term: when the tilt becomes large the Fermi surface can go from an isolated point to two Fermi pockets with contact at the Weyl point. Materials with such strongly tilted Weyl cones are called Type-II Weyl semimetals, see 1.3

The immediate question is then: where/why/when does a two-band crossing occur? The reasoning that follows is largely inspired by the work of [Murakami, 2007]. Consider a generic two-band Hamiltonian in d-dimensional momentum space,

$$H(\vec{k}) = f_1(\vec{k})\sigma_x + f_2(\vec{k})\sigma_y + f_3(\vec{k})\sigma_z + f_0(\vec{k})\mathbb{1}, \tag{1.23}$$

where f_0, f_i are real functions. Note that the identity term has no influence on the matter of band degeneracies; it merely shifts the energy of the two bands. We can therefore set $f_0 = 0$ before carrying on. A band crossing will occur if there exists a point $\vec{K}$ such that $f_i(\vec{K}) = 0,\ i = 1, 2, 3$. These three equations will constrain 3 of the d degrees of freedom which determine[1] $\vec{K}$.

If there are more constraints than degrees of freedom, $d < 3$, the problem has no solutions. Fine tuning of additional external parameters is required. This is the case for $d = 2$; an extra symmetry is required to cancel one of the f_i and lower the number of constraints. In graphene a mirror symmetry plays this role [Chiu et al., 2016].

When $d = 3$, $\vec{K}$ is entirely determined by the set of equations: there is a discrete set of solutions. The robustness against weak perturbations implies that these solutions exist in a finite region of external parameters. Thus in $3d$ solids two-band crossings occur generically. The question of whether these crossings are close to the Fermi Surface then determines the semimetallic nature of the material.

When $d > 3$, the problem is under-determined: there is an infinite number of solutions, which form a vector space of dimension $d - 3$. It can be a line, a surface... Similarly, specific crystal symmetries in 3D can lower the number of constraints and protect line degeneracies, see section 1.4.3.

1.6 Organisation of the thesis

Semimetals share similar spectrum properties: they are gapless semiconductors with band degeneracies in the Brillouin Zone. A variety of them are relativistic, showing linear dispersion around the crossing.

We have seen that the relativistic nature of electrons has physical consequences, measurable via transport or spectroscopic experiments. The stability of these phases has different origins. It may come from an underlying robustness or be enforced by symmetries. Other crossings occur as critical phases and require fine tuning. This thesis addresses the question whether each relativistic semimetal has to be considered as a unique specimen or whether they form a class of material sharing common trends. To attempt to answer this question, we have studied relativistic semimetals from the point of view of the stability of the crossings in relation with their topological properties and in the presence of disorder. We have also investigated how the relativistic nature of electrons in these materials manifests in electronic transport.

Part I focuses on the stability and robustness of nodal points where relativistic quasiparticles emerge. Chapter 2 aims at a unified characterization of nodal points in terms of symmetries and topological invariants. Chapter 3 concerns the effect of disorder, i.e. impurities in the system.

---

[1] The number of constraints is also called the codimension of the set of solutions.

In part II, we study transport properties of semimetals in relation with the relativistic properties of the electrons. Chapter 4 presents our study on the conditions of existence of a finite conductivity at the nodal point. In chapter 5 we report about our investigation of the chiral anomaly in ballistic Weyl junctions, a unique property of Weyl fermions and its consequences on magnetotransport.

The original work presented in this thesis has led to the following publications:

[Louvet et al., 2015] Louvet, T., Delplace, P., Fedorenko, A. A., and Carpentier, D. (2015). On the origin of minimal conductivity at a band crossing. *Physical Review B*, 92(15):155116.

[Louvet et al., 2016] Louvet, T., Carpentier, D., and Fedorenko, A. A. (2016). On the disorder-driven quantum transition in three-dimensional relativistic metals. *Physical Review B*, 94(22):220201.

[Louvet et al., 2017a] Louvet, T., Carpentier, D., and Fedorenko, A. A. (2017). New quantum transition in Weyl semimetals with correlated disorder. *Physical Review B*, 95(1):014204.

[Louvet et al., 2017] Louvet, T., Houzet, M., and Carpentier, D. (2017). Signature of the Chiral Anomaly in Ballistic Magneto-Transport. *arXiv:1711.06657 [cond-mat]*.

Part I

Stability and Robustness of Band Crossings

Chapter 2

Topological Properties of Nodal Points

Some peculiar physical properties of band crossings take their origin in geometrical and topological properties of electronic states. Geometrical phase effects, windings of the phase of electronic states around band degeneracies have observable consequences like the existence of protected edge states. These properties have a strong connection with topology: they are topological in the sense that they are insensitive to continuous local deformations. We first introduce the notion of topological properties of electronic phases in the context of insulators where these notions have been developed, before applying them to the characterization of band crossings.

The section 2.1 of this chapter presents, in analogy with electromagnetism, the notions of Berry phase and Chern number. These notions will be useful to characterize the topological properties of electronic phases in solids. Section 2.2 reviews the topological properties of insulators. Section 2.3 presents why semi-metals exist as critical phases at topological transitions between different topological insulators. Then, section 2.4 reviews the usual characterization of the stability of semi-metallic phases, based on crystal symmetries and symmetry-related topological invariants. Finally in section 2.5, we propose a topological characterization of semi-metals independent of the Brillouin Zone symmetries and investigate its validity on simple extensions of graphene, three-band semimetals.

2.1 Topological characterization: Berry phase and Chern number

The Berry phase is the momentum space analog of the phase dephasing acquired by an electron moving in a magnetic potential. In electromagnetism, this phase dephasing can be measured by an interference experiment such as the one considered by Aharonov and Bohm [Aharonov and Bohm, 1959]. The Berry phase is related to the gauge degree of freedom for the definition of a phase for wavefunctions, similarly to the gauge invariance for electrodynamics. This phase is measurable and detects the presence of singularities in the band structure, associated with degeneracy points that are sources or sinks of Berry flux, analogous to the Dirac monopoles for magnetic field.

2.1.1 Measuring a source of magnetic flux at distance? The Aharonov Bohm effect

The Aharonov-Bohm experiment [Aharonov and Bohm, 1959] allows to detect the presence of a magnetic flux even though the electrons are never in interaction with the magnetic field. It has brought to light the physical reality behind vector potentials in quantum mechanics.

Consider two electron paths going opposite sides of a solenoid, as in Figure 2.1. The solenoid of radius R is threaded by a magnetic field $\mathbf{B}$, orthogonal to the electrons' trajectory. in the absence of magnetic field, the electronic wavefunctions take the simple plane wave form[1] $\psi(\mathbf{r}) = Ae^{\mathrm{i}\int_0^{\mathbf{r}} \mathbf{k}\cdot d\mathbf{x}}$. After the solenoid, the two wavefunctions amplitudes recombine and the electron density probability reads

---

[1] The choice of the origin 0 corresponds to a global phase.

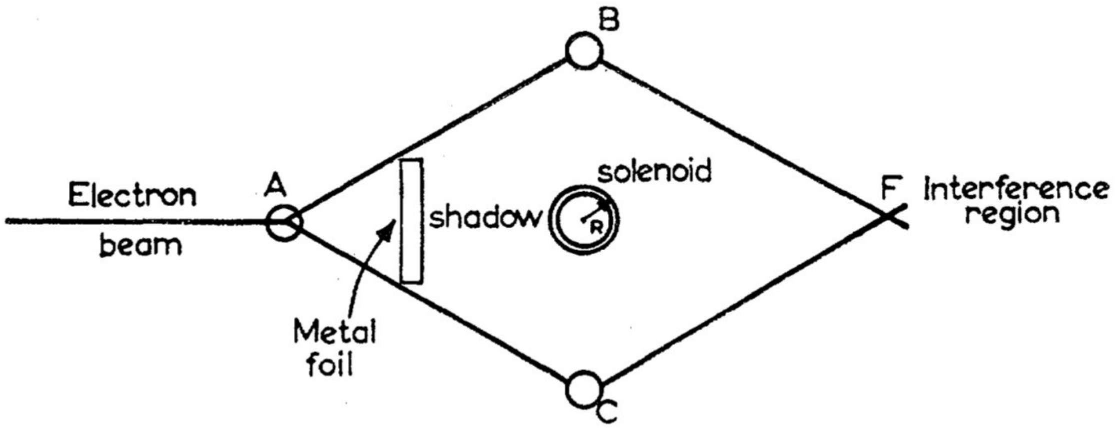

Figure 2.1: Schematics of the interference experiment proposed by Aharonov and Bohm to demonstrate the effect of a time-independent magnetic vector potential on charged particles even in regions where there is no magnetic field. From [Aharonov and Bohm, 1959].

$|Ae^{i\int_{C_1}\mathbf{k}d\mathbf{x}} + Ae^{i\int_{C_2}\mathbf{k}d\mathbf{x}}|^2 = 2A^2\left(1+\cos k\left(\int_{C_1}\mathbf{k}d\mathbf{x} - \int_{C_2}\mathbf{k}d\mathbf{x}\right)\right)$. The dephasing between paths C_1 and C_2 is simply proportional to the path difference, as for the usual two-slits interference experiment.

When the magnetic field is present, the free electron Hamiltonian modifies according to:

$$H = \frac{(\hat{\mathbf{p}} + e\mathbf{A})^2}{2m}, \tag{2.1}$$

where m is the electron mass and $(-e)$ the electron charge. In the regions away from the solenoid where $\mathbf{B} = \mathbf{0}$ but $\mathbf{A} \neq \mathbf{0}$ the presence of the magnetic vector potential gives the free-electron solution ψ_0 an extra phase term: $\psi_{\mathbf{A}}(\mathbf{r}) = e^{i\frac{e}{\hbar}\int_0^{\mathbf{r}}\mathbf{A}d\mathbf{x}}\psi_0(\mathbf{r})$. The additional dephasing between electrons moving on either sides of the solenoid is therefore:

$$\Delta\phi = \frac{e}{\hbar}\left(\int_{C_1}\mathbf{A}d\mathbf{x} - \int_{C_2}\mathbf{A}d\mathbf{x}\right). \tag{2.2}$$

Outside the solenoid where the magnetic field vanishes $\mathbf{B} = \mathbf{0}$, the vector potential is irrotational since $\mathbf{B} = \boldsymbol{\nabla}\times\mathbf{A} = \mathbf{0}$, so the integral of $\mathbf{A}$ along a closed loop vanishes. Therefore

$$\Delta\phi = \frac{e}{\hbar}\oint_{\partial\mathcal{S}}\mathbf{A}d\mathbf{x} = \frac{e}{\hbar}\oiint_{\mathcal{S}}\mathbf{B}d\mathbf{S} = 2\pi\frac{\Phi}{\phi_0}, \tag{2.3}$$

where $\mathcal{S}$ is the solenoid section, Φ the magnetic flux threading the solenoid and $\phi_0 = \frac{h}{e}$ the magnetic flux quantum. The dephasing is independent of the choice of paths C_1 and C_2 encircling the solenoid. It is non local in the sense that it detects the magnetic flux between the electrons trajectories, no matter how far the electrons are from the solenoid. Magnetoresistance measurements on a gold ring at low temperature and weak magnetic field have evidenced the Aharonov-Bohm effect, as shown on Fig. 2.2. For a thin and large enough ring, and when the magnetic field is low, the dephasing between electron trajectories within the same ring arm and the Lorentz force on individual trajectories can be neglected. Hence, the effect of the field in the ring itself can be neglected compared to the effect of the flux threading through the ring. The observation of oscillations in the magnetoresistance confirms that, in a real material, even though the presence of multiple scatterers affect the electrons, phase coherent interference effects have a measurable impact on electronic transport on scales close to 1μm.

The magnetic flux dephases the electrons wavefunctions even though there is no direct interaction between the electrons and the magnetic field. Rejecting the possibility of a non local interaction between the electrons and the field, this dephasing is a measurable physical manifestation of the vector potential action. Vector potentials are often considered as a purely mathematical object because they are defined up to a gauge freedom: $\mathbf{A}$ and $\mathbf{A}' = \mathbf{A} + \boldsymbol{\nabla}f$ describe the same magnetic field. Here one can verify that the Aharonov Bohm effect (2.3) is gauge invariant. The prediction of the Aharonov Bohm effect and its experimental confirmation proved the physical reality of vector potentials in quantum mechanics.

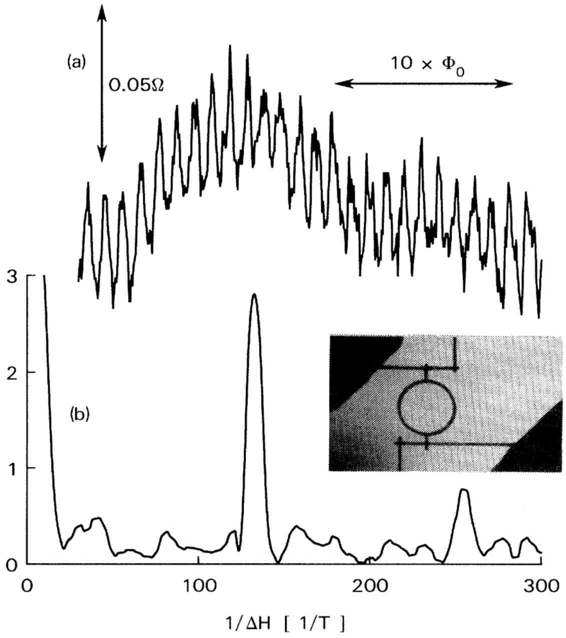

Figure 2.2: (a) Magnetoresistance of a gold ring (shown in inset) measured at $T = 0.01K$. Interference effects between electron trajectories on opposite sides of the ring cause magnetoresistance oscillations. A Fourier transform (b) shows peaks at frequencies h/e and $2h/e$ corresponding to Aharonov-Bohm oscillations. The inside loop diameter is 784mm and the diameter of the wires 41mm. Taken from [Webb et al., 1985].

2.1.2 The Dirac monopole of electromagnetism

How is the Aharonov Bohm effect relevant to topological properties of solids? The presence of a magnetic flux can be detected by interference effects between electrons traveling around it. In theory, one could detect a source of magnetic flux. The existence of such a source, a magnetic monopole, contradicts Gauss's law, $\boldsymbol{\nabla} \cdot \mathbf{B} = \mathbf{0}$. Although its existence is in contradiction with Maxwell equations, Dirac found [Dirac, 1931] that the contradiction could be solved theoretically by connecting the monopole to a half tube of flux carrying the opposite of the monopole flux. With the addition of this half tube which he called a Dirac string, he could define a well behaved magnetic vector potential. This Dirac string necessarily connects two monopoles with opposite charge: Dirac thus established that monopoles must come by pair, source and sink.

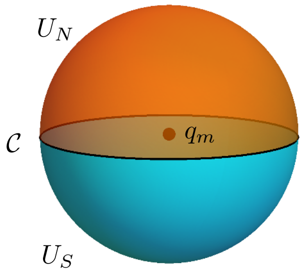

Figure 2.3: A Dirac monopole creating a flux q_m is located a the origin. It is impossible to find a unique gauge choice covering the sphere: the vector potential defined on the northern (southern) hemisphere U_N (U_S) is singular at the opposite pole. At the equator $\mathcal{C}$, a gauge transformation relates the two gauge choices.

The existence of the Dirac string can be derived as follows. Take a magnetic monopole with charge q_m

located at the origin. It creates a field

$$\mathbf{B_m} = \frac{q_m}{4\pi r^2}\mathbf{e_r}. \tag{2.4}$$

Consider a sphere of finite radius R, centered at the origin. Since $\oiint \mathbf{B}_m \cdot d\mathbf{S} = q_m \neq 0$ for any surface that encloses the origin, no vector potential can be associated to $\mathbf{B}$ on the whole sphere. The finite monopole charge makes it impossible to continuously contract a surface, such as the sphere, that contains the monopole, into a point. However, in a similar fashion as in the Aharonov-Bohm experiment, one can define a vector potential in any simply connex region that excludes the monopole. In such a region, any closed loop or surface is contractible to a point. Therefore, on each hemisphere U_N and U_S it is possible to define a vector potential, respectively $\mathbf{A}_N$ and $\mathbf{A}_S$, see Figure 2.3:

$$\mathbf{A}_N = \frac{q_m}{4\pi R}\frac{1-\cos\theta}{\sin\theta}\mathbf{e}_\phi, \tag{2.5}$$

$$\mathbf{A}_S = -\frac{q_m}{4\pi R}\frac{1+\cos\theta}{\sin\theta}\mathbf{e}_\phi. \tag{2.6}$$

$\mathbf{A}_N$ has a singularity a the South pole, for $\theta = \pi$. Elsewhere on the sphere it is well defined and verifies $\boldsymbol{\nabla} \times \mathbf{A}_N = \mathbf{B}_m$. Similarly the southern vector potential $\mathbf{A}_S$ is well defined for $\theta \neq 0$. In fact, one can show that in addition to the magnetic field (2.4), each vector potential creates an extra magnetic field carried by an infinitesimally thin half-solenoid: a Dirac string. The singularities of vector potentials (2.5) and (2.6) along the opposite semi axis indicate the existence of the semi-infinite flux tube. It is possible to compute the flux associated with the Dirac string: take for demonstration the $\mathbf{A}_N$ potential (2.5). One can derive the flux it creates through a disk of radius $R\sin\theta$ centered on the z axis for a fixed polar angle θ. When closing the angle around the z-axis, one finds

$$\lim_{\theta\to 0}\oint \mathbf{A}_N d\mathbf{r} = 0 \tag{2.7a}$$

$$\lim_{\theta\to \pi}\oint \mathbf{A}_N d\mathbf{r} = q_m. \tag{2.7b}$$

Hence $\mathbf{A}_N$ creates a Dirac string with magnetic flux $-q_m\mathbf{e}_z$ along the semi-axis $z < 0$. Similarly $\mathbf{A}_S$ creates a Dirac string with flux $+q_m\mathbf{e}_z$ along the semi-axis $z > 0$. At the other end of the Dirac string there is a monopole with opposite charge. The existence of two monopoles with opposite charge related by a Dirac string satisfy the Maxwell equations and is therefore possible in theory.

Let us go back to our initial monopole and a sphere surrounding it, with the two hemispheres associated with a different choice of vector potential (2.5) and (2.6). On each hemisphere, the choice of vector potential $\mathbf{A}_{N/S}$ defines a gauge for the electronic wavefunction. On the equator $\mathcal{C}$, the two vector potentials are well defined and related by a gauge transformation:

$$\mathbf{A}_N - \mathbf{A}_S = \frac{q_m}{2\pi R}\frac{1}{\sin\theta}\mathbf{e}_\phi = \boldsymbol{\nabla}\left(\frac{q_m}{2\pi}\phi\right) = \boldsymbol{\nabla} f(\mathbf{r}). \tag{2.8}$$

while for electronic wavefunctions:

$$\psi_S(\mathbf{r}) = \exp\left(i\frac{e}{\hbar}f(\mathbf{r})\right)\psi_N(\mathbf{r}) = \exp\left(i\frac{e}{\hbar}q_m\phi\right)\psi_N(\mathbf{r}). \tag{2.9}$$

The magnetic charge of the monopole thus corresponds to the winding of the gauge transformation function $f(\mathbf{r})$. Since wavefunctions must be monovaluated, the charge is quantized: $q_m = \frac{h}{e}n, n \in \mathbb{Z}$.

Note that the connection between the magnetic flux from the monopole and the winding of the gauge transformation function can alternatively be derived using Stokes' theorem:

$$\begin{aligned}\oiint \mathbf{B}\cdot d\mathbf{S} &= \oiint_{U_N}\mathbf{B}\cdot d\mathbf{S} + \oiint_{U_S}\mathbf{B}\cdot d\mathbf{S}\\ &= \oint_{\partial U_N}\mathbf{A}_N d\mathbf{r} + \oint_{\partial U_S}\mathbf{A}_S d\mathbf{r}\\ &= \oint_{\mathcal{C}}\left(\mathbf{A}_N - \mathbf{A}_S\right)d\mathbf{r}\\ &= \oint_{\mathcal{C}}\boldsymbol{\nabla} f(\mathbf{r})d\mathbf{r}\\ &= q_m.\end{aligned} \tag{2.10}$$

We have seen that the existence of the magnetic monopole translates into the impossibility to fix a unique gauge for the electronic wavefunctions. Singularities in the phase of wavefunctions thus signal the presence of a monopole. We are also convinced that vector potentials rather than fields are the appropriate tools to describe the physics of monopoles. The monopole forbids to define a global potential: one must proceed by regions. The different potential choices are related by a gauge transformation, which defines a winding number that is exactly the monopole charge. These notions will prove useful to describe topological properties of crystals.

2.1.3 A Magnetic field analog in momentum space? Berry phase, Berry curvature

Now let us go back to the description of electronic states in a crystal. We are interested in the modifications of the electronic phase during an arbitrary evolution of the Hamiltonian, for example when the momentum is smoothly modified and visits the Brillouin Zone. We will see that the presence of a band crossing manifests as a source of so-called Berry curvature and introduces a non-trivial dephasing between electronic states encircling it. We introduce the notions of Berry phase, Berry connection and Berry curvature that allow to describe the topology of the ensemble of electronic states.

The Berry phase is related to the notion of adiabatic evolution: it describes the change of wavefunctions when a parameter of the Hamiltonian varies slowly (compared to other energy scales involved.) In this section and the following, we present some of the tools and concepts useful to characterize the topology of band gaps and band crossings. Complete introductions to the Berry phase, Chern number and the topological characterization of solids can be found in [Bernevig and Hughes, 2013, Fruchart and Carpentier, 2013].

Consider an electronic system described by the Bloch Hamiltonian $H(\mathbf{k})$. Suppose the crystal momentum $\mathbf{k}$ is made to vary slowly with time t within the Brillouin Zone. We introduce an instantaneous basis of eigenstates of H:

$$H|\psi_n(\mathbf{k}(t))\rangle = \varepsilon_n(\mathbf{k}(t))|\psi_n(\mathbf{k}(t))\rangle. \tag{2.11}$$

When varying $\mathbf{k}$ adiabatically, $|\psi_n(\mathbf{k}(t))\rangle$ remains an eigenstate: $H(\mathbf{k}(t))|\psi_n(\mathbf{k}(t))\rangle = \varepsilon_n(\mathbf{k}(t))|\psi_n(\mathbf{k}(t))\rangle$. We are interested in the evolution of a state $|\psi(t)\rangle$ prepared initially in band n. We assume that the n band is nondegenerate and the evolution is adiabatic, so that the system remains in band n. The evolution can then be described by a phase transformation:

$$|\psi(t)\rangle = e^{-\mathrm{i}\theta(t)}|\psi_n(\mathbf{k}(t))\rangle. \tag{2.12}$$

The Schrödinger equation governing time evolution yields:

$$\begin{aligned} H|\psi(t)\rangle &= \mathrm{i}\hbar\partial_t|\psi(t)\rangle \\ \varepsilon_n(\mathbf{k}(t))\ e^{-\mathrm{i}\theta(t)}\ |\psi_n(\mathbf{k}(t))\rangle &= \hbar\ e^{-i\theta(t)}\ \left((\partial_t\theta) + \mathrm{i}\partial_t\right)|\psi_n(\mathbf{k}(t))\rangle. \end{aligned} \tag{2.13}$$

Projecting (2.13) on $|\psi_n(\mathbf{k}(t))\rangle$ and integrating over time leads to:

$$\theta(t) - \theta(0) = \frac{1}{\hbar}\int_0^t \varepsilon_n(\mathbf{k}(t))dt' - \mathrm{i}\int_0^t \langle\psi_n(\mathbf{k}(t))|\partial_{t'}|\psi_n(\mathbf{k}(t))\rangle dt'. \tag{2.14}$$

The first term in the right hand side of (2.14) is the dynamical phase. The second term defines the Berry phase. It takes the form:

$$\begin{aligned} \gamma_n &= \mathrm{i}\int_0^t \langle\psi_n(\mathbf{k}(t))|\partial_{t'}|\psi_n(\mathbf{k}(t))\rangle dt' \qquad (2.15) \\ &= \mathrm{i}\int_{\mathcal{C}} \langle\psi_n(\mathbf{k})|\boldsymbol{\nabla}_{\mathbf{k}}|\psi_n(\mathbf{k})\rangle d\mathbf{k}, \qquad (2.16) \end{aligned}$$

where $\mathcal{C}$ is the path followed by $\mathbf{k}$ in the Brillouin Zone along the evolution. The Berry phase encodes the variation of wavefunctions between $\mathbf{k}(t)$ and $\mathbf{k}(t+dt) = \mathbf{k} + d\mathbf{k}$ along the evolution path.

By analogy with the Aharonov-Bohm experiment for electrons moving in a magnetic potential (see section 2.1.1) we define a vector potential associated to the Berry phase, the so-called Berry connection:

$$\begin{aligned} \gamma_n &= \int_{\mathcal{C}} \mathbf{A}_n \cdot d\mathbf{k} \qquad (2.17) \\ \implies \mathbf{A}_n &= \mathrm{i}\langle\psi_n(\mathbf{k})|\boldsymbol{\nabla}_{\mathbf{k}}|\psi_n(\mathbf{k})\rangle. \qquad (2.18) \end{aligned}$$

Note that the Berry phase and Berry connection are real quantities, in spite of the i factor. The Berry connection can be written as

$$\mathbf{A}_n = -\mathrm{Im}\langle\psi_n(\mathbf{k})|\boldsymbol{\nabla}_{\mathbf{k}}|\psi_n(\mathbf{k})\rangle. \tag{2.19}$$

When the parameter space is three-dimensional, it is possible to define a Berry curvature, analogous to a magnetic field in parameter space:

$$\mathbf{F}_n = \boldsymbol{\nabla}_{\mathbf{k}} \times \mathbf{A}_n \tag{2.20}$$

The Berry phase $\gamma_n(\mathcal{C})$ (2.16) along a closed loop $\mathcal{C}$ is thus given by the flux of $\mathbf{F}_n$ through any surface bounded by $\mathcal{C}$

$$\gamma_n = \iint_{\mathcal{S}} \mathbf{F}_n \cdot d\mathbf{S}, \tag{2.21}$$

where $\partial\mathcal{S} = \mathcal{C}$. Note that since the Berry curvature $\mathbf{F}_n$ is by definition gauge invariant, the Berry phase γ_n along a closed loop is also gauge invariant (modulo 2π). It can be non zero if a flux of Berry curvature goes through $\mathcal{C}$; then, there is an obstruction to define continuous, single-valued wavefunctions in the whole Brillouin zone. An equivalent formulation of the Berry curvature reveals that it originates from the proximity of level n with different energy levels $m \neq n$:

$$\mathbf{F}_n(\mathbf{k}) = -\mathrm{Im}\sum_{m\neq n}\frac{\langle\psi_n(\mathbf{k})|\boldsymbol{\nabla}_{\mathbf{k}}H|\psi_m(\mathbf{k})\rangle \times \langle\psi_m(\mathbf{k})|\boldsymbol{\nabla}_{\mathbf{k}}H|\psi_n(\mathbf{k})\rangle}{(\varepsilon_n(\mathbf{k}) - \varepsilon_m(\mathbf{k}))^2} \tag{2.22}$$

Because the energy difference between bands appears at the denominator in (2.22), dominating contributions to the Berry curvature will come from energy bands that are close to each other, and one can expect singularities at level crossings where $|\varepsilon_n - \varepsilon_m| \to 0$.

2.1.4 Illustration of the notion of Chern Number on a simple two-bands system

Sources of Berry flux can be expected around level crossings or when bands come close to each other. Neighbouring bands can be described within a two-level approach. The generic two-band Bloch Hamiltonian reads:

$$H = \mathbf{h}(\mathbf{k}) \cdot \boldsymbol{\sigma} + h_0(\mathbf{k})\mathbb{1}. \tag{2.23}$$

Its energy spectrum is given by

$$\varepsilon_\pm(\mathbf{k}) = \pm h(\mathbf{k}) + h_0(\mathbf{k}). \tag{2.24}$$

It is gapped by $2h(\mathbf{k})$. The $h_0(\mathbf{k})$ term only shifts the energy: since it has no influence on topological properties, we chose to neglect it for clarity. The system (2.23) is analogous to a spin-$\frac{1}{2}$ in a effective magnetic field $\mathbf{h}$. We take $\mathbf{h}$ as a parameter that defines the Hamiltonian. When $\mathbf{k}$ visits the Brillouin Zone, $\mathbf{h}$ goes around a compact surface in 3-d space. Berry phase properties of the wavefunctions characterize the topology of the mapping $\mathbf{k} \to \hat{\mathbf{h}}(\mathbf{k})$ with $\hat{\mathbf{h}} = \mathbf{h}/h$. Introducing spherical coordinates for $\mathbf{h}$:

$$\mathbf{h} = h\begin{pmatrix} \sin\theta\ \cos\varphi \\ \sin\theta\ \sin\varphi \\ \cos\theta \end{pmatrix}, \tag{2.25}$$

a possible basis of eigenstates of (2.23) takes the form

$$\psi_+(\mathbf{k}) = \begin{pmatrix} \cos\frac{\theta}{2}\ e^{-i\varphi} \\ \sin\frac{\theta}{2} \end{pmatrix}, \tag{2.26}$$

$$\psi_-(\mathbf{k}) = \begin{pmatrix} \sin\frac{\theta}{2} \\ -\cos\frac{\theta}{2}\ e^{i\varphi} \end{pmatrix}. \tag{2.27}$$

This two-band crossing will serve as a pedagogical example to illustrate the notion of Chern number. The Chern number is a topological index which counts the number of Berry monopoles. By analogy with electrodynamics, the presence of a source of Berry flux would forbid to define a single gauge for eigenvectors, see section 2.1.2. Let us now consider the condition of existence of such an obstruction. First, note that the valence band eigenvector (2.27) is singular in the $\theta \to 0$ limit i.e. on the $z > 0$ semi-axis: it depends on the phase φ, but φ is ill defined in this limit. To remove this singularity we could change the phase convention by adding a factor $e^{-i\varphi}$ to the eigenvector. Doing this cancels the singularity at $\theta = 0$, but creates a new one at the opposite pole $\theta = \pi$ ($z < 0$ axis). The singularity can be moved in $\mathbf{h}$ space, but not suppressed: it is analogous to the Dirac string. Because of the singularity, we have to define two different phase conventions to define eigenstates for all values of $\mathbf{h}$: we note ψ_-^S the eigenvector (2.27), defined for $\theta \neq 0$ and $\psi_-^N = e^{-i\varphi}\psi_-^S$ the eigenvector defined for $\theta \neq \pi$. The Berry connections associated with these conventions are

$$\mathbf{A}_-^S = -\mathrm{Im}\langle\psi_-^S|\boldsymbol{\nabla}|\psi_-^S\rangle, \tag{2.28}$$

$$\begin{aligned}\mathbf{A}_-^N &= -\mathrm{Im}\langle\psi_-^N|\boldsymbol{\nabla}|\psi_-^N\rangle \\ &= \mathbf{A}_-^S + \boldsymbol{\nabla}\varphi.\end{aligned} \tag{2.29}$$

Following section 2.1.2, it is straightforward to compute the Berry flux going through any surface encircling the origin, such as the sphere, as the sum of the flux through the hemispheres U_N and U_S (see Fig. 2.3):

$$\begin{aligned}\oint\!\!\!\!\oint \mathbf{F}_- \cdot d\mathbf{S} &= \oint\!\!\!\!\oint_{U_N} \mathbf{F}_- \cdot d\mathbf{S} + \oint\!\!\!\!\oint_{U_S} \mathbf{F}_- \cdot d\mathbf{S} \\ &= \oint_{\partial U_N} \mathbf{A}_-^N \cdot d\boldsymbol{\ell} + \oint_{\partial U_S} \mathbf{A}_-^S \cdot d\boldsymbol{\ell} \\ &= \oint_{\mathcal{C}} \left(\mathbf{A}_-^N - \mathbf{A}_-^S\right) \cdot d\boldsymbol{\ell} \\ &= \oint_{\mathcal{C}} \boldsymbol{\nabla}\varphi \cdot d\boldsymbol{\ell} \\ &= 2\pi.\end{aligned} \tag{2.30}$$

The integral of the Berry curvature through the sphere is non zero due to the presence of the degeneracy point $h = 0$. The degeneracy acts as a monopole of Berry flux in parameter space, similar to a Dirac monopole for the magnetic flux, with charge 2π.

The vector $\hat{\mathbf{h}}$ describes a portion of the unit sphere when $\mathbf{k}$ visits the Brillouin Zone. If the mapping $\mathbf{k} \to \hat{\mathbf{h}}(\mathbf{k})$ covers only a portion of the sphere, it is trivial i.e. it can be shrinked to a point. In that case, a single phase convention is sufficient to define the eigenstates $|\psi_\pm(\mathbf{k})\rangle$. If it covers the whole sphere, it is topologically non trivial and two conventions are necessary to define the eigenstates $|\psi_\pm(\mathbf{k})\rangle$.

The integral of the Berry curvature over the Brillouin Zone is a topological invariant called a Chern number C_1:

$$C_1 = \frac{1}{2\pi}\oint\!\!\!\!\oint_{BZ} \mathbf{F} \cdot d\mathbf{S}. \tag{2.31}$$

It is an integer: it counts whether or not $\hat{\mathbf{h}}(\mathbf{k})$ covers the whole sphere, and how many times.

When $\mathbf{h}(\mathbf{k}) = \hbar v\mathbf{k}$, it is straightforward to obtain $C_1 = 1$. In this case the Hamiltonian (2.23) describes a single Weyl cone located at $\mathbf{k} = \mathbf{0}$. Hence, a Weyl point is a Berry monopole with topological charge $|C_1| = 1$.

We will now describe how the notion of Chern number applies to the characterization of insulators.

2.2 Topological indices for insulators

The simplest example of an insulator is the vacuum. It has an energy gap of $2m_ec^2 \simeq 10^6$ eV, corresponding to the energy required to produce an electron-positron pair. The vacuum gap is much larger than that of band insulators. For example solid Argon has an energy gap of 10 eV. Semiconductors like Silicon have an even smaller gap, of the order of 1 eV. However different their gap energies, the vacuum, Argon and Silicon are related in the sense of topology: their band structures can be continuously deformed into one another. We can define an insulator as topologically trivial when it is equivalent to the vacuum in the sense of topology, i.e. when its atoms can be separated, without closing the energy gap, by a continuous deformation. All phases with an energy gap are not topologically equivalent to the vacuum: the first known example of such a phase is the Quantum Hall Effect. The existence of chiral edge states immune from backscattering are a signature of the underlying topological property of the Quantum Hall state, a non-zero Chern number. Another class of topological insulators is the class of 2-d and 3-d time reversal invariant topological insulators. The 2-d topological insulators class contains the Quantum Spin Hall state. Time reversal invariant topological insulators are characterized by a different class of invariants different from the already mentioned Chern number, the $\mathbb{Z}_2$ or Kane-Mele invariants. The discovery of these phases has opened entirely new perspectives for condensed matter studies. In this section, we provide the general idea behind the definition and classification of topological insulators. A pedagogical review on the subject can be found in [Hasan and Kane, 2010].

2.2.1 Quantum Hall effect and Chern insulators

A two-dimensional electron gas submitted to a strong magnetic field exhibits properties characteristic of a new phase of matter: the Quantum Hall Effect. This phase is characterized by a vanishing longitudinal conductance $\sigma_{xx} = 0$ and a quantized transverse conductance $\sigma_{xy} = \nu \frac{e^2}{h}$, $\nu = 1, 2, ...$ independent of details or perturbations present in the system [v. Klitzing et al., 1980]. The quantization is precise to one part in a billion. This amazing precision is not only interesting for metrology applications, it is the manifestation of a new fundamental property of matter: an intrinsic topological property. The quantized conductance originates from the contribution of robust edge states. The edge states of the Quantum Hall effect are chiral, and can not be backscattered by impurities. Their robustness is a manifestation of the intrinsic topological property. in the presence of a magnetic field, electronic energy levels freeze into Landau Levels. Fig. 2.4 gives a semi-classical description of the origin of edge states and Landau Levels: in a magnetic field, electron trajectories form cyclotron orbits. Near the edges, the orbits bounce of the edges and propagate unidirectionally. It has been shown by [Thouless et al., 1982] that the ν index counting the number of filled Landau levels and chiral edge states is a topological invariant of filled bands, a Chern number. Quantum Hall edge states are chiral: they propagate only in one direction, with perfect transmission even in the presence of disorder. Time-reversal symmetry must be broken to allow for chiral edge states. Similarly, since time-reversal flips the sign of σ_{xy}, a non-zero Hall conductance requires $\mathcal{T}$-breaking. In the QH state, the $\mathcal{T}$-breaking manifestly originates from the strong magnetic field.

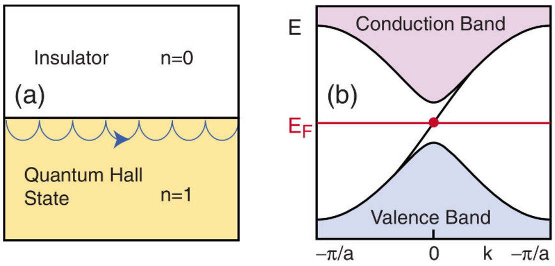

Figure 2.4: Edge states at the interface between a trivial insulator and a Chern insulator showing Quantum Hall effect. (a) Sketch of the origin of Chiral edge state from semi-classical cyclotron orbits bouncing off the boundary. (b) Band structure of an armchair ribbon of graphene in the Haldane model, showing a single edge state. From [Hasan and Kane, 2010]

A magnetic field breaks translational symmetry. To discuss topological properties in the context of band theories, consider a more convenient system showing chiral edge states in the absence of a net magnetic field [Haldane, 1988]. Haldane's model can be seen as a modified version of graphene, where a gap can be opened near the $\mathbf{K}$ Dirac point:

$$H(\mathbf{K}+\mathbf{q}) = \hbar v_F \mathbf{q}\cdot\boldsymbol{\sigma} + m\sigma_z. \tag{2.32}$$

The gap-opening term m, analogous to a mass for Dirac fermions, is obtained by breaking inversion $\mathcal{P}$ or time-reversal $\mathcal{T}$ symmetry. A different onsite energy on the two sublattices of the honeycomb lattice breaks $\mathcal{P}$. $\mathcal{T}$ can be broken by an appropriate staggered magnetic flux within the unit cell without any net magnetic flux and thus without breaking lattice translation symmetries. The time-reversal operation $\mathcal{T}:\ t \to -t$ is anti-unitary and changes the sign of the wave-vector, thus exchanging valleys ($\mathbf{K}' = -\mathbf{K}$). It corresponds to the operator $\Theta = \mathbb{1}\cdot\kappa$ where κ is the complex conjugation operator. Invariance under time-reversal enforces the following relation between Hamiltonians $\hat{H}_{\mathbf{K}}$ and $\hat{H}_{\mathbf{K}'}$:

$$\Theta H_{\mathbf{K}}(\mathbf{q})\Theta^{-1} = H^*_{\mathbf{K}}(\mathbf{q}) = H_{\mathbf{K}'}(-\mathbf{q}). \tag{2.33}$$

The spatial inversion $\mathcal{P}:\ \mathbf{x} \to -\mathbf{x}$ operation exchanges valleys $\mathbf{K}$ and $\mathbf{K}' = -\mathbf{K}$ and sublattices A and B (see Fig. 1.4, and therefore $P = \sigma_x$. Hence, invariance under $\mathcal{P}$ requires

$$PH_{\mathbf{K}}(\mathbf{q})P^{-1} = \sigma_x H_{\mathbf{K}}(\mathbf{q})\sigma_x = H_{\mathbf{K}'}(-\mathbf{q}). \tag{2.34}$$

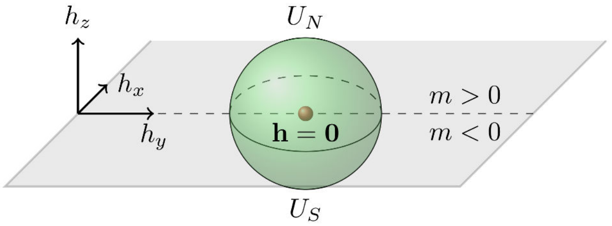

Figure 2.5: A source of Berry curvature is located at the origin in $\mathbf{h}$ space, corresponding to the massless Dirac point $\mathbf{k} = \mathbf{K}$, $m = 0$. The Berry flux threads through any closed surface encircling the Dirac point in $\mathbf{h}$ space. The variation of Berry flux induced locally by the change of sign of m corresponds to a Chern number: $\Delta\nu = \nu(m > 0) - \nu(m < 0) = 1$.

Whereas invariance under $\mathcal{T}$ (2.33) or $\mathcal{P}$(2.34) alone enforce relations between $H_{\mathbf{K}}$ and $H_{\mathbf{K}'}$, invariance under the combination of $\mathcal{T}$ and $\mathcal{P}$ imposes restrictions on the Hamiltonian in each valley, for instance:

$$TPH_{\mathbf{K}}(TP)^{-1} = \sigma_x H^*_{\mathbf{K}} \sigma_x = H_{\mathbf{K}}. \tag{2.35}$$

If the system is symmetric under both $\mathcal{T}$ and $\mathcal{P}$, condition (2.35) immediately tells us that a σ_z term is forbidden in the expression of $H_{\mathbf{K}}$ (2.32), and we recover graphene. Note that $\mathcal{T}$ enforces the Dirac Hamiltonian in the opposite valley $\mathbf{K}'$ to have the same mass $m_{\mathbf{K}'} = m_{\mathbf{K}}$. On the contrary, when only $\mathcal{T}$ is broken, $\mathcal{P}$ requires the mass to be opposite, $m_{\mathbf{K}'} = -m_{\mathbf{K}}$.

Following the path of section 2.1.4, we compute the change of Berry flux induced locally when m changes sign. We have seen that contributions to the Berry curvature come from the proximity between different energy levels. Therefore, we consider contributions to the Berry flux near the band crossing. The system (2.32) corresponds to Hamiltonian (2.23) with $\mathbf{h}(\mathbf{q}) = (q_x, q_y, m)$. At the $\mathbf{K}'$ point the Hamiltonian corresponds to $\mathbf{h}(\mathbf{q}) = (-q_x, q_y, m')$. In the massless case, $\mathbf{h}$ is confined to the equator and winds by $\pm\pi$ around each Dirac point $\mathbf{K}$, $\mathbf{K}'$. We assume that the contributions to the change of Berry curvature at the gap closing come from the proximity of the band crossing only, i.e. near $q = 0$. We therefore extend the local Hamiltonian defined for small q to the whole $\mathbb{R}^2$. For $m > 0$, $\hat{\mathbf{h}} = \mathbf{h}/h$ visits the North pole U_N when $\mathbf{q}$ visits $\mathbb{R}^2$. Respectively when $m < 0$, $\hat{\mathbf{h}}$ visits the South pole, as depicted on Fig. 2.5. The local change of Berry flux for the valence band is therefore

$$\Delta\nu_-^{\mathbf{K}} = \nu_-(m_{\mathbf{K}} > 0) - \nu_-(m_{\mathbf{K}} < 0) = \frac{1}{2\pi}\oiint_{U_N} \mathbf{F} \cdot d\mathbf{S} - \frac{1}{2\pi}\oiint_{U_S} \mathbf{F} \cdot d\mathbf{S} = 1. \tag{2.36}$$

Near the $\mathbf{K}'$ point, $\hat{h}_{\mathbf{K}'}$ winds the opposite way around the sphere, hence the contribution has opposite sign: $\Delta\nu_-^{\mathbf{K}'} = -1$. Based on the local Hamiltonian (2.32) we have computed the change of Chern number associated with the gap closing occurring for $\mathbf{h} = \mathbf{0}$ i.e. either at $\mathbf{K}$ and $m_{\mathbf{K}} = 0$ or $\mathbf{K}'$ and $m_{\mathbf{K}'} = 0$. Hence, topological phase transitions occur when the gap closes where the Chern number changes by ±1, when the gap closes in a single valley, or ±2, when m changes sign and the gap closes simultaneously in the two valleys, with m having opposite sign in each valley. Now going back to the full Haldane model, starting from one point of the phase diagram where the Chern number can be easily computed one can obtain the full phase diagram. Besides, Haldane has shown [Haldane, 1988] that the $\mathcal{T}$ symmetric phase is topologically trivial, $C_1 = 0$. The Chern number then gives the quantization of the transverse Hall conductance σ_{xy} [Thouless et al., 1982].

At the interface between a trivial and a topological phase, the gap must close and chiral surface states appear. In the context of the Haldane model it is straightforward to see that m cancels at the transition. In general, at the boundary of a topological insulator chiral metallic edge states must appear, as illustrated on Figure 2.4. Details of the system near the edge can allow for an extra pair of left and right moving edge states, but they can annihilate each other through backscattering. The difference between the number of right movers N_R and left movers N_L is protected and given by the Chern number

$$N_R - N_L = C_1. \tag{2.37}$$

In particular, Chern insulators with $|C_1| > 1$ are allowed [Fruchart and Carpentier, 2013].

2.2.2 $\mathbb{Z}_2$ Topological insulators: 2-d quantum spin Hall effect and 3-d topological insulators

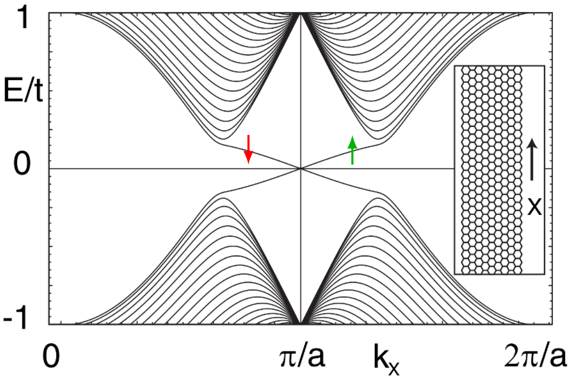

Figure 2.6: Quantum spin Hall phase in a one-dimensional strip of graphene with spin-orbit coupling. Spin-filtered edge states cross the gap. From [Kane and Mele, 2005a].

Chern insulators can only be realized in systems where $\mathcal{T}$ is broken either by an external magnetic field, or by magnetic ordering. A different kind of topological order with $\mathcal{T}$-symmetry exists for systems with spin-orbit interaction [Kane and Mele, 2005b]. The simplest realisation of such a phase can be seen as two copies of a Quantum Hall state for each spin, where the spin up and spin down chiral edge state propagate in opposite directions, see Figure 2.6. Such a system indeed preserves $\mathcal{T}$. Since the edge states have their spin and momentum locked, they are called helical edge states. Time-reversal symmetry forbids electrons from one channel to get backscattered in the counterpropagating channel. Hence, the helical edge states are robust to non-magnetic disorder. The first proposal for the Quantum Spin Hall phase was based on graphene with spin-orbit coupling [Kane and Mele, 2005a]. It turns out that the amplitude of spin-orbit coupling is too weak in graphene. The Quantum Spin Hall state was finally realised in HgCdTe quantum wells, see Fig. 2.7a, based on a later proposal by [Bernevig et al., 2006]. The first proposal by Kane and Mele [Kane and Mele, 2005a] is a superposition of two Haldane models [Haldane, 1988] with opposite sign of the Hall conductivity for up and down spins.

This new class of topological insulators is characterized by a $\mathbb{Z}_2$ index $\nu = 0$ or 1 [Kane and Mele, 2005b]. To understand these new topological phases, we must say a few words about $\mathcal{T}$ symmetry for spin 1/2 fermions. Time-reversal acts as an antiunitary operator that reads

$$\Theta = \exp\left(i\pi\frac{\hat{S}_y}{\hbar}\right)K, \tag{2.38}$$

where $\hat{S}_y$ is the spin operator along y (spin is quantized along z) and K is the complex conjugation operator. Since rotating a spin 1/2 by 2π amounts to a mere sign flip, time-reversal for spin 1/2 fermion verifies: $\Theta^2 = -\mathbb{1}$. Kramers' theorem is a consequence of $\Theta^2 = -\mathbb{1}$: it requires that $\varepsilon_{\mathbf{k},\sigma} = \varepsilon_{-\mathbf{k},-\sigma}$, where $\sigma = \pm 1/2$ is the spin along z. Eigenstates thus form Kramer pairs with equal energy : $(\psi_{\mathbf{k},\sigma},\psi_{-\mathbf{k},-\sigma})$. The degeneracy is local in $\mathbf{k}$ only at time reversal invariant momenta (TRIM) $\mathbf{\Lambda} = -\mathbf{\Lambda}$. Depending on whether Kramers pairs switch partners or not between different TRIMs, edge states will cross an odd or even number of times the Fermi level. Protected boundary states will exist for an odd number of crossing. The presence of protected edge states corresponds to a non trivial value of a $\mathbb{Z}_2$ invariant ν of filled bands. Computing ν is not trivial in general. However, in materials with inversion symmetry there is a direct correspondence between the invariant and the product of the filled Bloch states' inversion eigenvalues $\xi_m(\mathbf{\Lambda}_a)$ at the four TRIMs $\mathbf{\Lambda}_a$ [Fu and Kane, 2007]:

$$(-1)^\nu = \Pi_{a=1}^4 \Pi_m \; \xi_m(\mathbf{\Lambda}_a), \tag{2.39}$$

where m is the band index, summed on filled bands. Hence, whenever there is a band inversion between a conduction and valence band with different parity the product (2.39) changes sign and ν changes. Because carbon is a light element, in graphene the spin-orbit interaction is too weak for the Quantum Spin Hall effect to be observed: the gap is too small. The first experimental realization of a 2D $\mathbb{Z}_2$ topological

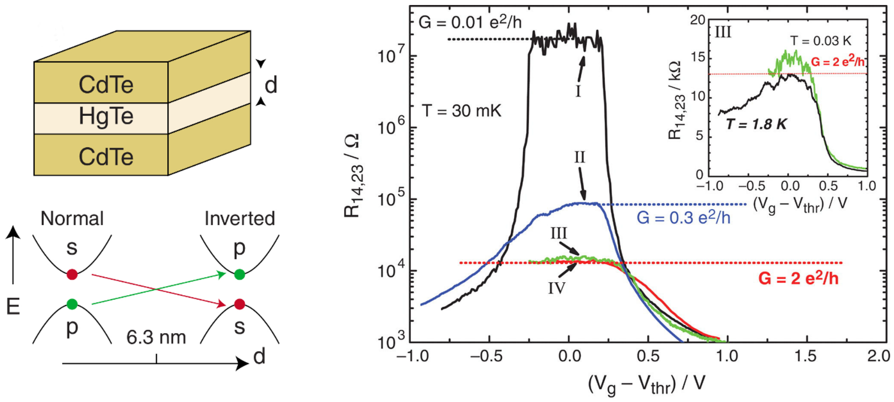

(a) (b)

Figure 2.7: Quantum spin Hall effect in HgTe/CdTe quantum wells. (a) The HgTe quantum well of thickness d is sandwiched between CdTe layers. Beyond a critical thickness the electronic state has an inverted band structure. From [Hasan and Kane, 2010]. (b) Resistance measured as the chemical potential is varied through the gap, for various thicknesses. When $d > d_c$ (samples III and IV) a conductance plateau is observed in the gap, with the expected quantized value signalling a pair of helical edge states. The inset shows persistence of the plateau at higher temperature. From [König et al., 2007].

insulator has been realized in HgTe/CdTe quantum wells. Since Hg, Cd, Te are heavy atoms, the spin-orbit coupling is strong in these compounds, leading to an observable energy gap, corresponding to a mass for Dirac fermions [Bernevig et al., 2006]. In CdTe, the conduction band orbital has s-like symmetry while the valence band has p-like symmetry. In contrast HgTe has inverted band ordering: the conduction band is p like and the valence band s like. The gap is inverted between these two compounds. As shown on figure 2.7a, for quantum wells of HgTe sandwiched between CdTe, a band inversion will occur for a critical thickness of HgTe, leading to a non trivial topological phase with quantum spin Hall effect [Bernevig et al., 2006]. Figure 2.7b shows the first measurement of the quantized quantum spin Hall conductance revealing the presence of edge states in HgTe/CdTe quantum wells [König et al., 2007]. The notion of $\mathbb{Z}_2$ topological

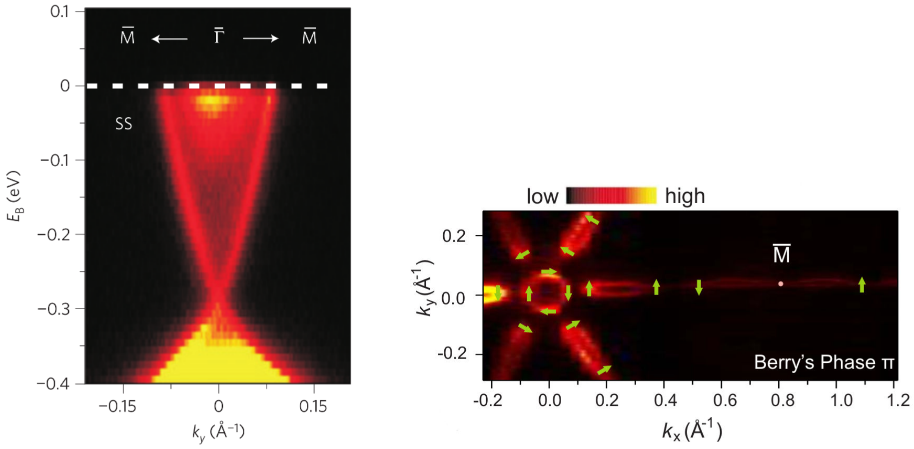

(a) (b)

Figure 2.8: 3D Topological Insulators' surface states. (a) ARPES measurement showing a single Dirac cone on the surface of topological insulator Bi_2Se_3. From [Xia et al., 2009]. (b) Spin-resolved ARPES results showing momentum locking around the Dirac cone on the surface of topological insulator $Bi_{1-x}Sb_x$. Adapted from [Hsieh et al., 2009, Hasan and Kane, 2010].

order can be extended to 3D materials [Fu et al., 2007, Moore and Balents, 2007, Roy, 2009]. Four $\mathbb{Z}_2$ indices $(\nu_0; \nu_1, \nu_2, \nu_3)$ characterize the material, related to the existence of robust surface states characterized by Fermi circles around the Surface TRIMs. Two types of three-dimensional topological insulators can be distinguished, characterized by the strong topological index ν_0. Trivial insulators have $\nu_0 = \nu_i = 0$ for all i. Weak topological insulators have $\nu_0 = 0$ but at least one $\nu_i \neq 0$. It can be seen as a stacked QSH phase along the direction characterized by Miller indices $(\nu_1\nu_2\nu_3)$. Surface states are not protected against external perturbations and thus may not be present in a real material with disorder. Strong topological insulators have $\nu_0 = 1$. They show protected surface states characterized by Fermi circles surrounding an odd number of surface TRIMs (one or three) on any surface. Surface states of 3D Topological Insulators are 2D massless Dirac fermions. In graphene, there are four Dirac cones because of the two valleys and the spin degeneracy. Contrary to graphene, on the surface of a 3D topological insulator there is just a single Dirac cone, with spin-momentum locking: the spin winding around the Dirac cone can be measured by spin resolved ARPES, Fig. 2.8b. The partner Dirac point with opposite spin winding around the cone is located on the opposite surface. Figure 2.8a shows the single Dirac cone on the surface of the large gap topological insulator Bi_2Se_3.

We are now familiar with Chern and $\mathbb{Z}_2$ topological insulators. These two classes of materials are characterized by an insulating bulk and conducting edge states. Chern insulators have topologically protected chiral edge states of any symmetry. $\mathbb{Z}_2$ topological insulators have helical edge states protected by time-reversal symmetry. Edge states of 3D $\mathbb{Z}_2$ topological insulators are 2D massless Dirac fermions, analogous to low-energy electrons in graphene. Beyond this analogy, there is a deep relation between semi-metals and topological insulators.

2.3 Semimetals as critical phases between insulators

2.3.1 Existence of a band Crossing

Semi-metallic phase as a critical phase

We have seen in the previous section that, in the Haldane model, at the topological phase transitions where the Chern number varies the gap closes at one or two points in the Brillouin Zone: the critical phase is semi-metallic. In general, at the transition between a topological and a trivial insulator, the gap must close because it is not possible to deform smoothly the band structure of one into another: they belong to two different topological classes of materials, characterised by different topological indices, the Chern numbers. Figure 2.9 depicts a phase transition between a trivial and a topological insulator driven by an external parameter m. At the transition the system is necessarily gapless. The topological order can be induced by band inversion, as in the case of topological insulators like HgCdTe [Bernevig et al., 2006] or BiSb [Fu and Kane, 2007] : then, conduction and valence bands cross exactly a the transition and the system is in a semi-metallic phase.

Hence, quantum phase transitions between topological and trivial insulators opens a new route for the study of phases with band crossings and their condition of existence.

Semi-metallic phase as a boundary state

We have considered the transition between distinct topological phases in dimension d, as a function of an external parameter m. At the critical point m_c, the gap closes and the system is semi-metallic. Similarly, take the boundary between two d-dimensional insulators belonging to distinct topological classes. Metallic states appear at the $(d-1)$-dimensional edge. The non-trivial topological property of an insulator manifests itself as metallic edge states: this is the bulk-boundary correspondence. In 2D, the Quantum Hall state has 1D chiral edge states, while the Quantum Spin Hall state shows helical edge states. 3D topological insulators have 2D massless Dirac fermions on their surface, with single Dirac cones of opposite chirality on opposite surfaces. Conversely, one can think of semi-metallic states in dimension d as boundary states of $d+1$ dimensional topological insulators [Morimoto and Furusaki, 2014].

2.3.2 Stability of band Crossings as critical phases

Let us now study the stability of band crossings appearing at transitions between insulators or as edge states. A band crossing will be stable if it exists in a finite region of parameter space: it is then robust against a class of weak perturbations. In the contrary the crossing requires fine tuning of all the parameters to exist and can then be gapped out even by a weak perturbation. In the case of a transition driven by an external parameter m, the stability of the critical semi-metallic phase depends whether the transition occurs for a single value of m or in a finite region of parameter space. The dimensionality and the presence of extra symmetry constraints play a crucial role in determining this stability condition.

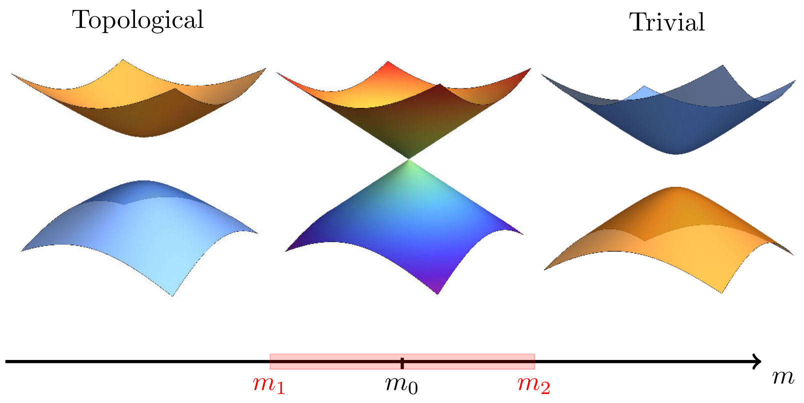

Figure 2.9: Phase transition between a topological and a trivial insulator. The gap closes at the transition, either for a single critical value m_0 of the transition parameter or for a finite region $[m_1, m_2]$.

In two dimensions

Let us take $d = 2$ and consider first the phase transitions occurring in the Haldane model before considering the transition between the 2D Quantum Spin Hall phase and a trivial insulator.

In the Haldane model previously introduced, topological phase transitions occur for critical values of the external parameters which control $\mathcal{P}$ and $\mathcal{T}$ breaking perturbations. When $\mathcal{T}$ is preserved, the system is topologically trivial. When $\mathcal{T}$ is broken, but $\mathcal{P}$ is preserved, a topological phase transition occurs at a single point where the gap closes simultaneously at the two Dirac points of graphene. This band crossing is stable in the presence of both $\mathcal{T}$ and $\mathcal{P}$ symmetries. When both $\mathcal{T}$ and $\mathcal{P}$ are broken, topological transitions occur at critical values of the external parameters where the gap closes in a single Dirac valley $\mathbf{K}$ or $\mathbf{K}'$. Since these critical phases require fine tuning of the system parameters, they are unstable and can be gapped by perturbations. Graphene corresponds to the bicritical point where both $\mathcal{T}$ and $\mathcal{P}$ are present.

At the transition between a 2D Quantum Spin Hall ($\mathbb{Z}_2$) insulator and a trivial insulator, massless Dirac fermions emerge. The band inversion occurs simultaneously at time-reversal partners $\mathbf{k} = \pm\mathbf{K}$ and for a single value of the transition parameter m. At the transition point, $\mathcal{T}$ and $\mathcal{P}$ are present: the band crossings, analogous to the two Dirac points of graphene, are stable in the presence of these symmetries.

In three dimensions

In $d = 3$, topological insulators are constrained by time-reversal symmetry $\mathcal{T}$. We consider the stability of the critical gapless phase between a 3D topological insulator with inverted band ordering and a trivial insulator. The band inversion requires a band crossing to occur at the transition. The location of the band crossing point in the Brillouin Zone and its stability as a function of the external transition parameter m depend on the presence or absence of spatial inversion symmetry $\mathcal{P}$ [Murakami, 2007].

Consider the following Hamiltonian:

$$H = \begin{pmatrix} h_{\uparrow\uparrow} & h_{\uparrow\downarrow} \\ h_{\downarrow\uparrow} & h_{\downarrow\downarrow} \end{pmatrix}. \tag{2.40}$$

$\mathcal{T}$ symmetry constrains H following:

$$\sigma_y H^T(-\mathbf{k})\sigma_y = H(\mathbf{k}). \tag{2.41}$$

$\mathcal{T}$ symmetry also implies the existence of Kramers pairs: if $\psi_\uparrow(\mathbf{k})$ is an eigenstate of the Hamiltonian, then $\psi_\downarrow(-\mathbf{k})$ is also an eigenstate with the same energy. In particular, bands are doubly degenerate at time reversal invariant momenta $\mathbf{\Lambda}_a = -\mathbf{\Lambda}_a$. There are 4 such TRIMs in 2D and 8 in 3D. When in addition $\mathcal{P}$ symmetry is present, bands are doubly degenerate for any $\mathbf{k}$: inversion sends $\psi_\uparrow(\mathbf{k})$ onto $\psi_\uparrow(-\mathbf{k})$. Thus at TRIMs $\mathbf{k} = \mathbf{\Lambda}_a$ or when both $\mathcal{T}$ and $\mathcal{P}$ are present, band crossings imply at least four bands.

Inversion asymmetric systems - When $\mathcal{P}$ is broken, the crossing can occur away from TRIMs, $\mathbf{k} \neq \mathbf{\Lambda}_a$. Therefore, the crossing occurs between two bands only. The Hamiltonian describing the crossing is parametrized by three independent real parameters, corresponding to the three Pauli matrices:

$$H(\mathbf{k}) = E_0 \ \mathbb{1} + a\sigma_x + b\sigma_y + c\sigma_z. \tag{2.42}$$

The crossing occurs when the three parameters (a, b, c) vanish. Hence, three independent constraints must be satisfied: the co-dimension of the crossing is 3 [Murakami, 2007]. The Hamiltonian depends on three degrees of freedom corresponding to the three directions of momentum $\mathbf{k}$. By tuning these three parameters (k_x, k_y, k_z), one can make the two bands cross. Hence, the crossing is stable when it exists and the transition occurs for a finite region of parameters $[m_1, m_2]$. This stability of gapless points originates from their topological charge: indeed, two band crossings in 3D are Weyl points which carry a monopole charge of Berry flux, see section 1.3. Two pairs of gapless points emerge at two pairs of time-reversal partners $\pm\mathbf{K}_i$, then travel around the Brillouin zone as m visits the transition region until they merge and a gap reopens. Exactly at the merging point a 3D Dirac cone emerges.

Can the transition occur at TRIMs $\mathbf{k} = \mathbf{\Lambda}_a$? Because of Kramers theorem, the bands are doubly degenerate at TRIMs. The four-band Hamiltonian constrained by (2.41) is parametrized by 5 linearly independent matrices [Murakami, 2007]:

$$H(\mathbf{k}) = E_0\mathbb{1} + \sum_{i=1}^{5} a_i\Gamma_i, \tag{2.43}$$

where $\Gamma_1 = \mathbb{1} \otimes \tau_x$, $\Gamma_2 = \sigma_z \otimes \tau_z$, $\Gamma_3 = \mathbb{1} \otimes \tau_z$, $\Gamma_4 = \sigma_y \otimes \tau_y$, $\Gamma_5 = \sigma_x \otimes \tau_y$. Hence, the co-dimension of the crossing is 5: 5 parameters must be tuned to achieve the crossing. However, since the momentum is fixed we are left with only one free parameter m, so the crossing will not occur.

Inversion symmetric systems - In $\mathcal{P}$-symmetric systems, the transition follows a different scenario. The crossing can only happen at TRIMs and when it exists corresponds to a massless 3D Dirac point.

Because of the combination of $\mathcal{T}$ and $\mathcal{P}$, bands are doubly degenerate: the crossing therefore implies four bands. Following the same line of reasoning as for $\mathcal{P}$-asymmetric systems, it has been shown [Murakami, 2007] that in general the co-dimension of the crossing is greater than the number of tunable parameters, except at TRIMs when states within a Kramers pair have different parity eigenvalues. A four band crossing can occur at $\mathbf{k} = \Lambda_a$, $m = m_0$. The critical gapless point is a 3D Dirac cone [Murakami, 2007]. As in 2D, a massless Dirac cone emerges at TRIMs for a single value of m in systems with $\mathcal{T}$ and $\mathcal{P}$.

2.3.3 Conclusion

We have seen how the study of phase transitions between trivial and topological insulators give some insight on the condition of existence and stability of semi-metallic phases with Weyl or Dirac points in 2D and 3D. Dirac points in 2D occur for a single value of the transition parameter where $\mathcal{T}$ and $\mathcal{P}$ are restored. Weyl points appear at the transition between a trivial and a topological insulator in the presence of $\mathcal{T}$ in $\mathcal{P}$-asymmetric systems. They appear by pairs at time-reversed momenta and merge to form a Dirac cone before a gap reopens, when m varies through the transition.

Semimetals are a priori hard to find since they originate from accidental degeneracies. Studying transitions between normal and inverted band structure, in connection with symmetry properties, allows for a more systematic search of these phases. Even though Weyl nodes are stable of any symmetry, it is possible to predict the location of the nodes based on the study of crystal symmetries in non centrosymmetric materials [Murakami et al., 2017].

2.4 Topological indices and symmetries of gapless phases in two and three dimensions

We have seen that insulators can be classified into different topological classes characterized by topological indices as e.g. a Chern number or a $\mathbb{Z}_2$ index, depending on the symmetries of the system. For gapless phases, we have seen with the example of 2D Dirac and 3D Weyl and Dirac semi-metals that band crossings differ from the point of view of their stability. They can be stable of any symmetry, like Weyl points, or require extra symmetries or fine tuning of an external parameter to occur, like Dirac points. The robustness of Weyl points is related to a topological charge: they act as magnetic monopoles in momentum space. The flux threading any surface that encloses the Weyl point, see Fig. 2.10, is a topological invariant: the Chern number. Dirac points need to be stabilised by extra symmetry constraints. Is this symmetry-constrained stability related to a topological invariant?

In this section, we consider the topological characterization of band crossings in relation with symmetry constraints. In general, different topological invariants can be associated to a given material depending on the number of spatial dimensions and the symmetry class of the Hamiltonian. A general classification of gapped topological phases was achieved based on the three fundamental non spatial symmetries: time reversal $\mathcal{T}$, charge conjugation $\mathcal{C}$ and chiral symmetry Γ [Schnyder et al., 2008, Kitaev, 2009]. Time-reversal symmetry $\mathcal{T} : t \to -t$ is an anti-unitary operator. Charge conjugation is an antiunitary operator which anti-commutes with the Hamiltonian. The chirality operator is a unitary operator which anti-commutes with the Hamiltonian. This classification has been extended to gapless phases, depending on the dimension of the Fermi surface, the dimension of the material, and invariance of the Hamiltonian under $\mathcal{T}$, $\mathcal{C}$ and Γ [Chiu et al., 2016].

However, the classification based on non spatial symmetries is only partially satisfying. The robustness of Weyl semimetals can be understood from this approach. But to understand the stability of graphene and 3D Dirac semimetals observed in some materials, one must consider how the presence of crystal symmetries allows for new topological invariants. We will see that indeed, crystal symmetries play a role in stabilizing the crossings. Topological invariants associated with crystal symmetries can be defined. In some cases, several mechanisms concur to stabilise the crossing, with several topological invariants. This raises the question of a unified scheme for the topological characterization of band crossings.

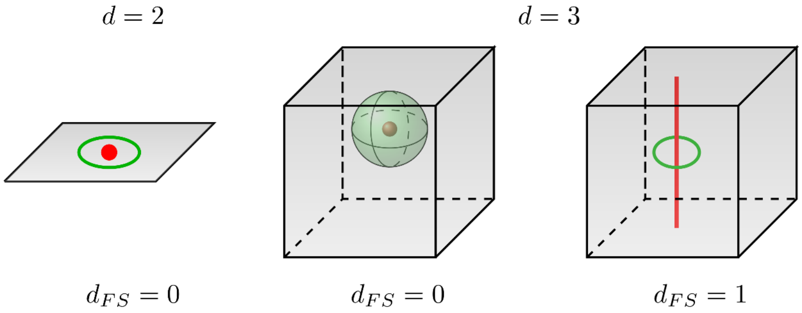

Figure 2.10: Depending on the dimension of the Brillouin Zone and the dimension of the Fermi Surface coloured in red, different topological invariants can be defined on the green contour around the Fermi Surface: a winding number when the contour is 1D, a $\mathbb{Z}_2$ invariant or Chern number when the contour is 2D.

2.4.1 A robust semimetal: 3D Weyl point

A Weyl point is a monopole of Berry flux, see section 2.1.4. The topological invariant associated to a Weyl point is a Chern number $C_1 = \pm 1$. It corresponds to the topological invariant class of 3D band crossings with no symmetry constraint [Chiu et al., 2016].

2.4.2 Symmetry-protected band crossing: 3D Dirac semi-metal

A 3D Dirac point is a four-band crossing. It requires time-reversal $\mathcal{T}$ and spatial inversion $\mathcal{P}$ symmetries: its existence and stability is thus relate to crystal symmetries. It can not be deduced from the characterization in terms of non spatial symmetries alone. Topological invariants have been associated with the crystal symmetries which can stabilize a 3D Dirac point.

Existence of the crossing

Crystal symmetries constrain the system Hamiltonian. At high symmetry points or along high symmetry lines, the Hamiltonian must commute with the operator defining the symmetry: therefore, the dimension of the Hamiltonian is given by the dimension of the irreducible representation of the symmetry[Dresselhaus et al., 2008]. The first proposal to find three-dimensional Dirac semimetal followed this direction: one should find crystal whose symmetry properties allowed for high symmetry points with isolated fourfold degeneracy [Young et al., 2012]. Isolated degeneracy means that the degeneracy is lifted away from the node in any direction of **k** space. However, the first material realisation of a 3D Dirac semimetal was achieved following a different scheme: one would look for a crossing between two doubly degenerate bands, in the spirit of section 2.3. The bands had to belong to two different two-fold irreducible representations otherwise the crossing would be avoided as an effect of level repulsion: bands would hybridize and a gap would open, lifting the degeneracy. In Na_3Bi, the Dirac cone emerge at the band inversion between two bands belonging to different representations of the threefold rotation symmetry [Wang et al., 2012].

Stability

More generally, it has been found that rotation and time-reversal $\mathcal{T}$ symmetry can stabilise 3D Dirac points [Yang and Nagaosa, 2014]. 3D Dirac points separate into two classes: single Dirac points located at TRIMs, and Dirac points coming by pairs on the rotation axis. The single Dirac points are critical phases, which can be destroyed through gap opening under an external perturbation. On the contrary, Dirac semimetals with pairs of Dirac points are protected by topological invariants [Yang et al., 2015]. These topological quantities are 2D invariants, $\mathbb{Z}_2$ indices or mirror Chern numbers protected by the rotation symmetry. Such quantities like the mirror Chern number were already known in the context of topological crystalline insulators, non trivial topological gapped phases protected by a crystal symmetry [Fu, 2011]. They characterize 2D sections of the 3D Brillouin Zone where the spectrum is gapped. As a consequence of these 2D topological invariants, protected surface states exist for this class of topologically non trivial 3D Dirac semimetals.

2.4.3 Stability of 2D graphene

Several mechanisms coexist to stabilize the two band crossings at the Dirac points $\mathbf{K}$ and $\mathbf{K}'$ in graphene. Let us recall the low-energy Hamiltonian:

$$H_{\mathbf{K},\mathbf{K}'}(\mathbf{q}) = \hbar v \left(\pm q_x \sigma_x + q_y \sigma_y\right). \tag{2.44}$$

Combination of time-reversal and spatial inversion

The low energy Hamiltonians at the $\mathbf{K}$ and $\mathbf{K}'$ Dirac points are related by a time-reversal operation $\mathcal{T}$ (2.33) and spatial inversion $\mathcal{P}$ (2.34), already defined in section 2.2.1. The local low energy Hamiltonian is thus invariant under the combination $\mathcal{PT}$, which enforces the relation (2.35) :

$$\sigma_x H^*_{\mathbf{K}}(\mathbf{q}) \sigma_x = H_{\mathbf{K}}(\mathbf{q}), \tag{2.45}$$

and forbids a mass term $m\sigma_z$ which would open a gap.

Mirror symmetry

The mirror symmetry along the x-axis, $R_x : x \to x,\ y \to -y$, exchanges A and B and is local in valley, see Fig. 2.11. Hence, the mirror symmetry of Graphene enforces the following relation on Hamiltonian (2.44):

$$\sigma_x H_{\mathbf{K}}(q_x, q_y) \sigma_x = H_{\mathbf{K}}(q_x, -q_y). \tag{2.46}$$

This relation forbids a mass term $m\sigma_z$ at the $\mathbf{K}$ point and protects the crossing from gap opening. In the literature, a topological invariant has been associated with this symmetry [Chiu et al., 2016].

Sublattice symmetry: chiral symmetry

The honeycomb lattice of graphene is bipartite: it is made of two identical sublattices A and B. In the nearest neighbour approximation, the only couplings are between the different sublattices A and B. The Bloch Hamiltonian is thus off-diagonal in the (A, B) basis. As a consequence, it anti-commutes with the unitary operator $C = \sigma_z$:

$$\sigma_z H_{\mathbf{K}}(\mathbf{q}) \sigma_z = -H_{\mathbf{K}}(\mathbf{q}). \tag{2.47}$$

This property of the Hamiltonian is called a chiral symmetry. It differs from a usual symmetry, since it relates states with opposite energies: $H|\psi\rangle = \varepsilon|\psi\rangle \implies H(C|\psi\rangle) = -\varepsilon(C|\psi\rangle)$. The chiral symmetry

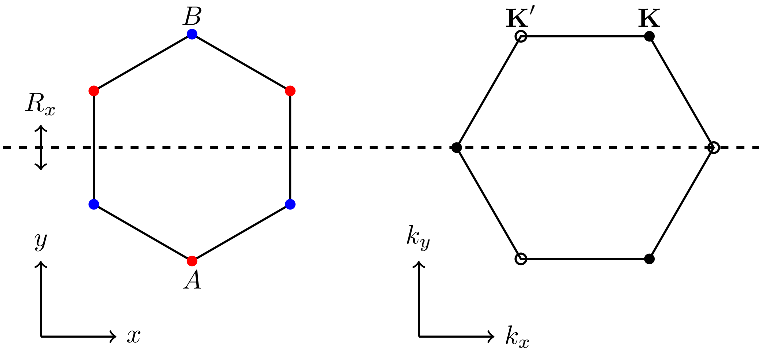

Figure 2.11: Unit cell (Left) and Brillouin Zone (Right) of Graphene's Honeycomb lattice. The mirror symmetry operation R_x exchanges A and B sublattices. In the Brillouin Zone, R_x acts locally in each valley $\mathbf{K}$, $\mathbf{K}'$.

(2.47) prevents a mass term $m\sigma_z$ from opening a gap. In Chapter 4 we investigate three-band semimetals with chiral symmetry and establish a relation between a topological property of the band crossing and the existence of a finite conductivity at the crossing.

We have listed three mechanisms related to different symmetries which coexist to explain the stability of the band crossings at the Dirac points in graphene. In the literature, different topological invariants have been associated with these symmetries. The case of graphene raises the question of the generality of symmetry related topological characterization of band crossings.

2.5 Towards a general topological characterization of band crossings? A study on crossings with a flat band

In the literature, the stability of the two band crossings in graphene have been associated to different symmetries and different topological invariants. There is no unique definition of a topological invariant associated to a band crossing, unique in the sense that it would be independent of the Brillouin Zone symmetries.

Considering the Haldane model [Haldane, 1988] where a single two-band crossing exists as a critical phase, we have seen that the crossing corresponds to a Chern number variation $\Delta\nu = \pm 1$, see section 2.2.1. We will show that the existence of a quantized Berry winding around the Dirac point of graphene can be seen as a 2D projection of a 3D Chern number. This characterization of the crossing as a critical phase, with a 3D Chern number and its 2D projection as a quantized Berry winding is local, independent of symmetries. To go from a 3D Chern number to a quantized Berry winding, we will see that the local Hamiltonian must possess an appropriate anti-unitary symmetry.

We then consider the topological characterization of three-band models with a flat band that generalize graphene. Following the approach above, we study 2D models as well as their possible extension to 3D and investigate whether the topological properties of the 2D crossing can be deduced from the dimensional reduction of a 3D Chern number. Our results indicate a more complex reality than we could have expected.

The work presented in this section has been carried in collaboration with Pierre Delplace and David Carpentier at the beginning of this thesis but not published.

2.5.1 Graphene: Dirac point as a 2D projection of a 3D Weyl point

2D: quantized Berry winding

In section 2.2.1 we have seen how along a critical line in the Haldane model the gap closes at a single Dirac point of Graphene, e.g. at point $\mathbf{K}$. The low-energy Hamiltonian reads

$$H_{\mathbf{K}}(\mathbf{q}) = \hbar v \begin{pmatrix} 0 & q_x - iq_y \\ q_x + iq_y & 0 \end{pmatrix}. \qquad (2.48)$$

A possible eigenstates basis is

$$\psi_+ = \frac{1}{\sqrt{2}}\begin{pmatrix} 1 \\ \mathrm{e}^{\mathrm{i}\varphi} \end{pmatrix}, \qquad \varepsilon_+ = \hbar v_F q, \tag{2.49a}$$

$$\psi_- = \frac{1}{\sqrt{2}}\begin{pmatrix} \mathrm{e}^{-\mathrm{i}\varphi} \\ -1 \end{pmatrix}, \qquad \varepsilon_- = -\hbar v_F q, \tag{2.49b}$$

where we have introduced polar coordinates for $\mathbf{q}$: (q, φ). We can define the Berry connections

$$\mathbf{A}_+ = -\mathrm{i}\langle\psi_+|\boldsymbol{\nabla}_{\mathbf{q}}|\psi_+\rangle = \frac{1}{2}\boldsymbol{\nabla}\varphi \tag{2.50a}$$

$$\mathbf{A}_- = -\mathrm{i}\langle\psi_-|\boldsymbol{\nabla}_{\mathbf{q}}|\psi_-\rangle = -\frac{1}{2}\boldsymbol{\nabla}\varphi. \tag{2.50b}$$

$$\tag{2.50c}$$

When circling the $\mathbf{K}$ point, electronic states acquire a Berry phase

$$\gamma_\pm = \int_0^{2\pi} q d\varphi \left(\pm\frac{1}{2}\boldsymbol{\nabla}\varphi\right) = \pm\pi. \tag{2.51}$$

Here we have computed the Berry winding around a circle of radius q: the result is independent of q. Even more, the π Berry winding (2.51) is topological: it is independent of the choice of eigenstates basis and of the closed path around the Dirac point $\mathbf{K}$.

3D: Chern number

Now consider the Hamiltonian around the critical phase in the Haldane model (2.32). Locally, the Hamiltonian (2.32)resembles that of a Weyl point

$$H = \hbar v \boldsymbol{\sigma}\cdot\mathbf{k} = \hbar v \begin{pmatrix} k_z & k_x - \mathrm{i}k_y \\ k_x + \mathrm{i}k_y & -k_z \end{pmatrix}, \tag{2.52}$$

where the mass m in the Haldane model is analogous to the third component of momentum k_z. The 2D projection of Hamiltonian (2.52) on the $k_z = 0$ plane gives the 2D massless Dirac Hamiltonian (2.48) with $\mathbf{q} \equiv \mathbf{k}$.

The Weyl point is a Berry monopole characterized by a Chern number $C_1 = \pm 1$, see section 2.1.4. We repeat here the computation of the Chern number presented in section 2.1.4 to highlight the correspondence between the 3D Chern number and the quantized Berry winding in graphene. Take a possible eigenstate basis of (2.52), with spherical coordinates for $\mathbf{k}$, (k, θ, φ)

$$\psi_+^N(\mathbf{k}) = \begin{pmatrix} \cos\frac{\theta}{2} \\ \sin\frac{\theta}{2}\,\mathrm{e}^{\mathrm{i}\varphi} \end{pmatrix}, \varepsilon_+ = \hbar v k, \tag{2.53a}$$

$$\psi_-^N(\mathbf{k}) = \begin{pmatrix} \sin\frac{\theta}{2}\,\mathrm{e}^{-\mathrm{i}\varphi} \\ -\cos\frac{\theta}{2} \end{pmatrix}, \varepsilon_- = -\hbar v k. \tag{2.53b}$$

Eigenstates (2.53a) and (2.53b) are well defined everywhere in the Brillouin Zone except on the negative k_z $(\theta = \pi)$ axis. A gauge transformation allows to define eigenstates of the ε_+ band on the negative k_z $(\theta = \pi)$ axis : $\psi_+^S = \mathrm{e}^{-\mathrm{i}\varphi}\psi_+^N$. ψ_+^S is defined everywhere except on the positive k_z $(\theta = 0)$axis. Because of the Berry monopole at $\mathbf{k} = \mathbf{0}$, there is an obstruction to define a continuous phase for the eigenstates all around the Brillouin Zone, see section 2.1.4.

The connections for the ε_+ band associated to the different gauge choices ψ_+^N and ψ_+^S read

$$\mathbf{A}_+^N = -\mathrm{Im}\langle\psi_+^N|\boldsymbol{\nabla}|\psi_+^N\rangle = \sin^2\left(\frac{\theta}{2}\right)\boldsymbol{\nabla}_{\mathbf{k}}\varphi, \tag{2.54a}$$

$$\mathbf{A}_+^S = -\mathrm{Im}\langle\psi_+^S|\boldsymbol{\nabla}|\psi_+^S\rangle = -\cos^2\left(\frac{\theta}{2}\right)\boldsymbol{\nabla}_{\mathbf{k}}\varphi = \mathbf{A}_+^N - \boldsymbol{\nabla}_{\mathbf{k}}\varphi. \tag{2.54b}$$

We now compute the Berry flux threading a closed surface in $\mathbf{k}$-space that encircles the Weyl point $\mathbf{k} = \mathbf{0}$. Since it corresponds to a Chern number, the computation is independent of the choice of the surface. Take for example a sphere centered on the origin, which we separate into two hemispheres U_N and U_S

where the connections $\mathbf{A}_N$ and $\mathbf{A}_S$ are well behaved, respectively, see Fig. 2.3. The Berry flux threading the surface is given by the integral of the Berry curvature $\mathbf{F}_+ = \boldsymbol{\nabla} \times \mathbf{A}$. Similarly as for the two-band model of section 2.1.4 we use Stokes' theorem to find

$$\begin{aligned} C_1^+ = \frac{1}{2\pi} \oiint \mathbf{F}_+ \cdot d\mathbf{S} &= \frac{1}{2\pi} \left(\oint_{\partial U_N} \mathbf{A}_+^N \cdot d\boldsymbol{\ell} + \oint_{\partial U_S} \mathbf{A}_+^S \cdot d\boldsymbol{\ell} \right) \\ &= \frac{1}{2\pi} \oint_{\partial U_N} (\mathbf{A}_+^N - \mathbf{A}_+^S) \cdot d\boldsymbol{\ell} \\ &= \frac{1}{2\pi} \int_0^{2\pi} d\varphi \\ &= 1. \end{aligned} \tag{2.55}$$

Hence, the ε_+ band has a Chern number $C_1^+ = 1$.

Berry winding as a 2D projection

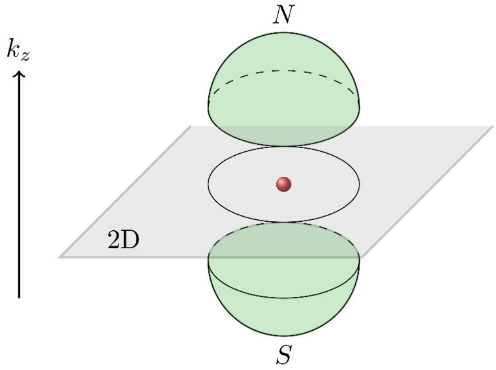

Figure 2.12: A 2D band crossing can be seen as a projection of a 3D band crossing. When an anti-unitary transformation of the 3D Hamiltonian relates the northern and southern sides of the plane, the Berry winding along a closed loop can be related to the 2D projection of the 3D integral of the Berry flux on any closed surface encircling the crossing.

We have computed the Chern number associated to the Weyl point as an integral of Berry flux threading a surface enclosing the origin in 3D $\mathbf{k}$ space. In the course of the derivation, we have seen that the integral of Berry flux (2.55) corresponds to the difference between the integrals of the different Berry connections (2.54a) and (2.54b) along the equator, i.e. on a closed loop circling the origin in the $k_z = 0$ ($\theta = \pi/2$) plane, see Fig. 2.12. Projecting the connections (2.54a) and (2.54b) on the $k_z = 0$ ($\theta = \pi/2$) plane, we find

$$\mathbf{A}_+^N(k_z = 0) = -\mathbf{A}_+^S(k_z = 0) = \frac{1}{2} \boldsymbol{\nabla} \varphi = \mathbf{A}_+^{2D}, \tag{2.56}$$

where $\mathbf{A}_+^{2D}$ is the 2D Berry connection for graphene (2.50a).

We therefore have the following relation between the 3D Chern number (2.55) and the 2D Berry winding (2.51):

$$\begin{aligned} C_1^+ &= \frac{1}{2\pi} \oint_{\partial U_N} (\mathbf{A}_+^N - \mathbf{A}_+^S) \cdot d\boldsymbol{\ell} \\ &= \frac{1}{2\pi} \oint_{\partial U_N} 2\mathbf{A}_+^{2D} \\ C_1^+ &= \frac{1}{\pi} \gamma_+. \end{aligned} \tag{2.57}$$

Thus, the π-quantization of the Berry winding around the Dirac point in graphene is a dimensional reduction of the topological Chern number of the Weyl point from 3D to 2D.

A condition for the planar projection: existence of an anti-unitary "North-South" transformation

Note that the relation $\mathbf{A}_N^+(k_z = 0) = -\mathbf{A}_S^+(k_z = 0) = \mathbf{A}_+^{2D}$ (2.56) between the different Weyl connections (2.54a) and (2.54b) projected onto the equator is crucial to obtain the equality (2.57) between the 3D Chern number and the 2D Berry winding. This relation $\mathbf{A}_N^+(k_z = 0) = -\mathbf{A}_S^+ = \mathbf{A}_+^{2D}$ (2.56) is related to the existence of an anti-unitary transformation of Hamiltonian (2.52) which relates the two hemispheres U_N and U_S. This transformation reads

$$U = \mathcal{K}\sigma_x, . \tag{2.58}$$

Its action on Hamiltonian (2.52) yields

$$U^{-1}H(k_x,k_y,k_z)U = \sigma_x H^*(k_x,k_y,k_z)\sigma_x = H(k_x,k_y,-k_z). \tag{2.59}$$

In particular, U is a symmetry of the Hamiltonian on the equator plane $k_z = 0$ ($\theta = \pi/2$), where we have

$$\psi_+^N(k_z = 0) = U\psi_+^S(k_z = 0). \tag{2.60}$$

From (2.60) we deduce the relation between connections (2.54a) and (2.54b) at the equator:

$$\begin{aligned}
\mathbf{A}_+^N(k_z = 0) &= \mathrm{Im}\langle\psi_+^N(k_z = 0)|\boldsymbol{\nabla}_{\mathbf{k}}|\psi_+^N(k_z = 0)\rangle \\
&= \mathrm{Im}\langle U\psi_+^S(k_z = 0)|\boldsymbol{\nabla}_{\mathbf{k}}|U\psi_+^S(k_z = 0)\rangle \\
&= \mathrm{Im}\langle\left(\psi_+^S(k_z = 0)\right)^*|\sigma_x\boldsymbol{\nabla}_{\mathbf{k}}\sigma_x|\left(\psi_+^S(k_z = 0)\right)^*\rangle \\
&= \mathrm{Im}\left(\langle\psi_+^S(k_z = 0)|\boldsymbol{\nabla}_{\mathbf{k}}|\psi_+^S(k_z = 0)\rangle\right)^* \\
&= -\mathrm{Im}\langle\psi_+^S(k_z = 0)|\boldsymbol{\nabla}_{\mathbf{k}}|\psi_+^S(k_z = 0)\rangle \\
\mathbf{A}_+^N(k_z = 0) &= -\mathbf{A}_+^S(k_z = 0).
\end{aligned} \tag{2.61}$$

Thus, a two-band crossing in 2D can be characterized by a quantized Berry winding (2.51) which is a 2D projection of a 3D Chern number (2.55). The projection is possible because of the presence of an anti-unitary transformation (2.59) which relates the "northern" and "southern" side of the 2D plane that contains the crossing, see Fig. 2.12. This anti-unitary transformation constrains the planar projections of the northern and southern connections to be opposite (2.56). Stokes theorem then implies a direct relation between the Chern number and the 2D Berry winding (2.57) that enforces the quantization of the Berry winding.

2.5.2 Topological characterization of three-band crossings with a flat band

We have seen with the simple example of graphene how a general topological characterization of a 2D band crossing can be obtained. Considering the 2D crossing as a critical phase, we have characterized the 2D quantized Berry winding as a 2D projection of a 3D Chern number. This projection is associated to the presence of an anti-unitary transformation between the "northern" and "southern" sides of the 2D plane containing the crossing, see Fig. 2.12. Let us now follow our investigation on semi-metallic phases beyond graphene.

A two-band crossing in 2D is described by the low-energy Dirac Hamiltonian of graphene. The simplest extensions of graphene consist either in two-band crossings in higher dimensions, or 2D band-crossings with higher number of bands. A two-band crossing in 3D is a Weyl point, which is well characterized from the point of view of topology by a non trivial topological invariant, the Chern number. Let us therefore consider the simplest 2D extensions of graphene, i.e. planar models with three-band crossings. Following the reasoning of section 2.5.1 we consider local Hamiltonians describing the crossings and investigate whether they can be characterized by a quantized Berry winding that is obtained from the 2D projection of a 3D Chern number.

The 2D three-band crossings we consider correspond to the modified dice lattice, so-called α-T$_3$ model [Raoux et al., 2014], the three-band hexagonal, so-called H$_3$ model [Louvet et al., 2015] and the Lieb lattice model [Lieb, 1989]. In a different study, we have also investigated these three-band extensions of graphene from the point of view of transport. In Chapter 4 it is shown that these models do not necessarily have a quantized Berry winding around the crossing. The existence of a quantized Berry winding is related to a finite conductivity at the crossing coming from evanescent states mediated transport. Here, we investigate the windings around the crossing as possible dimensional reductions of 3D Chern numbers. Even though in the seminal case of graphene the quantized Berry winding around any closed loop circling the Dirac point in the 2D BZ is in direct correspondence with the Chern number characterizing the Sphere around the Weyl point in 3D, we find that flat-band systems provide examples where is no equivalence between the existence of a non-trivial Chern number in 3D and a quantized winding in 2D.

2.5.3 The spin-1 Hamiltonian of the Lieb lattice

2D Lieb lattice model

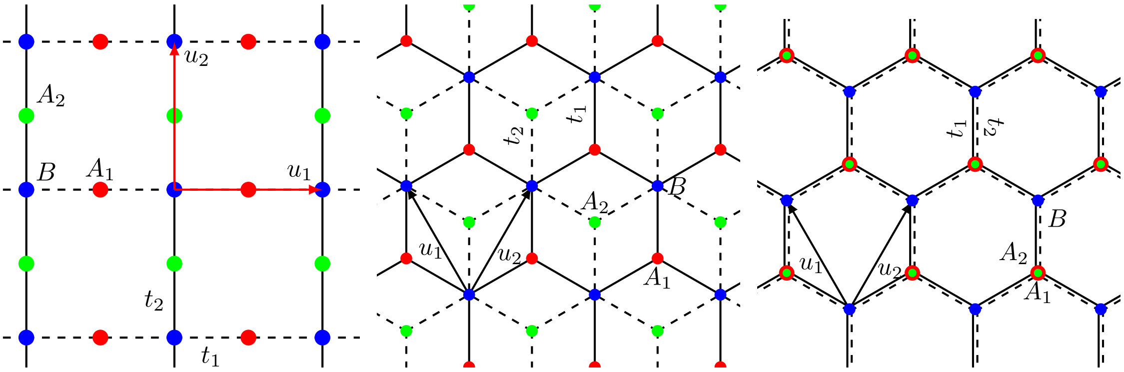

(a) (b) (c)

Figure 2.13: (a) The Lieb lattice model. (b) The α-T$_3$ model. (c) The three band hexagonal (H$_3$) model: honeycomb lattice with two decoupled orbitals on one sublattice. In all three cases bonds between sites correspond to nearest neighbour hoppings, between A_i and B only. $\vec{u_i}$ are Bravais lattice vectors.

The Lieb lattice model [Lieb, 1989] is a bipartite lattice model on a square lattice, with three sites per unit cell, as shown on Fig. 2.13a. The three bands cross at $\mathbf{k} = \mathbf{0}$ in the Brillouin Zone, and the low-energy Hamiltonian in the (A_1, A_2, B) basis reads

$$H_{\text{Lieb}} = \hbar v \begin{pmatrix} 0 & 0 & -\mathrm{i}k_x \\ 0 & 0 & \mathrm{i}k_y \\ \mathrm{i}k_x & -\mathrm{i}k_y & 0 \end{pmatrix}. \tag{2.62}$$

A possible eigenstates basis reads

$$\psi_\pm = \frac{1}{\sqrt{2}} \begin{pmatrix} -\mathrm{i}\cos\theta \\ \mathrm{i}\sin\theta \\ \pm 1 \end{pmatrix}, \qquad \varepsilon_\pm = \pm\hbar v k, \tag{2.63a}$$

$$\psi_0 = \begin{pmatrix} \sin\theta \\ \cos\theta \\ 0 \end{pmatrix}, \qquad \varepsilon_0 = 0, \tag{2.63b}$$

where we have introduced polar coordinates for $\mathbf{k}$: (k, θ). Because the Hamiltonian and wavefunctions have no imaginary components, the Berry connections are trivial:

$$\mathbf{A}_\pm = \mathrm{Im}\langle\psi_\pm|\boldsymbol{\nabla}_\mathbf{k}|\psi_\pm\rangle = \mathbf{0}, \tag{2.64a}$$

$$\mathbf{A}_0 = \mathrm{Im}\langle\psi_0|\boldsymbol{\nabla}_\mathbf{k}|\psi_0\rangle = \mathbf{0}, \tag{2.64b}$$

hence the Berry windings around the crossing are trivially zero:

$$\gamma_\pm = \oint \mathbf{A}_\pm \cdot d\boldsymbol{\ell} = 0, \tag{2.65a}$$

$$\gamma_0 = \oint \mathbf{A}_0 \cdot d\boldsymbol{\ell} = 0. \tag{2.65b}$$

So far, the three-band crossing described by (2.62) is topologically trivial. However, the crossing is a dimensional reduction of a 3D three-band crossing that corresponds to a spin-1 particle and has Chern number $C_1 = \pm 2$.

3D spin-1 Hamiltonian

The 2D Hamiltonian (2.62) has the form $k_xS_x + k_yS_y$. Defining a third matrix S_z as $S_z = -\mathrm{i}[S_x, S_y]$ we find that the S_i matrices describe a spin-1 algebra: $[S_i, S_j] = \mathrm{i}\epsilon_{ijk}S_k$. Adding a gap opening term k_zJ_z to (2.62) we get the following Hamiltonian, which describes a three-band crossing in 3D associated with a Spin-1 particle:

$$H_{S=1}(\mathbf{k}) = \hbar v \begin{pmatrix} 0 & ik_z & -ik_x \\ -ik_z & 0 & ik_y \\ ik_x & -ik_y & 0 \end{pmatrix} = \hbar v \mathbf{S}\cdot\mathbf{k}. \tag{2.66}$$

A possible eigenstates basis reads, in spherical coordinates for $\mathbf{k}$ (k, β, θ):

$$\psi_0 = \begin{pmatrix} \sin\beta\ \sin\theta \\ \sin\beta\ \cos\theta \\ \cos\beta \end{pmatrix},\ \varepsilon_0 = 0 \tag{2.67a}$$

$$\psi_\pm = \frac{1}{\sqrt{2}} \begin{pmatrix} \cos\beta\sin\theta \pm i\cos\theta \\ \cos\beta\cos\theta \mp i\sin\theta \\ -\sin\beta \end{pmatrix},\ \varepsilon_\pm = \pm k. \tag{2.67b}$$

The eigenstates only depend on $\hat{\mathbf{k}} = \mathbf{k}/k$ so we can focus on the unit sphere around the crossing in the 3D Brillouin Zone. Notice that the wavefunction for the upper and lower band $\psi_\pm$ (2.67b) is singular along the z-axis $(\beta = 0, \pi)$, where θ is ill-defined. For the ε_+ band at the North Pole we get

$$\lim_{\beta\to 0} \psi_+ = \frac{1}{\sqrt{2}} \begin{pmatrix} ie^{-i\theta} \\ e^{-i\theta} \\ 0 \end{pmatrix}. \tag{2.68}$$

Similarly than for the two-band model of section 2.1.4 it is possible to regularize the wave function at the North pole or the South pole separately, through a redefinition of its phase. Away from the z-axis the two conventions are related by the gauge transformation $\psi^N_\pm = e^{\pm 2i\theta}\psi^S_\pm$. The Berry connections $\mathbf{A}^{N/S}_\pm = -i\langle\psi^{N/S}_\pm|\boldsymbol{\nabla}_\mathbf{k}|\psi^{N/S}_\pm\rangle$ thus verify $\mathbf{A}^N_\pm - \mathbf{A}^S_\pm = \pm 2\boldsymbol{\nabla}_\mathbf{k}\theta$. We give for illustration the expression of the Berry connection for the upper band:

$$\mathbf{A}^N_+ = (1-\cos\beta)\boldsymbol{\nabla}_\mathbf{k}\theta \tag{2.69}$$

$$\mathbf{A}^S_+ = -(1+\cos\beta)\boldsymbol{\nabla}_\mathbf{k}\theta. \tag{2.70}$$

A straightforward calculation of the integral of connection $\mathbf{A}^N_+$ (2.69) around a circle of radius $k\sin\beta$ around the z-axis shows that $\mathbf{A}^N_+$ describes, in addition to the degeneracy located at the origin which acts as a source of Berry flux, a half tube of flux along the negative k_z carrying a flux $4\pi\hat{e}_z$:

$$\lim_{\beta\to\pi} \oint \mathbf{A}^N_+ \cdot d\boldsymbol{\ell} = \lim_{\beta\to\pi} \int_0^{2\pi} d\theta(1-\cos\beta) = 4\pi. \tag{2.71}$$

By analogy with the two-band model of section 2.1.4, we can then compute the integral of the Berry curvature $\mathbf{F}_\pm$ on the unit sphere S around the crossing point in momentum space:

$$\begin{aligned} C_1^\pm &= \frac{1}{2\pi} \oiint_S \mathbf{F}_\pm d\mathbf{S} \\ &= \frac{1}{2\pi}\left(\iint_{\beta<\frac{\pi}{2}} (\boldsymbol{\nabla}_\mathbf{k}\times\mathbf{A}^N_\pm)d\mathbf{S} + \iint_{\beta>\frac{\pi}{2}} (\boldsymbol{\nabla}_\mathbf{k}\times\mathbf{A}^S_\pm)d\mathbf{S} \right) \\ &= \frac{1}{2\pi}\oint_{k_z=0} (\mathbf{A}^N_\pm - \mathbf{A}^S_\pm)d\mathbf{k} = \pm 2, \end{aligned} \tag{2.72}$$

which yields the Chern number $C_1^\pm = \pm 2$ carried by the upper (lower) band.

The anti-unitary transformation

$$U = \begin{pmatrix} 1 & 0 & 0 \\ 0 & 1 & 0 \\ 0 & 0 & -1 \end{pmatrix}\mathcal{K} \tag{2.73}$$

acts on the spin-1 Hamiltonian (2.66) following

$$U^{-1}H_{S=1}(k_x, k_y, k_z)U = H_{S=1}(k_x, k_y, -k_z). \tag{2.74}$$

Hence, U is a symmetry of the Hamiltonian at the equator $k_z = 0$ ($\beta = \pi/2$). It relates eigenstates in the North and South gauge following $U\psi_N(k_z = 0) = \psi_S(k_z = 0)$, so that the Berry connections verify $\mathbf{A^N}(k_z = 0) = -\mathbf{A^S}(k_z = 0)$. Therefore the 2D Berry winding at the equator is derived from the Chern number (2.72) through

$$C_1^{\pm} = \frac{1}{2\pi} \oint_{k_z=0} 2\mathbf{A}_{\pm}^{N} d\mathbf{k} = \frac{1}{\pi}\gamma_{\pm}^{N}. \tag{2.75}$$

Since $C_1^{\pm} = \pm 2$, the Berry winding is trivial $\gamma_{\pm}^{N} = \pm 2\pi \equiv 0 \bmod 2\pi$.

We were able to apply our dimensional reduction approach and identify a 3D topological invariant related to the three-band crossing of the Lieb model, even though the 2D Berry winding is trivial. We have shown that the three-band crossing of the Lieb model is a 2D projection of a 3D spin-1 crossing. The 3D Chern number $|C_1| = 2$ of the spin-1 Hamiltonian projects onto a trivial Berry winding in 2D $\gamma \equiv 0 \bmod 2\pi$. A topologically non trivial 3D crossing can have trivial planar cuts: there can be a “loss of information“ with the dimensional reduction operation.

2.5.4 The α-T$_3$ model

The α-T$_3$ model is a natural extension of graphene [Raoux et al., 2014]. We investigate its topological properties, and first derive the Berry windings around the crossing in the 2D Brillouin zone: we find that the windings are not quantized and vary continuously with a parameter describing the hopping amplitudes. Then, we consider a 3D extension of the model and find that it has a quantized, non zero Chern number. We explain this discrepancy between a non zero quantized Chern number and non quantized windings by the absence of an anti-unitary transformation between the northern and southern sides of the 2D plane, see Fig. 2.12.

The 2D model

As shown on Fig. 2.13b, the α-T$_3$ consists of a honeycomb lattice with an extra atomic site located in the centre of each hexagon, which only connects to one of the two sublattices of the honeycomb lattice. The system is bipartite: the only hoppings are between the A_i and the B sites. As a consequence, the Hamiltonian possesses a chiral symmetry which relates eigenstates with opposite energies and enforces the third band to be flat at $E = 0$. The three bands cross at the $\mathbf{K}$ and $\mathbf{K}'$ points of graphene in the Brillouin Zone, and the low-energy Hamiltonian near point $\mathbf{K}$ reads

$$H_{T_3}(\mathbf{k}, \phi) = \hbar v \begin{pmatrix} 0 & 0 & \cos\phi\ (k_x - \mathrm{i}k_y) \\ 0 & 0 & \sin\phi\ (k_x + \mathrm{i}k_y) \\ \cos\phi\ (k_x + \mathrm{i}k_y) & \sin\phi\ (k_x - \mathrm{i}k_y) & 0 \end{pmatrix}, \tag{2.76}$$

where $\tan\phi = t_1/t_2$ gives the relative strength of nearest-neighbour hoppings, see Fig. 2.13b. The eigenstates read, in polar coordinates for $\mathbf{k}$ (k, θ):

$$\psi^{\pm}(\mathbf{k}) = \frac{1}{\sqrt{2}} \begin{pmatrix} \cos\phi\ \mathrm{e}^{-\mathrm{i}\theta} \\ \sin\phi\ \mathrm{e}^{\mathrm{i}\theta} \\ \pm 1 \end{pmatrix}, \qquad \varepsilon(\mathbf{k}) = \pm\hbar v k; \tag{2.77a}$$

$$\psi^{0}(\mathbf{k}) = \begin{pmatrix} -\sin\phi\ \mathrm{e}^{\mathrm{i}\theta} \\ \cos\phi\ \mathrm{e}^{-\mathrm{i}\theta} \\ 0 \end{pmatrix}, \qquad \varepsilon(\mathbf{k}) = 0. \tag{2.77b}$$

They only depend on $\hat{\mathbf{k}} = \mathbf{k}/k$. The Berry connections read

$$\mathbf{A}_{\pm} = -\frac{1}{2}\cos 2\phi\ \boldsymbol{\nabla}_{\mathbf{k}}\ \theta, \tag{2.78a}$$

$$\mathbf{A}_{0} = \cos 2\phi\ \boldsymbol{\nabla}_{\mathbf{k}}\ \theta. \tag{2.78b}$$

We have then computed the integrals of the Berry phases around the crossing in the Brillouin Zone:

$$\gamma_{\pm} = -\pi\cos 2\phi, \tag{2.79a}$$

$$\gamma_{0} = 2\pi\cos 2\phi. \tag{2.79b}$$

Surprisingly, we find that theses phases are not quantized. They depend on the hopping parameter ϕ and vary from $\gamma_{\pm}(\phi = 0) = -\pi$ to $\gamma_{\pm}(\phi = \pi/4) = 0$. The band crossing of the α-T$_3$ model is a complex singularity which can not be described unambiguously with 2D Berry windings. We have then studied a possible 3D extension of this model as an attempt to define a topological invariant related to the crossing and consider its possible 2D projection.

A possible 3D extension

We start from the 2D Hamiltonian H_{T_3} (2.76) and add an appropriate k_z dispersing term to extend it to three dimensions. The 3D Hamiltonian reads

$$H_{T_3}^{3D}(\mathbf{k},\phi) = \begin{pmatrix} k_z & 0 & \cos\phi\ k_- \\ 0 & -k_z & \sin\phi\ k_+ \\ \cos\phi\ k_+ & \sin\phi\ k_- & -\cos 2\phi\ k_z \end{pmatrix}, \tag{2.80}$$

with $k_\pm = k_x \pm i k_y$. Introducing spherical coordinates for $\mathbf{k}$ (k,θ,β), the eigenstates only depend on θ, β and the hopping parameter ϕ:

$$\begin{aligned} \psi_\pm &= \frac{1}{\sqrt{2(1\pm\cos\beta\cos 2\theta)}} \begin{pmatrix} (1\pm\cos\beta)\cos\phi\ e^{-i\theta} \\ (1\mp\cos\beta)\sin\phi\ e^{i\theta} \\ \pm\sin\beta \end{pmatrix}, \\ \varepsilon_\pm &= \pm k, \end{aligned} \tag{2.81a}$$

$$\begin{aligned} \psi_0 &= \frac{1}{\sqrt{1-\cos^2\beta\cos^2 2\phi}} \begin{pmatrix} -\sin\beta\sin\phi\ e^{-i\theta} \\ \sin\beta\cos\phi\ e^{i\theta} \\ \cos\beta\sin 2\phi \end{pmatrix}, \\ \varepsilon_0 &= -k\cos\beta\cos 2\phi, \end{aligned} \tag{2.81b}$$

We focus now on the upper band for illustration: the wavefunction shows vortices at the North pole $\beta = 0$ and the South Pole $\beta = \pi$. We can regularize it at the North (South) pole through $\psi_+^N = e^{i\theta}\psi_+$ $(\psi_+^S = e^{-i\theta}\psi_+.)$ ψ_+^N (ψ_+^S) has a unique vortex at the South (North) pole and is well defined elsewhere. We can define the associated Berry phase in the regions where there is no ambiguity on the wavefunction's phase. The Berry connections read for the ε_+ band:

$$\mathbf{A}_+^{\mathbf{N}} = \frac{\sin^2\beta + 2(1-\cos\beta)^2\sin^2\phi}{2(1+\cos\beta\cos 2\phi)}\nabla_{\mathbf{k}}\theta \tag{2.82}$$

$$\mathbf{A}_+^{\mathbf{S}} = -\frac{\sin^2\beta + 2(1+\cos\beta)^2\cos^2\phi}{2(1+\cos\beta\cos 2\phi)}\nabla_{\mathbf{k}}\theta. \tag{2.83}$$

As in the magnetic monopole case, these connections describe a source of Berry flux at the origin together with a half flux tube on the $z < 0$ $(z > 0)$ semi-axis. To see this, consider the winding of the connection around a circle of radius $k\sin\beta$ at polar angle β:

$$\begin{aligned} \oint_\beta \mathbf{A}_+^{\mathbf{N}} d\mathbf{k} &= \int_0^{2\pi} \frac{\sin^2\beta + 2(1-\cos\beta)^2\sin^2\phi}{2(1+\cos\beta\cos 2\phi)} d\theta \\ &= \pi\frac{(\sin^2\beta + 2(1-\cos\beta)^2\sin^2\phi)}{(1+\cos\beta\cos 2\phi)}. \end{aligned} \tag{2.84}$$

(2.84) contains the flux from the Berry monopole located at the origin through the surface of the disk and possible contribution from the half-flux tube. The first contribution increases with the solid angle of the surface. In the limit $\beta \to 0$ (North pole) or $\beta \to \pi$ (South pole) we get an extra contribution:

$$\lim_{\beta\to 0}\oint \mathbf{A}_+^{\mathbf{N}} d\mathbf{k} = 0, \quad \lim_{\beta\to\pi}\oint \mathbf{A}_+^{\mathbf{N}} d\mathbf{k} = \frac{8\pi\sin^2\phi}{1-\cos 2\phi}. \tag{2.85}$$

Similarly, we find that the South connection $\mathbf{A}_+^S$ describes a half-flux tube located on the positive k_z semi-axis

$$\lim_{\beta\to 0}\oint \mathbf{A}_+^{\mathbf{S}} d\mathbf{k} = -\frac{8\pi\cos^2\phi}{1+\cos 2\phi}, \quad \lim_{\beta\to\pi}\oint \mathbf{A}_+^{\mathbf{N}} d\mathbf{k} = 0. \tag{2.86}$$

For $\phi = \pi/4$ the difference $\mathbf{A}_+^N - \mathbf{A}_+^S$, corresponding to the gauge transformation $\psi \to e^{2i\theta}\psi$, describes an infinite solenoid of flux $4\pi\hat{e}_z = 2\pi\nu\hat{e}_z$, where ν is the Chern number associated to the upper band. When $\phi \neq \pi/4$, the flux is not quantized by units of 2π, similar to a Dirac string that would terminate at a non quantized magnetic monopole. This non-quantization is analogous to the non quantization we found for 2D Berry windings (2.79b) that are not quantized in units of π. Thus, this three band crossing is a complex singularity that is hard to describe using the same notions as for two band crossings.

We have computed the Chern number, the integral of the Berry connection $\mathbf{F}$ along a sphere S encircling the nodal point:

$$C_1^+ = \frac{1}{2\pi}\oiint_S \mathbf{F}_+ d\mathbf{S} = \frac{1}{2\pi}\left(\iint_{U_N}\mathbf{F}_+ d\mathbf{S} + \iint_{U_S}\mathbf{F}_+ d\mathbf{S}\right) \tag{2.87}$$

$$= \frac{1}{2\pi}\oint_{\beta=\pi/2}(\mathbf{A}_+^N - \mathbf{A}_+^S)d\boldsymbol{\ell} \tag{2.88}$$

$$= 2. \tag{2.89}$$

The Chern number is well quantized, independent on ϕ. Note that for $\phi = \pi/4$ i.e. $tan\phi = t_1/t_2 = 1$, the Hamiltonian (2.80) takes the form $H_{T_3}^{3D} = \hbar v k_i S_i$ where the S_i matrices form a spin-1 algebra. As we have shown previously, spin-1 particles have a Chern number $|C_1| = 2$ (2.72): thus the result (2.89) for the Chern number is not unexpected.

The reason why the fluxes at each single pole are not quantized is that the Berry sink at the origin does not correspond to a monopole of well-defined spin: the linear Hamiltonian $H_{T_3}^{3D} = \hbar v \mathbf{J}\cdot\mathbf{k}$ is not rotationally invariant and therefore the fluxes through each hemisphere spanned by the $\mathbf{J}$ matrix vector when varying $\mathbf{k}$ are not equal. For the same reason, one finds that the windings at the equator are not quantized except when $\phi = \pi/4$. For $\phi = \pi/4$ the system describes a spin-1 particle and exhibits an anti-unitary transformation relating the two poles

$$U = \begin{pmatrix} 0 & -1 & 0 \\ -1 & 0 & 0 \\ 0 & 0 & 1 \end{pmatrix}\mathcal{K}, \tag{2.90}$$

which acts as

$$UH(k_x,k_y,k_z)U^{-1} = H(k_x,k_y,-k_z), \tag{2.91}$$

is a symmetry at the equator and enforces $\mathbf{A}^N = -\mathbf{A}^S$. For $\phi \neq \pi/4$ the symmetry is broken.

Our results show that in the α-T$_3$ model there is no correspondence between the 3D Chern number and the 2D Berry windings. The three-band crossing is a complex singularity that shows non-quantized Berry windings in 2D and connections with non-quantized half tubes of flux in 3D, a very unusual situation compared to the case of two-band crossings. We explain this singular behaviour by the absence of rotational invariance of the Hamiltonian. The absence of an anti-unitary transformation relating the north and south gauge (see Fig. 2.12) is consistent with the discrepancy between the non quantized 2D Berry windings and the $|C_1| = 2$ Chern number.

A material related to the α-T$_3$ crossing: critical HgCdTe

For a critical Cd concentration, a linear crossing occurs between three doubly degenerate bands in Hg$_{1-x}$Cd$_x$Te [Orlita et al., 2014]. The crossing can be described by the linear $\mathbf{k}\cdot\mathbf{p}$ Hamiltonian of the Kane model. It describes the band structure of Zinc-blende semiconductors at the Γ point. The conduction band has orbital degeneracy 1 and is s-type ($|u_s\rangle$) whereas the valence band is p-type ($|u_x\rangle, |u_y\rangle, |u_z\rangle$). From the atomic-like states of the valence band one forms the following basis of eigenfunctions of the total angular momentum projection on the z-axis: the band is split into two subspaces of total angular momentum $J = 1/2$ and $J = 3/2$, the first manifold being set far down under the topmost valence band because of spin-orbit coupling: $E(J = 1/2) \ll E(J = 3/2), E(|u_s\rangle)$. In the new basis $(|u_s,\uparrow\rangle, |u_{3/2,+3/2}\rangle, |u_{3/2,-1/2}\rangle, |u_s,\downarrow\rangle, |u_{3/2,-3/2}\rangle, |u_{3/2,+1/2}\rangle)$ the low-energy Hamiltonian reads

$$H(\mathbf{k}) = \begin{pmatrix} 0 & \frac{\sqrt{3}}{2}k_- & 0 & 0 & 0 & 0 \\ \frac{\sqrt{3}}{2}k_+ & 0 & -\frac{k_-}{2} & -k_z & 0 & 0 \\ 0 & -\frac{k_+}{2} & 0 & 0 & -k_z & 0 \\ 0 & -k_z & 0 & 0 & \frac{k_-}{2} & 0 \\ 0 & 0 & -k_z & \frac{k_+}{2} & 0 & -\frac{\sqrt{3}}{2}k_- \\ 0 & 0 & 0 & 0 & -\frac{\sqrt{3}}{2}k_+ & 0 \end{pmatrix}, \tag{2.92}$$

where we used the notation $k_\pm = k_x \pm i k_y$ for compactness. The spectrum is given by $\varepsilon = 0, \pm k$, each energy level being doubly degenerate. An eigenstate basis is given by:

$$\psi_A^\pm = \frac{1}{\sqrt{2}} \begin{pmatrix} \frac{\sqrt{3}}{2} e^{-i\theta} \sin\beta \\ \pm 1 \\ -\frac{1}{2} e^{i\theta} \sin\beta \\ -\cos\beta \\ 0 \\ 0 \end{pmatrix}, \tag{2.93a}$$

$$\psi_B^\pm = \frac{1}{\sqrt{2}} \begin{pmatrix} 0 \\ 0 \\ \cos\beta \\ -\frac{1}{2} e^{-i\theta} \sin\beta \\ \mp 1 \\ \frac{\sqrt{3}}{2} e^{i\theta} \sin\beta \end{pmatrix}, \ \varepsilon_\pm = \pm k, \tag{2.93b}$$

$$\psi_A^0 = \begin{pmatrix} \frac{1}{2} e^{-3i\theta} \sin\beta \\ 0 \\ \frac{\sqrt{3}}{2} e^{-i\theta} \sin\beta \\ 0 \\ 0 \\ -\cos\beta \end{pmatrix}, \tag{2.93c}$$

$$\psi_B^0 = \begin{pmatrix} \cos\beta \\ 0 \\ 0 \\ \frac{\sqrt{3}}{2} e^{i\theta} \sin\beta \\ 0 \\ \frac{1}{2} e^{3i\theta} \sin\beta \end{pmatrix}, \ \varepsilon_0 = 0, \tag{2.93d}$$

where we have used spherical coordinates around the degeneracy point (k, β, θ). Note that these wavefunctions do not exhibit any vortex or phase winding: in particular their phase is well defined at the poles. Hence, the Chern number must be zero for any band around the crossing. This absence of topological protection could be expected since the crossing is achieved by fine tuning of the Cd concentration [Orlita et al., 2014].

Nevertheless, at the equator $k_z = 0$ $(\beta = \pi/2)$ the bands exhibit a non-zero Berry winding. This is expected since at the equator the Hamiltonian (2.92) becomes block diagonal, where each block A/B corresponds to one valley of the α-T_3 model for $\tan\phi = \alpha = \frac{1}{\sqrt{3}}$ [Raoux et al., 2014, Malcolm and Nicol, 2015]. The windings are given by

$$\gamma_\xi^\pm = -\xi \, \frac{\pi}{2}, \tag{2.94a}$$

$$\gamma_\xi^0 = -\xi \, 3\pi = \pi \bmod 2\pi, \tag{2.94b}$$

where $\xi = \pm 1$ for the A/B sector.

The critical semi-metallic phase in $\mathrm{Hg}_{1-x}\mathrm{Cd}_x\mathrm{Te}$ [Orlita et al., 2014] provides a 3D extension of the α-T_3 model for a specific value of the parameter $\tan\phi = \alpha = \frac{1}{\sqrt{3}}$. Although the 3D phase is trivial with Chern number $C_1 = 0$, it projects onto a 2D crossing with non zero, although non quantized, Berry windings. This situation is very different from graphene where there is a correspondence between quantized Berry windings in 2D and the Chern number of a 3D Weyl point.

2.5.5 The hexagonal three-band (H_3) model

We consider another simple extension of graphene, with two atomic orbitals superposed on one of the two sublattices of the hexagonal lattice, see Fig. 2.13c. The H_3 model has two three-band crossings in the 2D Brillouin Zone, at points $\mathbf{K}$ and $\mathbf{K}'$. We find that although the Berry windings around the nodal point are non trivial and quantized $\gamma_\pm = \pi$, the 2D model can be obtained as a planar projection of a trivial 3D three-band crossing with Chern number $C_1 = 0$. We had expected a non trivial 2D topological property to manifest itself in higher dimensions. To check this surprising result, we have considered another possible 3D extension of the crossing. This second extension exhibits not an isolated point crossing but a line of degeneracies. We have computed the Chern number using non-abelian Berry connections to account for the line degeneracy.

The 2D model

The low-energy Bloch Hamiltonian describing the crossing takes the form

$$H(\vec{k}) = \hbar v \begin{pmatrix} 0 & 0 & k_- \cos\phi \\ 0 & 0 & k_- \sin\phi \\ k_+ \cos\phi & k_+ \sin\phi & 0 \end{pmatrix}, \tag{2.95}$$

in the (A_1, B, A_2) basis, with $\tan\phi = t_1/t_2$, see Fig. 2.13c. Note that the Hamiltonian (2.95) has chiral symmetry: it anticommutes with the operator $C = \mathrm{diag}(1, -1, 1)$. The chiral symmetry causes the third band to be flat. In polar coordinates for $\mathbf{k}$ (k, θ), the eigenstates are independent of k:

$$\psi_\pm(\mathbf{k}) = \frac{1}{\sqrt{2}} \begin{pmatrix} \cos\phi \ \mathrm{e}^{-\mathrm{i}\theta} \\ \sin\phi \ \mathrm{e}^{-\mathrm{i}\theta} \\ \pm 1 \end{pmatrix}, \qquad \varepsilon(\mathbf{k}) = \pm\hbar v k, \tag{2.96a}$$

$$\psi_0(\mathbf{k}) = \begin{pmatrix} -\sin\phi \\ \cos\phi \\ 0 \end{pmatrix}, \qquad \varepsilon(\mathbf{k}) = 0, \tag{2.96b}$$

We compute the Berry connections

$$\mathbf{A}_0 = \mathbf{0} \tag{2.97a}$$

$$\mathbf{A}_\pm = -\frac{1}{2}\boldsymbol{\nabla}_{\mathbf{k}}\theta, \tag{2.97b}$$

and the Berry windings around the crossing

$$\gamma_\pm = -\pi, \tag{2.98a}$$

$$\gamma_0 = 0. \tag{2.98b}$$

The Berry windings of the $\varepsilon_\pm$ bands are quantized to π mod 2π. We will see in Chapter 4 that this quantization is characteristic of a class of chiral symmetric three-band semimetals in relation with a duality transformation, a geometrical property of the lattice model different from a symmetry.

The 2D H$_3$ model has quantized Berry windings similar to graphene. Are these quantized Berry windings also related to a 3D Chern number as it is the case of graphene?

A possible 3D extension

We investigate a possible 3D extension of the band crossing of the H$_3$ model and compute the associated Chern number. The Hamiltonian

$$H = \begin{pmatrix} k_z & 0 & k_- \cos\phi \\ 0 & -k_z & k_- \sin\phi \\ k_+ \cos\phi & k_+ \sin\phi & -k_z \cos 2\phi \end{pmatrix}, \tag{2.99}$$

describes a three-band crossing at $\mathbf{k} = \mathbf{0}$. For $k_z = 0$, it gives the 2D H$_3$ Hamiltonian (2.95). The eigenstates in spherical coordinates (k, β, θ) are still independent of k:

$$\psi_\pm = \frac{1}{\sqrt{2(1 \pm \cos\beta \cos 2\phi)}} \begin{pmatrix} (1 \pm \cos\beta) \cos\phi \\ (1 \mp \cos\beta) \sin\phi \\ \pm \sin\beta e^{i\theta} \end{pmatrix}, \varepsilon_\pm = \pm k, \tag{2.100}$$

$$\psi_0 = \frac{1}{\sqrt{\sin^2\beta + \sin^2 2\phi \cos^2\beta}} \begin{pmatrix} \sin\phi \sin\beta e^{-i\theta} \\ \cos\phi \sin\beta e^{-i\theta} \\ \sin 2\phi \cos\beta \end{pmatrix}, \varepsilon_0 = -k\cos\beta \ \cos 2\phi, \tag{2.101}$$

(2.102)

We find that eigenstates (2.100) and (2.101) are continuously defined everywhere: a single gauge covers the whole unit sphere (θ, β) in the 3D Brillouin Zone. The connections read:

$$\mathbf{A}_{\pm} = \frac{\sin^2 \beta}{2(1 \pm \cos\beta \cos 2\phi)} \nabla_{\mathbf{k}}\theta, \tag{2.103}$$

$$\mathbf{A_0} = -\frac{\sin^2 \beta}{\sin^2 \beta + \sin^2 2\phi \cos^2 \beta} \nabla_{\mathbf{k}}\theta. \tag{2.104}$$

$$\tag{2.105}$$

The Berry windings (2.98a) are quantized at the equator:$\gamma_{\pm} = \pi \bmod 2\pi$, but the Chern number is zero because of the singleness of the gauge choice for covering the sphere around $\mathbf{k} = \mathbf{0}$. No anti-unitary transformation has been found that relates $H(k_x, k_y, k_z)$ to $H(k_x, k_y, -k_z)$; our earlier assumption, see section 2.5.1, on the role of such an anti-unitary transformation still holds in this case.

This result is puzzling: we have seen that a topologically non trivial 3D crossing can have trivial planar cuts, see section 2.5.3. But in the case of the H_3 model, a topologically trivial 3D crossing with Chern number $C_1 = 0$ has non trivial planar cuts with π Berry windings around the crossing. To get a better understanding of the topological properties of the H_3 model, we have examined a different 3D extension of the model.

Another possible 3D extension, with a degeneracy line

Let us now refine the study of the H_3 model and take a different 3D Hamiltonian describing a crossing which projects on the H_3 model for $k_z = 0$:

$$H = \begin{pmatrix} k_z & 0 & k_- \cos\phi \\ 0 & k_z & k_- \sin\phi \\ k_+ \cos\phi & k_+ \sin\phi & -k_z \end{pmatrix}. \tag{2.106}$$

The spectrum reads $\varepsilon_{\pm} = \pm k,\ \varepsilon_0 = k_z$, see Fig. 2.14. Levels ε_+ and ε_0 are degenerate along the positive k_z semi-axis and levels ε_- and ε_0 are degenerate along the negative k_z semi-axis. The eigenstates in spherical coordinates (k, θ, β) depend on angles β and θ:

$$\psi_+ = \begin{pmatrix} \cos\phi \cos\beta/2 \\ \sin\phi \cos\beta/2 \\ \sin\beta/2 \ \mathrm{e}^{\mathrm{i}\theta} \end{pmatrix}, \tag{2.107}$$

$$\psi_0 = \begin{pmatrix} -\sin\phi \\ \cos\phi \\ 0 \end{pmatrix}, \tag{2.108}$$

$$\psi_- = \begin{pmatrix} \cos\phi \sin\beta/2 \ \mathrm{e}^{-\mathrm{i}\theta} \\ \sin\phi \sin\beta/2 \mathrm{e}^{-\mathrm{i}\theta} \\ -\cos\beta/2 \end{pmatrix}. \tag{2.109}$$

In this gauge, the wavefunctions have a singularity for $\beta = \pi$. We call it the North gauge from there on. The South gauge, defined everywhere except for $\beta = 0$ is given by $\psi_+^S = e^{-i\theta}\psi_+^N,\ \psi_-^S = e^{i\theta}\psi_-^N$.

Is there an anti-unitary transformation $\hat{U} = P\mathcal{K}$ that relates North and South Poles and would enforce North and South connections to be opposite at the equator $\beta = \pi/2$? We look for the existence of a unitary matrix P that would satisfy $PH^*(k_x, k_y, k_z)P^{-1} = H(k_x, k_y, -k_z)$. Defining the J_i matrices through $H = \mathbf{k} \cdot \mathbf{J}$ (2.106) we get the following conditions for P:

$$PJ_x = J_xP,\ PJ_y = -J_yP,\ PJ_z = -J_zP. \tag{2.110}$$

One finds that the last requirement $PJ_z = -J_zP$ leads to $\det P = 0$. Thus, no antiunitary transformation relating $H(k_z)$ to $H(-k_z)$ exists. Note that since the spectrum is not symmetric under $k_z \to -k_z$ (see Fig. 2.14b) this is not surprising.

We now compute the connections in both gauges to deduce corresponding Berry curvatures and calculate the Chern number. In the Northern hemisphere, levels ε_+ and ε_0 are degenerate: we thus compute the non-abelian Berry connection $\mathbf{A}_{mn} = -i\langle\psi_m|\nabla_{\mathbf{k}}|\psi_n\rangle$. The Berry curvature is then given by $F = dA + A \wedge A$, where A is a 1-form and F a 2-form. Then to get the contribution to the Chern number

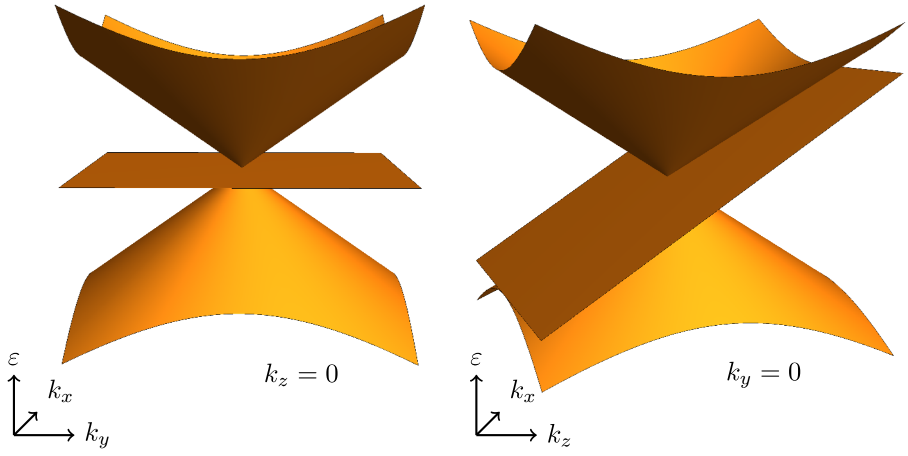

(a) (b)

Figure 2.14: 3D extension of the H$_3$ model with degeneracy line (2.106). (a) Dispersion in the k_xk_y plane for $k_z = 0$. (b) Dispersion in the k_xk_z plane for $k_y = 0$. The spectrum exhibits a two-fold degenerate line along the k_z axis.

we integrate Tr F over the northern hemisphere.

$$\mathbf{A}^N_{++} = \mathrm{Im}\langle\psi_+|\nabla_{\mathbf{k}}|\psi_+\rangle = \sin^2(\beta/2)\ \nabla_{\mathbf{k}}\theta, \tag{2.111}$$

$$\mathbf{A}^N_{0+} = \mathbf{A}^N_{+0} = \mathbf{A}^N_{00} = \mathbf{0}. \tag{2.112}$$

If we write $A = A_\beta d\beta + A_\theta d\theta$, then $A \wedge A = [A_\beta, A_\theta] d\beta \wedge d\theta$, which is zero since $A_\beta = 0$. Thus the trace of the Berry curvature is Tr $F = \nabla_{\mathbf{k}} \times \mathbf{A}^N_{++}$. For the non degenerate valence band we get:

$$\mathbf{A}^N_{-} = -\sin^2(\beta/2)\ \nabla_{\mathbf{k}}\theta. \tag{2.113}$$

In the Southern hemisphere, the upper ε_+ band is non degenerate; its Berry connection is

$$\mathbf{A}^S_{+} = -\cos^2(\beta/2)\ \nabla_{\mathbf{k}}\theta. \tag{2.114}$$

The ε_- and ε_0 bands are degenerate. The non-abelian Berry connection is given by:

$$\mathbf{A}^S_{--} = \cos^2(\beta/2)\ \nabla_{\mathbf{k}}\theta, \tag{2.115}$$

$$\mathbf{A}^S_{0-} = \mathbf{A}^S_{-0} = \mathbf{A}^S_{00} = \mathbf{0}, \tag{2.116}$$

leading to the Berry curvature's trace Tr $F = \nabla_{\mathbf{k}} \times \mathbf{A}^S_{--}$.

We find that the difference $\mathbf{A}^N_{++} - \mathbf{A}^S_{+}$ describes an infinite solenoid of flux 2π along the z-axis.

Finally, we compute the Chern number for the ε_+ band as the sum of the integrals on each hemisphere U_N and U_S around the crossing:

$$\nu_+ = \frac{1}{2\pi}\left(\iint_{U_N} \nabla_{\mathbf{k}} \times \mathbf{A}^N_{++} + \iint_{U_S} \nabla_{\mathbf{k}} \times \mathbf{A}^S_{+}\right) \tag{2.117}$$

$$= \frac{1}{2\pi}\oint_{\theta=0}^{2\pi} (\mathbf{A}^N_{++}(\beta = \pi/2) - \mathbf{A}^S_{+}(\beta = \pi/2))d\mathbf{k} \tag{2.118}$$

$$= 1. \tag{2.119}$$

Similarly, we find for the ε_- band

$$\nu_- = \frac{1}{2\pi}\left(\iint_{U_N} \nabla_{\mathbf{k}} \times \mathbf{A}^N_{-} + \iint_{U_S} \nabla_{\mathbf{k}} \times \mathbf{A}^S_{--}\right) \tag{2.120}$$

$$= \frac{1}{2\pi}\oint_{\theta=0}^{2\pi} (\mathbf{A}^N_{-}(\beta = \pi/2) - \mathbf{A}^S_{--}(\beta = \pi/2))d\mathbf{k} \tag{2.121}$$

$$= -1, \tag{2.122}$$

and for the ε_0 band

$$\nu_0 = 0, \tag{2.123}$$

the connections being trivial. Thus, the $\varepsilon_\pm$ bands have a non trivial Chern number $C_1 = \pm 1$. However, our derivation does not give any argument to establish a relation between the Chern number $C_1 = 1$ and the π Berry windings. Besides, we note that this way of computing the Chern number seems a bit sketchy since the degenerate levels are not the same in each hemisphere.

2.5.6 Conclusion

Our study on three-band semi-metals beyond graphene has revealed a richer reality than we had expected. We have considered 3D extensions of the 2D band crossings by adding an effective third direction of momentum k_z and a corresponding extra term to the Hamiltonian $k_z J_z$. It turns out that the correspondence between quantized Berry windings and a 3D Chern number is not general. It seems to be related, when it exists, to an anti-unitary transformation of the 3D Hamiltonian relating the Northern and Southern sides of the 2D phase: $H(k_z) \to H(-k_z)$. Three band crossing are complex singularities for the phases of electronic states. By considering the crossings as critical phases, we could get a deeper understanding of the topological properties of each crossing we considered. Although the general rule we proposed could not apply to every complex crossing we have investigated, we are confident that considering the crossing as critical phases, i.e. 2D projections of higher dimensional crossings, is a valid point of view that should be investigated further in future studies.

Chapter 3

Disordered Semimetals

3.1 Introduction

The electronic properties of solids can be described in the framework of non-interacting electrons propagating in an infinite, perfectly periodic crystal potential. This simplified description can amazingly reproduce many properties of the real materials, even though they are far from perfect crystals. Defects, dislocations, impurities, lattice vibrations, electron electron interactions affect the behaviour of electrons. How disorder, temperature or interactions affect electronic properties depends on the nature of the material. For instance in semiconductors increasing the temperature will favour electron transport by exciting electrons above the gap, whereas in a metal vibrations induced from heating can scatter off electrons and increase the resistivity. In this chapter, we study the effect of disorder on relativistic semimetals. Disorder is unavoidably present in any material, in the form of impurities, dislocations or vacancies for example. The question is whether and how it affects the physical observables of the system? In conventional electronic systems, the presence of static scatterers can drastically change the nature of the phase by localizing the electrons and making the system insulating. In three dimensional metals, a transition occurs for strong disorder towards this localized regime: the Anderson transition. In relativistic semimetals, the linear dispersion relation of electronic states causes the wavelength to diverge near the crossing: hence, electronic states will feel the impurities on a much larger scale compared to conventional conductors. It has been shown in early theoretical papers [Fradkin, 1986a, Fradkin, 1986b] that the physics of disordered semimetals with linear band crossing is very specific, different from conventional materials.

We have seen in previous chapters that topological properties of band crossings imply a robustness of relativistic semimetals towards external perturbations. As a consequence of their topological protection, Graphene and Weyl semimetals are protected against localization when the disorder does not couple different cones. When disorder is smooth on the lattice scale, the cones decouple and the problem can be reduced to considering a single cone.

As we will see in this chapter, a new disorder-driven quantum transition was found in these phases, with lower critical dimension $d_c = 2$. The new quantum transition can be monitored by focusing on the density of states at the band crossing. In the pure case, the density of states ρ vanishes at the crossing because of the linear dispersion relation, $\rho(E = 0) = 0$. For a weak disorder strength $\Delta < \Delta_c$ the system remains in the semimetallic phase with $\rho(E = 0) = 0$. For a stronger disorder, when $\Delta > \Delta_c$, there is a transition towards a disordered metal phase where the conductivity becomes finite, $\rho(E = 0) > 0$, and transport occurs in the diffusive regime [Fradkin, 1986a, Fradkin, 1986b]. The recent realization of 3D Dirac and Weyl semimetals has renewed the interest in this transition. 3D relativistic semimetals are the only materials where a disorder-driven quantum transition distinct from the Anderson transition occurs. Besides, we will see that the physics involved in this new quantum transition is related to known models from high energy physics.

The critical behaviour of the density of states and electronic correlation functions near the transition is characteristic of critical points in the same symmetry class. It is now widely believed that the transition can be mapped onto the chiral symmetry breaking transition of the $U(N)$ Gross Neveu model from high energy physics [Roy and Das Sarma, 2014, Syzranov et al., 2015]. However, we have identified problems with this initial description of the transition within a renormalization group study of the $U(N)$ Gross Neveu model. The $U(N)$ Gross Neveu model is not multiplicatively renormalizable. When expanding the generating functional perturbatively, an increasing number of additional operators has to be taken into account to describe the critical behaviour with increasing precision. We have proposed an alternative route to describe the transition based on a renormalizable, self-contained expansion of an equivalent model from high energy physics, the Gross Neveu Yukawa model.

Correlations are expected to change the nature of disorder. In a second project we predict a new phase transition in the presence of spatial-correlated disorder. We find that the correlations can induce a new intermediate phase between short range and mean field disorder where a new long range disorder driven quantum transition occurs.

After a reminder on the effect of disorder on conventional metals and the Anderson transition, we contrast the case of disordered conventional conductors with disordered graphene, section 3.1. In a second section 3.2 we consider a single disordered Weyl cone. Section 3.2.1 introduces the new quantum phase transition for disordered Weyl fermions. Then section 3.2.2 presents the Renormalization Group study of the transition based on a $d = 2 + \varepsilon$ expansion of the Gross Neveu model. To overcome the non-renormalizability issues encountered with the Gross Neveu model, in section 3.2.3 we propose an alternative description of the transition based on a $d = 4 - \varepsilon$ expansion of the Gross Neveu Yukawa model. In section 3.2.4 we consider the possibility that the transition is avoided because of rare events. Section 3.2.5 proposes an alternative description of the transition based on the multifractal spectrum of wavefunctions. Finally in section 3.2.6 we introduce disorder correlations and characterize the new transition obtained for intermediate correlation range.

3.1.1 Disordered systems

Sources of disorder in crystals can be dislocations, vacancies, impurities (adatoms), or grain boundaries. Within a statistical approach, the effect of disorder can be modelled by a random perturbation potential added to the Hamiltonian $\hat{H}_0$ of the clean system [Akkermans and Montambaux, 2007]:

$$\hat{H} = \hat{H}_0 + \hat{V}(\mathbf{r}). \tag{3.1}$$

We consider random scalar potentials $\hat{V}(\mathbf{r})$. The potential is zero on average: $\langle V(\mathbf{r})\rangle = 0$. Here $\langle ... \rangle$ is a statistical average on many disorder realisations. The potential is defined by a probability distribution $P[V(\mathbf{r})]$:

$$\langle F[V(\mathbf{r})]\rangle = \int F[V(\mathbf{r})]P[V(\mathbf{r})]\mathcal{D}V(\mathbf{r}) \tag{3.2}$$

The random disorder potential originates from the sum of the contributions of many independent scatterers. As we will see below, central limit theorem states that on statistical average the random disorder follows the Gaussian distribution, entirely characterized by its variance $\langle V(\mathbf{r})V(\mathbf{r}')\rangle = \Delta(\mathbf{r} - \mathbf{r}')$. The function Δ encodes spatial correlations of disorder, and typically decays over short distances. Often Δ is approximated by a δ Dirac distribution in the long wavelength limit. The Gaussian distribution is related to a simple model for randomly distributed local impurities, the Edwards model [Akkermans and Montambaux, 2007], in the thermodynamic limit. In Edwards model, the disorder potential for N_i impurities is given by

$$V(\mathbf{r}) = \sum_{j=1}^{N_i} v(\mathbf{r} - \mathbf{r}_j). \tag{3.3}$$

We first take the thermodynamic limit $L \to \infty$ while keeping the impurity density fixed, $n_i = N_i/L^d =$ const. Then in the limit of a high density of weakly scattering impurities $N_i/L^d \to \infty$, $v(\mathbf{r}) \to 0$ we recover the Gaussian model with variance $\Delta(\mathbf{k}) = n_i v(\mathbf{k})^2$.

Disordered metals

Electrons in the vacuum propagate ballistically, like plane waves, with a well-defined momentum. In a perfect crystal, the electronic wave functions are still plane waves, only modulated by the crystal potential. As a result their propagation is still ballistic with an effective mass characteristic of the crystal structure. Impurities, vibrations of the lattice (phonons) or other electrons can collide with electrons and change their momentum and/or their phase. To determine the transport regime, three length scales are relevant: the Fermi wavelength λ_F, the mean free path ℓ and the phase-relaxation length L_ϕ [Akkermans and Montambaux, 2007, Datta, 1997]. A material with dimensions far greater than any of these lengths $L \gg \lambda_F, \ell, L_\phi$ is in the classical transport regime, in which Ohm's law is valid.

The quantum regime requires phase coherence over the sample, i.e. $L < L_\phi$. Loss of coherence, i.e. phase randomizing, occurs when electrons collide with dynamic scatterers like phonons or other electrons, or when electrons collide with magnetic scatterers which possess a fluctuating internal degree of freedom, their spin. Such scattering events make the phase-relaxation length, or coherence length L_ϕ, finite.

Momentum relaxation occurs when electrons collide with static scatterers like static impurities. The elastic mean free path ℓ gives the characteristic distance over which momentum relaxation occurs. Electron transport is ballistic when $L \ll \ell < L_\phi$. When $\lambda_F \ll \ell < L < L_\phi$, transport is diffusive: when travelling through the sample electrons undergo many elastic collisions, see Fig.3.1a. At equilibrium there is no electron flow in any particular direction, but when an electric field is applied, electrons get accelerated and a current can flow through the sample. The Drude formula gives the conductivity

$$\sigma_{\text{Drude}} = \frac{ne^2\tau_m}{m^*}, \tag{3.4}$$

where τ_m is the momentum relaxation time and m^* the effective mass. The Drude formula is valid for $\lambda_F \ll \ell = v_F\tau_m$.

Weak localization

We consider the diffusive regime where multiple elastic collisions occur along electron trajectories. In the quantum regime, interference effects between electrons trajectories must be taken into account, and give corrections to the Drude conductivity. The dominant correction to the Drude conductivity comes from interferences between time-reversed trajectories, Fig. 3.1b, which increase the probability for an electron to be backscattered and return to its starting point. Because it reduces the probability for the electron to move away from its initial position, this effect is called weak localization: it manifests as a negative correction $-\delta\sigma$ to the conductivity (3.4), with $\delta\sigma/\sigma \sim 1/(k_F\ell)$.

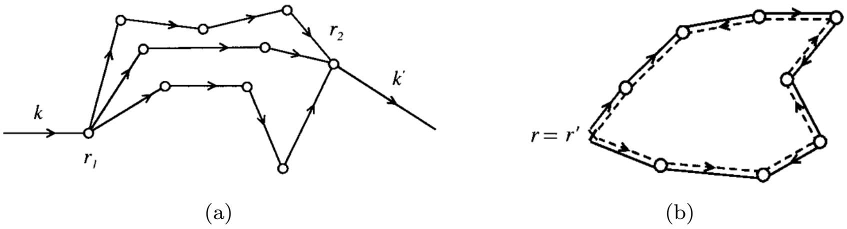

(a) (b)

Figure 3.1: (a) In the presence of disorder, typical electron trajectories contain multiple scattering events which modify the quasi momentum **k**. (b) Interference between time-reversed trajectories is at the origin of the weak localization effect. From [Akkermans and Montambaux, 2007]

How the system is affected by localization effects depends on its dimensionality. One can define a localization length ξ for which the correction to the conductance becomes large $\delta g/g \simeq 1$: for systems larger than the localization length, the correction to the Drude conductivity is no more a perturbation. The weak localization regime breaks down for $L > \xi$, and the system enters a strong localization regime where diffusion of electronic waves is lost. Electronic states are fully localized on scales larger than ξ. In 1D and 2D, even for an infinitesimal disorder strength all electrons wavefunctions eventually get localized in the thermodynamic limit $L \to \infty$. In 3D systems, electronic states remain extended for weak disorder ($\xi \to \infty$) but when the disorder increases a transition occurs towards the strong localization regime (ξ becomes finite). This transition is called the Anderson transition [Anderson, 1958, Lee and Ramakrishnan, 1985, Kramer and MacKinnon, 1993].

Anderson transition

In the strong localization regime, the system is insulating: since electronic states are exponentially localized in space, they can not contribute to transport and therefore the DC conductivity vanishes at zero temperature: $\sigma_{\text{dc}}(T = 0\ K) = 0$. The Anderson transition is a metal-insulator transition with no gap opening. It has been related to a second order phase transition: the critical behaviour of the conductivity or the localization length near the transition depend on the universality class of the Hamiltonian. It is characterized by a set of universal exponents which describe how thermodynamic variables vary near the critical point.

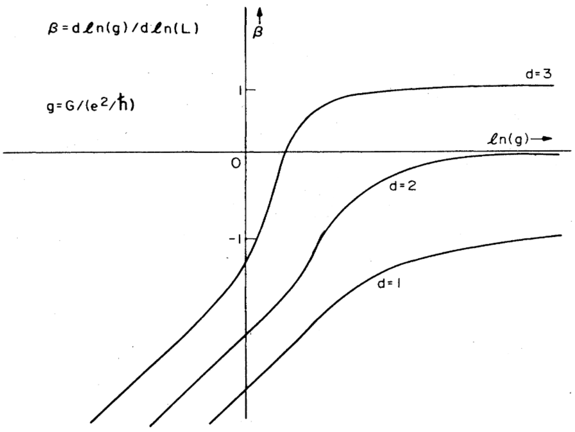

Figure 3.2: The scaling function β as a function of conductance g at zero temperature, for dimension $d = 1, 2, 3$. The sign of β tells whether g increases or decreases with system size L. The Anderson transition occurs at $\beta = 0$, which is only accessible for $d = 3$. Taken from [Kramer and MacKinnon, 1993].

The existence of universal critical exponents for the Anderson transition is related to the scaling behaviour of the conductance g. The scaling function β describes how the conductance scales with system size and is useful to characterize the phase transition:

$$\beta(g) = \frac{d\ln g}{d\ln L}. \tag{3.5}$$

The scaling function's asymptotic behaviour in the metallic and in the insulating limit gives a hint on the existence and the nature of the transition depending on the dimensionality. In the metallic limit, or the limit of very weak disorder, g is large and the electronic transport is governed by Ohm's law. For a sample of size L^d it reads:

$$g = \sigma L^{d-2}, \tag{3.6}$$

which is a generalization of the formula $g_{3D} = \sigma S/L$ to d dimensions. The scaling function is fixed by d only

$$\beta(g) = d - 2, \tag{3.7}$$

it is negative for $d < 2$ and so g flows to zero in the thermodynamic limit and positive for $d > 2$, in which case g flows to infinity. $d = 2$ is a special case.

In the opposite insulating limit, g is small, the disorder is strong and electrons get localized. At $T = 0K$, the conductance decays exponentially with system size:

$$g \propto e^{-L/\xi}, \tag{3.8}$$

where ξ is the localization length. This leads to the following scaling behaviour

$$\beta(g) = \ln L + \text{const}, \tag{3.9}$$

independent of the dimensionality.

From Figure 3.2 we can predict the scaling behaviour of the conductance. In dimension 1 and 2, g always decreases with L: this is a manifestation of the localization of all electronic states in lower dimensions. On the contrary in dimension 3 a metal-insulator transition occurs for a critical conductance g_c where β changes sign. From the behaviour of β near the transition as a function of the different thermodynamic variables, one can access the different universal exponents and characterize the critical point g_c.

We have seen how disorder affects the behaviour of electronic states in a metal. What about semimetals like graphene where the density of states vanishes and the wavelength diverges at the band crossing?

3.1.2 Disordered graphene

Pristine graphene is a zero-gap semiconductor: the electronic bands cross linearly at a few points in the Brillouin zone. At the crossing, the carrier density vanishes linearly: $\rho(E) \propto E$, see Fig. 1.9, and the electronic wavelength diverges: $\lambda \to \infty$.

If the disorder couples the two valleys of graphene, a gap can open and the system becomes insulating. in the absence of intervalley scattering the problem reduces to a single cone. Contrary to conventional electrons, relativistic electrons in graphene do not localize in the absence of intervalley scattering. In the presence of disorder, the density of states at the crossing becomes finite. Remarkably, the density of states and the conductivity at the crossing increase with disorder.

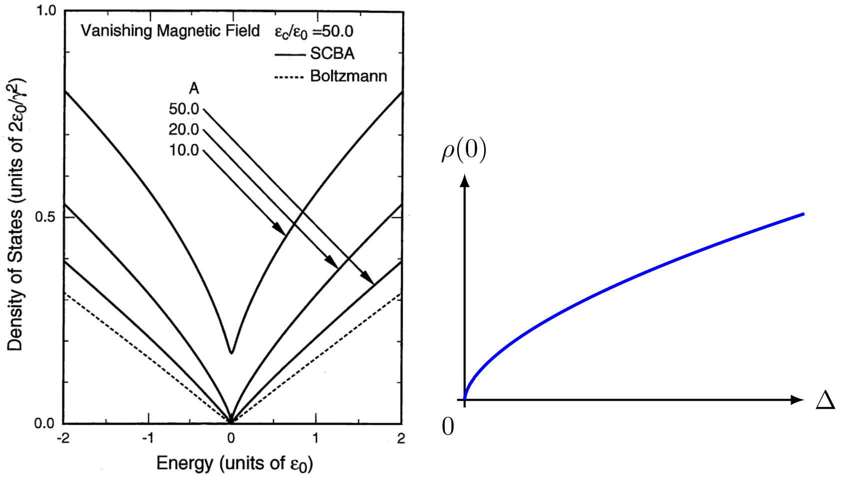

(a) (b)

Figure 3.3: (a) Electronic density of states in graphene, in the absence of disorder (dotted lines) and with increasing disorder (continuous lines). A measures the disorder strength. From [Shon and Ando, 1998]. (b) Behaviour of the density of states at the crossing point as a function of disorder.

The low energy spectrum near the two band touching points $\mathbf{K}$ and $\mathbf{K}'$ is relativistic: excitations above the crossing behave like massless Dirac particles and excitations below the crossing like anti-particles. Because of their relativistic nature, electrons in graphene are not affected by defects or impurities in the same way as conventional electrons. The particle-hole symmetry of the Dirac cone allow an electron from the upper Dirac cone, a Dirac “particle“ to be transmitted through a potential barrier as a Dirac ”anti-particle“. The quantized Berry phase prevents Dirac electrons from being backscattered and is at the origin of a weak anti-localization effect in graphene [McCann et al., 2006]. As a result, disorder in graphene does not localize electronic states as long as it does not couple $\mathbf{K}$ and $\mathbf{K}'$ valleys [Ostrovsky et al., 2006]. Instead, in the presence of disorder the Dirac point gets populated with midgap states and the density of states at the crossing point becomes finite [Shon and Ando, 1998], see Fig.3.3a. Disorder drives the semimetallic phase towards a diffusive metal phase. Since the density of states increases, the conductivity also increases with increasing disorder strength.

At high energy and carrier density, electronic states behave like in a conventional disordered metal, except for the absence of localization when the cones are not coupled, and transport occurs in the diffusive Drude-Boltzmann regime. When the chemical potential is lowered towards the Dirac point, the Fermi wavelength becomes large and the diffusive Drude-Boltzmann approximation breaks down: quantum effects become dominant, and explain the peculiar behaviour of the conductivity at the Dirac point [Adam et al., 2009].

The impact of disorder on electronic states in graphene depends crucially on its spatial correlations. Short-range disorder couples the two Dirac valleys $\mathbf{K}$ and $\mathbf{K}'$ and electrons get localized [Altland, 2006, Aleiner and Efetov, 2006]. When the disorder is smooth on the lattice scale, the two cones decouple and the problem is equivalent to a single disordered Dirac cone. Long range scattering due to the presence of charged impurities is expected to be dominant in graphene [Adam et al., 2007].

Disorder comes from charged impurities, edges, cracks, grain boundaries, vacancies. Besides, a very important source of disorder in real graphene is unavoidable ripples and corrugations of the sample which cause fluctuations of the chemical potentials and the formation of electron-hole puddles [Katsnelson et al., 2006]. The Gaussian scalar potential is a natural description for this source of disorder. By analogy with relativistic physics, disorder in graphene manifests as a fluctuating vacuum energy for Dirac fermions.

3.2 Disordered three-dimensional semimetals

3.2.1 Disorder-driven quantum phase transition

Effect of disorder: dimensional analysis

Weyl semimetals have been introduced in section 1.3. The two-band Weyl Hamiltonian describing the crossing reads

$$H = \hbar v \boldsymbol{\sigma} \cdot \mathbf{k}. \tag{3.10}$$

It is topologically protected from a gap opening against small perturbations. Hence, the behaviour of a disordered Weyl semimetal is expected to contrast significantly from conventional disordered electronic systems. It is natural to investigate how properties like the conductivity or the electronic density of states vary with disorder. At the nodal point, the clean system is characterized by a density of states (DOS) vanishing quadratically with energy. It exhibits a vanishing zero-frequency optical conductivity [Roy et al., 2016] and a pseudoballistic transport [Sbierski et al., 2014].

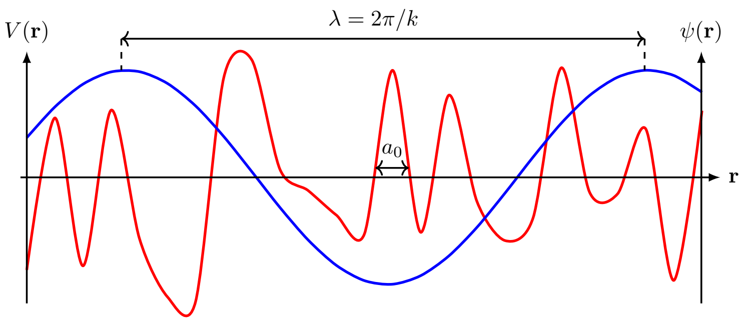

Figure 3.4: Illustration for the dimensional analysis of the effect of disorder. Disorder potential $V(\mathbf{r})$ is shown in red and a sketch of the electron wavefunction $\psi(\mathbf{r})$ in blue. Whether the electrons can be trapped in a disorder valley depend on the relative weight of the average value of the potential over an electron wavelength with respect to the kinetic energy.

If scattering occurs between the different cones, electronic states will localize and the system will undergo an Anderson transition towards an insulating regime. Here, the disorder distribution is assumed to be sufficiently smooth on the lattice scale so that no intervalley scattering occurs. We therefore consider a single disordered Weyl cone:

$$H = \hbar v \ \boldsymbol{\sigma} \cdot \mathbf{k} + V(\mathbf{r})\mathbb{1}, \tag{3.11}$$

with disorder amplitude Δ, defined by $\langle V(\mathbf{r})V(\mathbf{r}')\rangle = \Delta f(|\mathbf{r}-\mathbf{r}'|/a_0)$. f characterises the disorder correlations, and a_0 gives the correlation length. A simple heuristic argument shows that the impact of disorder depends strongly on the dimension of the electronic system. For a single disorder realization, the number of distinct values of the disorder potential felt by an electron of wavelength λ is roughly

$$N \simeq \left(\frac{\lambda}{a_0}\right)^d, \tag{3.12}$$

where a_0 is the disorder correlation length, Fig. 3.4. The typical value of disorder is then the normalized sum of these N random values

$$\begin{aligned} V_{typ} &\simeq \frac{\sqrt{\Delta}}{\sqrt{N}} \\ &\simeq \sqrt{\Delta}\,(ka_0)^{\frac{d}{2}}\,. \end{aligned} \tag{3.13}$$

This amplitude has to be compared with the kinetic energy $E_c = \hbar v k$. Hence, disorder will be dominant in the low energy limit for low dimensions $d \leq 2$. In particular, in two-dimensional graphene disorder is marginally relevant and there is no transition: the system becomes diffusive even for an infinitesimal disorder strength. Weak disorder is irrelevant for $d > 2$, in particular in three-dimensional semimetals like Weyl materials. Weyl semimetals are stable for weak disorder: the density of states remains quadratic, and transport displays a pseudo-ballistic regime. However, a strong enough disorder may drive the system into a diffusive phase with a finite DOS, optical conductivity and diffusive transport at zero energy. This was pointed for the first time in [Fradkin, 1986a, Fradkin, 1986b] The scattering rate was computed self consistently at leading order in perturbation theory. In two dimensions, the scattering rate is always finite: there is no transition, any amount of disorder destabilizes the semimetallic phase. In three dimensions the scattering rate remains zero for weak disorder, showing that the system still behaves qualitatively as a clean system. For stronger disorder there is a transition towards a disordered phase with finite scattering rate.

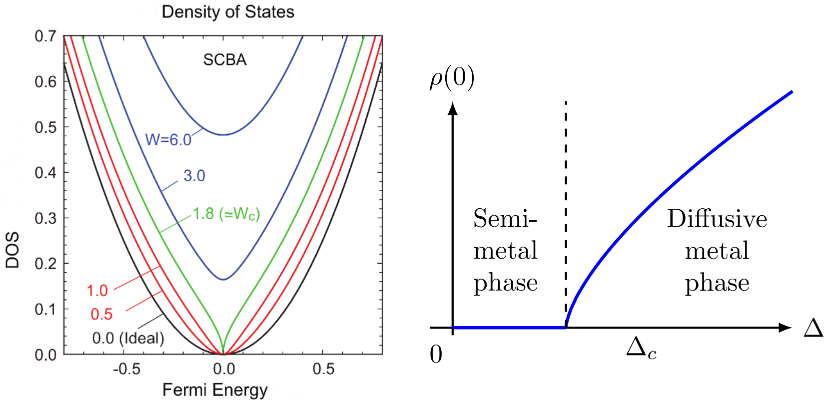

(a) (b)

Figure 3.5: Disorder-driven transition in three-dimensional Dirac and Weyl semimetals. (a) SCBA-calculated DOS as a function of Fermi energy, for various disorder amplitudes. Adapted from [Ominato and Koshino, 2014]. (b) Behaviour of the DOS at the Weyl point as a function of disorder.

This new disorder-driven transition is distinct from the standard Anderson localization transition. It occurs at a single energy, exactly at the band crossing, while the Anderson transition occurs for any energy below a characteristic mobility edge. It manifests as a change in the density of states $\rho(E = 0)$, which is zero in the semimetallic phase and becomes finite at the transition. On the contrary, the density of states is irrelevant to characterize the Anderson transition, which requires the description of the conductivity. Finally, this novel non-Anderson transition occurs in systems such as the single disordered Weyl cone (3.11) where localisation is forbidden by topology. Beyond Weyl, a class of electronic systems with quasiparticle dispersion $\varepsilon_{\mathbf{k}} \propto k^\alpha$ for $d > 2\alpha$ have been predicted to show this transition [Syzranov et al., 2015].

Characterization of the transition

The averaged density of states (DOS) $\rho(E = 0)$ becomes finite at the transition: beyond a critical disorder strength Δ_c, the semimetallic phase is destabilized and the system enters a diffusive metallic phase. In the clean system, the band crossing separates relativistic quasi-particles from relativistic quasi-antiparticles: it is the analogue of the relativistic vacuum. The description of the transition can be thought of as the question of the stability of the vacuum in the presence of disorder. Following this line of thought, one could say that beyond the critical disorder strength, disorder starts filling up the relativistic vacuum.

The transition can be described within the language of critical phenomena. It is a second order phase transition, the average DOS playing the role of the order parameter. The critical behaviour of the DOS and other observables near the transition depends on the distance to the transition $|\Delta - \Delta_c|$ through critical exponents. The correlation length ξ, well defined on the diffusive side of the transition, diverges near the critical point:

$$\xi \propto |\Delta - \Delta_c|^{-\nu}, \tag{3.14}$$

with ν the correlation-length exponent. Note that in the diffusive metal phase ξ corresponds to the mean-free path. It decreases with increasing disorder, indicating the onset of a metallicity in the system. The transition occur at the critical energy $E = E_c = 0$ corresponding to the band crossing. The characteristic energy scales like:

$$|E - E_c| \propto \xi^{-z}, \tag{3.15}$$

where z is the universal dynamical exponent. $E^* = |E - E_c|$ defines a scale for the crossover regime between weak and strong disordered phases:

$$E^* = |E - E_c| \propto |\Delta - \Delta_c|^{z\nu}, \tag{3.16}$$

see Fig. 3.6. The order parameter scales like

$$\rho(0) \propto |\Delta - \Delta_c|^{\nu(d-z)}. \tag{3.17}$$

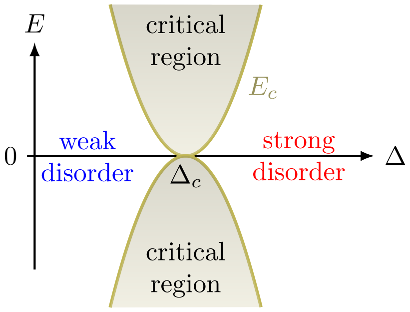

Figure 3.6: The non standard transition in Weyl semimetals occurs at $E_c = 0$.

The transition has been described first within the Self Consistent Born Approximation [Fradkin, 1986b, Ominato and Koshino, 2014], then using numerical techniques through either density of states scaling [Kobayashi et al., 2014] or conductance scaling analysis [Sbierski et al., 2015], Renormalization Group [Goswami and Chakravarty, 2011, Roy and Das Sarma, 2014, Syzranov et al., 2015, Louvet et al., 2016], or Functional Renormalization Group [Sbierski et al., 2017, Balog et al., 2017]. A comprehensive comparison of these results for critical exponents can be found in this review [Syzranov and Radzihovsky, 2018]. In the following we show that the previous renormalization group studies are not well controlled beyond two-loop order and we propose a new analysis based on the analogy with the Gross-Neveu Yukawa model from high energy physics.

3.2.2 Renormalization group analysis of the transition: $2 + \epsilon$ expansion

Averaging over disorder: replica trick

The transition can be studied using the Renormalization Group (RG) [Goldenfeld, 1992, Ryder, 1996]. It amounts to studying how physical observables of the system change when lowering the energy scale. Changing the scale can be viewed as a coarse graining operation, which integrates out high energy or short length scale degrees of freedom, thus effectively lowering the energy or momentum cut-off of the effective model. Through this procedure we get the properties of the system in the low energy, large scale limit. The Wilson RG consists in renormalizing the momentum cut-off incrementally, from Λ to $\Lambda - \delta\Lambda$. It works well at the leading order in perturbation theory. Here we use the field theoretical method together with dimensional regularization that is more convenient for calculations in higher orders: the expansion is controlled by a small parameter $\varepsilon = d - d_c$, where d_c is a critical dimension of the transition. Here, the lower critical dimension of the transition is $d_c = 2$.

Relativistic fermions moving in a d-dimensional space in the presence of an external potential $V(r)$ can be described by the euclidean action

$$S = \int d^d r \int d\tau \bar{\psi}(\mathbf{r}, \tau)(\partial_\tau - i\gamma_j \partial^j + V(\mathbf{r}))\psi(\mathbf{r}, \tau), \tag{3.18}$$

where ψ and $\bar{\psi}$ are independent Grassmann fields and τ is the imaginary time. The three-dimensional (3D) Weyl fermions (3.11) corresponds to $\gamma_j = \sigma_j$, $j = 1, 2, 3$ given by the Pauli matrices. In general the

γ_j are elements of a Clifford algebra satisfying the anti-commutation relations: $\gamma_i\gamma_j + \gamma_j\gamma_i = 2\delta_{ij}\mathbb{I}$, and $i, j = 1, ..., d$. We assume that the disorder potential $V(\mathbf{r})$ is a random Gaussian variable with zero mean and the variance $\overline{V(\mathbf{r})V(\mathbf{r}')} = g(\mathbf{r}-\mathbf{r}')$.

We want to compute physical observables and response functions like $\langle\bar{\psi}(\mathbf{r})\psi(\mathbf{r}')\rangle$ at fixed energy $E = 0$. Here $\langle ...\rangle$ is the average over the disorder distribution $P[V]$. Note that we need to average over disorder not the partition function but the free energy as follows:

$$\begin{aligned}\langle F\rangle &= \langle \ln Z[V]\rangle \\ &= \int \mathcal{D}V\ P[V]\ \ln\ Z[V],\end{aligned} \tag{3.19}$$

where Z is the partition function of the system. It can not be analytically computed. Hence, to average over the disorder distribution $P[V]$ we use the Replica trick [Mezard et al., 1987] and introduce N copies of the original system in the same disorder configuration, so that physical observables like (3.19) can be calculated in the limit of $N \to 0$ using the replicated action

$$\begin{aligned}\int \prod_{\alpha=1}^{N} \mathcal{D}\{\psi_\alpha\} e^{-S_{\mathrm{repl}}} &= \int \mathcal{D}V P[V] \prod_{\alpha=1}^{N} \mathcal{D}\{\psi_\alpha\} e^{-S^{\alpha}_{\mathrm{Weyl}}}, \\ &= \langle \prod_{\alpha=1}^{N} Z_\alpha\rangle \\ &= \langle Z^N\rangle,\end{aligned} \tag{3.20}$$

where $\mathcal{D}\{\psi_\alpha\} = \mathcal{D}\bar{\psi}_\alpha\mathcal{D}\psi_\alpha$. With the Replica trick, the free energy (3.19) rewrites:

$$\begin{aligned}\langle \ln Z\rangle &= \lim_{N\to 0} \frac{\langle Z^N\rangle - 1}{N} \\ &= \lim_{N\to 0} \frac{1}{N}\left(\int \prod_{\alpha=1}^{N} \mathcal{D}\{\psi_\alpha\} e^{-S_{\mathrm{repl}}} - 1\right).\end{aligned} \tag{3.21}$$

We neglect the possible presence of long-range spatial correlations which can modify the critical properties [Fedorenko et al., 2012] and take the distribution of disorder potential to be Gaussian,

$$P_V[V] \sim \exp\left(-\frac{1}{2\Delta_0}\int d^d r V(\mathbf{r})^2\right). \tag{3.22}$$

After averaging over disorder we arrive at the replicated effective action

$$\begin{aligned}S_{\mathrm{eff}} \;=\; & \int d\tau d^d r \bar{\psi}_\alpha(\mathbf{r},\tau)(\partial_\tau - i\gamma_j\partial^j)\psi_\alpha(\mathbf{r},\tau) \\ & -\frac{1}{2}\int d\tau_1 d\tau_2 d^d r_1 d^d r_2 g(\mathbf{r}_1 - \mathbf{r}_2) \\ & \times\bar{\psi}_\alpha(\mathbf{r}_1,\tau_1)\psi_\alpha(\mathbf{r}_1,\tau_1)\bar{\psi}_\beta(\mathbf{r}_2,\tau_2)\psi_\beta(\mathbf{r}_2,\tau_2),\end{aligned} \tag{3.23}$$

where summation over repeated replica indices $\alpha, \beta = 1, ..., N$ is implied. From (3.23) we see that disorder generates an attractive interaction between different replicas. The properties of the original system with quenched disorder can be obtained by taking the limit $N \to 0$. Introducing the Matsubara frequency ω the action (3.23) can be rewritten in the Fourier space as

$$\begin{aligned}S = & \int_{k,\omega} \bar{\psi}_\alpha(-\mathbf{k},-\omega)(\boldsymbol{\gamma}\mathbf{k} - i\omega)\psi_\alpha(\mathbf{k},\omega) \\ & -\frac{1}{2}\int_{k_i,\omega_i} \tilde{g}\,(\mathbf{k}_1 + \mathbf{k}_2)\,\bar{\psi}_\alpha(\mathbf{k}_1,-\omega_1)\psi_\alpha(\mathbf{k}_2,\omega_1) \\ & \times\bar{\psi}_\beta(\mathbf{k}_3,-\omega_2)\psi_\beta(-\mathbf{k}_1-\mathbf{k}_2-\mathbf{k}_3,\omega_2),\end{aligned} \tag{3.24}$$

where $\int_k := \int \frac{d^d k}{(2\pi)^d}$ and $\int_\omega := \int \frac{d\omega}{(2\pi)}$. The disorder variance in Fourier space reads

$$\tilde{g}\,(\mathbf{k}) = \Delta_0. \tag{3.25}$$

We now define the correlation functions with insertions of the composite operator $\mathcal{O}(r) := \bar{\psi}_\alpha(r)\psi_\alpha(r)$,

$$G^{(2n,l)}(\{x\},\{y\},\{z\}) = \left\langle \bar{\psi}_{\alpha_1}(x_1)\psi_{\alpha_1}(y_1)...\bar{\psi}_{\alpha_n}(x_n)\psi_{\alpha_n}(y_n)\mathcal{O}(z_1)...\mathcal{O}(z_l)\right\rangle, \tag{3.26}$$

where we used the short-cut notation $x_i := (r_i, \tau_i)$. For example, the local DOS can be found from the retarded Green function

$$\rho(E) = -\frac{1}{\pi}\mathrm{Im}G^R(r,r,E), \tag{3.27}$$

which is related to $G^{(0,1)}(r,\omega)$ by the analytic continuation $i\omega \to E + i0$. The correlation functions (3.26) can be calculated perturbatively in small Δ_0. Each term of this perturbation series can be represented as a Feynman diagram, represented in Fig. 3.8, in which lines stand for the the bare propagator

$$\langle \bar{\psi}_\alpha(\mathbf{k},\omega)\psi_\beta(-\mathbf{k},-\omega)\rangle_0 = \delta_{\alpha\beta}\frac{\boldsymbol{\gamma}\mathbf{k} + i\omega}{k^2+\omega^2}. \tag{3.28}$$

and the dashed lines are vertices corresponding to the Δ_0 term in action (3.24) with $\tilde{g}(k)$ given by Eq. (3.25). The vertices do not transmit frequency but only momenta.

$U(N)$ Gross-Neveu model

It turns out that the Green's functions computed for the action (3.23) at fixed energy ω in the limit $N \to 0$ can be deduced from the d-dimensional $U(N)$ Gross-Neveu (GN) model

$$S_{\mathrm{GN}} = -\int d^d r \left[\bar{\boldsymbol{\chi}} \cdot (\not{\partial} + \omega)\boldsymbol{\chi} - \frac{\Delta}{2}(\bar{\boldsymbol{\chi}}\boldsymbol{\chi})(\bar{\boldsymbol{\chi}}\boldsymbol{\chi})\right], \tag{3.29}$$

which appears here with a negative (attractive) coupling constant in terms of new fields $\bar{\boldsymbol{\chi}} = i\bar{\boldsymbol{\psi}}(\boldsymbol{r},-\omega)$ and $\boldsymbol{\chi} = \boldsymbol{\psi}(\boldsymbol{r},\omega)$ [Syzranov et al., 2016]. The massless GN model describes N fermions coupled with repulsive interactions: the disordered Weyl cone is analog to a GN model with unusual attractive interactions in the limit $N \to 0$. The GN model possesses a chiral symmetry which is spontaneously broken for sufficiently strong interactions. A finite fermionic mass is generated at the transition, which breaks the chiral symmetry [Zinn-Justin, 2002]. For the disordered Weyl fermions this transition translates into the appearance of a finite DOS at the nodal point for disorders stronger than a critical value. This relation has been confirmed by direct calculations to two-loop order on the initial Weyl model using either supersymmetry [Syzranov et al., 2016] or replica methods [Roy and Das Sarma, 2014, Roy and Das Sarma, 2016].

Renormalization group analysis of the Gross-Neveu model

We build up a perturbation theory in small disorder by expanding the generating functional of the correlation and vertex functions perturbatively in Δ. Each term can be represented as a Feynman diagram, see Fig. 3.8 where the solid lines stand for the the bare propagator (3.28) and the dashed line corresponds to the disorder vertex $\frac{1}{2}\Delta$. Note that the dashed line transmit only momenta but not frequency. These terms turn out to be diverging in $d = 2$ which is the lower critical dimension of the transition. Simple scaling analysis shows that weak disorder is irrelevant for $d > 2$. To make the theory finite we use the dimensional regularization and compute all integrals in $d = 2 + \varepsilon_2$. At the end we set $\varepsilon_2 = 1$ for Weyl fermions. To regularize the divergences we employ the minimal subtraction scheme [Ryder, 1996]. The diagrams corresponding to one-loop order perturbation theory are shown on Fig. 3.8. The β-function encodes the scaling of disorder amplitude when changing the energy renormalization scale μ:

$$\beta(\Delta) = -\mu\frac{d\Delta}{d\mu}. \tag{3.30}$$

The scaling of Δ in the low energy limit $\mu \to 0$ determines whether the system is on the weakly disordered ($\Delta(\mu \to 0) \to 0$) or the strongly disordered side ($\Delta(\mu \to 0) \to \infty$) of the transition, see Fig. 3.7. The RG equation describing the transition reads

$$\beta(\Delta) = -\varepsilon_2\Delta - 2\Delta^2(N-2), \tag{3.31}$$

where we kept the dependence on N. In the limit $N \to 0$, the system described by (3.31) has a fixed point

$$\Delta^* = \frac{\varepsilon_2}{4}. \tag{3.32}$$

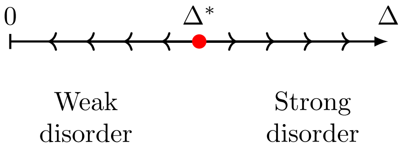

Figure 3.7: Schematic flow of the disorder strength Δ when the renormalization energy scale μ is reduced towards low energies. There is a transition at the fixed point Δ^* where the scaling function (3.30) vanishes: $\beta(\Delta^*) = 0$.

When $\varepsilon_2 \to 0$ ($d \to 2$), $\Delta^* \to 0$ and the system is always in a strong disordered phase, i.e. $\Delta(\mu \to 0) \to \infty$. When $\varepsilon_2 > 0$ there is a transition at $\Delta = \Delta^*$. The stability of the fixed point is given by the derivative of the β-function, $\partial\beta/\partial\Delta(\Delta = \Delta^*)$. Here the correlation length exponent is given by [Zinn-Justin, 2002]

$$\frac{1}{\nu} = -\frac{\partial \beta}{\partial \Delta}|_{\Delta^*} = \varepsilon_2 + \mathcal{O}(\varepsilon_2^2). \tag{3.33}$$

Other critical exponents can be computed in the vicinity of the fixed point, see Appendix A.1. In particular, the dynamical exponent reads

$$z = 1 + \frac{\varepsilon_2}{2} + \mathcal{O}(\varepsilon_2^2). \tag{3.34}$$

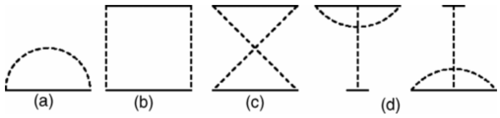

Figure 3.8: Diagrams entering the renormalization of the generating functional of the GN model. Solid lines stands for fermionic propagators and dashed lines for disorder vertices. Taken from [Ostrovsky et al., 2006]

Non-renormalizability of the Gross-Neveu model beyond two-loops

The quantum transition in Weyl and Dirac semimetals has been described using Renormalization Group with expansion around the lower critical dimension up to two-loop order. In the previous section we have seen that there is a direct correspondence between the replicated action of a disordered Weyl cone and the $U(N)$ Gross Neveu model with negative (i.e. attractive) interactions in the $N \to 0$ limit. However, we recall here that the $U(N)$ GN model is not multiplicatively renormalizable in dimension $d = 2 + \epsilon_2 > 2$ [Zinn-Justin, 2002]. This manifests itself in the generation of an infinite number of relevant operators along the RG flow beyond the two-loop order of previous studies [Schuessler et al., 2009, Roy and Das Sarma, 2014, Syzranov et al., 2016]. These relevant operators collapse into a few operators when extrapolating this technique to $d = 3$. Performing this collapse in a controlled way is still an open problem. This casts some doubts about the direct applicability of this approach to the Weyl fermion problem in $d = 3$. At the technical level, this problem is related to the extension to arbitrary dimensions of the Clifford algebra of γ_i matrices,defined by $\gamma_i\gamma_j + \gamma_j\gamma_i = 2\delta_{ij}\mathbb{I}$, and $i, j = 1, ..., d$. This extension is necessary within the renormalization scheme where we work in dimension $d = 2 + \varepsilon_2$. In $2 < d = 2 + \varepsilon_2 < 3$, the product $\gamma_i\gamma_j$ cannot be expressed as a linear combination of γ_i any more so that the Clifford algebra becomes infinite-dimensional. It is then convenient to use antisymmetrized products such as $\gamma^{(n)}_{\vec{A}} = \mathrm{As}[\gamma_{a_1}...\gamma_{a_n}]$, where we have introduced the notation $\vec{A} = \{a_1, ..., a_n\}$, as a basis in this infinite-dimensional space so that one does not need any explicit representation of these objects to perform calculations. Along the RG flow operators involving the product $\gamma_i\gamma_j$ are generated. Thus, an infinite number of additional operators must be taken into account, of the form $V^{(n)} = \left(\bar{\chi}_\alpha \gamma^{(n)}_{\vec{A}} \chi_\alpha\right) \cdot \left(\bar{\chi}_\beta \gamma^{(n)}_{\vec{A}} \chi_\beta\right)$, where a summation over α, β and $\vec{A}$ is implied. The minimal multiplicatively renormalizable model replacing (3.29) hence reads

$$S_{\rm GN} \quad = \quad -\int d^dr \left[\bar{\boldsymbol{\chi}} \cdot (\partial\!\!\!/ + \omega)\boldsymbol{\chi} - \frac{1}{2}\sum_{n=0}^{\infty} \Delta_n V^{(n)} \right]. \tag{3.35}$$

As an example, let us consider the three-loop order for which only the operators $V^{(3)}$ and $V^{(4)}$ are generated [Vasiliev and Vyazovsky, 1997]. We find the corresponding RG flow equations, given in the limit $N \to 0$ by the β-functions,

$$\frac{\partial \Delta_0}{\partial \ln L} = -\varepsilon_2 \Delta_0 + 4\Delta_0^2 + 8\Delta_0^3 + 28\Delta_0^4, \tag{3.36a}$$

$$\frac{\partial \Delta_3}{\partial \ln L} = -\varepsilon_2 \Delta_3 + a\Delta_0^4 + 16\Delta_0\Delta_4 + 8\Delta_0\Delta_3. \tag{3.36b}$$

$$\frac{\partial \Delta_4}{\partial \ln L} = -\varepsilon_2 \Delta_4 - 4\Delta_0\Delta_3 - 12\Delta_0\Delta_4, \tag{3.36c}$$

where $a = -4 + \zeta(3)$ and $\zeta(x)$ is the Riemann zeta function. To this order, we get the fixed point (FP) describing the transition

$$\Delta_0^* = \varepsilon_2/4 - \varepsilon_2^2/8 + \varepsilon_2^3/64 + O(\varepsilon_2^4), \tag{3.37}$$

$$\Delta_3^* = a\varepsilon_2^2/96 - 23a\varepsilon_2^3/1152 + O(\varepsilon_2^4), \tag{3.38}$$

$$\Delta_4^* = -a\varepsilon_2^2/384 + 49a\varepsilon_2^3/9216 + O(\varepsilon_2^4). \tag{3.39}$$

Note the peculiarity of the limit $N \to 0$ where, while Δ_0^* is of order ε_2, we obtain generated operators at the order of ε_2^2 instead of ε_2^3 expected in the three-loop order. The critical exponent of the correlation length divergence at the transition as $\xi \;\sim |\Delta - \Delta^*|^{-\nu}$ reads

$$1/\nu = \varepsilon_2 + \frac{1}{2}\varepsilon_2^2 + \frac{3}{8}\varepsilon_2^3 + O\left(\varepsilon_2^4\right), \tag{3.40}$$

which is consistent with the one-loop result (3.33). For a Weyl semimetal ($\varepsilon_4 = 1$) we find: $\nu = 0.533$ (direct substitution)[1] Crucially, the validity of this renormalization picture directly in dimension $d = 3$ is questionable: the Clifford algebra is then of finite dimension. Hence all the operators $V^{(n)}$ generated by the RG flow beyond three-loops either disappear (evanescent operators) or collapse on a few operators when extending $d = 2 + \varepsilon_2 \to 3$. Contrary to the two-dimensional case [Gracey, 2008] no standard projecting procedure exists to reduce the β-functions for these evanescent operators to the β-function for the remaining operators in $d = 3$.

3.2.3 A new approach to the transition: renormalizable $4 - \epsilon$ expansion

Gross-Neveu-Yukawa model

After having identified the problem of renormalizability of the GN model for the present transition, we propose another way to describe the quantum transition alternative to the use of (3.35). This new approach is of interest beyond the quantitative calculations since it provides an example of a physical model possessing the same quantum critical properties as the disordered Weyl fermions. It is based on the well known correspondence between the critical properties of the $U(N)$ GN and Gross Neveu Yukawa (GNY) models [Zinn-Justin, 2002] which we transpose in the context of the disordered relativistic fermions associated with the $N \to 0$ limit. Contrary to the GN model, the GNY model is renormalizable close to the upper critical dimension, in dimension $d = 4 - \varepsilon_4$: critical properties of the transition can be obtained to any order without generating additional relevant operators. In the $U(N)$ GNY model, an additional scalar field ϕ is introduced, and the action at $E = 0$ reads

$$S_{GNY} = \int d^dr \Big[-\bar{\chi}_\alpha(\partial\!\!\!/ + \sqrt{g}\phi)\chi_\alpha + \frac{1}{2}(\nabla\phi)^2 + \frac{\mu}{2}\phi^2 + \frac{\lambda}{4!}\phi^4 \Big]. \tag{3.41}$$

In terms of the initial fields $\bar{\boldsymbol{\psi}} = -i\bar{\boldsymbol{\chi}}, \boldsymbol{\chi} = \boldsymbol{\psi}$, the GNY model (3.41) corresponds to the Weyl fermions at $\omega = 0$ coupled to an imaginary "random" potential ϕ [2]

$$S^\alpha = \int d^dr \ \bar{\psi}_\alpha(-i\partial\!\!\!/ - i\sqrt{g}\phi)\psi_\alpha, \tag{3.42}$$

---

[1] Other re-summation methods give $\nu = 0.333$ by Padé [2/1] and $\nu = 0.375$ by Padé [1/2]. Note that the Padé-Borel[2/1] has a pole, but the principal value integral gives $\nu = 0.57$

[2] Similarly to going from (3.23) to (3.29), the coupling between fermions of different frequencies is irrelevant for constant ω properties in the limit $N \to 0$.

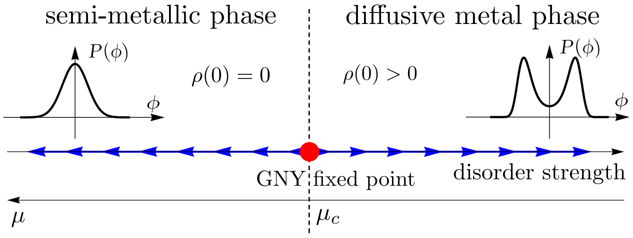

Figure 3.9: Schematic projection of the RG flow for the $U(N)$ GNY model (3.41) in the three-parameter space: g, λ and μ onto an unstable direction along μ. On the left side from the GNY FP, the flow towards large μ corresponds to the semimetallic phase with vanishing DOS at the band crossing and a Gaussian distribution of field ϕ. On the right side the flow towards small μ drives the system towards a diffusive metal with a finite DOS and non-Gaussian distribution of field ϕ.

with the random potential distribution given by

$$P[\phi] \propto \exp\left(-\int d^d r \left[\frac{1}{2}(\nabla\phi)^2 + \frac{\mu}{2}\phi^2 + \frac{\lambda}{4!}\phi^4\right]\right). \tag{3.43}$$

Such a random imaginary potential is unusual: it can be interpreted as an effective inverse life-time (imaginary part of a self-energy), which appears to be randomly distributed. The transposition of the GN - GNY correspondence in the context of disordered Weyl fermions amounts to the equivalence between a random Gaussian scalar potential and a non-Gaussian imaginary field distributed according to (3.43). Studying the relevance of this correspondence beyond these simple distribution functions will be of great interest but is beyond the scope of this thesis.

Within the GNY model, the disorder driven transition of relativistic semimetals can be understood at the mean-field level: (i) For $\mu > 0$, the typical (most probable) value of the scalar field ϕ vanishes and we recover a theory of free fermions. This corresponds to a phase where the disorder potential $\sqrt{g}\phi$ is Gaussian, distributed around $\phi = 0$; (ii) on the other hand, for $\mu < 0$, the scalar field acquires a finite typical value. This typical value of ϕ gives a finite mass for the fermions fields $\boldsymbol{\psi}$ which, by a mechanism analogous to the GN model, then translates into a finite density of states $\rho(0) > 0$ for the Weyl fermions. In this phase, the mean-field distribution of the disorder potential $P[\phi]$ is peaked around opposite values (see Fig. 3.9) and the distribution is no longer Gaussian. In the context of the high energy physics the generation of a finite typical value ϕ corresponds to breaking the chiral/spatial parity symmetry (in even/odd dimensions) by generating a fermionic mass [Zinn-Justin, 2002].

Renormalization group analysis of the Gross-Neveu-Yukawa model

Let us now present our results on the critical properties of the transition obtained from a renormalization group analysis of the GNY model (3.41).

The correspondence between the critical properties of the GN and GNY models has been shown using $1/N$ expansion and numerically for finite N [Kärkkäinen et al., 1994]. Since the GNY model shows analytical behaviour with N, we extend this correspondence between the two models in the limit $N \to 0$. To renormalize the model (3.41) we use a minimal subtraction scheme with dimensional regularization. Introducing the momentum scale Λ, we define the dimensionless parameters: $\tilde{g} = \Lambda^{-\varepsilon_4} g$, $\tilde{\lambda} = \Lambda^{-\varepsilon_4}\lambda$, $\tilde{\mu} = \Lambda^{-2}\mu$. Whereas the couplings λ, g are multiplicatively renormalized, the parameter μ driving the transition acquires a non-universal shift. Hence, we consider the flow of the deviation from the critical value, $\delta\mu = \mu - \mu_c$. We get for the RG flow equations:

$$\frac{\partial\tilde{\lambda}}{\partial \ln L} = \varepsilon_4\tilde{\lambda} - 3\tilde{\lambda}^2 + \frac{17}{3}\tilde{\lambda}^3, \tag{3.44a}$$

$$\frac{\partial\tilde{g}}{\partial \ln L} = \varepsilon_4\tilde{g} - 6\tilde{g}^2 + \frac{9}{2}\tilde{g}^3 + 4\tilde{\lambda}\tilde{g}^2 - \frac{1}{6}\tilde{\lambda}^2\tilde{g}. \tag{3.44b}$$

The critical fixed point is defined by $g^* = \frac{1}{6}\varepsilon_4 + \frac{71}{1296}\varepsilon_4^2 + O(\varepsilon_4^3)$, $\lambda^* = \frac{1}{3}\varepsilon_4 + \frac{17}{81}\varepsilon_4^2 + O(\varepsilon_4^3)$ and $\mu = \mu_c$. The total RG flow in the three parameter space is shown in Fig.3.10. The FP is IR stable in the directions λ and g. μ is the only relevant variable; around the fixed point its scaling with the correlation length ξ defines the critical length exponent ν: $|\delta\mu| \sim \xi^{-1/\nu}$. We find to two-loop order [Louvet et al., 2016], see

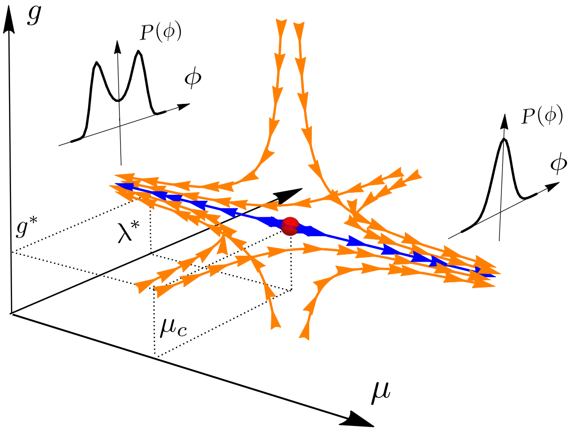

Figure 3.10: Schematic representation of the RG flow for the $U(N)$ GNY model (3.41) in the three-parameter space: g, λ and μ. The transition is described by a fixed point of the flow (g^*, λ^*, μ_c) which possesses only one unstable direction along μ.

section A.2:

$$\frac{1}{\nu} = 2 - \frac{\varepsilon_4}{3} - \frac{19}{162}\varepsilon_4^2 + O(\varepsilon_4^3). \tag{3.45}$$

The numerical value of the exponent ν to two-loop order is given by $\nu = 0.65$ (direct substitution $\varepsilon_4 = 1$) [3].

Discussion

We studied the disorder driven transition of the 3D Weyl semimetals towards a diffusive metal. We showed that the description of this transition using the $U(N)$ GN model in $2 + \varepsilon_2$ dimensions in the limit of $N \to 0$ encounters significant difficulties already at two-loop order. They are related to the multiplicative non-renormalizability of the model and generation of an infinite number of vertices whose three-loop corrections unexpectedly shift the fixed point to the order ε_2^2. We have proposed an alternative approach based on the correspondence between the $U(N)$ GNY and GN models. The previous numerical and analytical studies give values of the correlation length exponent ν which lie in a broad range from 0.6 to 1.5 [Kobayashi et al., 2014, Sbierski et al., 2015, Goswami and Chakravarty, 2011, Syzranov et al., 2016, Roy and Das Sarma, 2014, Roy et al., 2016], that can be related to the existence of a large number of relevant operators in the GN model. The GNY model has only one relevant operator and we find $\nu \approx 0.65 - 0.67$. Beyond offering a well defined framework for an unambiguous description of the critical properties it relates the quantum transition of disordered Weyl fermions with chemical potential fluctuations to that of a model with spatially correlated and non Gaussian imaginary disorder. We are confident that this novel correspondence between two models of identical fermions with distinct disorder potentials opens interesting perspectives for further investigations such as functional renormalization group studies of this transition. The work presented in this section has been published in [Louvet et al., 2016].

3.2.4 Avoided transition. Rare events

Let us now discuss the results of the previous section in view of recent work on the relevance of rare disorder realizations around the transition [Nandkishore et al., 2014, Pixley et al., 2016]. This is an important issue, since the semimetal phase can be destabilized not only by finite doping but also by the zero energy states emergent from these rare disorder configurations. The stability of a disordered fixed point with respect to fluctuations effects is related to the extended Harris criterion $\nu_{\mathrm{FS}} > 2/d$ [Chayes et al., 1986] for the correlation length critical exponent ν. The values of ν for both the GN and GNY models violate this criterion at the order considered until now. Note that this inequality has to be satisfied by the finite size correlation exponent, while there is no restriction on the intrinsic exponent usually probed by the RG methods: In principle, it can be different from the first one [Pázmándi et al., 1997].

On the other hand, the relevance of rare fluctuations around the transition can manifest itself in the RG context by the development of a strong deviation from the Gaussian distribution of disorder. The

---

[3] Re summation methods give $\nu = 0.67$ (Padé [1/1]), $\nu = 0.699$ (Padé-Borel [1/1]).

corresponding cumulants of the disorder distribution are related to the composite operators $\mathcal{O}_q = (\bar{\psi}_\alpha \psi_\alpha)^q$. We find the scaling dimension of these operators to order one-loop in the GN model

$$[\mathcal{O}_q] = (d-1)q - 2q^2\Delta_0^* + O(\Delta_0^{*2}). \tag{3.46}$$

Thus, these operators with $q \geq 4$ become naively relevant at the FP of (3.36a) for $\varepsilon_2 > 2/5$. This observation suggests that strong deviations from the Gaussian distribution of disorder develop in $d = 3$ ($\varepsilon_2 = 1$), which could explain the importance of rare disorder realizations. Indeed, in Refs. [Nandkishore et al., 2014, Pixley et al., 2016] it was shown that the *average* DOS at zero energy can be finite in the semimetallic phase due to contributions from rare events that leads to an avoided quantum transition. For the GNY model we also find instanton-like solutions similar to those observed in the GN model [Nandkishore et al., 2014, Pixley et al., 2016] and which are responsible for the contribution of the rare events to the DOS, see Appendix A.2. Whether such instanton solutions can be accounted for by a more refined renormalization of the distribution of disorder beyond the GNY model remains a question of interest.

3.2.5 Multifractal spectrum

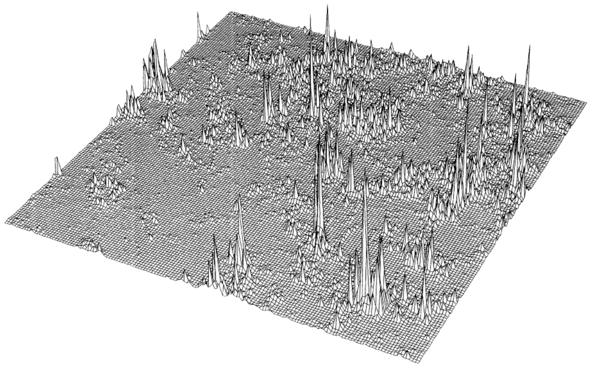

Figure 3.11: The electronic local density of states $|\psi(\mathbf{r})|^2$ can show large fluctuations: here in the context of the Quantum Hall Effect. Taken from [Huckestein, 1995]

An characterization of the transition alternative to the use of the average density of states at $E = 0$ exists. It focuses on the scaling properties of the critical wavefunctions and is less sensitive to the rare region effects, in a similar fashion to the Anderson transition [Pixley et al., 2015]. The disorder averaged inverse participation ratios (IPR's) are defined in terms of the electron wavefunction $\psi(\mathbf{r})$

$$P_q = \int d^d r |\psi(\mathbf{r})|^{2q}. \tag{3.47}$$

The nature of the wavefunction is probed through the scaling of P_q with the size of the system L $\overline{P_q} \sim L^{-\tilde{\tau}_q}$. The exponents $\tilde{\tau}_q$ describe the multifractal spectrum of the wavefunctions. The exponent $\tilde{\tau}_q$ interpolates between localized states for which $\tilde{\tau}_q = 0$ and extended plane wave states with $\tilde{\tau}_q = d(q-1)$. The wavefunction distribution can exhibit large spatial fluctuations which translate into a non-trivial scaling for the IPR's, as exemplified on Fig. 3.11. In the critical regime of the Anderson transition, the wavefunction has a fractal structure characterized by an infinite set of exponents $\tilde{\tau}_q$ [Evers and Mirlin, 2008]. At the disorder-driven quantum transition Weyl fermions wavefunctions also exhibit a multifractal behaviour. In the semimetallic phase the only possible states at the nodal point are the algebraically-decaying instanton-like solutions predicted in [Nandkishore et al., 2014] and observed numerically in [Pixley et al., 2016]. Since these states, if present with finite density, are localized, we still obtain $\tilde{\tau}_q = 0$ in the semimetallic phase, at least for small q. In the diffusive metal phase the system has a finite density of extended states at zero energy that results in $\tilde{\tau}_q = d(q-1)$. Exactly at the transition the exponent modifies to

$$\tilde{\tau}_q = d(q-1) + \tilde{\Delta}_q, \tag{3.48}$$

where $\tilde{\Delta}_q$ also governs the scaling of the moments of the local DOS (LDOS), $\overline{\rho^q} \sim L^{-\tilde{\Delta}_q}$. It is related by $\tilde{\Delta}_q = x_q^* - qx_1^*$ to the scaling dimension x_q^* of the local composite operator representing the qth moment of the LDOS. Fortunately, the scaling dimension of this operator has been calculated within the GN model to two-loop order in [Foster, 2012] and reads

$$x_q^* = (d-1)q - 2q\Delta_0^* - 2\Delta_0^{*2}[3q(q-1)+q] \tag{3.49}$$

with Δ_0^* obtained from (3.36a). Note that $\tilde{\Delta}_q = \frac{3}{8}q(1-q)\varepsilon_2^2$ satisfies the convexity inequality $\partial^2 x_q^*/\partial q^2 \leq 0$ [Duplantier and Ludwig, 1991] and the identity $\tilde{\Delta}_q = \tilde{\Delta}_{1-q}$, i.e. $\overline{\tilde{\rho}^q} \sim \overline{\tilde{\rho}^{1-q}}$ with $\tilde{\rho} = \rho/\overline{\rho}$. The latter holds for the multifractal exponents in the different Wigner-Dyson classes [Evers and Mirlin, 2008] and follows from a very general symmetry of the LDOS distribution $P_\rho(\tilde{\rho}) = \tilde{\rho}^{-3}P_\rho(\tilde{\rho}^{-1})$ [Mirlin et al., 2006]. Then the two-point correlation function is expected to scale as

$$\overline{\tilde{\rho}^p(r)\tilde{\rho}^q(0)} \sim (r/a)^{-\tilde{\Delta}_p - \tilde{\Delta}_q}(r/L)^{\tilde{\Delta}_{p+q}}, \tag{3.50}$$

where a is the microscopic cut-off. Crucially, this description of the multifractal spectrum of the critical wavefunctions, at least for small q is weakly sensitive to the presence of rare events which are contained in the tails of the LDOS distribution. The multifractal spectrum indeed characterizes the underlying avoided critical point. Hence, it proposes an alternative and interesting description of the criticality of disordered Weyl fermions.

3.2.6 Effect of disorder correlations

Let us now turn to the study of the effect of spatial correlations of disorder on this transition. It is well known that correlations of the disorder potential, neglected in this previous study, can be present experimentally and change the nature of the transition. This is indeed the case for the Anderson transition [Croy et al., 2011]. Moreover, the low energy properties of the Dirac phase in graphene are known to be sensitive to disorder correlations [Fedorenko et al., 2012] . Such correlations may originate from the presence of linear dislocations, planar grain boundaries, unscreened charge impurities, etc.

In the present section we consider the effects of spatial disorder correlations on the semimetal-diffusive metal transition introduced in the previous section. We restrict ourselves to the case of algebraic correlations of disorder, and a single Weyl cone.

The presentation is organized as follows. After introducing the model we perform a renormalization group analysis. We study the phase diagram and calculate the critical exponents to two-loop order, before concluding. This work has been published in [Louvet et al., 2017a].

Model

We start again from the Fourier space replicated action for the disordered Weyl cone (3.24). We now assume that the disorder potential $V(\mathbf{r})$ is a random Gaussian variable with zero mean and the variance $\overline{V(\mathbf{r})V(\mathbf{r}')} = g(\mathbf{r}-\mathbf{r}')$, $g(r) \sim r^{-a}$. For convenience, we fix the normalization of the variance in the Fourier space

$$\tilde{g}(k) = \Delta_1 + \Delta_2 k^{a-d}, \tag{3.51}$$

which must be positive. The Δ_1 term in Eq. (3.51) corresponds to the short-range (SR) part of disorder since it becomes the Dirac δ-function in real space: the impact of such uncorrelated disorder has been described in previous sections 3.2.2 and 3.2.3. The strength of the long-range (LR) correlated part of the disorder is given by Δ_2.

The correlation functions (3.26) can be calculated perturbatively in small Δ_1 and Δ_2. Each term of this perturbation series can be represented as a Feynman diagram in which lines stand for the the bare propagator (3.28) and there are two types of vertices which correspond to Δ_1 and Δ_2 terms in action (3.24) with $\tilde{g}(k)$ given by Eq. (3.51). Both of them transmit only momenta but not frequency and the second vertex explicitly depends on the transmitted momenta as k^{a-d}.

Renormalization and scaling behaviour

Dimensional analysis shows that weak disorder is irrelevant for $d > 2$, nevertheless the system can undergo a phase transition to a diffusive metal for strong enough disorder. The correlation functions (3.26) computed perturbatively in small disorder turn out to be diverging in $d = 2$ which is the lower critical dimension of the transition. To describe the scaling behaviour of the system in the vicinity of this transition we apply the field-theoretic renormalization group to two-loop order. To that end we calculate the correlation functions using dimensional regularization. Following [Dudka et al., 2016] we perform a double expansion in $\varepsilon = d-2$ and $\delta = a-2$ in such a way that the UV divergences are converted into the poles in ε and δ. In the framework of the minimal subtraction scheme we consider ratios like ε/δ to be finite in the limit $\varepsilon, \delta \to 0$. We do not include them into the counter-terms, choosing the latter to be the pole part only. The poles in ε and δ can be accumulated in the renormalization factors: Z_ψ, Z_ω, Z_1 and Z_2, so that the renormalized action can be written as

$$S_R = \int_{k,\omega} \bar{\psi}_\alpha(Z_\psi \boldsymbol{\gamma}\mathbf{k} - iZ_\omega\omega)\psi_\alpha - \frac{1}{2}\int_{k_i,\omega_i} \left(\mu^{-\varepsilon} Z_1\Delta_1 + \mu^{-\delta} Z_2\Delta_2|\mathbf{k}|^{a-d}\right)\bar{\psi}_\alpha\psi_\alpha\bar{\psi}_\beta\psi_\beta. \tag{3.52}$$

Here we have introduced the renormalized fermionic fields ψ, $\bar{\psi}$ and the renormalized dimensionless coupling constants Δ_1 and Δ_2 on the mass scale μ. In what follows we will denote the bare variables by $\mathring{A}$. The renormalized fields and variables are related to the bare ones by

$$\mathring{\psi} = Z_\psi^{1/2}\psi, \quad \mathring{\bar{\psi}} = Z_\psi^{1/2}\bar{\psi}, \tag{3.53}$$

$$\mathring{\omega}_j = Z_\omega Z_\psi^{-1}\omega_j, \quad \mathring{O} = Z_\omega Z_\psi^{-1} O, \tag{3.54}$$

$$\mathring{\Delta}_1 = \frac{2\mu^{-\varepsilon}}{K_d}\frac{Z_1}{Z_\psi^2}\Delta_1, \quad \mathring{\Delta}_2 = \frac{2\mu^{-\delta}}{K_d}\frac{Z_2}{Z_\psi^2}\Delta_2. \tag{3.55}$$

For the sake of simplicity we have also included $K_d/2$ into definition of the renormalized coupling constants in Eqs. (3.55). $K_d = 2\pi^{d/2}/((2\pi)^d\Gamma(d/2))$ is the surface area of the d-dimensional unite sphere divided by $(2\pi)^d$ coming from the angular integration in the Feynman diagrams. The renormalized and the bare Green functions are related by

$$\mathring{G}^{(2n,l)}(\{p, \mathring{\omega}\}, \mathring{\Delta}) = Z_\omega^l Z_\psi^{n-l} G^{(2n,l)}(\{p,\omega\}, \Delta, \mu), \tag{3.56}$$

where $\Delta := \{\Delta_1, \Delta_2\}$. Using that the bare Green functions $\mathring{G}^{(2n,l)}$ do not depend on the renormalization scale μ one can derive the RG flow equation

$$\Big[\sum_j p_j\frac{\partial}{\partial p_j} + (1+\gamma(\Delta))\sum_j \omega_j\frac{\partial}{\partial\omega_j} + \sum_{i=1,2}\beta_i(\Delta)\frac{\partial}{\partial\Delta_i} + d(2n-1) \\ - n(d-1+\eta_\psi(\Delta)) + l(1+\gamma(\Delta))\Big] G^{(2n,l)}(\{p,\omega\},\Delta,\mu) = 0, \tag{3.57}$$

where we have defined the scaling functions

$$\beta_i(\Delta) = -\mu\frac{\partial\Delta_i}{\partial\mu}\bigg|_{\mathring{\Delta}}, \tag{3.58}$$

$$\eta_\psi(\Delta) = -\sum_{i=1,2}\beta_i(\Delta)\frac{\partial \ln Z_\psi}{\partial\Delta_i}, \tag{3.59}$$

$$\eta_\omega(\Delta) = -\sum_{i=1,2}\beta_i(\Delta)\frac{\partial \ln Z_\omega}{\partial\Delta_i}, \tag{3.60}$$

$$\gamma(\Delta) = \eta_\omega(\Delta) - \eta_\psi(\Delta). \tag{3.61}$$

The solutions of Eq. (3.57) can be found by using the method of characteristics. The characteristics are lines in the space of p_i, Δ, ω_i along which Eq. (3.57) can be rewritten as an ordinary differential equation of the first order. The characteristics lines can be parametrized by the auxiliary parameter ξ which will be later identified with the correlation length. The lines are given by equations:

$$\frac{dp_j(\xi)}{d\ln\xi} = p_j(\xi), \tag{3.62}$$

$$\frac{d\Delta_i(\xi)}{d\ln\xi} = \beta_i(\Delta(\xi)), \tag{3.63}$$

$$\frac{d\omega_j(\xi)}{d\ln\xi} = [1+\gamma(\Delta(\xi))]\omega_j(\xi), \tag{3.64}$$

with the initial conditions $\Delta(1) = \Delta$, $p_j(1) = p_j$, and $\omega_j(1) = \omega_j$. The solution of Eq. (3.57) propagates along the characteristics lines according to the ordinary differential equation

$$\frac{d\ln H_{2n,l}(\xi)}{d\ln\xi} = d(2n-1) - n(d-1+\eta_\psi(\Delta(\xi))) + l(1+\gamma(\Delta)), \tag{3.65}$$

with the initial conditions $H_{2n,l}(1) = 1$. Thus the solution of Eq. (3.57) satisfies

$$G^{(2n,l)}(p_j, \omega_j, \Delta) = H_{2n,l}(\xi) G^{(2n,l)}(p_j(\xi), \omega_j(\xi), \Delta(\xi)). \tag{3.66}$$

Since the DOS is related to $G^{(0,1)}$ by Eq. (3.27) it obeys the scaling relation

$$\rho(\omega, \Delta) = H_{0,1}(\xi)\rho(\omega(\xi), \Delta(\xi)). \tag{3.67}$$

Let us now assume that the RG flow (3.63) has a fixed point (FP) $\Delta^* = (\Delta_1^*, \Delta_2^*)$ defined as

$$\beta_i(\Delta^*) = 0, \quad i = 1, 2. \tag{3.68}$$

To determine the stability properties of the FP one can linearise the flow equation in its vicinity to compute the stability matrix

$$\mathcal{M}_{ij} = \left. \frac{\partial \beta_i(\Delta)}{\partial \Delta_j} \right|_{\Delta^*}, \tag{3.69}$$

which has two eigenvalues λ_1 and λ_2. The positive eigenvalues of the matrix (3.69) correspond to the unstable directions in the plane (Δ_1, Δ_2). The transition, if it exists, is controlled by a FP which has only one unstable direction, e.g. $\lambda_1 > 0$ and $\lambda_2 < 0$. Introducing the eigenvector $\Delta - \Delta^*$ associated with $\lambda_1 > 0$ the scaling formula (3.66) in the vicinity of the FP (3.68) can be written as

$$G^{(2n,l)}(p_i, \omega_i, \Delta) = \xi^{d(2n-1)-2nd_\psi + lz} g_{2n,l}(p_i\xi, \omega_i\xi^z, |\Delta - \Delta^*|\xi^{1/\nu}). \tag{3.70}$$

Here $|\Delta - \Delta^*|$ is the length of the eigenvector and we have defined the critical exponents for the correlation length ξ,

$$\xi \sim |\Delta - \Delta^*|^{-\nu}, \qquad \frac{1}{\nu} = \lambda_1, \tag{3.71}$$

the dynamic critical exponent

$$\omega \sim k^z, \qquad z = 1 + \gamma(\Delta^*) \tag{3.72}$$

and the anomalous dimension of the fields ψ and $\bar{\psi}$

$$d_\psi = \frac{1}{2}[d - 1 + \eta_\psi(\Delta^*)]. \tag{3.73}$$

For instance, the two-point correlation function, which gives the momentum distribution at the transition, behaves as

$$G^{(2,0)}(p) \sim p^{-1+\eta_\psi(\Delta^*)}, \quad G^{(2,0)}(r) \sim \frac{1}{r^{d-1+\eta_\psi(\Delta^*)}}. \tag{3.74}$$

The scaling formula (3.67) for the DOS in the vicinity of the FP (3.68) has the form

$$\rho(\omega) = \xi^{z-d}\rho_0(\omega\xi^z, |\Delta - \Delta^*|\xi^{1/\nu}). \tag{3.75}$$

Transitions: existence and critical behaviour

Using the two-loop diagrams computed in [Dudka et al., 2016] we derive the beta functions (3.58):

$$\beta_1(\Delta_1, \Delta_2) = -\varepsilon\Delta_1 + 4\Delta_1^2 + 4\Delta_1\Delta_2 + 8\Delta_1^3 + 20\Delta_1^2\Delta_2 + 4\Delta_2^3 + 16\Delta_1\Delta_2^2, \tag{3.76}$$

$$\beta_2(\Delta_1, \Delta_2) = -\delta\Delta_2 + 4\Delta_2^2 + 4\Delta_1\Delta_2 + 4\Delta_2^3 + 4\Delta_1^2\Delta_2 + 8\Delta_1\Delta_2^2, \tag{3.77}$$

the dynamic critical exponent (3.72):

$$z(\Delta_1, \Delta_2) \quad = \quad 1 + 2(\Delta_1 + \Delta_2) + 2(\Delta_1 + \Delta_2)^2, \tag{3.78}$$

and the anomalous dimension (3.59) of the fermionic fields

$$\eta_\psi(\Delta_1, \Delta_2) = -2\Delta_1^2 + 2\Delta_2^2 - \frac{4\varepsilon}{\delta}\Delta_2(\Delta_1 + \Delta_2). \tag{3.79}$$

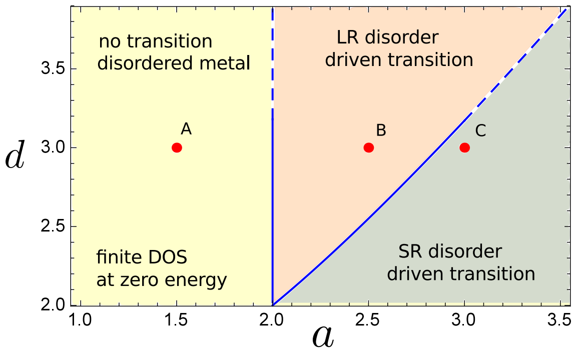

Figure 3.12: Domains of existence of the transition as a function of the power a of disorder correlations and dimension d: (i) in the left (yellow) region for slowly decaying correlations the physics resemble a mean-field description: there is no transition, the disorder is always relevant and the disordered metal is the only phase. The typical RG flow computed at the point A $[a = 3/2,\ d = 3]$ is shown in Fig. 3.13; in the middle (pink) region a new transition is present, from a semimetal phase to a metallic phase, which is controlled by the LR FP. The typical RG flow computed at the point B $[a = 5/2,\ d = 3]$ is shown in Fig. 3.14; in the right (green) region there is a transition from a semimetal phase to a metallic phase which is controlled by the SR FP previously studied: LR correlations of disorder are irrelevant. The typical RG flow computed at the point C $[a = 3,\ d = 3]$ is shown in Fig. 3.15.

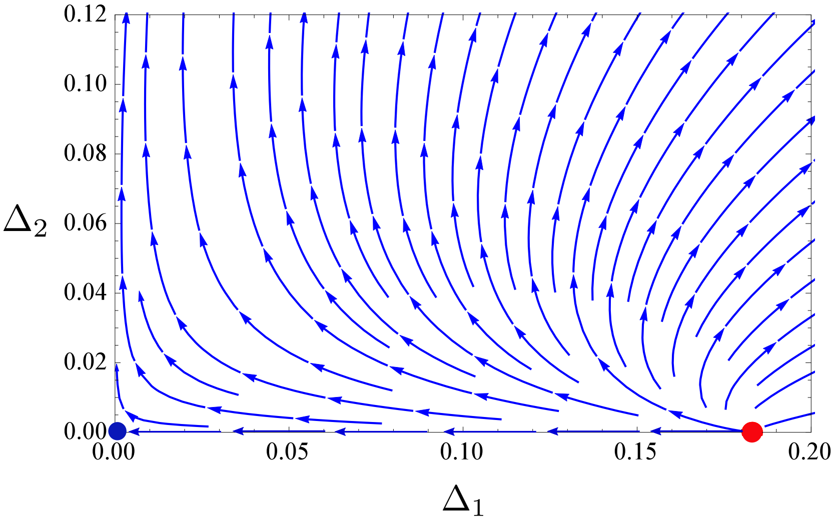

Figure 3.13: *Strongly disordered phase for strong disorder correlations:* runaway of the RG flow for $d = 3$ ($\varepsilon = 1$) and $a = 3/2$ ($\delta = -1/2$) corresponding to the point A in Fig. 3.12. The red dot is the SR FP which is fully unstable. The blue dot is the Gaussian FP corresponding to the semimetal phase which is also unstable towards such strong correlations of disorder, irrespective of the disorder amplitude.

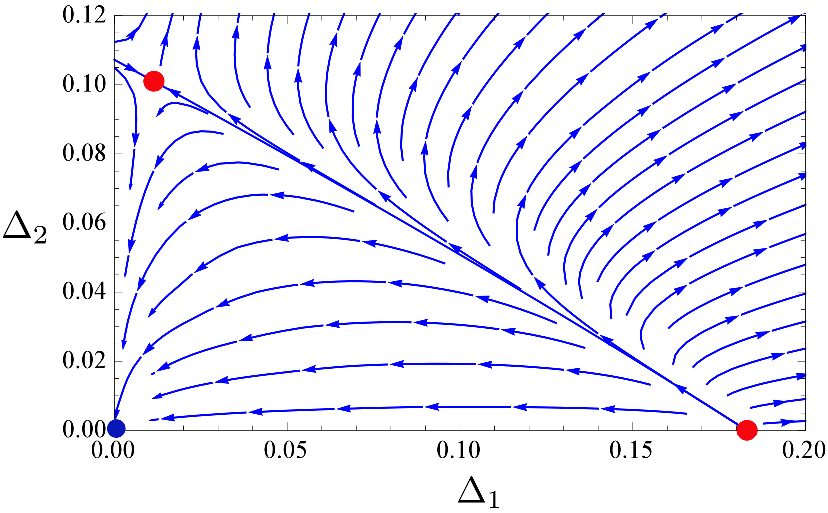

Figure 3.14: *New LR transition:* the RG flow for $d = 3$ ($\varepsilon = 1$) and $a = 5/2$ ($\delta = 1/2$) corresponding to the point B in Fig. 3.12. The right red dot is the SR FP which is fully unstable to disorder correlations. The left red dot is the new LR FP which controls the transition between a semimetal and a disordered metal phase and which gives rise to a new universality class different from the SR case. This transition is driven by the long range correlations of the disorder. The blue dot is the Gaussian FP corresponding to the semimetal phase.

Note that the ratio ε/δ in Eq. (3.79) is finite in our regularization scheme.

We now analyse the RG flow derived from Eqs. (3.76)-(3.79) that is summarized in Figures 3.12-3.15. We are interested in the effect of an additional LR correlated disorder on the SR disorder-driven transition: our results on the stability of the SR fixed point with respect to additional Δ_2 distinguish between three different domains, as shown on Fig. 3.12. First note that the case $d = 2$ ($\varepsilon = 0$), corresponding to graphene, is special since it corresponds to the lower critical dimension where no transition occurs: SR disorder is marginally relevant and drives the system to a strong disordered metallic phase, characterized by a finite zero-energy DOS [Fedorenko et al., 2012]. For dimension d greater than 2 we must distinguish three regimes of disorder correlations :

(A) For $a < 2$ ($\delta < 0$) i.e. when the long-range disorder correlations decay slower than $1/r^2$, the semimetallic phase becomes unstable to any small amount of disorder. This manifests itself into the instability of the SR fixed point to additional LR disorder: the transition is suppressed and the system always flows towards the strong disordered metallic phase as shown in Fig. 3.13. This can be interpreted as the "mean-field like" regime of correlations.

(C) For the opposite case of "short range" disorder correlation, defined by an exponent a larger than a critical value of a, $a > a_c(d)$ defined below (3.83), the SR fixed point is stable and the semimetal to metal SR transition remains unaffected. Fig. 3.15 shows that the relevant direction for the RG flow is still along Δ_1 axis.

(B) In the intermediate domain $2 < a < a_c(d)$ we find that in the presence of LR disorder a transition still exists between a semimetal and a disordered metal, but is different from the SR transition : this corresponds to the existence of a new LR fixed point of the RG, see Fig. 3.14. Correspondingly, the critical properties of this new LR disorder-driven transition are different from the previous SR one.

Thus, we have found that depending on the dimension and the type of algebraic decay, LR correlated disorder can strongly affect the disorder driven transition in semimetals. Indeed, depending on the values of ε and δ the RG flow equations (3.76) and (3.77) have up to three FPs:

(i) the Gaussian fixed point (Gaussian FP) is

$$\Delta_1^{\mathrm{G}} = \Delta_2^{\mathrm{G}} = 0. \tag{3.80}$$

The basin of attraction of this FP in the plane (Δ_1, Δ_2) corresponds to the semimetal phase. For instance, for $\delta < 0$ the basin of attraction collapses to the axis $\Delta_2 = 0$ so that the semimetal phase is washed out by any weak correlated disorder.

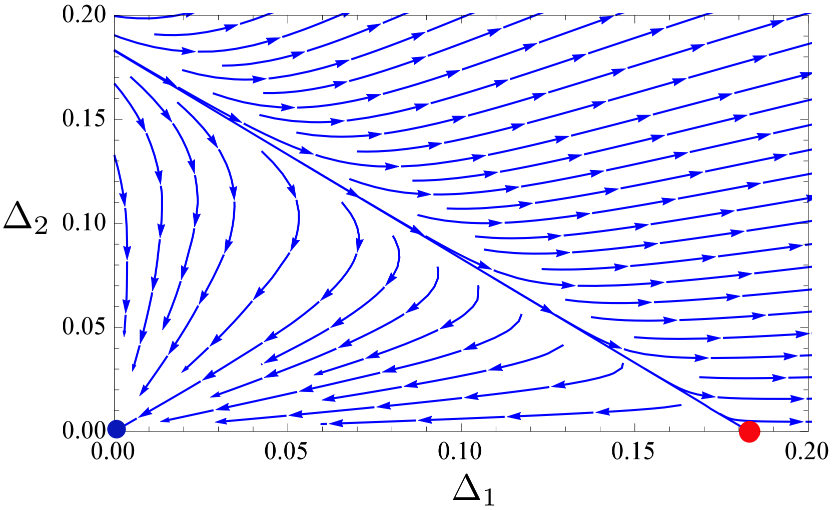

Figure 3.15: *SR transition*: the RG flow for d=3 ($\varepsilon = 1$) and $a = 3$ ($\delta = 1$) corresponding to the point C in Fig. 3.12. The red dot is the SR FP with a single unstable direction (relevant operator), describing the previously studied semimetal to disordered metal transition governed by the parameter Δ_1. The blue dot is the Gaussian FP corresponding to the semimetal phase.

(ii) the short-range fixed point (SR FP) reads

$$\Delta_1^{\mathrm{SR}} = \frac{1}{4}\left(\sqrt{2\varepsilon+1}-1\right) = \frac{\varepsilon}{4} - \frac{\varepsilon^2}{8} + O\left(\varepsilon^3\right), \tag{3.81}$$

$$\Delta_2^{\mathrm{SR}} = 0, \tag{3.82}$$

which has a single unstable direction for $\delta > \delta_{\mathrm{c}}(\varepsilon)$, where

$$\delta_{\mathrm{c}}(\varepsilon) = \frac{1}{2}(\sqrt{1+2\varepsilon}+\varepsilon-1) \approx \varepsilon - \frac{\varepsilon^2}{4} + O\left(\varepsilon^3\right), \tag{3.83}$$

and fully unstable otherwise. This defines $a_c(d) = 2 + \delta_c(d-2)$. In $d = 3$ we find $a_c(3) \approx 2.8$.

(iii) long-range fixed point (LR FP) reads

$$\Delta_1^{\mathrm{LR}} = \frac{(4+\delta)\sqrt{\delta+1}-3\delta-4}{2(\varepsilon-\delta)} \approx \frac{\delta^3}{16(\varepsilon-\delta)} + \ldots, \tag{3.84}$$

$$\Delta_2^{\mathrm{LR}} = \frac{(\varepsilon-2\delta-4)\sqrt{\delta+1}+4-\varepsilon+4\delta}{2(\varepsilon-\delta)} \tag{3.85}$$

$$\approx \frac{\delta}{4} - \frac{\delta^2\varepsilon}{16(\varepsilon-\delta)} + \ldots \tag{3.86}$$

The LR FP is physical, i.e. it corresponds to a positive $\tilde{g}(k)$ and has a single unstable direction for $0 < \delta < \delta_{\mathrm{c}}(\varepsilon)$.

We now discuss the critical properties at the transition. For $a < 2$ ($\delta < 0$) there is a runaway of the RG flow so that the correlated disorder is always relevant if present. In this case there is no semimetal phase and the DOS at zero energy is finite (see Fig. 3.13). For $2 < a < a_{\mathrm{c}}(d)$ ($0 < \delta < \delta_{\mathrm{c}}(\varepsilon)$) there is a line of phase transitions separating the semimetal and diffusive metal phases with the critical behaviour controlled by the LR FP (see Fig. 3.14). The corresponding critical exponents computed to two-loop order are

$$\frac{1}{\nu_{\mathrm{LR}}} = \delta + \frac{\delta^2(2\delta+\varepsilon)}{4\varepsilon} + O(\varepsilon^3, \delta^3), \tag{3.87}$$

$$z_{\mathrm{LR}} = 1 + \frac{\delta}{2} + O(\varepsilon^3, \delta^3), \tag{3.88}$$

$$\eta_{\mathrm{LR}} = -\frac{\delta(2\varepsilon-\delta)}{8} + O(\varepsilon^3, \delta^3). \tag{3.89}$$

Note that the two-loop correction to the dynamic critical exponent (3.88) vanishes. For $a_\mathrm{c}(d) < a$ ($\delta_\mathrm{c}(\varepsilon) < \delta$) there is also a line of phase transitions separating the semimetal and diffusive metal phases with the critical behaviour controlled by the SR FP (see Fig. 3.15). The critical exponents at the SR FP

$$\frac{1}{\nu_\mathrm{SR}} = \varepsilon + \frac{\varepsilon^2}{2} + O(\varepsilon^3), \tag{3.90}$$

$$z_\mathrm{SR} = 1 + \frac{\varepsilon}{2} - \frac{\varepsilon^2}{8} + O(\varepsilon^3), \tag{3.91}$$

$$\eta_\mathrm{SR} = -\frac{\varepsilon^2}{8} + O(\varepsilon^3), \tag{3.92}$$

reproduce the two-loop order result derived early for uncorrelated disorder in [Syzranov et al., 2016] and are in full agreement with the exponents calculated to three loop order in [Louvet et al., 2016]. We expect that these critical exponents evolve continuously from the SR to LR values at the change of critical regimes shown in Fig. 3.12. Indeed the values of the critical exponents at the LR FP (3.87)-(3.89) coincide with those at the SR FP (3.90)-(3.92) when evaluated at the borderline between the two regimes given by Eq. (3.83).

Finally let us discuss the connection of the problem we considered to the 2D Ising model with correlated random bond disorder. The latter can be formulated in terms of 2D Majorana fermions whose critical behaviour can be studied by RG methods using dimensional regularization (for details see [Dudka et al., 2016]). It turns out that the corresponding β functions are related to the β functions of the disordered Weyl fermions (3.76) and (3.77) as

$$\beta_i^{\mathrm{2DIsing}}(u, v) = \lim_{\varepsilon\to 0} \beta_i(\Delta_1 = -u, \Delta_2 = -v). \tag{3.93}$$

In spite of the exact relation between the β functions, the critical behaviour of both models belongs to different universality classes. Indeed, the critical behaviour of disordered 3D Weyl fermions is described by an unstable FP with $\Delta_1, \Delta_2 > 0$ for $\varepsilon = 1$ and $\delta > 0$: the transition is controlled by the strength of disorder whose deviation from the critical value is a relevant operator. The corresponding positive eigenvalue determines the correlation length exponent ν for the semimetal-disordered metal transition. The Matsubara frequency ω plays the role of mass and its scaling dimension defined in Eq. (3.64) yields the dynamic critical exponent z (3.72). To two-loop order it is given by Eq. (3.78) evaluated at the corresponding FP. On the other hand the critical behaviour of the disordered 2D Ising model is described by a stable FP with $u, v > 0$ for $\varepsilon = 0$ and $\delta < 0$: the transition is controlled by the mass which is now the reduced temperature. Its scaling dimension gives now instead of the dynamic exponent z the correlation length exponent ν_2DIsing. The RG function (3.78) used to compute the dynamic exponent z of the semimetal-disordered metal transition is thus related to that for the correlation length exponent ν_2DIsing of the 2D Ising model as

$$\frac{1}{\nu_\mathrm{2DIsing}(u, v)} = \lim_{\varepsilon\to 0} z(\Delta_1 = -u, \Delta_2 = -v). \tag{3.94}$$

Scaling arguments and $4-\varepsilon$ expansion suggest that at the transition controlled by the LR FP this exponent is exactly $\nu_\mathrm{Ising}(d) = 2/a$ in any $2 \leq d < 4$ [Weinrib and Halperin, 1983, Honkonen and Nalimov, 1989, Prudnikov et al., 2000]. This is in agreement with calculations in two dimensions using a fermionic representation performed in [Dudka et al., 2016]. There it was shown that the two-loop corrections to ν_2DIsing (3.94) vanish at the LR FP so that the one-loop result $\nu_\mathrm{2DIsing} = 2/a$ is exact. Taking into account the relation between the RG functions of both models and the fact that the two-loop corrections to z (3.88) also vanish we conjecture that the one-loop value $z_\mathrm{LR} = a/2$ is also exact.

This conjecture fixes the borderline between the regions with SR and LR criticality to $z_\mathrm{SR}(\varepsilon) = z_\mathrm{LR}(\delta_c) = a_c/2$. Substituting the two-loop result (3.91) one again arrives at Eq. (3.83). Using the results of [Louvet et al., 2016] one can then estimate the position of the borderline to three loop order

$$\delta_\mathrm{c}^{(3loop)}(\varepsilon) = \varepsilon - \frac{\varepsilon^2}{4} + \frac{3\varepsilon^3}{16} + O\left(\varepsilon^4\right). \tag{3.95}$$

Note that elucidating the critical properties following the $2+\varepsilon$ expansion requires particular care beyond two loop order. Indeed, we have shown, see section 3.2.2 that the consistent description of the transition with SR disorder beyond two loops involves an infinite number of relevant operators generated by the RG flow. To overcome this obstacle we proposed an alternative way based on a $4-\varepsilon$ expansion [Louvet et al., 2016], described in section 3.2.3. However, generalization of this approach to the case of LR disorder is a non trivial task which remains to be done.

Conclusions

We have studied the effect of LR disorder correlations on the semimetal - disordered metal transition. We have found that for slowly decaying correlations $a < 2$ the LR correlated disorder is always relevant and drives the system to a diffusive phase: the transition is suppressed and the DOS is finite at zero energy for arbitrary weak disorder. Let us note that in particular this result restricts the range of disorder correlations that can be used in simulations, necessary to uncouple the different Weyl cones, to actually observe the SR transition. More surprisingly, we have found an intermediate regime $2 < a < a_c(\varepsilon)$ where the system undergoes a new transition from semimetal to diffusive metal at finite disorder strength and the criticality is controlled by a LR FP. This change of criticality under addition of LR disorder correlations is a completely new phenomena distinct from what was known for graphene. It would be of great interest to explore the physical consequences of this crossover, e.g. on the behaviour of the DOS at finite energy along the lines of [Fedorenko et al., 2012]. Another interesting directions for future studies would be possible instantons occurring for rare disorder realisations, which are expected to decay algebraically [Nandkishore et al., 2014] and effects of Coulomb interactions [Hosur et al., 2012] .

Part II

Transport Properties of Relativistic Semimetals

Chapter 4

Minimal Conductivity at the Nodal Point

Transport measurements provide a powerful tool to probe the properties of relativistic excitations. We have seen in section 1.2 that the relativistic nature of the low energy excitations is at the origin of several characteristic signatures in transport. One of these peculiar features is the existence of a finite minimal conductivity at the band crossing, where the electronic density of states vanishes [Tworzydło et al., 2006, Katsnelson et al., 2006]. To characterize semimetallic phases beyond graphene via transport properties at the band crossing the question of the origin of this minimal conductivity has to be addressed. In the literature, different origins have been proposed to explain this finite conductivity. Using Landauer formalism, it has been attributed to evanescent relativistic modes occurring in a confined geometry [Tworzydło et al., 2006]. On the other hand, using the Kubo linear response approach, the minimal conductivity has been derived as a contribution from plane wave states [Katsnelson et al., 2006, Ryu et al., 2007], possibly related to the pseudo-spin or the Zitterbewegung of Dirac electrons. The minimal conductivity was initially related to the Zitterbewegung of Dirac particles, an intrinsic agitation characteristic of ultra relativistic particles, which has been predicted to lead to diffusive motion even in perfectly clean samples [Katsnelson et al., 2006].

In this chapter, we investigate the necessary ingredients for this minimal conductivity by considering three-band extensions of graphene. Among these possible ingredients we can list a priori the chiral symmetry, the pseudo-spin 1/2 structure, the Zitterbewegung, and the quantized Berry phase acquired by an electron when winding around the crossing point. Here we demonstrate that neither chiral symmetry nor pseudo-spin structure, nor Zitterbewegung are at the origin of the finite minimal conductivity. On the other hand, at least for the three-bands models with chiral symmetry, we relate the non vanishing minimal conductivity with the existence of topological Berry phases. This relation between the nature of evanescent modes in a confined geometry and a property of propagating wave states of a given gapless relativistic Hamiltonian is reminiscent of the bulk-boundary correspondence in gapped topological phases. In topological insulators a topological property of the bulk states manifests itself as robust surface states. In the relativistic semi-metals we have considered we find a correspondence between a topological property of bulk, plane wave states, the robust Berry winding, and the nature of evanescent states which gives a finite conductivity. To identify the origin of the non-vanishing conductivity we study the simplest models of chiral symmetric semimetals beyond graphene which are three band models in two dimensions. These models all possess the same spectrum, chiral symmetry and exhibit Zitterbewegung. As only some of them exhibit non-vanishing minimal conductivity we can rule out these properties as the origin of this phenomena. Moreover, the conductivity of three-band models corresponding to spin $S = 1$ vanishes, ruling out the relevance of the pseudo-spin structure. Instead, to discriminate between the models with non-vanishing conductivity and those without, we introduce a duality transformation. The duality generalizes the notion of symmetry of Bloch Hamiltonians and allows one to distinguish between models with different nature of evanescent states. We show that the same duality also discriminates between the models with and without topological Berry phase that allows one to link the transport property to the topological one.

This chapter is organized as follows. Section 4.1 reviews previous literature on the minimal conductivity in graphene. We then introduce a lattice realization of three bands models with chiral symmetry in section 4.2 and study the transport properties of wide junctions using both analytical and numerical Landauer approaches. We also discuss the Berry phase properties of a band crossing. We show that the lattice properties at the origin of a topological Berry phase are encoded by none of the standard symmetries of the Hamiltonian but rather by the duality transformation. This allows us to establish a link between a non-vanishing minimal conductivity and a topological Berry phase via duality transformation, setting a novel correspondence between a property of bulk plane wave states and the nature of evanescent states, reminiscent of the bulk-edge correspondence of insulators in section 4.3.

4.1 Existence of a minimal conductivity in graphene

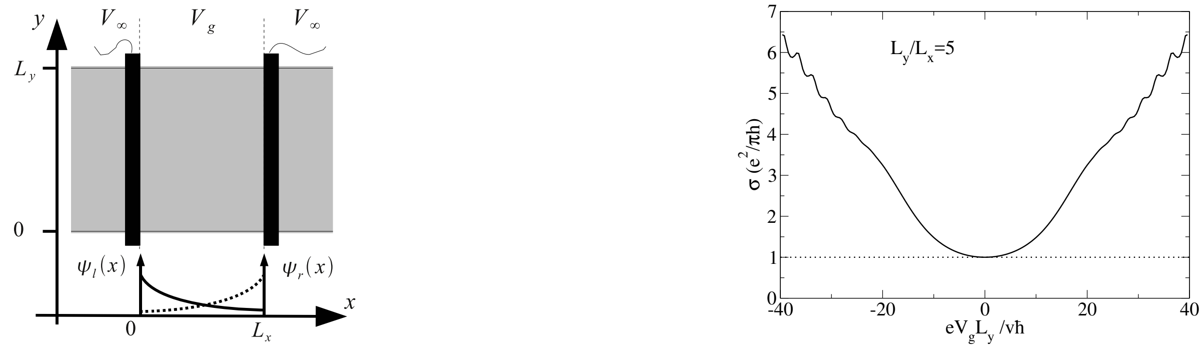

(a) (b)

Figure 4.1: (a) Schematic view of the graphene strip contacted by two electrodes (black rectangles). ψ_l and ψ_r represent evanescent electronic waves localized near the left (resp. right) edge of the sample. (b) Conductivity σ as a function of gate voltage V_g (chemical potential) for fixed aspect ratio.

4.1.1 Transport in absence of charge carrier

Landauer two-terminal conductance calculation

It has been shown both theoretically [Tworzydło et al., 2006, Katsnelson et al., 2006] and experimentally [Novoselov et al., 2005, Zhang et al., 2005, Danneau et al., 2008] that graphene has a finite minimal conductivity at charge neutrality point ($E = 0$), where the charge carrier concentration vanishes. We will compute this minimal conductivity and see that it is of the order of the quantum of conductance e^2/h. The calculations presented here reproduce in a large proportion those carried in [Katsnelson et al., 2006]. The Landauer formula relates the conductance of a material to the transmission probabilities T_n of electronic currents:

$$G = \frac{e^2}{h}\sum_n T_n, \tag{4.1}$$

where the sum runs over conduction channels (see appendix B.1 for details). T_n gives the probability for an electron in mode n to be transmitted through the sample. In two dimensions, the conductivity is then defined by

$$\sigma \equiv G\frac{L_x}{L_y}, \tag{4.2}$$

where L_x and L_y are the dimensions of the system, x being the direction of the current.

Consider a piece of graphene with dimensions L_x and L_y and whose chemical potential is fixed by a voltage V_g, applied through a gate electrode. The sample is contacted between two electrodes made of metallic doped graphene with a high chemical potential corresponding to voltage $V_\infty < 0$, in the configuration of Figure 4.1a. The results will not depend on V_∞, assuming $|V_\infty| \gg |V_g|$. The conductivity depends on the sample geometry via the aspect ratio L_x/L_y and boundary effects in the transverse direction, y. For a very short and very large strip of graphene ($L_y/L_x \gg 1$), details at the $y = 0$ and $y = L_y$ boundaries can be neglected and therefore arbitrary transverse boundary conditions can be chosen. We study transport at low energy, near a conical point described by the Dirac Hamiltonian (1.10). There are two such points $\mathbf{K}$, $\mathbf{K}'$ in graphene: all edges and potentials are assumed to be smooth on the lattice scale so that boundary effects do not mix the two cones, and each of them can be considered separately.

Electrons are confined in the y direction by opening a gap at the edges of the sample, following [Tworzydło et al., 2006]. We might just as well have chosen periodic boundary conditions as in [Katsnelson et al., 2006], but the physical meaning of such conditions is not clear. The gap is implemented by adding a mass term $v^2M(y)\sigma_z$ to the Hamiltonian, where $M(y)$ is zero inside the strip and goes to infinity at the edges $y = 0$ and $y = L_y$. The Dirac equation for the system then becomes:

$$[\hbar v k_x\sigma_x + \hbar v k_y\sigma_y + v^2M(y)\sigma_z + eV(x)]\Psi = \varepsilon\Psi, \tag{4.3}$$

with $V(x) = V_g$ for $x \in [0, L_x]$ and $V(x) = V_\infty$ otherwise. One can show that this choice of boundary conditions $M(y = 0, L_y) = +\infty$ gives the following quantization for transverse momenta [Tworzydło et al., 2006]:

$$q_n = \frac{\pi}{L_y}\left(n + \frac{1}{2}\right) , \tag{4.4}$$

for $0 \le n < N$. The number of transverse modes is given by: $N = (k_\infty L_y/\pi + 1/2)$, with $e|V_\infty| = \hbar v k_\infty$. This quantization is different from what one would get using periodic boundary conditions; however, it can be easily shown that in the present configuration where $L_y/L_x \gg 1$ the final result for conductivity is the same. Matching conditions for the Dirac equation at $x = 0$ and $x = L_x$ require the continuity of wave functions at the contacts – the Dirac equation only involves first order derivatives, unlike the Schrödinger equation. With the present choice of transverse boundary conditions, the transverse momentum is a well-defined quantum number: conservation of $k_y = q_n$ imposes that wave functions in the strip and in the electrodes have the same y-dependence: $\Psi(x, y) = \Psi(x)\text{exp}(\text{i}q_ny)$. Hence, there is a separate transmission probability T_n for each transverse mode.

One then computes the probabilities of transmission T_n through the graphene strip, at zero energy and zero chemical potential. First, one looks for solutions to the Dirac equation (4.3) in the sample for $\varepsilon = 0$, $V_g = 0$. For states of the form $\Psi(x, y) = 1/\sqrt{2}\ (\psi_1(x), \psi_2(x))^T\text{exp}(\text{i}q_ny)$, Eq. (4.3) reads:

$$\begin{aligned}(\hat{k}_x + i\hat{k}_y)\psi_1 = 0,\\ (\hat{k}_x - i\hat{k}_y)\psi_2 = 0,\end{aligned} \tag{4.5}$$

with $\hat{k}_j = -\text{i}\frac{\partial}{\partial x_j}$ in the coordinate representation. This yields:

$$\Psi(x, y) = \frac{1}{\sqrt{2}}\begin{pmatrix} a\ \text{e}^{q_nx} \\ b\ \text{e}^{-q_nx}\end{pmatrix}\text{e}^{\text{i}q_ny}. \tag{4.6}$$

Zero-energy wave functions are evanescent waves in the x-direction (see Figure 4.1a). In the electrodes where $V(x) = V_\infty < 0$, zero-energy solutions of Eq. (4.3) are plane waves propagating in both directions:

$$\Psi(x, y) = \frac{1}{\sqrt{2}}\begin{pmatrix} 1 \\ s\ \text{e}^{s\text{i}\theta}\end{pmatrix}\text{e}^{s\text{i}k_xx}\text{e}^{\text{i}q_ny}, \tag{4.7}$$

where $k_x^2 + q_n^2 = k_\infty^2$, $\sin(\theta) = q_n/k_\infty$ and $s = \pm 1$ defines the direction of propagation. Sending a plane wave from the left electrode propagating to the right into mode n, one obtains a reflected plane wave in the left electrode and a transmitted plane wave in the right electrode. The electronic wave functions then have the following form:

$$\psi_1(x) = \begin{cases}\text{e}^{\text{i}k_xx} + r_n\ \text{e}^{-\text{i}k_xx}, & x < 0\\ a\ \text{e}^{q_nx}, & 0 < x < L_x\\ t_n\ \text{e}^{\text{i}k_xx}, & x > L\end{cases} \tag{4.8}$$

$$\psi_2(x) = \begin{cases}\text{e}^{\text{i}\theta}\text{e}^{\text{i}k_xx} - r_n\ \text{e}^{-\text{i}\theta}\text{e}^{-\text{i}k_xx}, & x < 0\\ b\ \text{e}^{-q_nx}, & 0 < x < L_x\\ t_n\ \text{e}^{\text{i}\theta}\text{e}^{\text{i}k_xx}, & x > L,\end{cases}$$

and the matching conditions at the $x = 0,\ x = L_x$ contacts give the transmission coefficient for mode n:

$$T_n = |t_n|^2 = \frac{\cos^2\theta}{\cosh^2(q_nL_x) - \sin^2\theta}. \tag{4.9}$$

For a large enough $|V_\infty|$, one may assume $k_\infty L_x \gg 1$ and consider that the state comes from the left at normal incidence $\theta \simeq 0$. The expression for conductance is then given by the multi-channel Landauer formula (4.1), taking $N \to \infty$:

$$G = \frac{e^2}{h}\sum_{n=0}^{\infty} T_n = \frac{e^2}{h}\sum_{n=0}^{\infty}\frac{1}{\cosh^2(\pi(n+1/2)L_x/L_y)} = \frac{e^2}{h}\frac{L_y}{\pi L_x} \tag{4.10}$$

and the 2D conductivity is then: $\sigma \equiv G\frac{L_x}{L_y} = \frac{e^2}{\pi h}$. Surprisingly, this conductivity is finite: the sample still conducts at zero energy and zero chemical potential, even though the electronic density vanishes at this point (cf. Fig. 1.9). A finite minimal conductivity close to the theoretical value of $4e^2/\pi h$ has been measured in a 200nm long sample with aspect ratio $L_y/L_x = 24$ [Danneau et al., 2008]. The factor 4 accounts for the spin and valley degeneracy. In other studies [Novoselov et al., 2005], the measured minimal conductivity is close to e^2/h per valley per spin, i.e. three times the estimation given by Landauer formula. The difference might be due to the great sensitivity of the system to disorder: near the conical point, small inhomogeneities of the charge density, corresponding to small fluctuations of the chemical potential, can no longer be overlooked [Castro Neto et al., 2009].

We now evaluate numerically the conductance as a function of energy, or backgate voltage V_g. By finding the solutions of Eq. (4.3) which satisfy the matching conditions at $x = 0,\ L_x$ for a given potential V_g and aspect ratio L_y/L_x, we can compute the transmission coefficients T_n. We then compute the conductivity using Eqs. (4.1) and (4.2). Figure 4.1b shows the conductivity σ plotted against potential V_g, for a fixed aspect ratio $L_y/L_x = 5$. We can see the unexpected semi-plateau of conductivity at $\sigma = \frac{e^2}{\pi h}$ for zero doping $V_g = 0$. One can also check that the conductivity shows electron-hole symmetry $V_g \to -V_g$. The conductivity plot shows oscillations at large V_g; they signal the appearance of modes propagating in the x direction as the control voltage increases. Finally, note that spin and valley degeneracy values for conductivity accounts for an extra factor 4 for the conductance.

The linear response approach: Kubo conductivity

Let us now discuss the physics of minimal conductivity, within the linear response framework. We will employ the Kubo formula, which is a standard tool to describe electronic transport. The Kubo formalism is summarized in appendix B.2. The present derivation follows closely the one in [Ryu et al., 2007]. As in the previous section, we focus on transport at low energies and assume that the two conical points are decoupled: the system is then described by the Dirac Hamiltonian (1.10). As before, results for conductivity are given per valley and per spin. The starting point is the Kubo formula in two spatial dimensions:

$$\sigma_{\mu\nu}(\omega,\beta) = \frac{\pi}{\omega L^2}\int d\varepsilon \sum_{m,n}\delta(\varepsilon-\varepsilon_n)\langle n|\hat{j}_\mu|m\rangle\langle m|\hat{j}_\nu|n\rangle(f_\beta(\varepsilon)-f_\beta(\varepsilon_m))\delta(\varepsilon-\varepsilon_m+\hbar\omega)\ , \tag{4.11}$$

which gives the linear response of the system at temperature $1/\beta$ to an electric field oscillating at frequency ω (we keep only the real part of the response function, cf. appendix B.2). On the right hand side of Eq. (4.11) appears the Fermi-Dirac distribution function $f_\beta(\varepsilon)$. Consider an infinite size system $L \to \infty$; the results for conductivity are independent of L. Introduce the single-particle eigenstates of the Dirac Hamiltonian (1.10) in sublattice basis:

$$|m\rangle \equiv |\mathbf{p},\ \lambda = \pm\rangle = \frac{1}{\sqrt{2}p}\begin{pmatrix}\lambda(p_x - \mathrm{i}p_y)\\ p\end{pmatrix}, \tag{4.12}$$

with energy $\varepsilon_m = \lambda\varepsilon(p) = \lambda v_F p$ ($p = ||\mathbf{p}||$). Each of these single particle states represents a plane wave with momentum $\mathbf{p}$: to enforce momentum conservation, corresponding scalar product has to be defined as $\langle m|n\rangle \equiv \delta_{\mathbf{p}_m\mathbf{p}_n}\langle \mathbf{p}_n\lambda_m|\mathbf{p}_n\lambda_n\rangle$, with $\langle \mathbf{p}_n\lambda_m|\mathbf{p}_n\lambda_n\rangle$ the usual hermitian product for 2×2 spinors. The current operator is given by the functional derivative of $\hat{H}$ with respect to momentum. It reads in the sublattice basis :

$$\hat{j}_\mu = ev_F\sigma_\mu. \tag{4.13}$$

The current operator is diagonal in $\mathbf{p}$, due to momentum conservation:

$$\langle \mathbf{p},\lambda|\hat{j}_\mu|\mathbf{p}',\lambda'\rangle = ev_F\delta_{\mathbf{p}\mathbf{p}'}\langle \mathbf{p},\lambda|\sigma_\mu|\mathbf{p},\lambda'\rangle\ , \tag{4.14}$$

note that its expression does not depend on $\mathbf{p}$ because of the linearity of the spectrum. It is possible to rewrite the conductivity (4.11), introducing single particle Green functions: we will see later on how this can be done. By doing so, we introduce a parameter η, the imaginary part of the self-energy. In the diffusive regime, η corresponds to the inverse of an electronic lifetime, due to scattering of the electrons by impurities or defects. In our case we consider a sample of pristine graphene i.e. we are in the ballistic regime. However, near the conical point ($E_F \to 0$) the Fermi wavelength is no longer negligible compared to system size; hence, electrons become sensitive to boundaries and acquire a finite lifetime. In the Landauer configuration (see appendix B.1 and section 4.1.1) this finite lifetime – due to electrons escaping into the electrodes, is intrinsically taken into account. We will now compute the DC conductivity in both cases of an ideal (ballistic) infinite system $\eta \to 0$ and then with a phenomenological parameter $\eta > 0$ which models the inherent scattering time of electrons in a finite geometry. The ideal case is defined by taking the limit $\eta \to 0$ before sending ω to zero.

A. Infinite ballistic system: $\eta \to 0$ In this case, one can directly start from Eq. (4.11). For finite frequency $\omega > 0$ and temperature $1/\beta > 0$ the Kubo conductivity is given by:

$$\sigma_{\mu\nu}(\omega,\beta) = \frac{\pi(ev_F)^2}{\omega L^2}\sum_{m,n}\delta_{\mathbf{p}_m\mathbf{p}_n}\langle n|\sigma_\mu|m\rangle\langle m|\sigma_\nu|n\rangle(f_\beta(\varepsilon_n)-f_\beta(\varepsilon_m))\delta(\varepsilon_n-\varepsilon_m+\hbar\omega). \tag{4.15}$$

The current operator being diagonal in momentum, the linear dispersion of the Dirac spectrum states that only matrix elements between states with same or opposite energies will contribute to the conductivity: $\mathbf{p}_m = \mathbf{p}_n \Rightarrow \varepsilon_m = \pm\varepsilon_n$. Besides, the delta distribution on the right hand side of Eq. (4.15) enforces $\varepsilon_m - \varepsilon_n = \hbar\omega > 0$. Hence $\varepsilon_m = -\varepsilon_n (= \hbar\omega/2)$. For $\omega > 0$, the only contributions to the conductivity come from current matrix elements mixing states with opposite, non-vanishing energy (when $\varepsilon_m = \varepsilon_n$ the term $f_\beta(\varepsilon_n) - f_\beta(\varepsilon_m)$ in (4.15) vanishes). We will thus only consider matrix elements of the form $\langle \mathbf{p},\lambda|\sigma_\mu|\mathbf{p},(-\lambda)\rangle$. Rewriting momentum in polar coordinates $(p_x,p_y) = (p\cos\theta, p\sin\theta)$, we have:

$$\langle \mathbf{p},\lambda|\sigma_x|\mathbf{p},(-\lambda)\rangle\langle \mathbf{p},(-\lambda)|\sigma_x|\mathbf{p},\lambda\rangle = \frac{1}{2}(1-\cos 2\theta) \tag{4.16a}$$

$$\langle \mathbf{p},\lambda|\sigma_y|\mathbf{p},(-\lambda)\rangle\langle \mathbf{p},(-\lambda)|\sigma_y|\mathbf{p},\lambda\rangle = \frac{1}{2}(1+\cos 2\theta) \tag{4.16b}$$

$$\langle \mathbf{p},\lambda|\sigma_x|\mathbf{p},(-\lambda)\rangle\langle \mathbf{p},(-\lambda)|\sigma_y|\mathbf{p},\lambda\rangle = -\frac{1}{2}\sin 2\theta. \tag{4.16c}$$

Equation (4.16c) gives the general form of contributions to the transverse conductivity σ_{xy}. Since the right hand side vanishes when integrated over θ, one gets $\sigma_{xy} = 0$. The contributions to longitudinal conductivities in the x and y direction, respectively Eq. (4.16a) and Eq. (4.16b), both give π after integration, leading to $\sigma_{xx} = \sigma_{yy}$. This is in agreement with rotational symmetry of the Dirac Hamiltonian (1.10) in the p_xp_y plane. Rewriting the sum over basis as $\sum_m = \sum_{\lambda=\pm}\int d^2\mathbf{p}\frac{L^2}{(2\pi\hbar)^2}$ yields, after some calculation:

$$\sigma_{\mu\nu}(\omega,\beta) = \delta_{\mu\nu}\frac{\pi e^2}{8h}\tanh\left(\frac{\beta\hbar\omega}{4}\right) \tag{4.17}$$

This expression depends solely on the dimensionless parameter $\beta\hbar\omega$. In particular, it is independent of both the Fermi velocity v_F and system size L. When taking the limits $\omega \to 0$ and $\beta \to \infty$, the right hand side of Eq. (4.17) can take any value ranging between 0 and $\frac{\pi e^2}{8h}$, depending on the value of $\beta\hbar\omega$. For example, if we take the limit $\beta \to \infty$ before the limit $\omega \to 0$, then

$$\lim_{\omega\to 0}\lim_{\beta\to\infty}\sigma_{\mu\nu}(\omega,\beta) = \delta_{\mu\nu}\frac{\pi e^2}{8h}. \tag{4.18}$$

If on the other hand we send ω to zero before taking the zero temperature limit, we get

$$\lim_{\beta\to\infty}\lim_{\omega\to 0}\sigma_{\mu\nu}(\omega,\beta) = 0. \tag{4.19}$$

Thus, the Kubo conductivity exhibits a singularity in the limit of zero temperature and zero frequency. It is the linear dispersion of massless Dirac fermions that gives the dependence of the conductivity on the product $\beta\hbar\omega$, leading to this peculiar behavior. We observe (cf. Eq. (4.16)) that for $\omega > 0$, contributions to the conductivity come from the mixing of positive and negative energy states by the current operator. This is reminiscent of the explanation for minimal conductivity proposed by Katsnelson (see previous sections and [Katsnelson et al., 2006]), which states that the current operator in graphene allows for a special kind of interband transitions – the so-called Zitterbewegung effect, which in turn give rise to the minimal DC conductivity.

Results for the zero-energy Kubo conductivity in an infinite, ballistic graphene sample thus range between 0 and $\frac{\pi e^2}{8h}$. The universal value given by Landauer formula was $\frac{e^2}{\pi h}$; we do not recover the same expression here. This discrepancy manifests the difference between the two expressions: they both consider two different experimental situations. The present Kubo conductivity corresponds to the response of an infinite system, whereas the Landauer formula gives the conductivity of a sample contacted between two electrodes. To recover the Landauer formalism result within Kubo formalism, one should therefore phenomenologically take into account a finite electronic lifetime by introducing an imaginary part of the self-energy $\eta > 0$ [Ryu et al., 2007].

B. Finite geometry: case with inherent finite lifetime, $\eta > 0$ We want to include a finite scattering rate η in the formalism. To this end, we start by re-expressing Eq. (4.11) using single-particle Green functions. The advanced and retarded Green functions are defined by:

$$G_\eta^{R/A}(\varepsilon) \equiv (\varepsilon \pm \mathrm{i}\hbar\eta - \mathcal{H})^{-1} \ . \tag{4.20}$$

In Eq. (4.20), η corresponds to an inverse single-particle lifetime: it can either be seen as originating from disorder or as an escape time in the presence of electrodes. To a first approximation, a finite lifetime will lead to a broadening of energies by η. To account for this effect, we replace the two delta distributions in Eq. (4.11) by Lorentzians parametrized by a (sufficiently small) $\eta > 0$, and then re-express each Lorentzian as the difference between advanced and retarded Green functions. For instance:

$$\begin{aligned}\delta(\varepsilon - \varepsilon_n) \to \delta^\eta(\varepsilon - \varepsilon_n) &= \frac{\hbar\eta/\pi}{(\varepsilon - \varepsilon_n)^2 + (\hbar\eta)^2} \\ &= \frac{1}{2\mathrm{i}\pi}\left(\frac{1}{\varepsilon - \mathrm{i}\hbar\eta - \varepsilon_n} - \frac{1}{\varepsilon + \mathrm{i}\hbar\eta - \varepsilon_n}\right) \ ,\end{aligned} \tag{4.21}$$

which in turn yields:

$$\langle m|\hat{j}_\nu \delta(\varepsilon - \varepsilon_n)|n\rangle \to \frac{1}{2\mathrm{i}\pi}\langle m|\hat{j}_\nu G_\eta^{A-R}(\varepsilon)|n\rangle \ , \tag{4.22}$$

where

$$G_\eta^{A-R}(\varepsilon) \equiv G_\eta^A(\varepsilon) - G_\eta^R(\varepsilon) \ . \tag{4.23}$$

In the literature Im $(G_\eta^A(\varepsilon))$ is often used instead of $G_\eta^{A-R}(\varepsilon)$, both formulations being trivially equivalent. Our choice of notation (4.23) is coherent with [Ryu et al., 2007]. From Eq. (4.11) , we obtain for the conductivity:

$$\sigma_{\mu\nu}(\omega, \eta, \beta) = \frac{\hbar}{4\pi L^2}\int d\varepsilon \ \frac{f_\beta(\varepsilon + \hbar\omega) - f_\beta(\varepsilon)}{\hbar\omega} \ \mathrm{Tr}[G_\eta^{A-R}(\varepsilon)\hat{j}_\mu G_\eta^{A-R}(\varepsilon + \hbar\omega)\hat{j}_\nu] \ , \tag{4.24}$$

where the trace Tr runs over the basis of the Hamiltonian eigenstates (4.12).

As in the $\eta \to 0$ case, one can easily show that the transverse conductivity vanishes. Hence, from now on we consider only σ_{xx}. In order to perform the trace in (4.24), we first rewrite $G_\eta^{A-R}(\varepsilon)$ in the momentum representation as:

$$G_\eta^{A-R}(\mathbf{k}, \varepsilon) = \frac{\varepsilon - \mathrm{i}\hbar\eta + \hbar v_F \mathbf{k}\cdot\boldsymbol{\sigma}}{(\varepsilon - \mathrm{i}\hbar\eta)^2 + (\hbar v_F k)^2} - \frac{\varepsilon + \mathrm{i}\hbar\eta + \hbar v_F \mathbf{k}\cdot\boldsymbol{\sigma}}{(\varepsilon + \mathrm{i}\hbar\eta)^2 + (\hbar v_F k)^2} \ . \tag{4.25}$$

Remark that here we used a unique property of the spin 1/2 algebra, namely $\{\sigma_\mu, \sigma_\nu\} = 2\delta_{\mu\nu}\mathbb{I}$. One can rewrite the trace in Eq. (4.24) as:

$$\mathrm{Tr}[G_\eta^{A-R}(\varepsilon)\hat{j}_\mu G_\eta^{A-R}(\varepsilon + \hbar\omega)\hat{j}_\nu] = \frac{L^2}{(2\pi)^2}\int d^2\mathbf{k} \ \mathrm{tr}[G_\eta^{A-R}(\mathbf{k}, \varepsilon)\hat{j}_\mu G_\eta^{A-R}(\mathbf{k}, \varepsilon + \hbar\omega)\hat{j}_\nu] \ , \tag{4.26}$$

where the trace tr runs over sublattice indices. Using the trace properties of the Pauli matrices (tr $\sigma_\rho = 0$), the only terms whose trace does not vanish in Eq. (4.24) have the form tr$[\sigma_\rho\sigma_x\sigma_\rho\sigma_x]$ and tr$[\mathbb{I}\sigma_x\mathbb{I}\sigma_x]$. The first trace comes with $\rho = x$ and $\rho = y$; these two contributions cancel each other because of the anticommutativity of Pauli matrices. After simplification, Eq. (4.24) reads:

$$\begin{aligned}\sigma_{xx}(\omega, \eta, \beta) = &\frac{\hbar(ev_F)^2}{(2\pi)^2}\int d\varepsilon \frac{f_\beta(\varepsilon + \hbar\omega) - f_\beta(\varepsilon)}{\hbar\omega} \\ &\times \int_0^\infty kdk\left(\frac{\varepsilon - \mathrm{i}\hbar\eta}{(\varepsilon - \mathrm{i}\hbar\eta)^2 + (\hbar v_F k)^2} - \frac{\varepsilon + \mathrm{i}\hbar\eta}{(\varepsilon + \mathrm{i}\hbar\eta)^2 + (\hbar v_F k)^2}\right) \\ &\times \left(\frac{\varepsilon + \hbar\omega - \mathrm{i}\hbar\eta}{(\varepsilon + \hbar\omega - \mathrm{i}\hbar\eta)^2 + (\hbar v_F k)^2} - \frac{\varepsilon + \hbar\omega + \mathrm{i}\hbar\eta}{(\varepsilon + \hbar\omega + \mathrm{i}\hbar\eta)^2 + (\hbar v_F k)^2}\right) .\end{aligned} \tag{4.27}$$

Taking the limit of zero frequency and then of zero temperature we get:

$$\lim_{\beta\to\infty}\lim_{\omega\to 0}\frac{f_\beta(\varepsilon+\hbar\omega)-f_\beta(\varepsilon)}{\hbar\omega}=-\delta(\varepsilon)\ , \tag{4.28}$$

The integration over momenta in Eq. (4.27) can then be performed exactly:

$$\begin{aligned}\lim_{\beta\to\infty}\lim_{\omega\to 0}\sigma_{xx}(\omega,\eta,\beta)&=\frac{\hbar e^2 v_F^2}{4\pi^2}\int_0^\infty kdk\frac{4\hbar^2\eta^2}{\left((\hbar\eta)^2+(\hbar v_F k)^2\right)^2}\\ &=\frac{2e^2}{h}\int_0^\infty\frac{XdX}{\left(1+X^2\right)^2}\qquad\left(\text{with } X=\frac{v_F k}{\eta}\right)\\ &=\frac{e^2}{\pi h},\end{aligned} \tag{4.29}$$

which is the same result as the one derived with Landauer formula in section 4.1.1. Even though in the absence of disorder it is standard procedure to set $\eta\to 0$ prior to taking any other limit, in the case of graphene it gives a result different from the Landauer conductivity. In contrast, this second approach phenomenologically accounts for the finite electronic lifetime which arises near Fermi level because of the linear dispersion, and allows to recover the value derived with Landauer formula. We stress that no assumption has been made on the parameter η after having introduced the Green functions, and the final result is independent of η. In contrast with the infinite system case $\eta\to 0$, the present derivation doesn't allow for identification of the contributions originating from transitions between single-particles eigenstates. However, it has made clear that the unique properties of the spin 1/2 algebra play an important role in the phenomenon of minimal conductivity in graphene.

Zitterbewegung

Let us now illustrate the basic concept of Zitterbewegung for the case of graphene [Katsnelson, 2012]. Let us recall the Dirac Hamiltonian at the **K** point of the Brillouin zone:

$$\hat{H}=\hbar v_F\hat{\mathbf{q}}\cdot\boldsymbol{\sigma}, \tag{4.30}$$

with total momentum given by $\mathbf{k}=\mathbf{K}+\mathbf{q}$. The corresponding current operator is

$$\hat{\mathbf{j}}\equiv\frac{e}{\hbar}\frac{\delta\hat{H}}{\delta\hat{\mathbf{k}}}=ev_F\boldsymbol{\sigma}. \tag{4.31}$$

Note that as a direct consequence of the linear dispersion relation, the current operator $\hat{\mathbf{j}}$ is independent of momentum $\mathbf{k}$, something rather unusual in physics. All electronic excitations therefore have the same current amplitude $j=ev_F$, and the pseudo-spin determines the direction of $\mathbf{j}$. Now consider the following matrix (introducing θ through $(q_x,q_y)=q(\cos\theta,\sin\theta)$) :

$$U=\frac{1}{\sqrt{2}}(1+\mathrm{i}\sigma_x\sin\theta-\mathrm{i}\sigma_y\cos\theta), \tag{4.32}$$

which diagonalizes the Hamiltonian: $U^\dagger HU=\hbar v_F q\sigma_z$. We compute the time-evolved current operator in the Heisenberg representation. In the diagonal basis of $\hat{H}$ it is given by:

$$U^\dagger\hat{j}_x(t)U=ev_F\begin{pmatrix}\cos\theta & \mathrm{i}\sin\theta\ \mathrm{e}^{-\mathrm{i}\theta+2\mathrm{i}\varepsilon_q t/\hbar}\\ -\mathrm{i}\sin\theta\ \mathrm{e}^{+\mathrm{i}\theta-2\mathrm{i}\varepsilon_q t/\hbar} & -\cos\theta\end{pmatrix}\ , \tag{4.33}$$

with $\varepsilon_q=\hbar v_F q$. Let us point out the off-diagonal matrix elements of the current operator which oscillate at frequency $2\varepsilon_q/\hbar$. They correspond to interband transitions between positive and negative energy states. For a high energy ε_q these off-diagonal terms oscillate at a frequency significantly higher than typical measurement frequencies and therefore wash out on average; they will however become crucial for low-energy physics. Besides, the current operator being proportional to the velocity operator, these oscillating terms correspond to an oscillation of the averaged velocity: the so-called Zitterbewegung.

Finite minimal conductance in Weyl semimetals

Note that in Weyl semimetals where electrons near the crossing are described by a Weyl Hamiltonian (1.13), evanescent states also give a finite conductance [Baireuther et al., 2014, Trescher et al., 2015] which reads, in the limit of a large junction

$$G = \frac{e^2}{h}\frac{2\ln 2}{\pi}\left(\frac{W}{L}\right)^2 . \tag{4.34}$$

However the conductivity is zero in the large sample limit since in 3D $\sigma = GL/W^2$.

4.1.2 Transport through evanescent states

Evanescent states at the band crossing

In this section we provide a phenomenological argument for the existence of a finite minimal conductivity coming from evanescent states at the nodal point in graphene. When the chemical potential is brought towards the crossing, $\mu \to 0$, the Fermi surface shrinks to a point and the density of electrons vanishes $n_e \to 0$, see Fig. 1.9. There are no plane wave states at the crossing $\mu \to 0$, but in a confined geometry evanescent states appear even in the gapped regions of the bulk spectrum. These evanescent states are solutions of the Schrödinger equation

$$\mu\psi = \left(\sigma_x k_x + \sigma_y k_y\right)\psi, \tag{4.35}$$

with complex momentum k_x. Here, we assume that k_y is real, fixed by the transverse boundary conditions in the y direction, see Fig. 4.1a. A solution to (4.35) exists in the limit $\mu \to 0$ provided

$$k_x = ik_y \implies \psi \propto \exp(ik_x x) = \exp\left(-\frac{x}{\xi}\right). \tag{4.36}$$

Evanescent states are exponentially localized on a length ξ towards the leads of the junction, Fig. 4.1a. Since the transverse momentum is quantized according to

$$k_y = \frac{\pi}{W}(n + \frac{1}{2}), \tag{4.37}$$

the decay length becomes macroscopic in the large W limit:

$$\xi \sim \frac{W}{n} \tag{4.38}$$

so that the evanescent states located near the two leads can overlap, whatever the length of the sample, and contribute to transport.

Pseudo-diffusive transport

The importance of shot noise in electronic transport is encoded by the Fano factor, which describes the ratio between fluctuations of current and the average current:

$$F = \frac{\sum\limits_n (1 - T_n)}{\sum\limits_n T_n}. \tag{4.39}$$

In the ballistic regime, all transmission coefficients are $T_n = 1$ and the Fano factor is expected to be trivial $F = 0$. However it turns out that transport at the Dirac point in graphene is pseudodiffusive. Indeed, the distribution of transmission amplitudes T_n is characteristic of a disordered metal, encoded by a Fano factor $F = 1/3$ [Tworzydło et al., 2006]. Thus, the regime of transport through evanescent states at the nodal point in clean graphene is pseudo-diffusive, identical to the diffusive transport regime for plane waves in a disordered metal. This Fano factor $F = 1/3$ has been measured experimentally in [Danneau et al., 2008].

4.1.3 On the origin of the minimal conductivity

We have investigated the origin of the minimal conductivity. Is it a hallmark of semimetals, a signature of relativistic or Dirac fermions? Contrary to other transport properties, in the existing literature we haven't found any convincing and definite claim establishing the finite minimal conductivity as a manifestation of a property of relativistic excitations in graphene. Hints exist that the minimal conductivity would be a consequence of the Zitterbewegung [Katsnelson, 2012]. We have seen in the linear response derivation that the pseudo spin algebra plays a crucial role. We have adressed the connection of this remarkable property with the underlying physics near the band crossing in graphene and found that the finite minimal conductivity is a signature not of the plane wave states but of the evanescent states. In the following work we relate the nature of these contributing evanescent states to a topological property of the plane wave states: a quantized Berry winding. To unveil this relation, we study simple three-bands extensions of graphene.

4.2 Our study on three band models

4.2.1 Three-band models on the honeycomb lattice: generalization of graphene in 2D

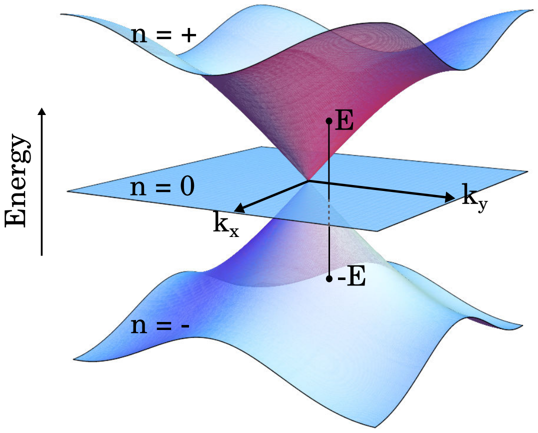

Figure 4.2: Energy spectrum of a three-band chiral semimetal which consists of two linear energy bands $n = \pm$ and a flat band $n = 0$. Chiral symmetry manifests itself as a symmetry of the spectrum $E(\vec{k}) \to -E(\vec{k})$.

We consider lattice models for three-band semimetals in two dimensions that realize the simplest generalizations of graphene: they are build from the honeycomb lattice with an extra atomic orbital (site) in the unit cell. The low-energy spectrum of these models is characterized by two linearly crossing energy bands $n = \pm$ and a third locally flat band $n = 0$, represented in Fig. 4.2. We focus here on spinless models. This spectrum can be observed in a local approximation in the Brillouin Zone of different materials in two and three dimensions, such as 3D critical HgCdTe [Orlita et al., 2014], square MoS_2 in 2D [Li et al., 2014], or in the 2D carbon allotrope SG-10b [Wang et al., 2013a]. Similarly to graphene, only nearest neighbor couplings can be kept when focusing around the band crossing points.

H_3: three-band hexagonal model

The three-band hexagonal model is a possible generalization of graphene, adding an extra orbital exactly on one sublattice as shown on Fig. 4.3 and Fig. 2.13c. To write the Bloch Hamiltonian of our system, we consider the triangular Bravais lattice with three sites per unit cell. The spectrum therefore consists of three energy bands, each carrying one-third of the electronic states. The Hamiltonian for a given value of

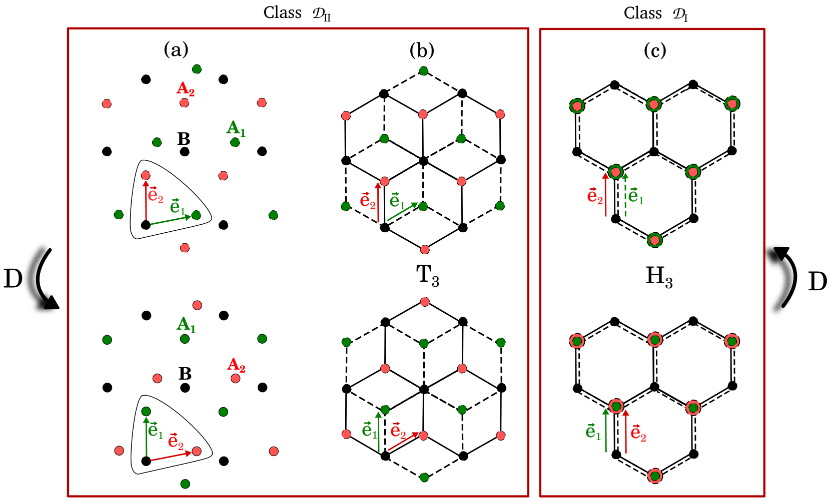

Figure 4.3: Triangular Bravais lattices with three orbitals (A_1, A_2 and B) per unit cell are represented. The position of the A_1 orbitals is chosen arbitrary (a), in the center of the BA_1 hexagons for the T_3 lattice (b), or at the same location than the A_2 orbitals for the H_3 lattice (c). The duality transformation $\mathcal{D}$ exchanges the location of the orbitals A_1 and A_2 and the hopping amplitudes symbolized by full/dashed lines. The original T_3 lattice is recovered after an inversion in case (b) whereas the dual and the original lattices coincide for the H_3 lattice in case (c).

$\varphi = \arctan(t_2/t_1)$ reads, in the (A_1, A_2, B) basis:

$$H(\vec{k}) = \begin{pmatrix} 0 & 0 & f(\vec{k})\cos\varphi \\ 0 & 0 & f(\vec{k})\sin\varphi \\ f^*(\vec{k})\cos\varphi & f^*(\vec{k})\sin\varphi & 0 \end{pmatrix}, \tag{4.40}$$

with $f(\vec{k}) = t(1 + \mathrm{e}^{\mathrm{i}\vec{k}.\vec{u}_1} + \mathrm{e}^{\mathrm{i}\vec{k}.\vec{u}_2})$, see Fig. 2.13c. $\vec{u}_1 = \frac{\sqrt{3}\mathrm{a}}{2}(-\vec{e}_x + \sqrt{3}\ \vec{e}_y)$ and $\vec{u}_2 = \frac{\sqrt{3}\mathrm{a}}{2}(\vec{e}_x + \sqrt{3}\ \vec{e}_y)$ are basis vectors of the triangular Bravais lattice. The spectrum does not depend on φ. It consists of a flat band at zero energy $\varepsilon_0(\vec{k}) = 0$ and two dispersive bands $\varepsilon_\pm(\vec{k}) = \pm|f(\vec{k})|$.

In sublattice basis, the eigenstates of (4.40) have the form:

$$\Psi^\pm(\vec{k}) = \frac{1}{\sqrt{2}}\begin{pmatrix} \cos\varphi\ \mathrm{e}^{-\mathrm{i}\theta} \\ \sin\varphi\ \mathrm{e}^{-\mathrm{i}\theta} \\ \pm 1 \end{pmatrix}, \qquad \varepsilon(\vec{k}) = \pm|f(\vec{k})|; \tag{4.41a}$$

$$\Psi^0(\vec{k}) = \begin{pmatrix} -\sin\varphi \\ \cos\varphi \\ 0 \end{pmatrix}, \qquad \varepsilon(\vec{k}) = 0, \tag{4.41b}$$

where $\theta = \arg(f(\vec{k}))$.

The three bands touch at the corners of the first Brillouin zone $\vec{K} = \frac{4\pi}{3\sqrt{3}a}\vec{u}_x$ and $\vec{K}' = -\vec{K}$. In the vicinity of the band touching point $\vec{K}$, the low-energy Hamiltonian reads:

$$H(\vec{K} + \vec{q}) = \hbar v_F \begin{pmatrix} 0 & 0 & q_-\cos\varphi \\ 0 & 0 & q_-\sin\varphi \\ q_+\cos\varphi & q_+\sin\varphi & 0 \end{pmatrix}. \tag{4.42}$$

where we denote $q_\pm = q_x \pm \mathrm{i}q_y$, and with $v_F = 3at/2\hbar$, a is the honeycomb lattice spacing and t the characteristic hopping strength. When $\varphi = 0$ or $\pi/2$ ($t_1 = 0$ or $t_2 = 0$), the 2D Dirac Hamiltonian of graphene is recovered, with an extra flat band acting as a mere spectator.

We have seen in Chapter 2 that the low-energy Hamiltonian of the H_3 model is equivalent to that of graphene with a spectator flat band. Thus, the H_3 model share the same properties, among which the Zitterbewegung.

The T_3 model

The T_3 lattice [Raoux et al., 2014] consists of a honeycomb lattice with one additional site at the center of each hexagon, connected only to one of the sublattices of the honeycomb lattice (see Fig. 4.3 and Fig. 2.13b): it can be seen as two shifted honeycomb lattices sharing one sublattice. The 3×3 Bloch Hamiltonian at wave vector $\vec{k}$ reads:

$$H(\vec{k}) = \begin{pmatrix} 0 & 0 & f(\vec{k})\cos\varphi \\ 0 & 0 & f^*(\vec{k})\sin\varphi \\ f^*(\vec{k})\cos\varphi & f(\vec{k})\sin\varphi & 0 \end{pmatrix} , \tag{4.43}$$

where the function $f(\vec{k})$ has been defined in the previous section, see (4.40). The spectrum is given by: $\varepsilon(\vec{k}) = 0, \pm|f(\vec{k})|$. It is identical to the spectrum of the H_3 model of the previous section.

Let us have a look at the eigenstates of Hamiltonian (4.43). The corresponding wavefunctions read:

$$\Psi^{\pm}(\vec{k}) = \frac{1}{\sqrt{2}} \begin{pmatrix} \cos\varphi\ \mathrm{e}^{-\mathrm{i}\theta} \\ \sin\varphi\ \mathrm{e}^{\mathrm{i}\theta} \\ \pm 1 \end{pmatrix}, \qquad \varepsilon(\vec{k}) = \pm|f(\vec{k})|; \tag{4.44a}$$

$$\Psi^{0}(\vec{k}) = \begin{pmatrix} -\sin\varphi\ \mathrm{e}^{\mathrm{i}\theta} \\ \cos\varphi\ \mathrm{e}^{-\mathrm{i}\theta} \\ 0 \end{pmatrix}, \qquad \varepsilon(\vec{k}) = 0, \tag{4.44b}$$

where $\theta = \arg(f(\vec{k}))$.

The low-energy Hamiltonian expanded around the band touching point $\vec{K}$ reads:

$$H(\vec{K} + \vec{q}) = \hbar v_F \begin{pmatrix} 0 & 0 & q_- \cos\varphi \\ 0 & 0 & q_+ \sin\varphi \\ q_+ \cos\varphi & q_- \sin\varphi & 0 \end{pmatrix} , \tag{4.45}$$

Note that when $t_1 = t_2$, this linearized Hamiltonian can be written in the form $H_{\mathbf{K}}(\mathbf{q}) = \hbar v_F \mathbf{S} \cdot \mathbf{q}$, where S_x, S_y and $S_z \equiv \mathrm{diag}(1, -1, 0)$ satisfy the spin-1 algebra $[S_i, S_j] = \mathrm{i}\epsilon_{ijk} S_k$. Hence the T_3 model realizes a continuous deformation of spin-1 massless fermions.

The current operator along x reads:

$$\hat{j}_x^{\varphi} = \frac{e}{\hbar} \frac{\delta \hat{H}_{\mathbf{k}}}{\delta \hat{k_x}} = e v_F \begin{pmatrix} 0 & 0 & \cos\varphi \\ 0 & 0 & \sin\varphi \\ \cos\varphi & \sin\varphi & 0 \end{pmatrix} . \tag{4.46}$$

As for graphene, we note that it is independent of momentum. Following the reasoning of section 4.1, we can express the time-evolved current operator in a basis of eigenstates of the Hamiltonian (4.45) $(\psi_{\mathbf{k},+}, \psi_{\mathbf{k},0}, \psi_{\mathbf{k},-})$ (with corresponding energies $(\varepsilon_k, 0, -\varepsilon_k)$) :

$$U_{\varphi}^{\dagger} \hat{j}_x(t) U_{\varphi} = \begin{pmatrix} \cos\theta & \frac{\mathrm{i}\sin\theta}{\sqrt{2}} \sin 2\varphi\ \mathrm{e}^{-\mathrm{i}\theta + \mathrm{i}\varepsilon_k t/\hbar} & \mathrm{i}\sin\theta\ \cos 2\varphi\ \mathrm{e}^{-\mathrm{i}\theta + 2\mathrm{i}\varepsilon_k t/\hbar} \\ \frac{-\mathrm{i}\sin\theta}{\sqrt{2}} \sin 2\varphi\ \mathrm{e}^{\mathrm{i}\theta - \mathrm{i}\varepsilon_k t/\hbar} & 0 & \frac{-\mathrm{i}\sin\theta}{\sqrt{2}} \sin 2\varphi\ \mathrm{e}^{\mathrm{i}\varepsilon_k t/\hbar} \\ -\mathrm{i}\sin\theta\ \cos 2\varphi\ \mathrm{e}^{\mathrm{i}\theta - 2\mathrm{i}\varepsilon_k t/\hbar} & \frac{-\mathrm{i}\sin\theta}{\sqrt{2}} \sin 2\varphi\ \mathrm{e}^{\mathrm{i}\varepsilon_k t/\hbar} & -\cos\theta \end{pmatrix} , \tag{4.47}$$

with $(k_x, k_y) = k(\cos\theta, \sin\theta)$. When φ goes to zero, we recover the current operator for graphene (4.33) with a spectator zero-energy band. Similarly to the case of graphene, the current operator exhibits oscillating matrix elements corresponding to interband transitions. But now two different types of transitions occur: between the two dispersive bands, corresponding to terms oscillating at frequency $2\varepsilon_k/\hbar$, as well as transitions between the flat band and one of the dispersive bands, associated to oscillations at frequency $\varepsilon_k/\hbar$. This result could have been anticipated from a simple generalization of the graphene case under addition of an extra flat band. Thus, the Zitterbewegung effect is still present in the T_3 system, irrespective of φ. However, we will see hereafter that for $\varphi \neq 0$ transport properties change drastically, something that could not have been predicted by a mere study of the spectrum.

Energy spectrum - chiral symmetry

The energy spectra $E(\vec{k})$ of the H_3 (4.40) and T_3 (4.40) Hamiltonians are identical. It exhibits the symmetry $E(\vec{k}) \to -E(\vec{k})$ at least locally around the crossing point. This spectrum symmetry naturally originates from a chiral symmetry of the corresponding (low energy) Hamiltonians. This symmetry is represented by a unitary operator C that *anticommutes* with the Hamiltonian: $\mathcal{H} = -C\mathcal{H}C$.

An explicit chiral operator can be defined when considering these pedagogical examples of tight-binding Hamiltonians defined on lattices. In the nearest neighbour approximation, chiral symmetry corresponds to a sub-lattice symmetry: couplings are only present between the two sub-lattices A and B of a bipartite lattice. This is the case of the nearest neighbor description of graphene on the honeycomb lattice. In the case we consider in this chapter, the three orbitals are distributed on three Bravais lattices A_1, A_2 and B of same geometry, as shown on Fig. 4.3. Chiral symmetry originates from the fact that the only couplings t_1, t_2 relevant at low energy are between orbitals on the B and the A_1, A_2 lattices whereas A_1 and A_2 stay uncoupled. The Bloch Hamiltonian in the orbital basis (A_1, A_2, B) takes the general form

$$H(t_1, t_2; \vec{k}) = \begin{pmatrix} 0 & 0 & t_1 f_1(\vec{k}) \\ 0 & 0 & t_2 f_2(\vec{k}) \\ t_1 f_1^*(\vec{k}) & t_2 f_2^*(\vec{k}) & 0 \end{pmatrix} . \tag{4.48}$$

Such a Hamiltonian anti-commutes with a chirality operator $C = \mathrm{diag}(1, 1, -1)$. The complex functions $f_j(\vec{k}) = |f_j(\vec{k})| e^{i\phi_j(\vec{k})}$ encode the geometry of the lattice of couplings, see (4.40). Their amplitudes determine the spectrum of the semimetal: $E_0(\vec{k}) = 0, E_\pm(\vec{k}) = \pm(t_1^2 |f_1(\vec{k})|^2 + t_2^2 |f_2(\vec{k})|^2)^{\frac{1}{2}}$. A three band crossing occurs when f_1 and f_2 vanish simultaneously at a point $\vec{K}$ in the Brillouin zone. Generically, additional crystalline symmetries are required to guarantee this vanishing. In the present paper we assume the existence of these band crossings and study some of their transport properties. In particular, we focus on properties which depend on the phases $\phi_j(\vec{k})$ and which are thus *independent* of the spectrum provided a band crossing occurs.

Quite generally, the linear expansion around the crossing of the chiral symmetric Hamiltonians we consider takes the form

$$H(\vec{K} + \vec{q}) = \begin{pmatrix} 0 & 0 & \Lambda_{11} q_x + \Lambda_{12} q_y \\ 0 & 0 & \Lambda_{21} q_x + \Lambda_{22} q_y \\ \Lambda_{11}^* q_x + \Lambda_{12}^* q_y & \Lambda_{21}^* q_x + \Lambda_{22}^* q_y & 0 \end{pmatrix} . \tag{4.49}$$

Such a Hamiltonian is entirely parametrized by a matrix $\Lambda = \{\Lambda_{ij}\}$ of complex coefficients. The phases of the coefficients Λ_{ij} encode the geometry of the underlying lattice. The low-energy Bloch Hamiltonian of the H_3 model (4.42) takes the form (4.49) with a matrix of coefficients

$$\Lambda_{\mathrm{H}_3} = \frac{3a}{2} \begin{pmatrix} t_1 & -\mathrm{i}t_1 \\ t_2 & -\mathrm{i}t_2 \end{pmatrix} . \tag{4.50}$$

For the T_3 model (4.45),

$$\Lambda_{\mathrm{T}_3} = \frac{3a}{2} \begin{pmatrix} t_1 & -\mathrm{i}t_1 \\ t_2 & \mathrm{i}t_2 \end{pmatrix} , \tag{4.51}$$

The constraint from the lattice on these phases must be independent of the amplitude of couplings between the orbitals. Hence it cannot result in a symmetry of the Hamiltonian which affects energies: in section 4.2.4 we show that it corresponds to a duality in a manner analogous to the Kramers-Wannier duality of statistical mechanics [Kramers and Wannier, 1941]. We now characterize both the topological Berry phase associated with the band crossing, as well as the electronic transport properties around the crossing, which turn out to be correlated and associated to the duality class of the semi-metal.

4.2.2 Transport study

Transport measurements constitute a powerful tool to probe the physical properties in the vicinity of the Fermi energy. We will show that close to the band crossing electronic transport is related to the phases $\phi_i(\vec{k})$ entering the Hamiltonian in (4.48) and not to the spectrum. As we recalled in section 4.1, the conductivity of graphene remains finite at the band crossing, despite a vanishing density of states. This result was first derived by considering the conductivity of a narrow strip of graphene between two contact electrodes as shown on Fig. 4.4.

Let us consider an analogous setup for a three band chiral semimetal, *i.e.* a finite sample of length L and width W. The conductance of a narrow sample is conveniently calculated from the set of the transmission probabilities T_n of the conduction channel labelled by n through the Landauer formula (4.1). The longitudinal conductivity σ is related to this conductance as $\sigma = LW^{-1}G$. The explicit calculation of the transmission probabilities T_n requires solving the Schrödinger equation piecewise and matching the solutions at the boundaries of the sample.

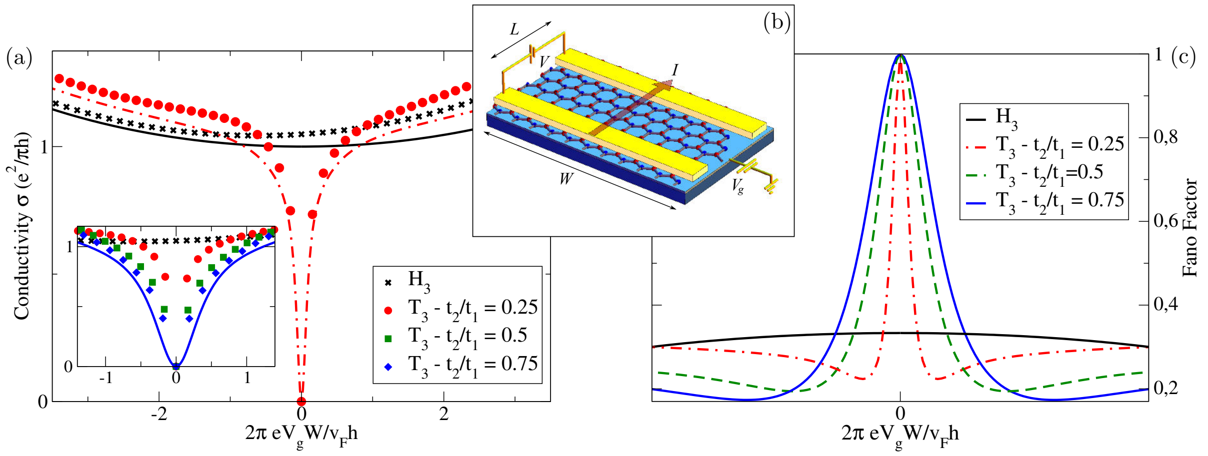

Figure 4.4: Conductivity (a) and Fano factor (c) as a function of a gate potential V_g applied to the sample in the geometry represented in (b). The inset in (a) shows a zoom on the region of the crossing. Results for nearest neighbour lattices models on the H$_3$ and T$_3$ lattices are shown. They are independent on the coupling amplitudes for the H$_3$ model, but depend on these couplings for the T$_3$ model, as illustrated by a choice of three ratio t_2/t_1. The symbols correspond to the results of a numerical Landauer approach on a system of size $L = 20, W = 100$ in units of lattice spacing a. The curves correspond to analytical results of a continuous description around a single cone.

Heuristic argument for transport through evanescent states

Confinement of the sample between the leads gives rise to zero-energy evanescent states. At the band crossing, the conductivity depends entirely on the nature of these evanescent states. Prior to an explicit calculation of the conductivity, it is instructive to consider the current operator $j_x(\vec{k}) = \langle \partial_{k_x} H(\vec{k}) \rangle_\psi$ defined from the tight-binding Bloch Hamiltonian (4.48). Introducing the amplitudes $(\psi_{A_1}, \psi_{A_2}, \psi_B)$ of the electronic wavefunction in the three sub-lattices the longitudinal current can be expressed as

$$j_x(\vec{k}) = 2 \text{ Re} \left[\psi_B(\vec{k}) \left(\sum_i \partial_{k_x} f_i(\vec{k}) \psi^*_{A_i}(\vec{k}) \right) \right] \tag{4.52}$$

and is found to be proportional to the amplitude ψ_B on the B sub-lattice [Häusler, 2015]. This hints that electronic transport at the band crossing will occur provided the zero-energy evanescent modes have a non-vanishing component on the B sub-lattice.

Analytical Landauer approach

As expected from the previous qualitative argument, the existence of a finite minimal conductivity at the threefold band crossing point is uniquely determined by the non vanishing weight of the wave function on the hub lattice B as we have checked using a Landauer description of transport in Appendix C.2.1. From (4.49), this component is found to satisfy

$$\Lambda . \begin{pmatrix} q_x \\ q_y \end{pmatrix} \psi_B = 0 \ . \tag{4.53}$$

Hence a necessary condition for the existence of a non-vanishing minimal conductivity at the band crossing is simply $\det \Lambda = 0$. This condition is satisfied for the H$_3$ lattice model, and the minimal conductivity corresponds exactly to the value $\sigma^{(\min)} = e^2/(\pi h)$ predicted for graphene. In contrast, for the T$_3$ model the conductivity vanishes $\sigma^{(\min)} = 0$. Beyond the minimal conductivity, the fluctuations of this conductivity can also be considered : their amplitude is encoded in the ratio between the shot noise power and the averaged current, the so-called Fano factor. This Fano factor is related to the transmission coefficients as $F = \sum_n T_n(1 - T_n)/\sum_n T_n$. We find that this factor F takes a constant value $F = 1/3$ for the H$_3$ model, a value already encountered in graphene [Tworzydło et al., 2006] and characteristic of diffusive metals [Beenakker, 1997]. Such a result demonstrates that for all semi-metals in this class the transport through perfectly clean narrow junctions displays the characteristic features of diffusive metals.

Numerical Kwant study

We have evaluated the conductivity of different lattice models in the geometry of Fig. 4.4. We compare the analytical results to a numerical Landauer approach to check for possible inter-crossing point effects, neglected in the analytical approach. Numerical calculations were performed using the Kwant code [Groth et al., 2014], based on a Green function recursive technique to evaluate the transmission amplitude across a sample. Typical samples of dimensions $L = 20$, $W = 100$ in lattice units were considered, with semi-infinite one-dimensional chains modelling the leads. A good agreement is found between both approaches. The results for the H_3 model are shown as a function of the Fermi-energy, or gate potential V_g on Fig. 4.4: the conductivity exhibits a plateau around the band crossing point $V_g = 0$, corresponding to $\sigma = e^2/(\pi h)$. The results of a similar study for the T_3 model are also shown on Fig. 4.4 and display a collapse of the conductivity around the band crossing point $V_g = 0$ for three different values of the couplings between orbitals (Inset). Fig. 4.4 displays the analytical results for the dependence of the Fano factor on the gate potential V_g. We show that for the T_3 model $F(V_g = 0) = 1$, whereas for the H_3 model the Fano factor reaches the value $F = \frac{1}{3}$ at the band crossing, characteristic of a disordered metal.

A word on the linear response - Kubo conductivity

Finally, let us mention that for graphene the result of the Landauer formula for a narrow junction can be recovered for a long junction by an approach based on the Kubo formula, see section 4.1.1. While this equivalence remains valid for the H_3 model, it does not hold for the T_3 model: we found that the Kubo conductivity diverges at the band crossing (see Appendix C.2.2), as opposed to the vanishing Landauer conductivity for a narrow junction, in agreement with a previous result in the disordered limit [Vigh et al., 2013].

4.2.3 Topological Berry winding around a band crossing

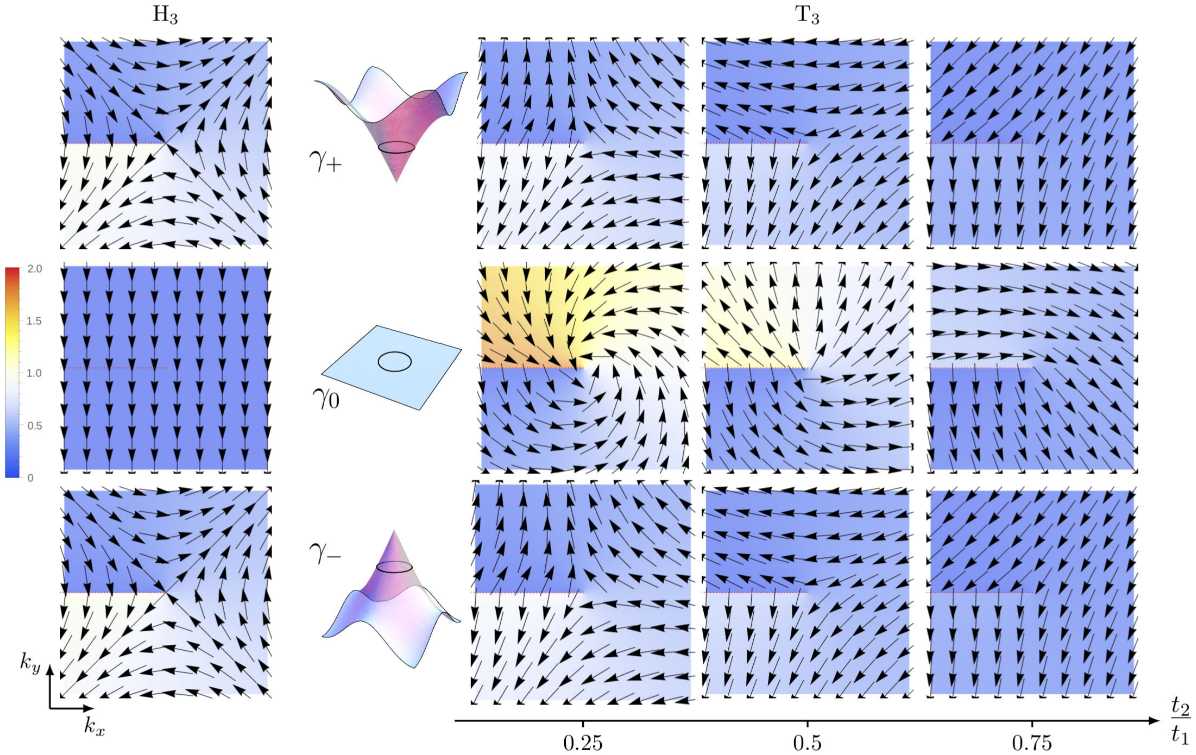

Figure 4.5: The Berry phase acquired by eigenstates around the band crossing point is shown for the three energy levels $n = -, 0, +$ for nearest neighbours models on the T_3 (Right) and on the H_3 model (Left). For the H_3 lattice model, the Berry phase γ_n is independent on the coupling amplitudes t_1, t_2 : it is quantized. The windings by $\pm\pi$ in the $\pm$ bands signals the presence of topological Berry vortices at the band crossing points. This is not the case for the T_3 lattice model: the Berry phase continuously depends on the ratio of hopping amplitudes t_2/t_1 for all bands and is not topological.

Let us now consider another characterization of the band crossings. When evolved along a closed loop in momentum space, Bloch eigenstates can acquire a geometrical Berry phase. Moreover, band touching points act as sources of this Berry phase in two dimensions: it is natural to characterize these points by the Berry phases acquired by the different eigenstates around it. In two dimensions these phases are independent of the choice of loop winding once around the point $\vec{K}$, and are defined as:

$$\gamma_n(\vec{K}) = \frac{-i}{\pi} \oint d\vec{q}.\langle \Psi_n | \vec{\nabla}_{\vec{q}} | \Psi_n \rangle \ . \tag{4.54}$$

Besides being only dependent on the homotopy class of the loop around $\vec{K}$, these Berry phases can also be robust against perturbations of the Hamiltonian which do not lift the band crossing, such as in graphene. In such cases, they are called *topological Berry phases*. Such a robustness occurs when this Berry winding is quantized. Note that one has to distinguish the topological nature of such a Berry phase from the protection of such a band crossing which generically involves consideration of crystalline symmetries like in graphene. In the following, we will consider general perturbations of Hamiltonians which preserve both the chiral symmetry and the band crossing, irrespective of the existence of additional symmetries.

Figure 4.5 shows the phase winding of Bloch eigenstates Ψ_n around the nodal point for the H_3 model and for the T_3 model. The $\vec{k}$ dependence of the phase is represented by vectors in the two-dimensional momentum space. The colour scale gives the accumulated phase with respect to the negative k_x semi-axis. A clockwise vortex corresponds to a winding of π, *i.e.* to a Berry phase 1. Eigenstates of the H_3 model (4.50) are characterized by Berry phases $\gamma_\pm = -1$, $\gamma_0 = 0$ as shown in Fig. 4.5. These Berry phases are in particular robust to variations of hopping amplitudes t_1, t_2. Remarkably for the T_3 model (4.51), while the Berry phases γ_n are still independent of the path winding, they are shown to vary continuously upon variation of the ratio t_2/t_1 of nearest neighbour couplings, in agreement the results of a previous study by Raoux et al.[Raoux et al., 2014] (see also Appendix C.1.1). In particular, they generically take non quantized values as illustrated by the discontinuity of the vector field.

We find that the Berry phase is quantized in the H_3 model, while it is not robust in the T_3 model. We have seen in section 4.2.2 that the conductivity at the crossing is finite in the H_3 model but vanishes in the T_3 model. We will see below that there is a correlation between the existence of a finite conductivity at the crossing and the robust Berry winding.

4.2.4 Duality

Since the Berry windings are a property of the band crossing solely, they can be conveniently computed from the low energy Hamiltonian(4.49). We find that these windings are topological only when:

$$\frac{\Lambda_{12}}{\Lambda_{11}} = \frac{\Lambda_{22}}{\Lambda_{21}} \equiv \lambda \ . \tag{4.55}$$

The only semimetals characterized by a topological Berry winding are those which fulfil the condition (4.54), with values

$$\gamma_+ = \gamma_- = \operatorname{sgn} \operatorname{Im} \lambda \quad , \quad \gamma_0 = 0 \ . \tag{4.56}$$

Note that these values are defined modulo a gauge choice for the wavefunctions of the different bands. The calculations are detailed in Appendix C.1.1: we find that the quantized Berry windings γ_+, γ_- are stable with respect to any perturbation compatible with the duality constraint detailed below, *i.e.* which does not break the geometry of the underlying lattice. In contrast, for any chiral symmetric semimetal which does not verify (4.54), the Berry phase can take any real value and depends continuously on deformations of the Hamiltonian.

The constraint (4.54) is fulfilled for a specific class of three-orbitals lattice models. It is a manifestation of a geometric property of the lattice, distinct from a symmetry, which encodes a constraint on the phase of complex parameters Λ_{ij} in (4.49).

The geometry of the lattice can be described by two vectors $\vec{e}_1$ and $\vec{e}_2$ relating a vector of the lattice B to neighbour sites of the A_1 and A_2 lattices, as shown on figure 4.3. The duality transformation $\mathcal{D}$ exchanges the lattices A_1 and A_2, or equivalently the vectors $\vec{e}_1$ and $\vec{e}_2$, while simultaneously exchanging the couplings between B and A_1 orbitals with couplings between B and A_2 orbitals. Quite generally, this duality is an involutive transformation *i.e.* $\mathcal{D}^2 = \mathbf{I}$ which relates a Hamiltonian $\mathcal{H}$ on a lattice $\mathcal{L}$ to a Hamiltonian $\tilde{\mathcal{H}}$ on a *different* lattice $\tilde{\mathcal{L}}$. However, on symmetric lattices where initial and dual lattices $\mathcal{L}, \tilde{\mathcal{L}}$ are related by a geometrical transformation $\mathcal{R}$, this duality translates into constraints on Hamiltonians defined on the same lattice (or same Hilbert space). In this case, and focusing for simplicity on nearest neighbour Hamiltonians, the duality transformation can be recast into the form

$$(DU)H(t_2, t_1; \mathcal{R}\vec{k})(DU)^{-1} = H(t_1, t_2; \vec{k}) \tag{4.57}$$

where U is a unitary operator, $\mathcal{R}$ is the symmetry relating initial and dual lattices and D the operator swapping A_1 and A_2 orbitals:

$$D = \begin{pmatrix} 0 & 1 & 0 \\ 1 & 0 & 0 \\ 0 & 0 & 1 \end{pmatrix} . \tag{4.58}$$

A very special case, which we call the duality class $\mathcal{D}_{\mathrm{I}}$ corresponds to the situation where two orbitals lie on the same site, *i.e.* when $\vec{e}_1 = \vec{e}_2 \neq \vec{0}$. In this class, the duality transformation simplifies and U and $\mathcal{R}$ reduce to the identity. In this case, Bloch Hamiltonians encode the geometrical properties of a bipartite lattice, whereas in the other case, which we denote the duality class $\mathcal{D}_{\mathrm{II}}$, the underlying lattices are either Bravais lattices or possess three distinct sublattices. This duality restricts the form of the chiral tight-binding Hamiltonian (4.48): in the class $\mathcal{D}_{\mathrm{I}}$ we have $f_1(\vec{k}) = f_2(\vec{k})$ while a much weaker constrain $f_1(\vec{k}) = f_2(\mathcal{R}\vec{k})$ holds in class $\mathcal{D}_{\mathrm{II}}$ for symmetric lattices. Specifying this constraint to a local Bloch Hamiltonian (4.49) around a three band crossing, the duality in class $\mathcal{D}_{\mathrm{I}}$ implies the condition (4.54) while generically it only relates Hamiltonians at different crossing points in class $\mathcal{D}_{\mathrm{II}}$.

The H_3 model 4.50 belongs to class $\mathcal{D}_{\mathrm{I}}$. It verifies condition 4.54 with $\lambda = -\mathrm{i}$. The T_3 model 4.51 belongs to the duality class $\mathcal{D}_{\mathrm{II}}$, with the inversion $\mathcal{R}\vec{k} = -\vec{k}$ relating initial and dual lattices.

We have seen that Hamiltonians belonging to the duality class $\mathcal{D}_{\mathrm{I}}$ describe the only three-band semimetals possessing quantized topological Berry windings. They are also those whose conductivity does not vanish at the band crossing and display a pseudo-diffusive regime: indeed the condition $\det \Lambda = 0$ is equivalent to the duality constraint (4.54) defining the class $\mathcal{D}_{\mathrm{I}}$: the only three band semi-metals with a non-vanishing minimal conductivity belong to this duality class $\mathcal{D}_{\mathrm{I}}$. Reciprocally, any model in this duality class has a finite minimal conductivity, as shown in Appendix C.2.1.

4.3 Bulk plane wave states - Evanescent states correspondence

As follows from our results, the occurrence of a transport regime at the band crossing with a non vanishing conductivity through evanescent modes is not a generic property of linear dispersion relations near this crossing nor a hallmark of relativistic physics of the associated electronic excitations such as the Zitterbewegung, chiral symmetry or pseudo-spin structure. However, at least for three-band models with chiral symmetry in two-dimensions, a non-vanishing conductivity is surprisingly found to be related to a quantized Berry phase of the Bloch bands. This result highlights a new connection between the nature of evanescent states (and associated minimal conductivity) and a topological property (topological Berry phase) of wave-like eigenstates. This evanescent-bulk states correspondence is reminiscent of the standard bulk-edge correspondence in topological insulating phases.

In topological insulators, the existence of a non trivial topological invariant associated to the Bulk plane wave states encodes for the presence of protected edge states at the boundary of the insulator. There is a connection between a bulk property of plane wave states and the existence of metallic edge states. Here in semimetallic systems we found a correspondence between a property of bulk plane-wave states, namely the robustness of the Berry phase around the crossing, and the nature of evanescent states which manifests as a finite minimal conductivity.

Our study showed that the minimal conductivity allows to probe properties of electronic excitations not included in the spectrum. Through the study of evanescent modes, one can discriminate between systems with different transport properties. They open perspectives for the understanding of evanescent states in semi-metals, in relation with physical properties of these systems like conductance or shot noise. Along the same lines, we have extended our analysis to a band crossing described by the simple Hamiltonian $H(\vec{q}) = S_x q_x + S_y q_y$, with S_x, S_y satisfying a spin-S algebra.[Dóra et al., 2011] Again, we find that the Berry topological winding and the minimal conductivity are correlated and vanish for integer spin S. Interesting perspectives for future studies would be to investigate for possible extensions of this bulk-evanescent states correspondence beyond 2D or chiral symmetric systems.

Chapter 5

Magnetotransport Close to the Nodal Point in Weyl Junctions

We have seen in section 1.3 that one of the most remarkable hallmarks of 3D massless relativistic particles is the chiral anomaly. This chiral anomaly manifests itself as an anomalous electromagnetic response, leading to the propagation of a chiral current in the presence of parallel electric and magnetic fields. The chiral anomaly, once a theoretical object of studies for high energy physicists, has become an object of great interest for many condensed matter physicists with the recent advent of bulk Weyl and Dirac materials. The experimental realization of these relativistic semimetals has opened perspectives to probe the chiral anomaly on solids via transport experiments. Many theoretical [Nielsen and Ninomiya, 1983, Son and Spivak, 2013] and experimental [Xiong et al., 2015, Huang et al., 2015] studies of this effect exist in the literature. Existing experimental studies have focused on the diffusive transport regime where the chiral anomaly is expected to manifest itself as a quadratic, positive contribution to the longitudinal magnetoconductivity. Here, we propose another, experimentally relevant and conceptually simpler way to probe it. We consider ballistic, intrinsically out of equilibrium Weyl junctions. In our setup, we obtain a clear signature of the chiral anomaly: the chiral current can be directly measured in the high field regime as a linear magnetoconductance.

We start this chapter by introducing the notions of chiral symmetry and chiral anomaly in section 5.1. We recall the consequences of the chiral anomaly in transport and give a non exhaustive review of the existing literature on its detection. In section 5.2, we present our setup and comment on our analytical and numerical Landauer study of the ballistic magnetotransport of Weyl fermions. We discuss our results in relation to the dispersion of the relativistic Landau Levels and identify the contribution of the chiral current. We complete the study with a semi-classical description of transport that allows us to account for weak disorder effects. Then we discuss our results in section 5.3 and conclude in section 5.4.

5.1 Introduction

5.1.1 Chiral symmetry, chiral anomaly

Relativistic Fermions in 3D are described by the Dirac Hamiltonian

$$H_{\mathrm{Dirac}} = c\,\boldsymbol{\alpha}\cdot\mathbf{p} + mc^2\beta, \tag{5.1}$$

where α_i and β are four by four matrices. In the Weyl representation, the α_i matrices are block diagonal and the Hamiltonian reads

$$H_{\mathrm{Dirac}} = c\begin{pmatrix} -\sigma_i & 0 \\ 0 & \sigma_i \end{pmatrix} p_i + mc^2\begin{pmatrix} 0 & \mathbb{1} \\ \mathbb{1} & 0 \end{pmatrix}. \tag{5.2}$$

In the massless case $m = 0$, the Hamiltonian becomes block diagonal. The eigenvalue equation can be solved separately in the two blocks. This property of the massless Dirac Hamiltonian manifests as a symmetry, the chiral symmetry:

$$\gamma_5\, H^{m=0}_{\mathrm{Dirac}} \;=\; H^{m=0}_{\mathrm{Dirac}}\,\gamma_5, \qquad \gamma_5 = \begin{pmatrix} -\mathbb{1} & 0 \\ 0 & \mathbb{1} \end{pmatrix}. \tag{5.3}$$

Indeed, the four-component massless Dirac spinors decompose as

$$\psi = \chi_R + \chi_L, \text{ with } \chi_{R/L} = \frac{1 \pm \gamma_5}{2}\psi. \tag{5.4}$$

Note that this decomposition (5.4) is independent of the choice of representation for α_i and β matrices. $\chi_{R/L}$ are chiral (Left/Right) Weyl fermions, eigenstates of the (Left/Right) Weyl Hamiltonian

$$H^\chi = U_\chi^\dagger H_{\mathrm{Dirac}} U_\chi, \qquad U_{\chi=L/R} = \frac{1 \pm \gamma_5}{2}. \tag{5.5}$$

The Weyl Hamiltonian reads

$$H^\chi_{\mathrm{Weyl}} = \chi c \boldsymbol{\sigma}\mathbf{p}, \qquad \chi = \pm. \tag{5.6}$$

Thus, when 3D relativistic particles become massless, they acquire an additional symmetry, the chirality. Because of the chiral symmetry, Weyl fermions can only be created or annihilated by pairs of opposite chirality. In solids, Weyl cones come by pair of valleys with opposite chirality, corresponding to an opposite Berry monopole charge, see section 1.3. In the history of relativistic quantum physics, this chiral symmetry is associated with one of the major surprises of the development of field theory: a quantum anomaly. With the development of quantum field theory, physicists have discovered that classical symmetries, i.e. transformations that left the action invariant, were not necessarily conserved at the quantum level, i.e. they may not leave the path integral invariant [Zee, 2003]. Thus, while this chirality is a conserved quantity of the Hamiltonian, it is no longer conserved by the associated field theory. Historically, the discovery of this anomaly provided an explanation for the observed decay of a neutral pion into two photons. This very intriguing and unanticipated property was called a chiral anomaly, or Adler-Bell-Jackiw anomaly [Adler, 1969, Bell and Jackiw, 1969].

5.1.2 Consequences on transport

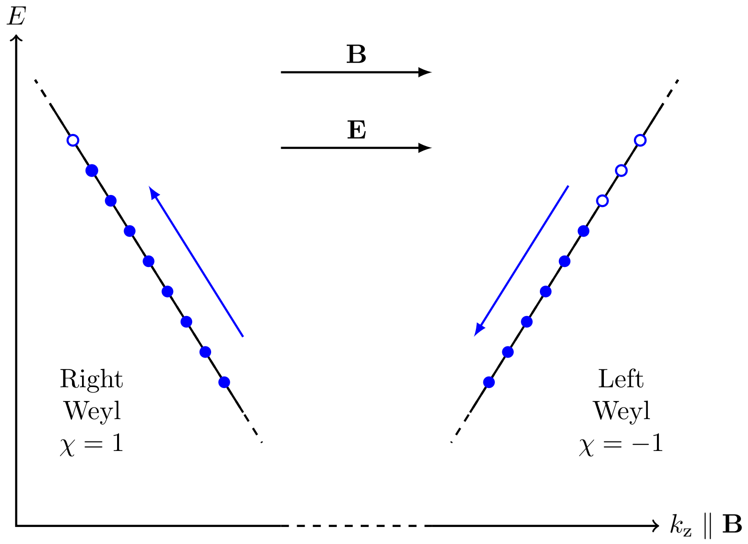

Figure 5.1: *1D Chiral Anomaly:* charged Weyl fermions disperse unidirectionally under a magnetic field. Filled (resp. empty) circles represent occupied (resp. unoccupied) Landau levels. A chiral current of Weyl fermions is created when an electric field is applied parallel to the magnetic field.

How does this anomaly manifests? The breakdown of the chiral symmetry implies that the number of left-right chiral fermions $n_5 = n_R - n_L$ is not a conserved quantity. Physicists have looked for measurable consequences of this anomaly and found that the chiral anomaly induces an anomalous electromagnetic response, corresponding to an anomalous term in Maxwell equations [Kharzeev, 2014]. In particular, it was realized that, in the presence of a magnetic field, an applied parallel electric field could pump particles from one chirality sector into the other in absence of any explicit coupling term in the Hamiltonian. This pumping leads to the generation of a chiral current. To derive the expression of this chiral current consider charged chiral massless Weyl fermions under a magnetic field **B**. The presence of the magnetic field constrains the motion in the transverse directions, while the particle propagates in the direction of the field z. The 1D dispersion is parallel or anti-parallel to the field depending on the chirality: $E = \chi\hbar v k_z$ where $\chi = \pm 1$ for Right/Left-handed Weyl. When an parallel electric field $\mathbf{E} = E\ \hat{\mathbf{z}}$ is applied, the electrons are pushed along the electric field according to

$$\hbar\frac{dk_z}{dt} = -eE. \tag{5.7}$$

Fig. 5.1 shows that the motion of electrons along the field induces a change rate of the density of Right-handed fermions n_R following

$$\frac{dn_R}{dt} = \frac{eB}{h}\frac{1}{2\pi}\left(-\frac{dk_z}{dt}\right) = \frac{e^2}{h^2}EB. \tag{5.8}$$

The term eB/h in (5.8) comes from the degeneracy of Landau levels, and the $1/2\pi$ term corresponds to the 1D density of states in momentum space. Similarly, we find for the Left-handed Weyl fermions $\dot{n}_L = -\dot{n}_R = -\frac{e^2}{h^2}EB$, leading to

$$\frac{d(n_R - n_L)}{dt} = 2\frac{e^2}{h^2}EB. \tag{5.9}$$

Note that the presence of the chiral current (5.9) does not violate the principle of conservation of the electric charge: while $\dot{n}_R - \dot{n}_L \neq 0$, we still have $\dot{n}_R + \dot{n}_L = 0$. The total number of charged particles is conserved.

5.1.3 Detection of the chiral anomaly

The Weyl Hamiltonian (5.9) was first thought to describe massless neutrinos. Later it was found that neutrinos have a finite mass, and Weyl fermions remained a theoretical object until the recent discovery of Weyl and Dirac semimetals, see Section 1.3. In Weyl semimetals, the Fermi level lies close to a linear crossing between energy bands. Near the crossing, electrons behave like massless relativistic particles. The low-energy Hamiltonian describing a two-band crossing in a Weyl semimetal is the Weyl Hamiltonian (5.6) with the Fermi velocity playing the role of the speed of light c. Thus, Weyl crossings have a given chirality, and Weyl valleys come by pairs. It then became possible for condensed matter physicists to probe the consequences of the chiral anomaly, which should manifest as a chiral current between Weyl valleys.

Positive magnetoconductivity

Detecting the chiral current (5.9) is not trivial. Indeed, the chiral current can be non zero while the charge current is zero: $j_5 = -e\frac{d(n_R - n_L)}{dt} = -2\frac{e^3}{h^2}\mathbf{E}\cdot\mathbf{B}$ but $j = -e\frac{d(n_R + n_L)}{dt} = 0$.

Besides, the charge pumping phenomena described in the previous section (5.9) will drive the system far out of equilibrium and must be equilibrated for the system to reach a steady state.

Existing studies of the chiral anomaly in Weyl or Dirac semimetals consider the linear response of Weyl samples in the diffusive regime, where energy relaxation occurs within a Weyl cone and intercone scattering induces momentum relaxation between the cones. As detailed below, in this regime the chiral anomaly manifests as a positive quadratic longitudinal magnetoconductivity [Nielsen and Ninomiya, 1983, Son and Spivak, 2013, Burkov, 2015]

$$\sigma(B) = \sigma(B = 0) + \frac{4\tau'}{\nu_0}\frac{e^4}{h^4}B^2, \tag{5.10}$$

where τ' is the momentum relaxation time from scattering between Weyl valleys. In conventional solids the longitudinal magnetoconductivity is negative. Hence a proposed signature of the chiral anomaly is a positive longitudinal magnetoconductivity, quadratic in B, and with an $\mathbf{E}\cdot\mathbf{B}$ angular dependence. The effect is maximum when **E** and **B** are aligned, yielding (5.10). It vanishes when **E** and **B** are perpendicular.

Derivation from Chiral Current Nielsen and Ninomiya where the first to predict a positive magnetoconductivity as a consequence of the chiral anomaly on a lattice [Nielsen and Ninomiya, 1983]. In the diffusive regime, when the intravalley scattering is much stronger than intervalley scattering, momentum

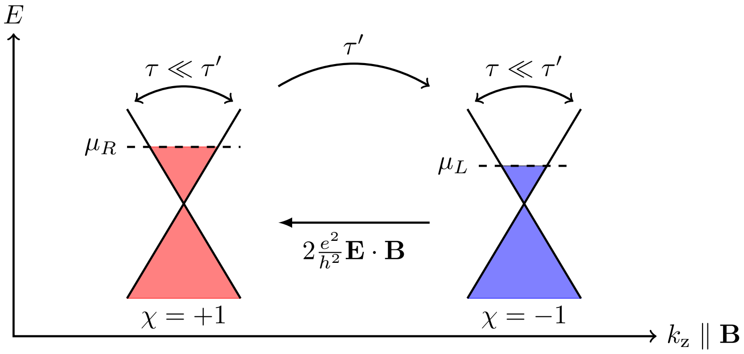

Figure 5.2: In the diffusive regime, the charge pumping $\dot{n}_R - \dot{n}_L = 2e^2/h^2\mathbf{E}\cdot\mathbf{B}$ between Weyl cones is balanced by scattering between the cones, characterized by τ'. Relaxation occurs within the cones with relaxation time $\tau \ll \tau'$.

relaxation occurs within each Weyl valley. Intervalley scattering and the anomalous chiral current (5.9) equilibrate to reach a non equilibrium steady state following

$$\frac{d(n_R - n_L)}{dt} = 0 = 2\frac{e^2}{h^2}\mathbf{E}\cdot\mathbf{B} - \frac{1}{\tau'}(n_R - n_L). \tag{5.11}$$

The resulting imbalance between the right and left valleys gives a chemical potential imbalance

$$\mu_R - \mu_L = \frac{1}{\nu_0}(n_R - n_L) = \frac{2\tau'}{\nu_0}\frac{e^2}{h^2}\mathbf{E}\cdot\mathbf{B}, \tag{5.12}$$

with ν_0 the electronic density of states near the Fermi level.

The anomalous chiral current causes a transfer of electrons from the Right to the Left valley at a rate $2\frac{e^2}{h^2}\mathbf{E}\cdot\mathbf{B}$ (5.9). The energy cost associated with the charge transfer between the two Weyl valleys is given by (5.12). This energy must be extracted from the electric field following the energy balance

$$\mathbf{j}\cdot\mathbf{E} = 2\frac{e^2}{h^2}\mathbf{E}\cdot\mathbf{B}(\mu_R - \mu_L), \tag{5.13}$$

leading to

$$\mathbf{j} = \frac{4\tau'}{\nu_0}\frac{e^4}{h^4}(\mathbf{E}\cdot\mathbf{B})\mathbf{B}. \tag{5.14}$$

The current (5.14) then gives the quadratic magnetoconductivity (5.10) through Ohm's law $\mathbf{j} = \sigma\mathbf{E}$.

Derivation from Berry Curvature and Semiclassical Equation of Motion An alternative derivation of the positive magnetoconductivity (5.10) relies on a semi-classical description of transport including Berry curvature effects [Son and Spivak, 2013]. The Weyl Hamiltonian (5.6) has energies $\varepsilon_{\alpha=\pm}(\mathbf{k}) = \alpha\hbar c k$ and eigenstates $|u_{\chi,\alpha,\mathbf{k}}\rangle$. Let us consider band electrons: their Berry curvature is

$$\Omega_{\chi\mathbf{k}} = i\langle\partial_{\mathbf{k}}u_{\chi,\alpha,\mathbf{k}}| \times |\partial_{\mathbf{k}}u_{\chi,\alpha,\mathbf{k}},\rangle = \chi\frac{\mathbf{k}}{2k^3}\ . \tag{5.15}$$

The presence of the Berry curvature modifies the semiclassical equations of motion, according to [Xiao et al., 2010]

$$\dot{\mathbf{r}} = \frac{1}{\hbar}\frac{\partial\varepsilon}{\partial\mathbf{k}} - \dot{\mathbf{k}}\times\mathbf{\Omega}, \tag{5.16}$$

$$\hbar\dot{\mathbf{k}} = -\frac{\partial\varepsilon}{\partial\mathbf{r}} - e\dot{\mathbf{r}}\times\mathbf{B}. \tag{5.17}$$

In the absence of an electric field, corresponding to $\partial_{\mathbf{r}}\varepsilon = 0$, and using the notation $\mathbf{v}^{(0)}_{\mathbf{k}} = \hbar^{-1}\partial_{\mathbf{k}}\varepsilon = v\hat{k}$, the modified electronic velocity $\mathbf{w}_{\chi,\mathbf{k}}$ reads

$$\mathbf{w}_{\chi,\mathbf{k}} = \left(\mathbf{v}^{(0)}_{\mathbf{k}} + \frac{e}{\hbar}(\mathbf{v}^{(0)}_{\mathbf{k}}\cdot\mathbf{\Omega}_{\chi,\mathbf{k}})\mathbf{B}\right) = v\hat{k} + \chi\frac{ev}{\hbar}\frac{\mathbf{B}}{2k^2}. \tag{5.18}$$

In the literature, the anomalous velocity (5.10) has been derived by solving the Boltzmann equation with this modified velocity [Son and Spivak, 2013]. The anomalous magnetoconductance is thus related to the topological Berry curvature: this confirms the relation between the chirality and the Berry topological charge of Weyl particles, see section 2.1.4.

Experimental probe of the chiral anomaly

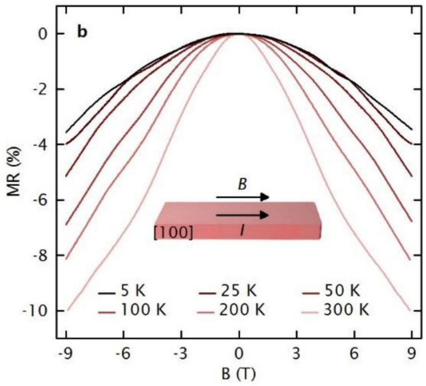

Figure 5.3: Longitudinal magnetoresistance of Weyl semi-metal NbP measured in parallel electric and magnetic fields, for various temperatures. A negative longitudinal magnetoresistance is observed up to room temperature [Niemann et al., 2016].

On the experimental side, the magneto-conductance was studied in various materials that were identified as candidates for this relativistic physics, including Dirac semi-metals Cd_3As_2 [Li et al., 2016], Na_3Bi [Xiong et al., 2015], and Weyl semi-metals TaAs [Huang et al., 2015], NbP [Niemann et al., 2016].

The results for Na_3Bi [Xiong et al., 2015] have been introduced in Fig. 1.13. In this Dirac semi-metal, the presence of the magnetic field breaks time-reversal symmetry and splits the Dirac cone into a pair of Weyl cones. Magnetoconductance measurements have been carried at $T = 4.5K$, for fields up to $B = 4$T oriented at angles ϕ ranging from 0 to 90° with respect to the current direction. When the field is aligned with, or close to the direction of the current, $\phi < 40°$, the observed conductance is positive with a B^2 dependence for low magnetic fields. When the field is perfectly aligned, no saturation of the magnetoconductance has been detected up to $B = 4$T. When the angle ϕ increases, the magnetoconductance saturates at lower and lower fields before decreasing. For $\phi > 60°$ the magnetoconductance is negative even for small fields.

Figure 5.3 shows longitudinal conductance results for Weyl semi-metal NbP [Niemann et al., 2016], for parallel electric and magnetic fields, and various temperatures ranging from cryogenic temperatures $T = 5$K to room temperature $T = 300$K. NbP is a non centro-symmetric Weyl semi-metal of the TaAs family, see section 1.3. Shifting the Fermi Energy by Ga-doping, well-separated Weyl cones located 5meV are obtained, which can contribute to an anomalous negative magneto resistance. The current measured in a 50µm × 2.46µm × 526nm Ga-doped NbP microribbon, see Fig. 5.4a. A negative magnetoresistance is observed up to room temperature. An enhancement of the negative magnetoresistance effect is even observed with increasing temperature, which the authors attribute to an ionization effect of Ga that brings the Fermi level closer to the Weyl points. Fig. 5.4b shows that the magneto-conductance reaches a linear regime at high fields, attributed to the contribution from a single occupied Landau level.

In these compounds, the positive magneto-conductance for a parallel magnetic field, as well as its sensitivity to the orientation of the magnetic field with respect to the electric field, were taken as manifestations of the underlying chiral anomaly of the relativistic massless equations of motion. However, there is no consensus on whether the positive magnetoconductance observed is a unique signature of the chiral anomaly [Armitage et al., 2018].

5.2 Chiral anomaly in ballistic transport

How can one unambiguously detect the chiral anomaly in Weyl semimetals? We propose to study the longitudinal magneto-conductance of ballistic junctions made with Weyl semi-metals in the regime where

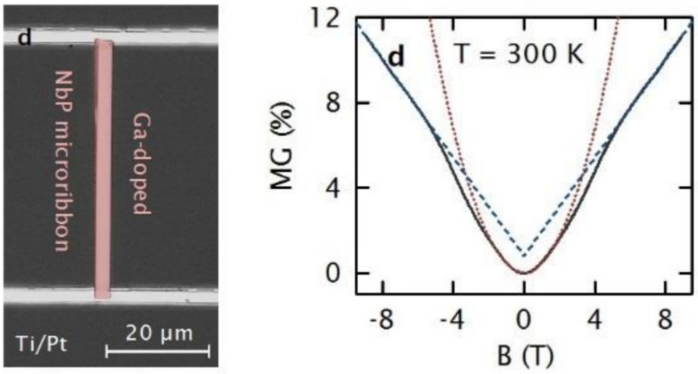

(a) (b)

Figure 5.4: (a) Crystalline structure of Weyl material NbP. (b) Room temperature longitudinal magnetoconductance measured when the magnetic field is applied parallel to the direction of the current [Niemann et al., 2016].

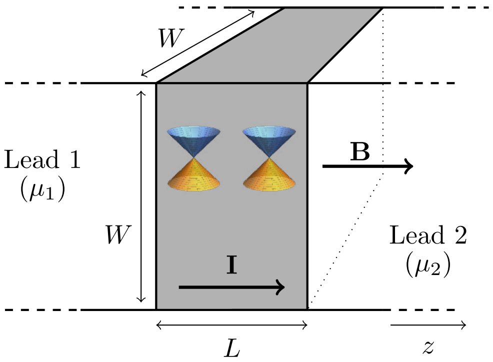

Figure 5.5: Schematic representation of a short junction of a Weyl semi-metal between two metallic leads at chemical potentials μ_1, μ_2, and submitted to a magnetic field $\mathbf{B}$ parallel to the direction of the current $\mathbf{I}$.

equilibration takes place only in the leads. This corresponds to so-called cold electrons, by contrast with the hot-electron regime of Refs. [Son and Spivak, 2013, Burkov, 2014, Burkov, 2015], where energy relaxation occurs within the conductor. The conceptual simplicity of the ballistic regime allows us to trace back unambiguously the relation between the chiral anomaly and the longitudinal magneto-conductance. We find that two regimes must be distinguished: (i) a low-field regime in which the magneto-conductance is still positive, behaves algebraically with $|\mathbf{B}|$, displays quantum oscillations at higher fields, but is not a unique manifestation of the chiral anomaly; (ii) a quantum regime reached for magnetic fields larger than $B_c \simeq (h/e)\lambda_F^{-2}$ where λ_F is the Fermi wavelength, in which the conductance is linear in field with a universal slope and constitutes an unambiguous signature of the chiral anomaly. Moreover this regime is found to be robust to weak elastic scattering. In this regime, the linear magneto-conductance is a direct measure of the chiral current. We will see how the chiral current is related to the existence of an anomalous chiral Landau level, discussed in relation with the chiral anomaly by Nielsen and Ninomiya [Nielsen and Ninomiya, 1983].

5.2.1 Ballistic Weyl junction

Setup

We consider the transport through a short junction made of a Weyl semi-metal in the presence of an external magnetic field $\mathbf{B}$, represented in Fig. 5.5. We assume that $\mathbf{B}$ is applied along the direction of the current, unless specified otherwise. In such a setup, the charge current is induced by the bias voltage between the leads on each side of the junction. For a short enough junction, scattering inside the conductor can be neglected. Hence, the energy and momentum relaxation only take place in the leads. This so-called ballistic regime is inherently out of equilibrium, in contrast with the linear response to an electric field, which has been considered so far. All Left-movers come from lead 2 with potential μ_2, while all Right-movers come from lead 1 with potential μ_1. The current induced by a small difference of chemical potentials across the junction, $\mu_{2/1} = \mu \mp \delta\mu/2$, takes the simple form $I = G(\delta\mu/e)$. The conductance of the junction, G, scales as its transverse area, $W \times W$, and does not depend on the junction's length, L, in the ballistic regime. We define a dimensionless and scale independent conductance, g

$$G = (e^2/h)(W/a)^2 g, \tag{5.19}$$

where a plays the role of an Ultra-Violet cut-off. We also introduce a dimensionless magnetic field, the rescaled magnetic flux per unit cell (in units of the flux quantum)

$$b = \phi/\phi_0 = a^2 Be/h = \mathrm{sign}(B)\ a^2/(2\pi l_B^2) \tag{5.20}$$

Numerical study

We perform a numerical study of transport on two lattice Hamiltonians displaying respectively four pairs and one pair of Weyl cones. We compute the conductance of a ballistic junction of size $W \times W \times L$ using the Kwant numerical software [Groth et al., 2014] applied to two tight-binding two-band models on a cubic lattice with nearest-neighbour couplings. We study the transport along the z-direction as a function of the magnetic field $\mathbf{B} \parallel z$ aligned with the junction.

Lattice model with four pairs of Weyl cones

The first lattice model is described by the Bloch Hamiltonian

$$H(\mathbf{k}) = t \sin k_x \sigma_x + u \sin k_y \sigma_y + \left[t_z(1 - \cos k_z) - \Delta\right] \sigma_z. \tag{5.21}$$

The corresponding dispersion relation,

$$E_\pm^2(\mathbf{k}) = t^2(\sin^2 k_x a + \sin^2 k_y a) + \left[t_z(1 - \cos k_z a) - \Delta\right]^2, \tag{5.22}$$

possesses four pairs of Weyl cones with opposite chiralities at quasi-wavectors $\mathbf{k} = (0/\pi, 0/\pi, \pm K_z)$ with $K_z = (2/a) \arcsin \sqrt{\Delta/(2t_z)}$, assuming $0 < \Delta/(2t_z) < 1$ (see Sec. III in Appendix D for details). Throughout our study, we use $a = 1$ for the lattice spacing, $t = 1$ and $t_z = 1$ for the hopping matrix elements in (xy)-plane and along z-direction, respectively, and various values of the energy threshold Δ.

Lattice model with one pair of Weyl cones

We also consider a $\mathcal{T}$-breaking model with a single pair of Weyl cones from [Delplace et al., 2012]. Its Bloch Hamiltonian reads

$$H = (2t\ \sin k_+)\,\sigma_x + (2t\ \sin k_-)\,\sigma_y + \ t_z\,(2m_1 + 2\cos k_z - m_2(\cos k_x + \cos k_y))\,\sigma_z, \tag{5.23}$$

where $k_\pm = (k_x \pm k_y)/2$. The associated energy bands are given by

$$E_\pm^2(\mathbf{k}) = 4\left[t^2\left(\sin^2 k_+ + \sin^2 k_-\right) + t_z^2\left(m_1 - m_2 \cos k_+ \cos k_- + \cos k_z\right)^2\right]. \tag{5.24}$$

The lattice spacing is set to $a = 1$ and we choose the parameters $t = 1, t_z = 0.2, m_1 = 3/4, m_2 = 1$ for which only two Weyl points exist and are located at $(0, 0, \pm K)$ with $K = \arccos(m_2 - m_1)$. Around these Weyl cones the Hamiltonian reads (up to spin rotation)

$$H(\pm\mathbf{K} + \mathbf{q}) = t(q_x + q_y)\sigma_x + t(q_x - q_y)\sigma_y \mp c_z q_z \sigma_z \tag{5.25}$$

with $c_z = 2t_z\sqrt{1 - (m_2 - m_1)^2}$.

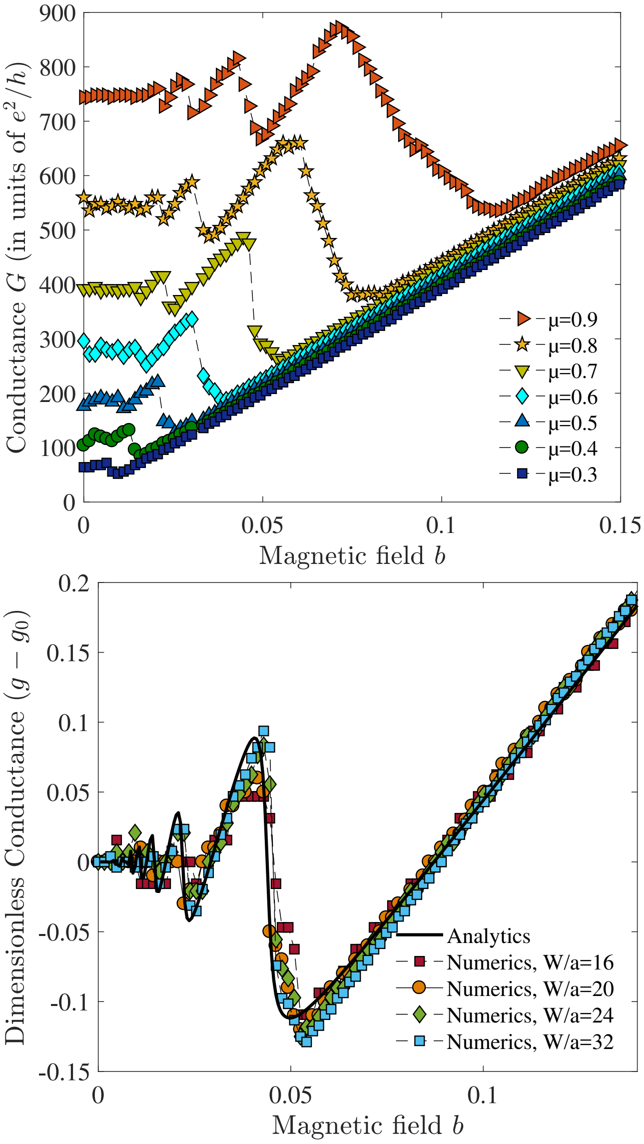

Figure 5.6: Conductance of a short ballistic Weyl junction, in units of the conductance quantum, as a function of the magnetic field along the junction, in units of the flux per lattice unit cell. At low magnetic field, the conductance oscillates before reaching a linear regime at high field, with a universal and positive slope. A lattice model with 8 Weyl cones is used. The top panel shows the magneto-conductance for a junction of transverse size $W/a = 32$, for various chemical potentials. The bottom panel shows the collapse of rescaled dimensionless conductances g for a fixed $\mu = 0.7$, and comparison (full line) with the expression (5.39) incorporating a Lorentz broadening of energy levels due to the leads ($\eta = 0.01$).

First results

Results for the model with four pairs of cones (5.21) for $\Delta = 1$ are shown in Fig. 5.6. The conductance of the junction is plotted as a function of the dimensionless magnetic flux b threading a lattice unit cell. We find that (i) at low magnetic field, the conductance $g(b)$ oscillates with b, with an amplitude of oscillations that increases linearly with b, (ii) at high magnetic field, the conductance $g(b)$ reaches a linear regime independent on energies, $g(b) \propto |b|$. Weyl semimetals are known to possess surface states with characteristic Fermi arcs, see section 1.3. We have checked that the dominant contribution to the conductance comes from bulk states by studying the scaling with transverse size W. As shown on Fig. 5.7, we find that the conductance show a scaling $G \propto W^2$ characteristic of bulk states while surface states give subdominant contributions $\propto W$. We have also checked that the conductance is independent of the length L of the junction (see Appendix D, Sec. IV).

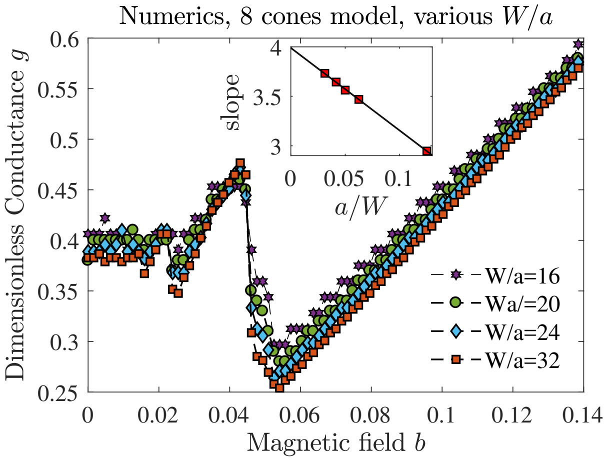

Figure 5.7: Dimensionless conductance g as a function of b for $\mu = 0.7$, $\Delta = 1.$, $L/a = 4$ and various W/a. Inset shows surface corrections to the slope scaling like a/W; in the limit $W/a \to \infty$ the slope extrapolates to 4 which corresponds to $g = 4b$, 4 being the number of Weyl pairs.

5.2.2 Relativistic Landau levels and anomalous magnetotransport

To understand the anomalous transport results reported in Fig. 5.6, we determine analytically the dispersion of Landau Levels for for the simplest model of two Weyl cones with opposite chiralities separated in momentum space. Using the Landauer formalism for transport (see Appendix B.1) we then consider the consequences of the relativistic dispersion of Landau Levels on the magnetoconductance.

We consider the following simplified model describing a pair of Weyl cones of opposite chiralities:

$$H(\mathbf{k}) = vp_x\sigma_x + vp_y\sigma_y + \left(\frac{(p_z)^2}{2m} - \Delta\right)\sigma_z. \tag{5.26}$$

$p_i = \hbar k_i$ are quasimomenta, while c and v_z are velocities in x, y- and z-directions respectively. (For simplicity, we assume same velocities along x and y.) For $\Delta > 0$, it admits two Weyl points of opposite charge at $k_x = k_y = 0$ and $\hbar k_z = \pm\sqrt{2m\Delta}$.

Around each valley, the local Bloch Hamiltonian can be written as

$$H = vp_x\sigma_x + vp_y\sigma_y + \chi v_z p_z \sigma_z. \tag{5.27}$$

with $\chi = \pm 1$ the right/left-handed chirality of the valley, $v_z = \sqrt{2\Delta/m}$ the velocity in the z-direction.

In the presence of a magnetic field $\mathbf{B} \parallel z$, the kinetic energy of electrons in the x, y-directions freezes into Landau levels, while the motion in the z-direction remains ballistic. By minimal coupling, with a charge of carriers $q = -e$, we replace in the Hamiltonian (5.27) $p_i = \hbar k_i$ by $\Pi_i = p_i - qA_i = p_i + eA_i$.

Relativistic Landau levels - 2D

We first focus on the 2D Hamiltonian in the xy plane transverse to the magnetic field $\mathbf{B}$:

$$H_{xy} = v\left[\sigma_x\hat{\Pi}_x + \sigma_y\hat{\Pi}_y\right]. \tag{5.28}$$

We naturally introduce the magnetic length $l_B^2 = \hbar/e|B|$ and the ladder operators

$$\hat{a} = \frac{l_B}{\sqrt{2}\hbar}\left(\hat{\Pi}_x - i\hat{\Pi}_y\right) \quad ; \quad \hat{a}^\dagger = \frac{l_B}{\sqrt{2}\hbar}\left(\hat{\Pi}_x + i\hat{\Pi}_y\right) \tag{5.29}$$

which satisfy $\left[\hat{a}, \hat{a}^\dagger\right] = \eta_B \mathbb{I}$, with $\eta_B = \pm 1$ the sign of B.

- Case $B > 0$:

  The Hamiltonian then reads

$$H = H_{xy} + \left(\frac{p_z^2}{2m} - \Delta\right)\sigma_z \ ; \ H_{xy} = \hbar\omega_0 \begin{pmatrix} 0 & \hat{a} \\ \hat{a}^\dagger & 0 \end{pmatrix}, \tag{5.30}$$

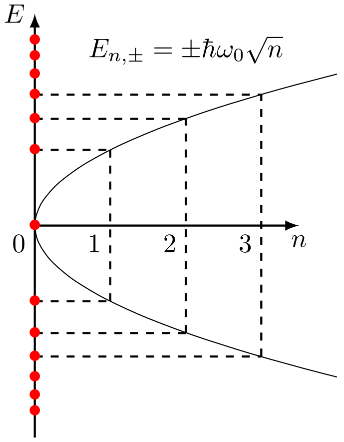

Figure 5.8: Dispersion of 2D Relativistic Landau Levels of H_{xy} (5.30) as a function of the Landau Level index n.

with $\hbar\omega_0 = \sqrt{2}\hbar v/l_B = \sqrt{4\pi\hbar^2 v^2|b|/a^2}$. Let us consider the quanta $|n\rangle$ defined by $\sqrt{n!}\,|n\rangle = (\hat{a}^\dagger)^n\,|0\rangle$. Fig. 5.8 shows the spectrum of relativistic Landau levels of H_{xy}. It is given by $E_n = \zeta\sqrt{n}\hbar\omega_0$, $\zeta = \pm 1, n \in \mathbb{N}$ with the corresponding eigenstates

$$|\psi_0\rangle = \begin{pmatrix} 0 \\ |0\rangle \end{pmatrix} \;\; ; \;\; |\psi_{\zeta,n}\rangle = \frac{1}{\sqrt{2}}\begin{pmatrix} |n-1\rangle \\ \zeta\,|n\rangle \end{pmatrix} \;\; , \;\; n \geq 1. \tag{5.31}$$

- Case $B < 0$:

  There the algebra of ladder is reversed,

$$H_{xy} = \hbar\omega_0 \begin{pmatrix} 0 & \hat{a}^\dagger \\ \hat{a} & 0 \end{pmatrix}, \tag{5.32}$$

  and the eigenstates take the form

$$|\psi_0\rangle = \begin{pmatrix} |0\rangle \\ 0 \end{pmatrix} \;\; ; \;\; |\psi_{\zeta,n}\rangle = \frac{1}{\sqrt{2}}\begin{pmatrix} |n\rangle \\ \zeta\,|n-1\rangle \end{pmatrix} \;\; , \;\; n \geq 1. \tag{5.33}$$

Relativistic Landau levels - 3D

To get the full spectrum near a single cone, we introduce a reduced version of Hamiltonian (5.27) in the basis $|\psi_{+,n}\rangle, |\psi_{-,n}\rangle$:

$$H = \sqrt{n}\hbar\omega_0\sigma_z + \chi v_z\hbar k_z\sigma_x. \tag{5.34}$$

The spectrum of each valley thus consists of a series of bands

$$E_{n,\pm} = \pm[n(\hbar\omega_0)^2 + (v_z\hbar k_z)^2]^{1/2} \tag{5.35}$$

with $n \geq 1$, which disperse along the z-direction, and which are separated from each other by gaps of the order $\hbar\omega_0 = \hbar v\sqrt{2}/l_B = \mu\sqrt{|B|/B_c}$ with $B_c\lambda_F^2 = \pi h/e$ where λ_F is the Fermi wavelength satisfying $\mu = \hbar v 2\pi/\lambda_F$ for $\mu > 0$ (see Sec. I of the Appendix D). Besides these bands, the energy spectrum admits an additional, linearly dispersing band, whose direction of propagation depends both on the chirality of the valley and the direction of the magnetic field,

$$E_0 = -\chi\;\eta_B\;v_z\hbar k_z, \tag{5.36}$$

as shown in Fig. 5.9. The Lowest Landau Level (LLL) is chiral. The sign of the group velocity of an electron, i.e. the slope of its dispersion along $\mathbf{B}$, is given by the chirality of the Weyl valley.

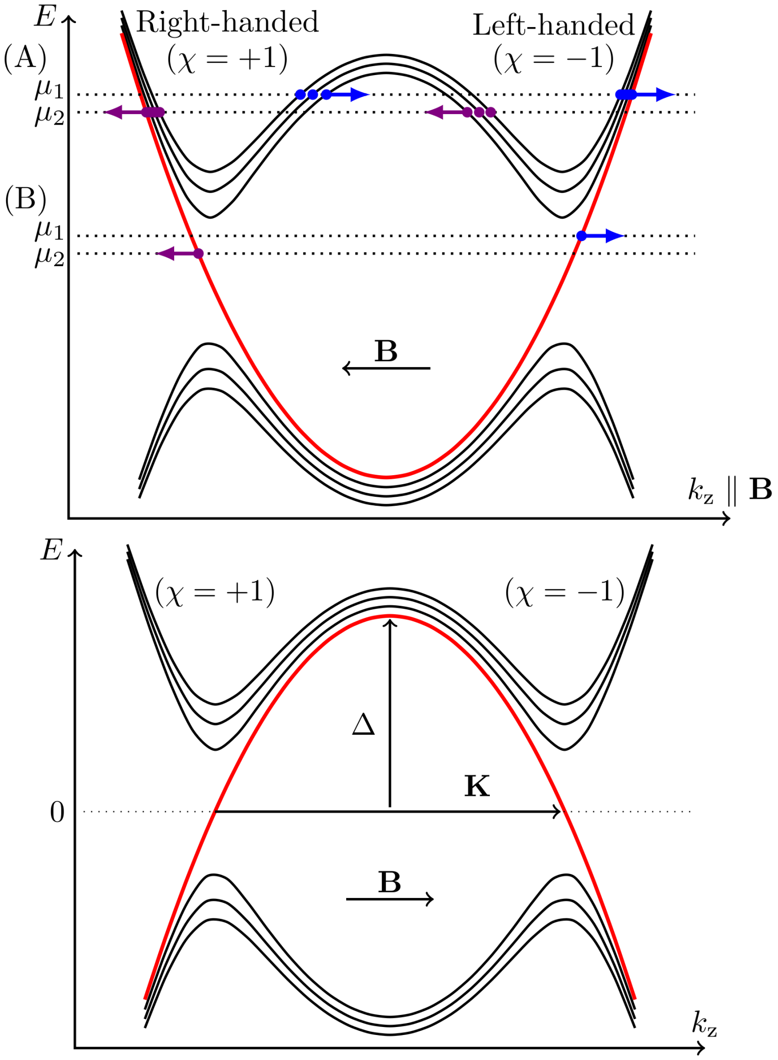

Figure 5.9: Schematic view of the Landau level dispersion for a pair of left- and right-handed Weyl cones (resp. $\chi = -1, +1$) separated by an energy threshold Δ. The chiral $n = 0$ Landau band depends on the orientation of the magnetic field $\mathbf{B}$ with respect to the vector $\mathbf{K}$ connecting the pair of Weyl cones of opposite chiralities. For $\mathbf{B}$ directed along $+\mathbf{K}$, this $n = 0$ Landau level exists for energies $\mu < \Delta$, while for $\mathbf{B}$ directed along $-\mathbf{K}$, this $n = 0$ Landau level exists for energies $\mu > -\Delta$. For a given pair of Weyl points, this defines the range of chemical potential, which depends on the orientation of magnetic field, for which a ballistic linear magneto-conductance is observed at high magnetic field. In the ballistic regime, all left movers (purple) come from lead 2 at chemical potential μ_2 and all right-movers (blue) come from lead 1 at μ_1. An equilibrium chiral current crosses the junction irrespective of the chemical potential, due to the presence of the $n = 0$ chiral Landau level. The out-of-equilibrium charge current is induced by the difference $\mu_1 - \mu_2$. The corresponding ballistic conductance is proportional to the number of Landau levels intercepted by the chemical potential (case A). The quantum regime is reached when only the level $n = 0$ crosses the chemical potential (case B).

Landau levels and ballistic transport

Let us now go back to studying transport through the junction of Fig. 5.5. **B** is applied along z, the direction of the current. Under **B**, electrons describe cyclotron orbits in the x, $y-$plane with a kinetic energy quantized into Landau bands we have described in the previous section. Each state in each Landau level provides a conduction channel in the ballistic junction with a left and right moving state along the junction. The number of such channels per Landau bands is $W^2/(2\pi l_B^2)$. This yields a conductance

$$G(\mu, B) = \frac{e^2}{h}\frac{W^2}{2\pi l_B^2}N(\mu, B), \tag{5.37}$$

where $N(\mu, B)$ is the number of Landau bands crossed by the chemical potential μ, i.e. of 2D Landau levels under μ.

Given the dispersion of LLs previously established, we now study the evolution of $N(\mu, B)$ for a ballistic junction built out of Weyl fermions. The oscillations at low B and linear regime at high B observed on Fig. 5.6 can now be understood in relation with the LL spectrum, see Fig. 5.9. At large magnetic field, $|B| \geq B_c$, only the anomalous Landau level $n = 0$ contributes to transport, a situation reminiscent to that of Ref. [Nielsen and Ninomiya, 1983] albeit considered here in the ballistic regime. We call this regime the quantum regime, in which $N(\mu, B) = 1$, and from Eq. (5.37) we find $G = (e^3/h^2)W^2|B|$. At smaller fields, $|B| \leq B_c$, other Landau bands intercept the Fermi level and contribute to the conductance with an additional $2(e^3/h^2)W^2|B|$. When $|B| = B_c$ the second Landau band crosses the Fermi level, and the conductance jumps to $3(e^3/h^2)W^2|B|$. Then, at even lower field when the third Landau band crosses the chemical potential, $E_{n=3} = \mu$ the conductance slope changes again according to $G = 5(e^3/h^2)W^2|B|$. Hence, the quantum conductance oscillates as a function of the magnetic field $|B|$ or the chemical potential μ. When lowering $|B|$, the slope of the conductance increases and the distance between jumps decreases.

5.2.3 Results

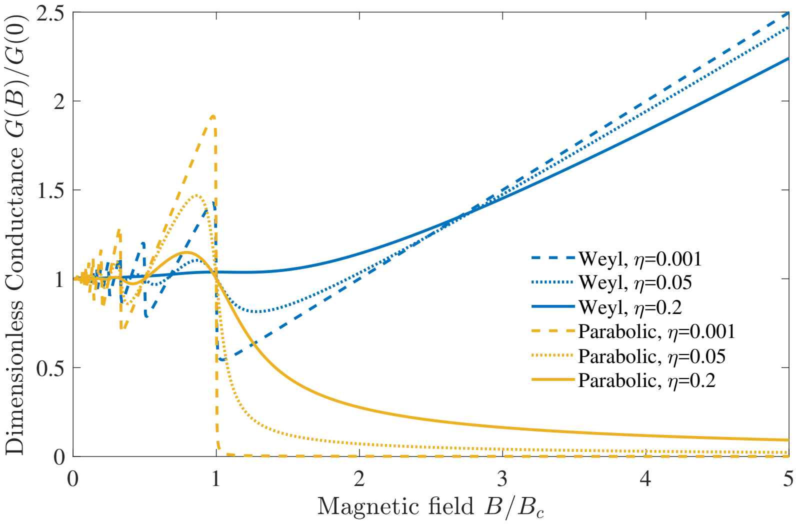

Figure 5.10: Magneto-conductance of ballistic junctions with Weyl (blue) and parabolic (yellow) dispersion relations. The finite dwell time of the electrons in the junction is included through the broadening amplitude η of the spectrum and we chose $\mu = 0.7, v = 1$. For small magnetic fields, several Landau bands contribute to the conductance. Correspondingly the conductance oscillates as a function of the magnetic field, reflecting the discontinuous change of the number of filled Landau bands as the later varies. At high magnetic fields, in the quantum regime, the Weyl and parabolic magneto-conductances differ. In this regime a single, $n = 0$ Landau band contributes to the conductance of the Weyl junction, and it increases linearly with $|b|$. By contrast, for a junction with a parabolic dispersion relation, no Landau band crosses the chemical potential, and the conductance vanishes.

Quantum oscillations and linear regime

The previous qualitative results can be cast into a simple analytical description of the conductance. For an ideal ballistic junction, the number of 2D Landau levels below the chemical potential $E_n < \mu$ is deduced from the expression of Landau levels, $N(\mu, B) = 1 + 2\lfloor(\mu/(\hbar\omega_0))^2\rfloor = 1 + 2\lfloor B_c/|B|\rfloor$, where $\lfloor x\rfloor$ stands for the integer part of x. By introducing the sawtooth function $\mathrm{sw}(x) = \lfloor x\rfloor - x + \frac{1}{2}$ we obtain the expression of the conductance of an ideal Weyl junction,

$$G(B) = G_{\mathrm{Sh}}\left(1 + \frac{|B|}{B_c}\,\mathrm{sw}\left(\frac{B_c}{|B|}\right)\right), \tag{5.38}$$

where $G_{\mathrm{Sh}}(\mu) = \lim_{B\to 0} G(B) = 2\pi(e^2/h)(W/\lambda_F)^2$, which is proportional to the number of conduction channels at $B = 0$, is the Sharvin conductance of the junction. Let us note that quantum oscillations of the longitudinal conductance, similar to those we identified in the ballistic regime, were also observed in the diffusive regime for hot electrons [Gorbar et al., 2014].

Effect of broadening

The limit $B \to 0$ of the conductance (5.38) for an ideal junction is actually ill-defined: the expression (5.38) is non analytical in this limit. To accurately describe this limit, we have to cut-off the quantum oscillations of (5.38) at low field by a broadening of the Landau bands [Ashby and Carbotte, 2014]. In the ballistic junction that we consider, the finite dwell time of the electrons between the leads, $\tau_d = L/v_z$ provides an inherent broadening of order $\eta \simeq \hbar/\tau_d = \hbar v_z/L$. We can phenomenologically incorporate this effect by a standard Lorentz broadening of the energy levels, leading to [1]

$$G(\mu, B) = G(\mu, 0) + G_{\mathrm{Sh}}(\mu)\frac{|B|}{B_c(\mu)}\int \frac{d\mu'}{\eta} f\left(\frac{\mu - \mu'}{\eta}\right)\mathrm{sw}\left(\frac{B_c(\mu')}{|B|}\right), \tag{5.39}$$

with $f(x) = 1/[\pi(1+x^2)]$. In the regime where a non-oscillating density of states is recovered, corresponding to $\hbar\omega_0 \ll \eta$, we find a non-analytic scaling of the positive magneto-conductance,

$$\frac{G(\mu, B)}{G_{\mathrm{Sh}}(\mu)} - \frac{G(\mu, 0)}{G_{\mathrm{Sh}}(\mu)} \simeq \tilde{\alpha}\;\frac{\mu}{\eta} f\left(\frac{\mu}{\eta}\right)\;\left(\frac{|B|}{B_c(\mu)}\right)^{3/2} \tag{5.40}$$

with $\tilde{\alpha} \simeq 0.59$, see Sec. II in Appendix D. Noteworthy, this scaling is different from the typical B^2-behaviour predicted in the diffusive regime [Son and Spivak, 2013]. Similarly if a thermal broadening of the levels supersedes the intrinsic broadening, we can still use Eq. (5.39), but now with $f(x) = -f_F'(x)$ with $f_F(x) = 1/(1 + e^x)$. For Weyl fermions, it yields

$$\frac{G(\mu, B)}{G_{\mathrm{Sh}}(\mu)} - \frac{G(\mu, 0)}{G_{\mathrm{Sh}}(\mu)} = \frac{1}{2}\frac{|B|}{B_c}\,f_F\left(\frac{\mu}{k_BT}\right) - \left(\frac{|B|}{B_c}\right)^{\frac{3}{2}}\frac{\mu}{8k_BT}f_F'\left(\frac{\mu}{k_BT}\right). \tag{5.41}$$

In particular, the anomalous magneto-conductance is exponentially suppressed at $\mu \gg k_BT$.

Note that the numerical Landauer technique that we use amounts to introducing semi-infinite systems on both sides of the conducting part, playing the role of leads with perfect contacts, thereby allowing to reach a ballistic regime. In doing so we effectively consider a long ballistic junction, corresponding to an artificially large dwell time for the electrons, which hampers the study of the algebraic low b regime. On the other hand, we expect this dwell time to be much shorter experimentally, leading to a cut-of of the quantum oscillations and an algebraic behaviour at low fields. The thermal broadening of the magneto-conductance is illustrated in Fig. 5.11. When the temperature is finite, the quantum oscillations are dampened as expected. For $kT = 0.025$ ($\mu/kT = 24$) the first oscillation is still visible. All oscillations are lost for $kT = 0.1$ ($\mu/kT = 6$). Note that the linear high field regime is still observed in presence of thermal broadening. In particular, it shows a vanishing of the conductance at low fields for finite temperature, compatible with the behaviour of Eq. (5.41) in the limit $\mu \gg kT$.

Weyl versus parabolic dispersion

Let us contrast the previous results for a Weyl fermion, with an anomalous magnetoconductance showing quantum oscillations at low fields followed by a linear positive regime at high magnetic fields, with the

---

[1] Note that the Lorentz broadening of the Sharvin conductance, $G(\mu, B = 0)$, requires a high-energy cut-off below which the Hamiltonian (5.27) is defined, as opposed to the B dependent correction described by Eq. (5.39).

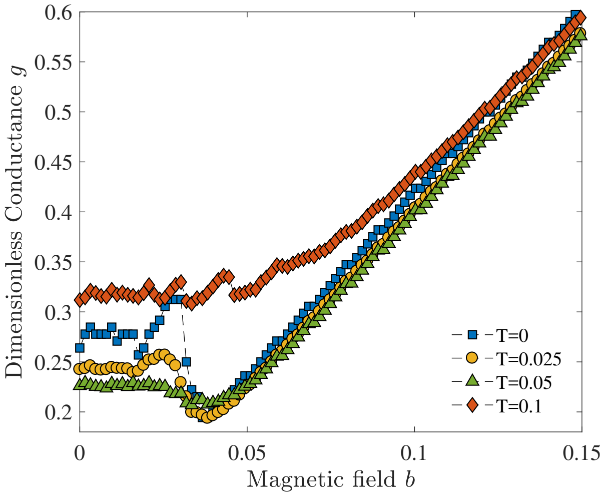

Figure 5.11: Thermal broadening of the magneto-conductance The parameters are identical to those of Fig 5.6 with $\mu = 0.6$ and a transverse size $W/a = 24, L/a = 4$.

case of a standard non-relativistic parabolic dispersion relation $E = p^2/(2m)$. In this case, the Landau bands read

$$E_n = \hbar\tilde{\omega}_0 \left(n - \frac{1}{2}\right) + \frac{p_z^2}{2m} \tag{5.42}$$

with $n \geq 1$, $\hbar\tilde{\omega}_0 = \hbar e|B|/m = \mu|B|/\tilde{B}_c$. The number of filled Landau bands is now

$$N(\mu, B) = \lfloor \mu/(\hbar\tilde{\omega}_0) + \frac{1}{2} \rfloor = \lfloor \tilde{B}_c/|B| + \frac{1}{2} \rfloor, \tag{5.43}$$

corresponding to a conductance

$$G(\mu, B) = G_{\text{Sh}}(\mu) \left(1 + (|B|/\tilde{B}_c)\ \text{sw}\left(\tilde{B}_c/|B| + \frac{1}{2}\right)\right). \tag{5.44}$$

It yields strikingly different predictions compared with Eq. (5.38). In particular, the conductance vanishes in the quantum regime, which is reached for fields $|B| \geq 2|\tilde{B}_c|$, as opposed to the positive linear magneto-conductance at high fields. Furthermore, a Lorentz broadening of the Landau levels leads to an exponentially suppressed magneto-conductance at low field, in contrast with Eq. (5.40) for the Weyl Hamiltonian. The sharp difference between the ballistic magneto-conductance of a Weyl junction with that of a standard material with a non-relativistic dispersion relation is highlighted in Fig. 5.10, which illustrates the presence vs absence of the positive magneto-conductance in the quantum regime.

5.2.4 Ballistic transport and chiral anomaly

Lowest Landau level - Onset of linear regime

The previous comparison between Weyl and standard parabolic dispersion showed that the linear magnetoconductance regime at high field is a special feature of Weyl materials. Let us now see how it relates with the chiral anomaly and the chiral current. The chiral current is defined as

$$I_5 = I_R - I_L, \tag{5.45}$$

where I_R is the current from the Right Weyl cone and I_L the current from the Left Weyl cone. Each state in each Landau Level contributes for one conduction channel to the current. In higher LLs (5.35) with $n \geq 1$, there is the same number of left-movers and right-movers in each valley, see Fig. 5.9. In contrast, the Lowest Landau Level (LLL) is anomalous: it is chiral with opposite slope in each valley, depending on the sign of B. Thus whenever the chemical potential crosses the LLL, a chiral current flows through the junction which is due to the LLL only:

$$I_5 = I_R - I_L = \frac{e^2}{\mu_2 - \mu_1}. \tag{5.46}$$

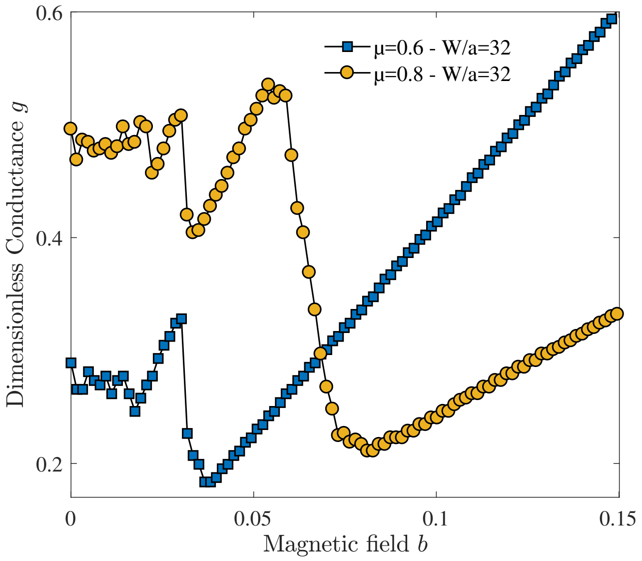

Figure 5.12: Magneto-conductance of a model with 4 pairs of Weyl points and energy threshold $\Delta = 0.7$ between them. Half of the pairs of Weyl cones have a "chirality vector" $\mathbf{K}$ between two Weyl cones (see Fig. 5.5) that is parallel to the magnetic field, while it is antiparallel for the other half. Hence for chemical potentials above the saddle point between Weyl valleys, the linear magneto-conductance at high fields is lost for half of the pairs: the slope of the resulting magneto-conductance is reduced by a factor two.

For low magnetic fields $B < B_c$ (case (A) in Fig. 5.9), the chemical potential crosses the LLL and other LLs: the total current contains more than the chiral contribution (5.46). The conductance is indeed proportional to the number of LL crossed. On the other hand at high magnetic fields $B > B_c$ (case (B)) only the chiral LLL crosses the chemical potential: the current identifies with chiral contribution, $I = I_5$. The corresponding conductance is linear, $G(B) = \frac{e^3}{h^2} W^2 B$.

We have shown that the linear conductance we observed in the linear regime gives a direct measure of the chiral current (5.46). Hence, we propose to probe this high field regime of ballistic Weyl junctions. Our setup is simple and experimentally relevant to mesoscopic physicists, and it provides a clear and unambiguous signature of the chiral anomaly in transport. The low field regime is more complex to analyse and associate with the chiral anomaly.

Chemical potential dependence

After having discussed the contribution of a pair of Weyl cones, we now discuss the dependence of the ballistic magneto-conductance on the chemical potential. This will allow us to show that the number of pairs of Weyl valleys contributing to this regime depends on this chemical potential. In particular, as shown in Fig. 5.12, we find that the linear regime at large fields survives even above the threshold energy separating the Weyl valleys $\mu > \Delta$ (here taken as $\Delta = 0.7$), though its slope is reduced by a factor two at large μ. To understand this reduction of the slope, we consider the simpler situation of a single pair of Weyl cones separated by an energy threshold Δ. It can be realized with a tight-binding two-band model on a cubic lattice introduced in [Delplace et al., 2012], where the Weyl points only occur at $\mathbf{k} = \pm\mathbf{K}/2 = (0, 0, \pm K_z)$ (see Appendix D, Sec. IV). The corresponding numerical results for the magneto-conductance are presented in Fig. 5.13. We observe that above the threshold energy Δ separating the Weyl valleys, the linear behaviour at large field is lost for one direction of the magnetic field oriented along the current with $\mathbf{B} \parallel \mathbf{I} \parallel \mathbf{K}$ (Figs. 5.13A and 5.13B). Moreover, the whole behaviour at small magnetic field is now asymmetric in b, irrespective of μ. Note that such a simple Weyl semi-metal with only two cones necessarily breaks time-reversal symmetry (TRS). This manifests itself in the breaking of Onsager relation $G(\mathbf{B}) \neq G(-\mathbf{B})$, and henceforth an asymmetry of the curves $G(\mathbf{B})$ (or $g(b)$). The amplitude of this TRS breaking and this asymmetry originates from the separation $\mathbf{K}$ of the two cones in the Brillouin zone, or more precisely on its projection onto the direction of magnetic field. Indeed, when the vector $\mathbf{K}$ is aligned perpendicular to both the magnetic field and the junction, no sign of this TRS breaking is observed on magneto-transport and a magneto-conductance symmetric in b is recovered as shown in Fig. 5.13C. A related effect was discussed in the diffusive regime in [Cortijo, 2016].

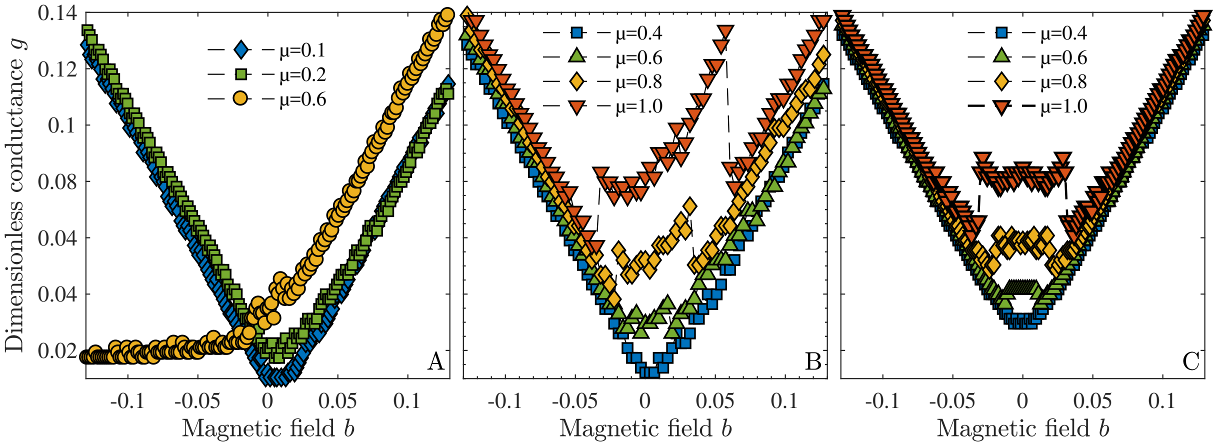

Figure 5.13: Magneto-conductance of a model with a single pair of Weyl cones separated by an energy threshold $\Delta = 0.3$ (A) and $\Delta = 1.5$ (B,C), for a conductor size $W/a = 24$. The linear regime at large field regime becomes asymmetric for $\mu > \Delta$ as shown in Fig. A: the regime $g(b) \simeq |b|$ is lost for $b < 0$. Similarly, the asymmetry of the small field regime for any chemical potential μ is clearly visible for $\Delta = 1.5$, Fig. B. In particular the minimum of $g(b)$ is shifted towards a positive field, reflecting the breaking of time-reversal symmetry for a model with a single pair of Weyl cones located at points $\pm\mathbf{K}/2$. For a magnetic field transverse to this direction $\mathbf{K}$, a symmetric conductance $g(b) = g(-b)$ is recovered as shown in Fig. C.

The change of linear magneto-conductance in the quantum regime can be understood by considering the simple Bloch Hamiltonian (5.26) that describes two Weyl valleys separated by an energy saddle point. For $\Delta > 0$, two Weyl points at $\pm\mathbf{K}/2 = (0, 0, \pm\sqrt{2m\Delta}/\hbar)$, and having opposite chirality, are separated by an energy barrier Δ. The chemical potential dependence in the large field regime can now be inferred from the behaviour of the Landau levels for the model (5.26) (see Appendix D, Sec. I). Depending on the sign of b, i.e., on the orientation of the field with respect to the "chirality vector" $\mathbf{K}$ pointing from the left-handed Weyl cone with $\chi = -1$ to the right-handed Weyl cone with $\chi = +1$, the dispersion of the $n = 0$ Landau level changes dramatically. Indeed, it either exists for μ smaller than Δ, or for μ larger than $-\Delta$ as illustrated in Fig. 5.9. We expect the larger energy barrier between the two Weyl valleys, neglected in the model (5.26), to cut-off the energy range of this $n = 0$ Landau band on the other side. Beyond this saddle point energy, the linear magneto-conductance for the pair of Weyl cones is lost. Depending on the sign of b, this happens either above the positive or below the negative energy saddle point $\pm\Delta$.

We are now ready to understand the reduction of the slope illustrated in Fig. 5.12 for the model with four pairs of Weyl cones. Indeed, due to the symmetrical distribution of the pairs of Weyl cones in momentum space in that model, above the saddle point energy, the linear magneto-conductance contribution vanishes for the half of Weyl pairs whose chirality vector is parallel with the magnetic field, while it persists for the other half having an anti-parallel chirality vector with respect to $\mathbf{b}$. Furthermore, the absence of an asymmetry of the magneto-conductance in that model can also be traced to the symmetrical distribution of Weyl cones in momentum space.

5.2.5 Semiclassics

Let us now describe within a semi-classical picture the ballistic magneto-transport we discussed previously. The advantage of such an approach is that it allows describing the smooth cross-over from the ballistic to the diffusive regime, as well as compare the results in both regimes. In this approach, the evolution of a semi-classical wave-packet of Weyl eigenstates described by a Hamiltonian $H^{\chi}_{\mathbf{k}} = \hbar v_F \chi\, \boldsymbol{\sigma} \cdot \mathbf{k}$ is described by the semi-classical equations of motion (5.16) and (5.17) [Xiao et al., 2010]. Solving these equations for $\mathbf{k}$ and $\dot{\mathbf{r}}$ yields

$$\hbar\dot{\mathbf{k}} = \frac{-\partial_{\mathbf{r}}\varepsilon - \frac{e}{\hbar}\partial_{\mathbf{k}}\varepsilon \times \mathbf{B} - e(\partial_{\mathbf{r}}\varepsilon \cdot \mathbf{B})\boldsymbol{\Omega}}{1 + \frac{e}{\hbar}(\boldsymbol{\Omega} \cdot \mathbf{B})}, \tag{5.47}$$

$$\dot{\mathbf{r}} = \frac{\frac{1}{\hbar}\partial_{\mathbf{k}}\varepsilon + \frac{1}{\hbar}\partial_{\mathbf{r}}\varepsilon \times \boldsymbol{\Omega} + \frac{e}{\hbar^2}(\partial_{\mathbf{k}}\varepsilon \cdot \boldsymbol{\Omega})\mathbf{B}}{1 + \frac{e}{\hbar}(\boldsymbol{\Omega} \cdot \mathbf{B})}. \tag{5.48}$$

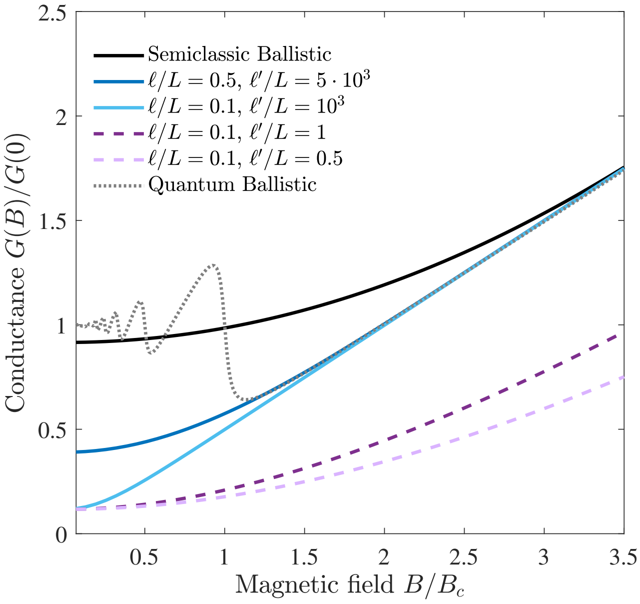

Figure 5.14: Semi-classical magneto-conductance $g(b) = G(B)/G_{\mathrm{Sh}}$ of a Weyl junction for different inter and intra cone scattering lengths ℓ, ℓ' and $\mu = 0.7$. The black plain line corresponds to the ballistic junction with $L \le \ell, \ell'$, and displays a b^2-correction for weak magnetic fields while a linear quantum magneto-conductance $g(b) = |b|$ is recovered at large fields. When only the intra-cone scattering length is smaller than the junction length, $\ell \le L \le \ell'$, a diffusive regime for cold electrons is found at small fields while the linear quantum regime is unaffected and reached at smaller fields as represented by the plain blue curves. Finally when $\ell \le \ell' \le L$ the linear regime at high fields only survives at very high magnetic fields.

In the absence of electric field, corresponding to $\partial_{\mathbf{r}}\varepsilon = 0$, and using the notation $\mathbf{v}_{\mathbf{k}}^{(0)} = \hbar^{-1}\partial_{\mathbf{k}}\varepsilon = c\hat{k}$, these equations simplify into

$$\hbar\dot{\mathbf{k}} = \frac{-e}{1+\frac{e}{\hbar}(\mathbf{\Omega}\cdot\mathbf{B})}\ \mathbf{v}_{\mathbf{k}}^{(0)} \times \mathbf{B}, \tag{5.49}$$

$$\dot{\mathbf{r}} = \frac{1}{1+\frac{e}{\hbar}(\mathbf{\Omega}\cdot\mathbf{B})}\left(\mathbf{v}_{\mathbf{k}}^{(0)} + \frac{e}{\hbar}(\mathbf{v}_{\mathbf{k}}^{(0)}\cdot\mathbf{\Omega})\mathbf{B}\right). \tag{5.50}$$

The current density in the z direction is expressed as

$$j_z = -e\sum_{\chi,\mathbf{k}} \mathbf{w}_{\chi,\mathbf{k}}\cdot\hat{z}\ f_\chi(\mathbf{r},\mathbf{k}). \tag{5.51}$$

We find the expression of the previously introduced anomalous velocity (5.18)

$$\mathbf{w}_{\chi,\mathbf{k}} = \left(\mathbf{v}_{\mathbf{k}}^{(0)} + \frac{e}{\hbar}(\mathbf{v}_{\mathbf{k}}^{(0)}\cdot\mathbf{\Omega}_{\chi,\mathbf{k}})\mathbf{B}\right) = v\hat{k} + \chi\frac{ec}{\hbar}\frac{\mathbf{B}}{2k^2}. \tag{5.52}$$

Introducing the rescaled magnetic flux we can express this anomalous velocity as

$$\mathbf{w}_{\chi,\mathbf{k}} = v\left(\hat{k} + \chi\frac{\mathbf{B}}{B_c}\right). \tag{5.53}$$

The distribution function satisfies the stationary Boltzmann equation (dropping the energy dependence of f)

$$(\mathbf{w}_\chi.\hat{z})\ \partial_z f_\chi(z,\hat{k}) = \frac{1}{\tau}\sum_{\hat{k}'}\left[f_\chi(z,\hat{k}') - f_\chi(z,\hat{k})\right] + \frac{1}{\tau'}\sum_{\hat{k}'}\left[f_{-\chi}(z,\hat{k}') - f_\chi(z,\hat{k})\right]. \tag{5.54}$$

Here τ and τ' are the intra-cone and inter-cone elastic scattering times, respectively, which are assumed to be larger than the dwell time in the ballistic regime. Furthermore, we neglected any inelastic process and assumed a vanishing electric field in the semimetal. The equilibration in the reservoirs is described by the boundary conditions [de Jong, 1994]

$$f = f_0(\varepsilon_{\mathbf{k}} - \mu_1)\Theta\left[\mathbf{w}_\chi \cdot \hat{z}\right] + f_0(\varepsilon_{\mathbf{k}} - \mu_2)\Theta\left[-\mathbf{w}_\chi \cdot \hat{z}\right]. \tag{5.55}$$

Here, f_0 is the Fermi function and $\mu_2 - \mu_1$ is the electro-chemical potential bias. We solve Eq. (5.54) with an ansatz for f that satisfies these boundary conditions, namely

$$f_\chi(z, \mathbf{k}) = f_0(\varepsilon_{\mathbf{k}} - \mu_1)T_\chi(z,\theta) + f_0(\varepsilon_{\mathbf{k}} - \mu_2)\left[1 - T_\chi(z,\theta)\right], \tag{5.56}$$

where $\cos\theta = \hat{k}\cdot\hat{z}$. $T_\chi(x,\theta)$ must solve the equation

$$v\left(\cos\theta + \chi\frac{e}{\hbar}\frac{B_z}{2k_F^2}\right)\partial_z T_\chi(z,\theta) = \frac{1}{\tau}\left[\langle T_\chi(z,\theta)\rangle_\theta - T_\chi(z,\theta)\right] + \frac{1}{\tau'}\left[\langle T_{\bar{\chi}}(z,\theta)\rangle_\theta - T_\chi(z,\theta)\right], \tag{5.57}$$

where $B_z = \mathbf{B}\cdot\hat{z}$ and we note $\langle\ldots\rangle_\theta = (1/2)\int_0^\pi d\theta\sin\theta\ldots$, together with the boundary conditions

$$T_\chi(z=0,\theta) = 1, \qquad \text{if} \qquad \cos\theta + \chi\frac{B_z}{B_c} > 0, \tag{5.58a}$$

$$T_\chi(z=L,\theta) = 0, \qquad \text{if} \qquad \cos\theta + \chi\frac{B_z}{B_c} < 0. \tag{5.58b}$$

Using $\sum_{\mathbf{k}}\cdots = \nu_0\int d\varepsilon_k\langle\ldots\rangle$ in Eq. (5.51), one can then straightforwardly perform the energy integration and find that the current $I = W^2 j_z$ obeys the Ohm's law, $I = GV$, with the conductance

$$G = e^2W^2v\nu_0\sum_\chi\left\langle\left(\cos\theta + \chi\frac{B_z}{B_c}\right)T_\chi(x,\theta)\right\rangle_\theta. \tag{5.59}$$

Here W^2 is the wire's cross section and $\nu_0 = \mu^2/(2\pi^2(\hbar c)^3) = k_F^2/(2\pi^2\hbar c)$ is the density of states at the Fermi level in a Weyl cone. Note that the kinetic equations guarantee the current conservation, so that Eq. (5.59) does not depend on z. By using the notation of the main text, $G = (e^2/h)(W/a)^2g$, we can rewrite Eq. (5.59) as

$$G = 2G_{\text{Sh}}\sum_\chi\left\langle\left(\cos\theta + \chi\frac{B_z}{B_c}\right)T_\chi(x,\theta)\right\rangle_\theta. \tag{5.60}$$

with $G_{\text{Sh}} \equiv G(B=0)$ is the Sharvin (or contact) conductance associated with the two Weyl cones

Ballistic regime

In the ballistic regime, $\tau, \tau' \to \infty$, we use the solution

$$T_\chi(z,\theta) = \begin{cases} 1, & \text{if} \quad \cos\theta + \chi\frac{B_z}{B_c} > 0, \\ 0, & \text{if} \quad \cos\theta + \chi\frac{B_z}{B_c} < 0. \end{cases} \tag{5.61}$$

to obtain

$$G = \begin{cases} G_{\text{Sh}}\left[1 + B_z^2/(4B_c)^2\right] & \text{for } |B_z| < 4B_c, , \\ G_{\text{Sh}}|B_z|/2B_c = e^3/h^2\ W^2|B_z| & \text{for } |B_z| \geq 4B_c. \end{cases} \tag{5.62}$$

The semi-classical description in the ballistic limit thus reproduces the linear regime previously obtained for the quantum conductance at high fields. At low fields, the semi-classical magnetoconductance is quadratic, similar to the expected behaviour in the diffusive regime [Son and Spivak, 2013]. Quite remarkably, incorporating the Berry curvature effect into the semi-classical description of the ballistic transport allows describing the anomalous linear magneto-conductance in the quantum regime at large field, as well as the cross-over towards an anomalous regime at low field. However, the semi-classical description is unable to accurately describe the $|B|^{3/2}$-dependence of the magneto-conductance, see Eq. (5.40), and predicts a B^2-behaviour, similar to the diffusive regime [Son and Spivak, 2013].

Diffusive regime

Let us now consider the diffusive regime where electrons undergo multiple scattering events. Such a diffusive regime is indeed recovered in the present situation at finite scattering times τ, τ'. When the mean-free path is short, $\ell \equiv v\tau \ll L$, the solution of Eq. (5.57) is almost isotropic. Inserting the expansion $T_\chi(z,\theta) \approx T_\chi(z) + \cos\theta\, \delta T_\chi(z)$ (with $\delta T_\chi(z) \ll T_\chi(z)$) in Eq. (5.57), and averaging it over angles, we find

$$\frac{c}{3}\,\partial_z \delta T_\chi(z) + \chi v \frac{B_z}{B_c} \partial_z T_\chi(z) = \frac{1}{\tau'}\left[T_{\bar\chi}(z) - T_\chi(z)\right]. \tag{5.63}$$

Multiplying Eq. (5.57) by $\cos\theta$, and then averaging it over angles, we get

$$v\ \partial_z T_\chi(x) \approx -\frac{1}{\tau}\delta T_\chi(x), \tag{5.64}$$

where we assumed $1/\tau', v/L, vB_z/(LB_c) \ll 1/\tau$. Thus the kinetic equation reduces to a diffusion equation including a magnetic-field induced ballistic contribution,

$$-D\partial_z^2 T_\chi(z) + \chi \frac{B_z}{B_c} c\ \partial_z T_\chi(z) - \frac{1}{\tau'}\left[T_{\bar\chi}(z) - T_\chi(z)\right] = 0, \tag{5.65}$$

where $D = v^2\tau/3$ is the diffusion constant, supplemented with the boundary conditions $T_\chi(z=0) = 1$ and $T_\chi(z=L) = 0$, while the conductance is

$$G = W^2 \nu_0 \sum_\chi \left(-D\partial_z + \chi\frac{B_z}{B_c}\right)\partial_z T_\chi(z). \tag{5.66}$$

These equations match with those of Ref. [Altland and Bagrets, 2016] provided one identifies $\tau' = 2\tau_n$.

An exact formula in the diffusive regime is provided in Ref. [Altland and Bagrets, 2016]. At $|B_z| \ll B_c\sqrt{\tau/\tau'}$, it reproduces the Drude conductance, $G_D = 2\nu_0 D W^2/L$, which can be rewritten as $G_D = 4G_{\text{Sh}}D/(cL)$, while at $|B_z| \gg B_c\sqrt{\tau/\tau'}$, it yields

$$G = \begin{cases} G_D, & |B|/B_c \ll \ell/L \\ 3(B/B_c)^2\ G_D, & |B|/B_c \ll L/\ell', \\ G_{\text{Sh}}|B_z|/2B_c = e^3/h^2\ W^2|B_z|, & \ell/L, L/\ell' \ll |B|/B_c. \end{cases} \tag{5.67}$$

Our expression for the conductance identifies with that previously derived *via* a topological non-linear sigma field theory [Altland and Bagrets, 2016].

As expected, when intra-cone disorder is increased a diffusive regime is reached at small magnetic field when $\ell = v\tau \leq L$, with a conductance now scaling as $G \propto W^2/L$. The correction at small field in this regime remains quadratic in B. However the diffusive regime considered here corresponds to a different situation from the one considered in [Son and Spivak, 2013], as inelastic scattering occurs in the leads in our case, and not in the junction, thus yielding a quantitatively different result. At high magnetic field, the previous ballistic quantum magneto-conductance regime $g(B) = e^3/h^2 W^2|B|$ is affected neither by intra-cone, nor by inter-cone disorder. Moreover as long as $L \ll \sqrt{\ell\ell'}$, including the situation when only the intra-cone disorder is relevant, $\ell \leq L \leq \ell' = v\tau'$, this ballistic linear regime is reached at smaller magnetic fields, $|B| \geq 4B_c\ell/L$. On the other hand, when $L \gg \sqrt{\ell\ell'}$, or $L \geq \ell' \geq \ell$, inter-cone disorder pushes this ballistic regime to high magnetic field (possibly outside of the experimental regime) for $|B| \geq 4B_c L/\ell'$.

Ballistic-to-diffusive crossover

The magneto-conductance corresponding to these different regimes as well as in the intermediate regime can be obtained by numerically solving the semi-classical diffusive equation. We follow the methods of Ref. [de Jong, 1994] to obtain the conductance at arbitrary magnetic field and disorder strength. For this, we first observe that Eq. (5.57) is a first-order differential equation on T_χ (assuming that $\langle T_\chi\rangle$ is known), which can be solved together with its boundary conditions as

$$T_\chi(z,\theta) = \begin{cases} e^{-z/\ell_\chi(\theta)} + \int_0^z dz' \langle \mathcal{T}_\chi(z')\rangle e^{-(z-z')/\ell_\chi(\theta)}/\ell_\chi(\theta), & \ell_\chi(\theta) > 0, \\ -\int_z^L dz' \langle \mathcal{T}_\chi(z')\rangle e^{-(z-z')/\ell_\chi(\theta)}/\ell_\chi(\theta), & \ell_\chi(\theta) < 0, \end{cases} \tag{5.68}$$

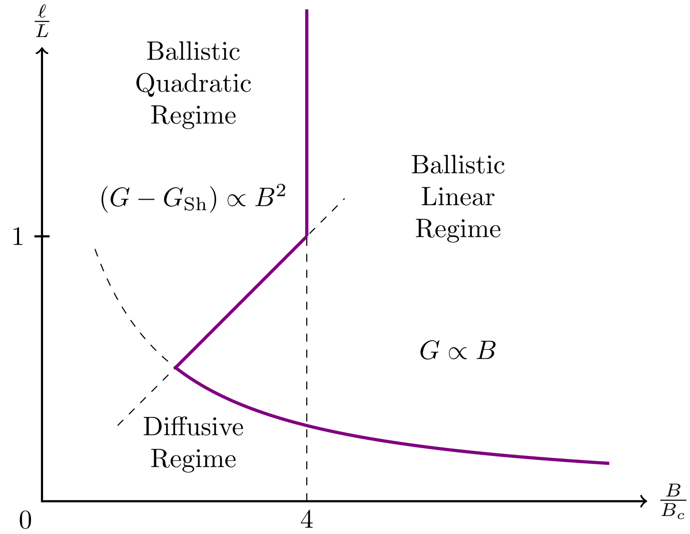

Figure 5.15: Transport regimes as established from a semi-classical description of transport, as a function of intra cone elastic scattering length ℓ/L and effective magnetic field B/B_c, for a fixed chemical potential and intercone scattering length $\ell' > \ell$. In the ballistic regime, the semi-classical conductance is linear at high fields and quadratic at low fields. Strikingly, in the presence of disorder, the high field ballistic linear regime still persists and occurs at even smaller fields, $B/B_c > 4\ell/L$. The conductance is quadratic at low fields, with a behaviour quantitatively different from the clean case. In the strongly diffusive regime $\ell \ll L$, the linear regime is suppressed except for very high fields $B/B_c > 4L/\ell$.

where $\ell_\chi(\theta) = \ell[\cos\theta + \chi B_z/B_c]$ and $\langle \mathcal{T}_\chi(z)\rangle = (\tau'\langle T_\chi(z)\rangle + \tau\langle T_{\bar\chi}(z)\rangle)/(\tau+\tau')$. Then averaging Eq. (5.68) on angles, one gets an integral equation on $\langle T_\chi\rangle$,

$$\langle T_\chi(z)\rangle = t_\chi(z) + \int_0^L dz' g_\chi(z,z')\langle \mathcal{T}_\chi(z')\rangle, \tag{5.69}$$

with

$$t_\chi(z) = \langle e^{-z/\ell_\chi(\theta)}\Theta(\ell_\chi(\theta))\rangle \tag{5.70}$$

and

$$g_\chi(z,z') = \langle e^{-(z-z')/\ell_\chi(\theta)}/\ell_\chi(\theta)\,[\Theta(\ell_\chi(\theta))\Theta(z-z') - \Theta(-\ell_\chi(\theta))\Theta(z'-z)]\rangle, \tag{5.71}$$

where Θ is the Heaviside function.

Once the functions $\langle T_\chi(z)\rangle$ solving Eq. (5.69) have been obtained, one can then compute the conductance as

$$G = \frac{W^2\nu_0}{\tau}\sum_\chi\left(s_\chi(z) + \frac{\tau+\tau'}{\tau\tau'}\int_0^L dz'\ h_\chi(z,z')\langle\mathcal{T}_\chi(z')\rangle\right), \tag{5.72}$$

(it can be evaluated at an arbitrary position z) with

$$s_\chi(z) = \langle \ell_\chi(\theta)e^{-z/\ell_\chi(\theta)}\Theta(\ell_\chi(\theta))\rangle \tag{5.73}$$

and

$$h_\chi(z,z') = \langle e^{-(z-z')/\ell_\chi(\theta)}\,[\Theta(\ell_\chi(\theta))\Theta(z-z') - \Theta(-\ell_\chi(\theta))\Theta(z'-z)]\rangle. \tag{5.74}$$

For the numerical solution, one should be careful with the log-divergence of $g_\chi(z,z')$ at $z\to z'$. As $\langle T_\chi(z)\rangle$ is a smooth function of z on the scale of L, we used the following regularization scheme: we transformed the integral equation (5.69) into a matrix equation,

$$\begin{aligned}\langle T_\chi(z_n)\rangle &\simeq t_\chi(z_n) + \sum_{m=1}^N\int_{-\Delta z/2}^{\Delta z/2} dy g_\chi(z_n, z_m+y)\langle\mathcal{T}_\chi(z_m)\rangle,\\ &= t_\chi(z_n) + \sum_{m=1}^N \tilde g_\chi(z_n,z_m)\langle\mathcal{T}_\chi(z_m)\rangle \end{aligned}\tag{5.75}$$

with $z_n = L(n-1/2)/N$ $(1 \leq n \leq N)$, $\Delta z = L/N$, and

$$\tilde{g}_\chi(z_n, z_m) = \begin{cases} t_\chi(z_n - z_m - \Delta z/2) - t_\chi(z_n - z_m + \Delta z/2), & n > m, \\ 1 - t_\chi(\Delta z/2) - t_{\bar{\chi}}(\Delta z/2), & n = m, \\ t_{\bar{\chi}}(z_m - z_n - \Delta z/2) - t_{\bar{\chi}}(z_m - z_n + \Delta z/2), & n < m, \end{cases} \tag{5.76}$$

where one can use Mathematica to get an explicit expression for $t_\chi(z)$. Similarly, Eq. (5.72) can be evaluated as

$$G = \frac{A\nu_0}{\tau} \sum_\chi \left(s_\chi(z_n) + \frac{\tau + \tau'}{\tau\tau'} \sum_{m=1}^{N} \tilde{h}_\chi(z_n, z_m) \langle \mathcal{T}_\chi(z_m) \rangle \right), \tag{5.77}$$

with

$$\tilde{h}_\chi(z_n, z_m) = \begin{cases} s_\chi(z_n - z_m - \Delta z/2) - s_\chi(z_n - z_m + \Delta z/2), & n > m, \\ \pm B/B_c - s_\chi(\Delta z/2) + s_{\bar{\chi}}(\Delta z/2), & n = m, \\ s_{\bar{\chi}}(z_m - z_n - \Delta z/2) - s_{\bar{\chi}}(z_m - z_n + \Delta z/2), & n < m, \end{cases} \tag{5.78}$$

where one can also use Mathematica to get an explicit expression for $s_\chi(z)$.

We present our results in Fig. 5.14 on the semi-classical description of diffusive transport in our junction. Inelastic scattering occurs within the leads. When only the intra-cone elastic scattering length is smaller than the junction $\ell < L < \ell'$ we obtain a quadratic magnetoconductance at low fields characteristic of a diffusive regime. At higher fields we recover the linear behaviour observed in the ballistic regime in spite of the presence of scattering. Surprisingly, this linear regime is even reached at smaller fields because of the presence of scattering. When the inter-cone scattering increases, $\ell \leq \ell' \leq L$, the linear regime is lost except for very high fields. The phase diagram of Fig. 5.15 summarizes these different transport regimes.

5.3 Discussion

We have shown that two regimes have to be distinguished when discussing the ballistic conductance of a Weyl junction in parallel magnetic field : (i) a linear regime at high fields with a universal slope; (ii) a weak magnetic field regime, in which the magneto-conductance behaves algebraically with the magnetic field, whose details are non-universal. Furthermore at intermediate fields the magneto-conductance displays quantum oscillations when the broadening of Landau levels is weak (such as in long ballistic junctions) and at low temperature.

Let us now discuss the relation between these different regimes and the underlying chiral anomaly. In the ballistic regime addressed in this work, there exists an *equilibrium chiral current* density $j_5 = j_R - j_L \propto |B|$ for non vanishing magnetic fields: the presence of the $n = 0$ Landau band implies that, irrespective of the chemical potential μ, there is an excess of Weyl electrons of, *e.g.*, left-chirality moving to the right of the junction, and electrons of right-chirality moving to the left. This equilibrium chiral current is obviously uncorrelated with a charge density current $j = j_R + j_L$, as the later vanishes in equilibrium. On the other hand, a chemical potential bias, $\mu_1 - \mu_2 = \delta\mu$, reveals this chiral current as a non-equilibrium charge current, as first discussed in Ref. [Nielsen and Ninomiya, 1983]. At high enough field, i.e. when transport is is fully taken over by the $n = 0$ state, charge current is fully chirally polarized and the charge current reflects the linear-in-field dependence of the chiral anomaly. At weak magnetic field only part of the conductance (5.37) is related to the $n = 0$ Landau band contribution, and thus can be related to the chiral anomaly. Hence the anomalous positive ballistic magneto-conductance in the low field regime is not a unique signature of the chiral anomaly. This is in contrast with the situation of hot electrons, close to equilibrium, considered in Ref. [Son and Spivak, 2013]. There, the chiral current driven by the $n = 0$ Landau level leads to a chiral chemical potential $\mu_R - \mu_L$ between left- and right-handed Weyl valleys, and a magneto-conductance via the chiral magnetic effect. Hence attributing the anomalous magneto-conductance at low fields to the chiral anomaly requires first identifying the relevant regime of transport, and the observation of a positive algebraic behaviour is not sufficient.

In contrast to the low field regime, the quantum regime of a linear magneto-conductance $G = W^2(e^3/h^2)|B|$ at high field is a unique contribution of the $n = 0$ Landau level. Thus it can be unambiguously associated with the chiral anomaly. This regime is reached for magnetic fields satisfying $B\lambda_F^2 \geq \pi h/e$ where λ_F is the Fermi wavelength. Thus it can be reached experimentally for chemical potentials sufficiently close to the band crossing. Moreover this regime is robust, and persists even in the presence of disorder: only its domain of existence is affected by elastic scattering. Furthermore, when energy relaxation occurs within the conductor the above ballistic conductance at high fields is replaced by $G = W^2(\ell'/L)(e^3/h^2)|B|$, also linear in magnetic field [Nielsen and Ninomiya, 1983, Aji, 2012, Gorbar et al., 2014]. In this regime the slope of the linear regime now depends explicitly on the amplitude of inter-cone scattering. Hence the study of this linear regime should provide an unambiguous determination of the regime of transport. In the exact same regime of transport a linear magneto-resistance in *transverse* magnetic field was also predicted by Abrikosov in [Abrikosov, 1998, Abrikosov, 2000] (see also [Lu et al., 2015a]). We believe that this quantum regime of transport in Weyl materials is of high experimental interest. As mentioned in section 5.1, a linear-in-field longitudinal magnetic conductance has already been observed in narrow wires of Weyl semi-metal NbP [Niemann et al., 2016]. In this experiment the linear regime is observed at room temperature, maybe in relation with “reentrance” of the linear regime that we have predicted for dominant intracone scattering. Although the experiment wasn’t designed to observe the ballistic magnetotransport of Weyl fermions, we think that it confirms that our proposal points in the right direction, and that the signature we propose is within experimental reach.

5.4 Conclusion

We have studied the conductance of a junction of Weyl material in the presence of a parallel magnetic field, and in the ballistic regime. We have shown that the low-field magneto-conductance displays low-temperature quantum oscillations, whose broadening results in an algebraic behaviour at vanishing field. At high fields, the magneto-conductance becomes linear in the field. Besides its experimental relevance, this ballistic regime allows discussing in details the relation between this conductance and the chiral anomaly of Weyl fermions. This allows to unambiguously identify the large field regime as a signature of the chiral anomaly. This work has been reported about in [Louvet et al., 2017b].

Chapter 6

Conclusion and Perspectives

Electrons with linear dispersion relation can be found near linear band crossings in bulk materials or on the boundaries of non trivial topological insulators. In the case of Weyl and Dirac fermions in 3D, the physics of electrons is described by a relativistic equation. Linear band crossings come in a lot of different flavors, with various number of bands, at isolated points or along extended regions of the Brillouin Zone. The great challenge is to classify and to outline the unifying trends of these phases. Relativistic fermions have specific properties which may not be unique to linearly dispersing particles but which have dramatic consequences. The projects carried during this thesis have shown that properties like their pseudospin and Berry phase, which originate from their relativistic nature, have consequences on their physical properties. Focusing on band and transport properties, we have seen that these features interact in a complex and intricate way.

Along this project, we have favored an approach based on low-energy models. We have considered linearized Hamiltonians describing the crossing. This approximation allowed us to use models and results known from high energy physics and field theory. It is remarkably efficient and predictive for Weyl and Dirac materials.

During our investigation on the topological characterization of band crossings we found a rich and complex variety of crossing. Existing litterature on new linear crossings beyond Dirac and Weyl has shown that the Berry phase properties of band crossings and their stability is eventually related to the crystalline symmetries of the full lattice. The existing zoology is frustrating because of its lack of unification. The cristallographic approach consisting of a thorough investigation of all space groups has proved efficient to exhibit new phases. However it has left physicists with as many different topological as there are different crossings: mirror Chern number, quantized Berry phase, mirror Chern number associated with a rotation symmetry, characterization of the connectivity of manifolds... Sometimes, as in graphene, different topological characterizations can be used and no criteria exists to differentiate between them. Hence, the search for a common framework in which to understand the topological properties and stability of crossings is still open. We have proposed to characterize the crossings as critical phases between insulating phases. This notion of critical topological phase allowed us to propose a local characterization, independent on the symmetries of the crystal: we view the crossing as a dimensional reduction of a higher dimensional crossing. We could thus understand the relation between the Chern number of a 3D Weyl point and the quantized Berry winding of graphene. When attempting to generalize these notions, we have understood that the relation between the stability of a crossing and its existence as a critical phase is far from trivial. No simple universal rule of correspondence between the topological properties of the crossing and the topological properties of the related higher dimensional phases could be established.

Our study on transport through evanescent states at the band crossing and the minimal conductivity highlights the importance of studying these evanescent states. They are often overlooked but emerge naturally at a linear band crossing in confined samples. We have shown that they somehow inherit from bulk properties and can thus be used to probe them, like the Berry phase of Bloch electrons. Recent developpments have been made in the design of photonic or microwave lattices. It opens great possibilities of modelization of low-energy models. Experimental realization of the three-band models from our study in artificial lattices could be made. It could provide an experimental verification of our predictions. Moreover the wavelength of excitations is large in these lattices. One could directly observe the spatial distribution of evanescent states in relation with transport properties.

Our study on the chiral anomaly proposes to consider ballistic Weyl junctions. This regime is well known in the field of mesoscopic physics, and we hope it will be relevant to experimentalists. Future lines of work should go towards a more realistic description of the sample. In particular the impact of disorder should be looked at. We have already considered the effect of a weak disorder using the semiclassical formalism. However, we know that a transition towards a diffusive metal is expected for stronger disorder, see Chapter 3. It would be interesting to study if the chiral magnetic effect survives through the transition, and conversely how the critical properties at the transition are affected by a magnetic field.

The disorder-driven transition in Weyl is still a subject of ongoing research. No consensus exists on the value of the critical exponents, neither on the nature or the mere existence of the transition. Moreover, the study of the diffusive metal phase beyond the critical point could prove fruitful.

Finally, we think that an improvement is needed regarding the implementation of Berry phase effects in the semi-classical formalism for transport. Existing studies are limited to the first order in magnetic field, and their validity for the description of a quadratic $\propto B^2$ behaviour of the magnetoconductance can be questionned. The role of the orbital magnetization and whether it can contribute to longitudinal magnetotransport should also be investigated in further studies.

Part III

Appendices

Appendix A

Renormalization Group Description of the Disorder-driven Quantum Phase Transition in Weyl Semimetals

A.1 Generalized Gross-Neveu model: $2 + \varepsilon$ expansion

The minimal action of the Weyl fermions in d dimensions can be rewritten in Fourier space as

$$S = \sum_{\alpha=1}^{N} \int_k \bar{\psi}_\alpha(-\mathbf{k})(\boldsymbol{\gamma}\mathbf{k} - i\omega)\psi_\alpha(\mathbf{k}) \\ - \sum_{\alpha,\beta=1}^{N} \sum_{n,\vec{A}} \frac{\Delta_n}{2} \int_{k_i} [\bar{\psi}_\alpha(\mathbf{k}_1)\gamma_{\vec{A}}^{(n)}\psi_\alpha(\mathbf{k}_2)] \times [\bar{\psi}_\beta(\mathbf{k}_3)\gamma_{\vec{A}}^{(n)}\psi_\beta(-\mathbf{k}_1 - \mathbf{k}_2 - \mathbf{k}_3)]. \quad \text{(A.1)}$$

One can build up a perturbation theory in small disorder calculating all correlation and vertex functions perturbatively in Δ_n. Each term can be represented as a Feynman diagram. In these diagrams the solid lines stand for the the bare propagator

$$\langle\bar{\psi}_\alpha(\mathbf{k}, \omega)\psi_\beta(-\mathbf{k}, -\omega)\rangle_0 = \delta_{\alpha\beta}\frac{\boldsymbol{\gamma}\mathbf{k} + i\omega}{k^2 + \omega^2}, \quad \text{(A.2)}$$

and the dashed line corresponds to one of the vertex $\frac{1}{2}\Delta_n$. Note that the dashed line transmit only momenta but not frequency. These terms turn out to be diverging in $d = 2$ which is the lower critical dimension of the transition. Simple scaling analysis shows that weak disorder is irrelevant for $d > 2$. To make the theory finite we use the dimensional regularization and compute all integrals in $d = 2 + \varepsilon_2$. At the end we put $\varepsilon_2 = 1$. To render the divergences we employ the minimal subtraction scheme and collect all poles in ε_2 in the Z-factors: Z_ψ, Z_ω and Z_n so that the correlation function calculated with the renormalized action

$$S_R = \sum_{\alpha=1}^{N} \int_k \bar{\psi}_\alpha(-\mathbf{k})(Z_\psi\boldsymbol{\gamma}\mathbf{k} - Z_\omega i\omega)\psi_\alpha(\mathbf{k}) - \sum_{\alpha,\beta=1}^{N} \sum_{n,A} Z_n \frac{\mu^{-\varepsilon}\Delta_n}{K_d} \int_{k_i} [\bar{\psi}_\alpha\gamma_A^{(n)}\psi_\alpha] \cdot [\bar{\psi}_\beta\gamma_A^{(n)}\psi_\beta] \quad \text{(A.3)}$$

remain finite in the limit $\varepsilon_2 \to 0$. Here we have introduced the renormalized fermionic fields ψ, $\bar{\psi}$ and the renormalized dimensionless coupling constants Δ_n on the mass scale μ, which are related to the bare parameters by

$$\mathring{\psi} = Z_\psi^{1/2}\psi, \quad \mathring{\bar{\psi}} = Z_\psi^{1/2}\bar{\psi}, \quad \text{(A.4)}$$

$$\mathring{\omega} = Z_\omega Z_\psi^{-1}\omega, \quad \mathring{\Delta}_n = \frac{2\mu^{-\varepsilon}}{K_d}\frac{Z_n}{Z_\psi^2}\Delta_n, \quad \text{(A.5)}$$

where $K_d = 2\pi^{d/2}/((2\pi)^d\Gamma(d/2))$ is the area of the d-dimensional unit sphere divided by $(2\pi)^d$. The renormalized and the bare vertex and Green functions are related by

$$\mathring{\Gamma}^{(\mathcal{N})}(p_i, \mathring{\omega}, \mathring{\Delta}) = Z_\psi^{-\mathcal{N}/2}\Gamma^{(\mathcal{N})}(p_i, \omega, \Delta, \mu), \quad \text{(A.6)}$$

$$\mathring{G}^{(\mathcal{N})}(p_i, \mathring{\omega}, \mathring{\Delta}) = Z_\psi^{\mathcal{N}/2}G^{(\mathcal{N})}(p_i, \omega, \Delta, \mu), \quad \text{(A.7)}$$

where Δ stands for all Δ_n. Using that the bare functions $\mathring{\Gamma}^{(\mathcal{N})}$ and $\mathring{G}^{(\mathcal{N})}$ do not depend on the renormalization scale μ we take the derivative of Eqs. (A.6) and (A.7) with respect to μ and obtain the RG flow equations for the renormalized Green and vertex functions:

$$\left[\mu\frac{\partial}{\partial\mu} - \sum_n \beta_n(\Delta)\frac{\partial}{\partial\Delta_n} - \frac{\mathcal{N}}{2}\eta_\psi(\Delta) - \gamma(\Delta)\omega\frac{\partial}{\partial\omega}\right]\Gamma^{(\mathcal{N})}(p_i,\omega,\Delta) = 0, \tag{A.8}$$

$$\left[\mu\frac{\partial}{\partial\mu} - \sum_n \beta_n(\Delta)\frac{\partial}{\partial\Delta} + \frac{\mathcal{N}}{2}\eta_\psi(\Delta) - \gamma(\Delta)\omega\frac{\partial}{\partial\omega}\right]G^{(\mathcal{N})}(p_i,\omega,\Delta) = 0. \tag{A.9}$$

Here we have defined the scaling functions

$$\beta_n(\Delta) = -\,\mu\frac{\partial\Delta_n}{\partial\mu}\bigg|_{\mathring{\Delta}}, \tag{A.10}$$

$$\eta_\psi(\Delta) = -\sum_n \beta_n(\Delta)\frac{\partial\ln Z_\psi}{\partial\Delta_n}, \tag{A.11}$$

$$\eta_\omega(\Delta) = -\sum_n \beta_n(\Delta)\frac{\partial\ln Z_\omega}{\partial\Delta_n}, \tag{A.12}$$

$$\gamma(\Delta) = \eta_\omega(\Delta) - \eta_\psi(\Delta). \tag{A.13}$$

Dimensional analysis gives the following rescaling formulas

$$\Gamma^{(\mathcal{N})}(p_i,\omega,\Delta,\mu) \;=\; \lambda^{-d+\mathcal{N}(d-1)/2}\times\Gamma^{(\mathcal{N})}(\lambda p_i,\lambda\omega,\Delta,\lambda\mu), \tag{A.14}$$

$$G^{(\mathcal{N})}(p_i,\omega,\Delta,\mu) \;=\; \lambda^{d(\mathcal{N}-1)-\mathcal{N}(d-1)/2}\times G^{(\mathcal{N})}(\lambda p_i,\lambda\omega,\Delta,\lambda\mu), \tag{A.15}$$

which can be rewritten in an infinitesimal form as

$$\left[\mu\frac{\partial}{\partial\mu} + \sum_i p_i\frac{\partial}{\partial p_i} + \omega\frac{\partial}{\partial\omega} - d + \frac{\mathcal{N}(d-1)}{2}\right]\Gamma^{(\mathcal{N})}(p_i,\omega,\Delta) = 0, \tag{A.16}$$

$$\left[\mu\frac{\partial}{\partial\mu} + \sum_i p_i\frac{\partial}{\partial p_i} + \omega\frac{\partial}{\partial\omega} + d(\mathcal{N}-1) - \frac{\mathcal{N}(d-1)}{2}\right]G^{(\mathcal{N})}(p_i,\omega,\Delta) = 0. \tag{A.17}$$

Subtracting Eqs. (A.8) and (A.9) from Eqs. (A.16) and (A.17) we obtain

$$\begin{aligned}\Bigg[\sum_n \beta_n(\Delta)\frac{\partial}{\partial\Delta_n} + \sum_i p_i\frac{\partial}{\partial p_i} + (1+\gamma(\Delta))\omega\frac{\partial}{\partial\omega}&\\ -d + \frac{\mathcal{N}}{2}\left[d-1+\eta_\psi(\Delta)\right]\Bigg]\Gamma^{(\mathcal{N})}(p_i,\omega,\Delta) = 0,&\end{aligned} \tag{A.18}$$

$$\begin{aligned}\Bigg[\sum_n \beta_n(\Delta)\frac{\partial}{\partial\Delta_n} + \sum_i p_i\frac{\partial}{\partial p_i} + (1+\gamma(\Delta))\omega\frac{\partial}{\partial\omega}&\\ +d(\mathcal{N}-1) - \frac{\mathcal{N}}{2}\left[d-1+\eta_\psi(\Delta)\right]\Bigg]G^{(\mathcal{N})}(p_i,\omega,\Delta) = 0.&\end{aligned} \tag{A.19}$$

The solutions of Eqs. (A.18) and (A.19) can be found by using the method of characteristics. The characteristics, i.e. lines in the space of p_i, ω, and Δ_n, parameterized by auxiliary parameter ξ which below will be identified with the correlation length, can be found from the equations

$$\frac{dp_i(\xi)}{d\ln\xi} = p_i(\xi), \tag{A.20}$$

$$\frac{d\Delta_n(\xi)}{d\ln\xi} = \beta_n(\Delta(\xi)), \tag{A.21}$$

$$\frac{d\omega(\xi)}{d\ln\xi} = [1+\gamma(\Delta(\xi))]\omega(\xi), \tag{A.22}$$

with initial conditions $\Delta_n(1) = \Delta_n$, $p_i(1) = p_i$, and $\omega(1) = \omega$. The solution of Eqs. (A.18) and (A.19) then propagate along the characteristics according to the equations

$$\begin{aligned}\frac{dM_{\mathcal{N}}(\xi)}{d\ln\xi} &= [-d + \frac{\mathcal{N}}{2}(d-1+\eta_\psi(\Delta(\xi)))]M_{\mathcal{N}}(\xi),\\ \frac{dH_{\mathcal{N}}(\xi)}{d\ln\xi} &= \left[d(\mathcal{N}-1) - \frac{\mathcal{N}}{2}(d-1+\eta_\psi(\Delta(\xi)))\right]H_{\mathcal{N}}(\xi),\end{aligned} \tag{A.23}$$

with the initial conditions $M_{\mathcal{N}}(1) = H_{\mathcal{N}}(1) = 1$. Thus the solutions of Eqs. (A.18) and (A.19) satisfy

$$\Gamma^{(\mathcal{N})}(p_i,\omega,\Delta) = M_{\mathcal{N}}(\xi)\Gamma^{(\mathcal{N})}(p_i(\xi),\omega(\xi),\Delta(\xi)), \tag{A.24}$$

$$G^{(\mathcal{N})}(p_i,\omega,\Delta) = H_{\mathcal{N}}(\xi)G^{(\mathcal{N})}(p_i(\xi),\omega(\xi),\Delta(\xi)). \tag{A.25}$$

We assume that the β-function has a fixed point (FP)

$$\beta(\Delta^*) = 0, \tag{A.26}$$

with a single unstable direction $\delta = \Delta - \Delta^*$, *i.e.* the stability matrix

$$\mathcal{M}_{nm} = \left.\frac{\partial\beta_n(\Delta)}{\partial\Delta_m}\right|_{\Delta^*}, \tag{A.27}$$

has only one positive eigenvalue $\lambda_1^{(+)}$ associated with the direction δ. Then the solutions (A.24) and (A.25) in the vicinity of the FP (A.26) can be rewritten as

$$\Gamma^{(\mathcal{N})}(p_i,\omega,\delta) = \xi^{\mathcal{N}d_\psi - d}f_{\mathcal{N}}(p_i\xi,\omega\xi^z,\delta\xi^{1/\nu}), \tag{A.28}$$

$$G^{(\mathcal{N})}(p_i,\omega,\delta) = \xi^{d(\mathcal{N}-1)-\mathcal{N}d_\psi}g_{\mathcal{N}}(p_i\xi,\omega\xi^z,\delta\xi^{1/\nu}), \tag{A.29}$$

where we defined the critical exponents ν, z, d_ψ. The parameter ξ can be identified with the correlation length that gives the critical exponent for the correlation length

$$\xi \sim \delta^{-\nu}, \qquad \frac{1}{\nu} = \lambda_1^{(+)}, \tag{A.30}$$

and the dynamic dynamic critical exponent

$$\omega \sim k^z, \qquad z = 1 + \gamma(\Delta^*). \tag{A.31}$$

The anomalous dimension of the fields ψ and $\bar{\psi}$ reads

$$d_\psi = \frac{1}{2}[d - 1 + \eta_\psi(\Delta^*)]. \tag{A.32}$$

Note, that the exponent η_ψ characterizes the scaling behavior of the two-point function

$$G^{(2)}(p) = \overline{\langle\bar{\psi}(p)\psi(-p)\rangle} \sim p^{-1+\eta_\psi(\Delta^*)}, \tag{A.33}$$

which can be viewed as the momentum distribution of fermions at the transition.

A.1.1 Critical exponents to three-loop order

To renormalize the theory we use the minimal substraction scheme

$$Z_\psi\mathring{\Gamma}^{(2)}(p,\omega = Z_\omega Z_\psi^{-1}\mu,\mathring{\Delta}(\Delta)) = \text{finite}, \tag{A.34}$$

$$Z_\psi^2\mathring{\Gamma}_n^{(4)}(p_i = 0,\omega = Z_\omega Z_\psi^{-1}\mu,\mathring{\Delta}(\Delta)) = \text{finite}, \tag{A.35}$$

where $\mathring{\Delta}(\Delta)$ is given by Eq. (A.4) and $\mathring{\Gamma}_n^{(4)}$ is the renormalized vertex V_n. The three-loop corrections to the vertex V_0 have been many times discussed in the literature in the context of the GN model [Zinn-Justin, 2002]. The corresponding β_0-function defined in Eq. (A.10) reads

$$\begin{aligned}\beta_0 \quad = \quad & -\varepsilon_2\Delta_0 - 2\Delta_0^2(N-2) - 4\Delta_0^3(N-2)\\ & +2\Delta_0^4(N-2)(N-7),\end{aligned} \tag{A.36}$$

where we kept the dependence on N. The 24 diagrams derived from the diagram (b) shown in Fig. A.1 by permutation of the dashed line ends which were neglected in [Roy et al., 2016] generate the vertex V_3 [Vasiliev and Vyazovsky, 1997]. Other diagrams which one has to take into account in calculation to order of ε_2^3 are the diagrams (c)-(e) shown in Fig. A.1. These diagrams with lines corresponding to V_0 and V_3 contribute to V_4 and with lines corresponding to V_0 and V_3 contribute to V_4. Since the contributions of the diagrams (b) are of order Δ_0^4 one may naively conclude that while Δ_0 is of order ε_2, the two over vertices Δ_3 and Δ_4 are of order ε_2^3. Indeed, the corresponding β-functions

$$\begin{aligned}\beta_3 &= -\varepsilon_2\Delta_3 + a\Delta_0^4 + 16\Delta_0\Delta_4 + 8\Delta_0\Delta_3. && \text{(A.37)}\\ \beta_4 &= -\varepsilon_2\Delta_4 - 4\Delta_0\Delta_3 - 12\Delta_0\Delta_4, && \text{(A.38)}\end{aligned}$$

have the fixed point

$$\begin{aligned}\Delta_0^* &= \frac{\varepsilon_2}{4-N} - \frac{\varepsilon_2^2}{2(2-N)^2} + \frac{(1+N)\varepsilon_2^3}{8(2-N)^3} + O(\varepsilon_2^4), && \text{(A.39)}\\ \Delta_3^* &= \frac{a\varepsilon_2^3(N-8)}{16N(N-6)(N-2)^3} + O\left(\varepsilon_2^4\right), && \text{(A.40)}\\ \Delta_4^* &= \frac{a\varepsilon_2^3}{8N(N-6)(N-2)^3} + O\left(\varepsilon_2^4\right), && \text{(A.41)}\end{aligned}$$

which has non analytic behavior in the limit $N \to 0$. Taking first the limit $N \to 0$ in the β-functions one finds the fixed point

$$\begin{aligned}\Delta_0^* &= \frac{\varepsilon_2}{4} - \frac{\varepsilon_2^2}{8} + \frac{\varepsilon_2^3}{64} + O(\varepsilon_2^4), && \text{(A.42)}\\ \Delta_3^* &= \frac{a\varepsilon_2^2}{96} - \frac{23a\varepsilon_2^3}{1152} + O\left(\varepsilon_2^4\right), && \text{(A.43)}\\ \Delta_4^* &= -\frac{a\varepsilon_2^2}{384} + \frac{49a\varepsilon_2^3}{9216} + O\left(\varepsilon_2^4\right), && \text{(A.44)}\end{aligned}$$

similar to $\sqrt{\varepsilon}$ expansion for the diluted Ising model [Shalaev et al., 1997]. The stability of the FP can be described by the eigenvalues of the stability matrix $\frac{\partial\beta_i}{\partial\Delta_j}|_{\Delta^*}$, $i,j \in 0,3,4$. Since one expects that the transition is controlled by an unstable IR FP, the stability matrix is expected to have only one positive eigenvalue which is related to the critical exponent $1/\nu = \lambda_1^{(+)}$. The stability eigenvalues read:

$$\begin{aligned}&\frac{1}{\nu} = \lambda_1^{(+)} = \varepsilon_4 + \frac{\varepsilon_4^2}{2} + \frac{3\varepsilon_4^3}{8} + O\left(\varepsilon_4^4\right), && \text{(A.45)}\\ &\lambda_2^{(-)} = -3\varepsilon_4 + \varepsilon_4^2 - \frac{\varepsilon_4^3}{8} + O\left(\varepsilon_4^4\right), && \text{(A.46)}\\ &\lambda_3^{(-)} = -\frac{\varepsilon_4^2}{2} + \frac{\varepsilon_4^3}{16} + O\left(\varepsilon_4^4\right). && \text{(A.47)}\end{aligned}$$

Only the first eigenvalue (A.45) associated with a single instability direction is positive.

The generation of vertices Δ_3 and Δ_4 at three-loop order might renormalize ω and thus give a correction to the other critical exponents via diagrams of the type of diagram (a) of Fig. A.1. The combinatorial factor associated to this diagram is 2. The contribution will take the form ($n = 3, 4$):

$$\begin{aligned}I_n &= \sum_{A=\{i_1,..,i_n\}} \gamma_A^{(n)} \int_{\mathbf{k}} \frac{\boldsymbol{\gamma}\mathbf{k} + i\omega}{k^2+\omega^2} \gamma_A^{(n)}\\ &= \sum_{A=\{i_1,..,i_n\}} \gamma_A^{(n)}\gamma_A^{(n)} \int_{\mathbf{k}} \frac{i\omega}{k^2+\omega^2}, && \text{(A.48)}\end{aligned}$$

besides

$$\gamma_A^{(n)} = As[\gamma_{i_1}....\gamma_{i_n}] \qquad = \epsilon^{i_1..i_n}\gamma_{i_1}....\gamma_{i_n}, \tag{A.49}$$

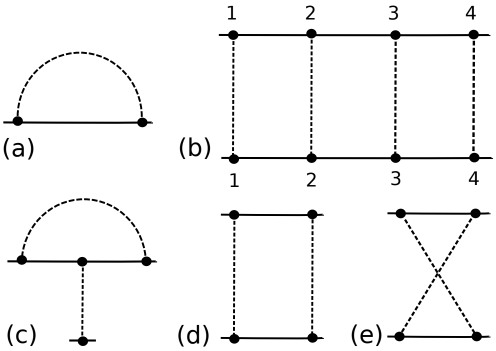

Figure A.1: Diagrams entering the renormalization of the generalized GN action. Solid lines stands for fermionic propagators and dashed lines for disorder vertices.

where the set of indices is set and $\epsilon^{i_1..i_n}$ is the corresponding element of the n-th Levi Civita tensor. Therefore (no contraction on A is implied here):

$$\begin{aligned}(\gamma_A^{(n)})^2 &= (\epsilon^{i_1..i_n})^2 \gamma_{i_1}....\gamma_{i_n}\gamma_{i_1}....\gamma_{i_n} \\ &= \gamma_{i_1}....\gamma_{i_n}\gamma_{i_1}....\gamma_{i_n} \\ &= (-1)^{n-1}\gamma_{i_2}....\gamma_{i_n}(\gamma_{i_1})^2\gamma_{i_2}....\gamma_{i_n} \\ &= (-1)^{(n-1)!}\mathbb{I} \end{aligned} \tag{A.50}$$

using the anticommutation relation $\{\gamma_\mu, \gamma_\nu\} = 2\delta_{\mu\nu}\mathbb{I}$ and assuming all indices $i_1, ..., i_n$ are distinct (otherwise, $\gamma_A^{(n)}$ vanishes trivially.) Note that since $n = 3$ or 4, $(-1)^{(n-1)!} = 1$. Performing the sum in (A.48) thus yields:

$$I_n = \binom{d}{n} \int_{\mathbf{k}} \frac{i\omega}{k^2+\omega^2} \propto (d-2) \int \frac{d^d\mathbf{k}}{(2\pi)^d} \frac{i\omega}{k^2+\omega^2} \tag{A.51}$$

For $n = 3, 4$, $\binom{d}{n} \propto (d-2) = O(\varepsilon)$, and thus the binomial coefficient cancels the pole in the integral, making the contribution $I_n = O(1)$ finite. At the end of the day we find that this diagram will give no contribution to the frequency renormalisation and a fortiori to the z exponent. Thus the critical exponents to three-loop order are given by

$$z = 1 + \frac{\varepsilon_2}{2} - \frac{\varepsilon_2^2}{8} + \frac{3\varepsilon_2^3}{32} + O(\varepsilon_2^4), \tag{A.52}$$

$$\eta = -\frac{\varepsilon_2^2}{8} + \frac{3\varepsilon_2^3}{16} - \frac{25\varepsilon_2^4}{128} + O(\varepsilon_2^5). \tag{A.53}$$

$$\begin{aligned} d_\psi &= \frac{1}{2}[d - 1 + \eta_\psi] \\ &= \frac{1}{2} + \frac{\varepsilon}{2} - \frac{\varepsilon^2}{16} + \frac{3\varepsilon_2^3}{32} - \frac{25\varepsilon_2^4}{256} + O(\varepsilon_2^5). \end{aligned} \tag{A.54}$$

To estimate numerical values of the exponents in $d = 3$ we use direct evaluation at $\varepsilon_2 = 1$ (D), Padé approximant P$[M/L]$ and Padé-Borel resummation PB$[M/L]$. We find $z = 1.469$ (D), $z = 1.429$ (P[2/1]) and $z = 1.425$ (PB[2/1]); $\eta = 0.0625$ (D) to three loop and $\eta = -0.133$ (D) to four loop.

A.1.2 Renormalization of composite operators

We now discuss the renormalization of the composite operators

$$\mathcal{O}_q(r) := \left(\bar{\psi}_\alpha(r)\psi_\alpha(r)\right)^q. \tag{A.55}$$

which are related to the the deviation of the disorder distribution from the Gaussian distribution. The bare scaling dimension of operators (A.55) is $[\mathcal{O}_q] = (d-1)q + O(\Delta)$. To find their scaling dimension in the GN FP we introduce the Z-factors

$$\mathring{\mathcal{O}}_q = \mathcal{Z}_q Z_\psi^{-q} \mathcal{O}_q. \tag{A.56}$$

which has to render the divergence of the correlation functions involving operators (A.55) . To one loop order the diagrams contributing to the Z_q factor are shown in Fig. A.2. We find to one-loop order

$$\mathcal{Z}_q = 1 + 2[q + q(q-1)]\frac{\Delta_0}{\varepsilon_2}. \tag{A.57}$$

The corresponding scaling function

$$\eta_q(\Delta) = -\sum_n \beta_n(\Delta)\frac{\partial \ln Z_q}{\partial \Delta_n}, \tag{A.58}$$

gives the scaling dimension of the composite operators (A.55)

$$[\mathcal{O}_q] = (d - 1 + \eta_\psi)q - \eta_q(\Delta^*). \tag{A.59}$$

To one loop order this yields

$$[\mathcal{O}_q] = (1 + \varepsilon_2)q - \frac{1}{2}q^2\varepsilon_2 + O(\varepsilon_2^2), \tag{A.60}$$

that is consistent with the conformal theory results of [Ghosh et al., 2016].

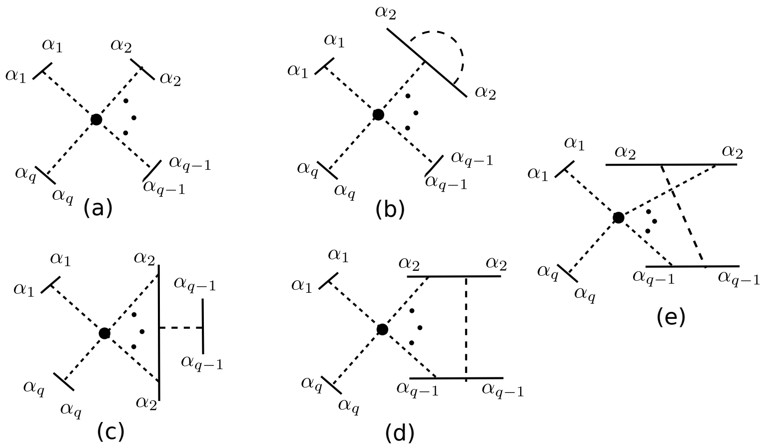

Figure A.2: Diagrams renormalizing the composite operators (A.55). (a) is the bare vertex corresponding to a composite operator (A.55), (a) - (e) are the one-loop diagrams contributing to renormalization (A.56): (b) $= qI_1$, (c)$= q(q-1)I_1$, (d)+(e) $= 0$, where I_1 is the one-loop integral.

In order to calculate the scaling behavior of the local DOS $\rho(\omega, \delta)$ it is enough to consider renormalization of the composite operator $\mathcal{O}_1$. The corresponding Z factor is not independent and is related to Z_ω by

$$\mathring{\mathcal{O}}_1 = Z_\omega Z_\psi^{-1} \mathcal{O}_1. \tag{A.61}$$

We can write the flow equation for the local DOS as

$$\begin{aligned}\Bigg[\sum_n \beta_n(\Delta)\frac{\partial}{\partial \Delta_n} + (1 + \gamma(\Delta))\omega\frac{\partial}{\partial \omega} \\ -(d-1) + \eta_\omega(\Delta) - \eta_\psi(\Delta)\Bigg]\rho(\omega, \Delta) = 0.\end{aligned} \tag{A.62}$$

The solution of Eq. (A.62) in the vicinity of the FP (A.26) has the form

$$\rho(\omega) = \xi^{z-d}\rho_0(\omega\xi^z, \delta\xi^{1/\nu}), \tag{A.63}$$

with $z = [\mathcal{O}_1]$ given to three-loop order by (A.52).

A.2 Gross-Neveu-Yukawa model: $4-\varepsilon$ expansion

A.2.1 Model

The action for the $U(N)$ GNY model is given by

$$S_{GNY} = \int d^d r[-\bar{\chi}_\alpha(\boldsymbol{\gamma}\cdot\boldsymbol{\nabla} + \sqrt{g}\phi)\chi_\alpha + \frac{1}{2}(\nabla\phi)^2 + \frac{1}{2}\mu\phi^2 + \frac{\lambda}{4!}\phi^4]. \tag{A.64}$$

We are interested in the $N\to 0$ limit. In Fourier space $(-i\boldsymbol{\gamma}\cdot\boldsymbol{\nabla}\to\boldsymbol{\gamma}\cdot\mathbf{k})$, the bare fermionic and bosonic propagators read

$$\langle\chi_\alpha(\mathbf{k})\chi_\alpha(-\mathbf{k}')\rangle = i\frac{\boldsymbol{\gamma}\cdot\mathbf{k}}{k^2} \tag{A.65a}$$

$$\langle\phi(\mathbf{q})\phi(-\mathbf{q})\rangle = \frac{1}{q^2+\mu}. \tag{A.65b}$$

A.2.2 Renormalization

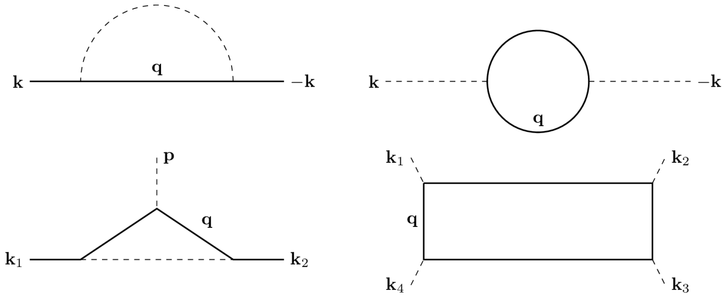

Figure A.3: Diagrams entering the renormalization of the GNY action to one-loop order. Solid lines stand for the fermionic propagator and dashed lines for the bosonic one. Diagrams from ϕ^4 theory not shown.

We perform a perturbative expansion of correlation and vertex functions in the disorder parameters g and λ. Fig. A.3 shows the diverging diagrams in $d=4$ that involve fermionic-bosonic vertices. Other diverging diagrams come from the expansion in λ and are known from the ϕ^4 theory. We use dimensional regularization in $d=4-\varepsilon_4$ and put $\varepsilon_4=1$ at the end of the day.

Following the minimal substraction scheme, we introduce the renormalization constants Z_χ, Z_ϕ, Z_μ, Z_g and Z_λ. Calling Λ the renormalization scale, the renormalized action reads:

$$\begin{aligned} S = \int d^d r[&-\bar{\chi}_\alpha(Z_\chi\boldsymbol{\gamma}\cdot\boldsymbol{\nabla} + \Lambda^{\varepsilon_4/2}\sqrt{gZ_g}\phi)\chi_\alpha \\ &+ \frac{1}{2}Z_\phi(\nabla\phi)^2 + \frac{1}{2}[\mu_c Z_\phi + \Lambda^2 Z_\mu\ \delta\mu]\phi^2 + \Lambda_4^{\varepsilon} Z_\lambda\frac{\lambda}{4!}\phi^4]. \end{aligned} \tag{A.66}$$

The renormalized fields are related to the bare ones through $\mathring{\chi} = Z_\chi^{1/2}\chi$, and $\mathring{\phi} = Z_\phi^{1/2}\phi$. Similarly, we define the renormalized bosonic mass $\mathring{\mu} = \mu_c + \Lambda^2 Z_\mu Z_\phi^{-1}\ \delta\mu$. The relations between bare and renormalized couplings read $\mathring{g} = \Lambda^{\varepsilon_4} Z_g Z_\chi^{-2} Z_\phi^{-1} g$ and $\mathring{\lambda} = \Lambda^{\varepsilon_4} Z_\lambda Z_\phi^{-2}\lambda$, where we have introduced the renormalization scale Λ to render the renormalized couplings dimensionless.

The bare and renormalized correlation and vertex functions are related as follows:

$$\mathring{\Gamma}^{(n,l)}(p_i, q_j, \mathring{\mu}-\mu_c, \mathring{g}, \mathring{\lambda}) = Z_\chi^{-n/2} Z_\phi^{-l/2}\Gamma^{(n,l)}(p_i, q_j, \delta\mu, g, \lambda, \Lambda), \tag{A.67a}$$

$$\mathring{G}^{(n,l)}(p_i, q_j, \mathring{\mu}-\mu_c, \mathring{g}, \mathring{\lambda}) = Z_\chi^{n/2} Z_\phi^{l/2} G^{(n,l)}(p_i, q_j, \delta\mu, g, \lambda, \Lambda). \tag{A.67b}$$

From Eq. (A.67a) we derive the RG flow equation for the vertex functions:

$$\left[\Lambda\frac{\partial}{\partial\Lambda} - \beta_g\frac{\partial}{\partial g} - \beta_\lambda\frac{\partial}{\partial\lambda} - \frac{n}{2}\eta_\chi - \frac{l}{2}\eta_\phi - \gamma_\mu\delta\mu\frac{\partial}{\partial\delta\mu}\right]\Gamma^{(n,l)}(p_i, q_j, \delta\mu, g, \lambda, \Lambda) = 0, \tag{A.68}$$

with the scaling functions:

$$\beta_g(g,\lambda) = -\,\Lambda \frac{\partial g}{\partial \Lambda}\bigg|_{\mathring{g},\mathring{\lambda}}, \tag{A.69a}$$

$$\beta_\lambda(g,\lambda) = -\,\Lambda \frac{\partial \lambda}{\partial \Lambda}\bigg|_{\mathring{g},\mathring{\lambda}}, \tag{A.69b}$$

$$\eta_\chi(g,\lambda) = -\sum_{u=\lambda,g} \beta_u \frac{\partial \ln Z_\chi}{\partial u}, \tag{A.69c}$$

$$\eta_\phi(g,\lambda) = -\sum_{u=\lambda,g} \beta_u \frac{\partial \ln Z_\phi}{\partial u}, \tag{A.69d}$$

$$\eta_\mu(g,\lambda) = -\sum_{u=\lambda,g} \beta_u \frac{\partial \ln Z_\mu}{\partial u}, \tag{A.69e}$$

$$\gamma_\mu(g,\lambda) = 2 + \eta_\mu - \eta_\phi. \tag{A.69f}$$

Besides, dimensional analysis gives

$$\Gamma^{(n,l)}(p_i, q_j, \delta\mu, g, \lambda, \Lambda) = X^{-d+n(d-1)/2+l(d-2)/2}\Gamma^{(n,l)}(Xp_i, Xq_j, \delta\mu, g, \lambda, X\Lambda), \tag{A.70a}$$

$$G^{(n,l)}(p_i, q_j, \delta\mu, g, \lambda, \Lambda) = X^{(n+l-1)d-n(d-1)/2-l(d-2)/2}G^{(n,l)}(Xp_i, Xq_j, \delta\mu, g, \lambda, X\Lambda). \tag{A.70b}$$

We rewrite the relation (A.70a) in an infinitesimal form as

$$\left[\Lambda\frac{\partial}{\partial\Lambda} + p_i\frac{\partial}{\partial p_i} + q_j\frac{\partial}{\partial q_j} - d + \frac{n(d-1)}{2} + \frac{l(d-2)}{2}\right]\Gamma^{(n,l)}(p_i, q_j, \delta\mu, g, \lambda, \Lambda) = 0, \tag{A.71}$$

Subtracting (A.68) from (A.71) to get rid of the derivative with respect to Λ we obtain

$$\left[\beta_g\frac{\partial}{\partial g} + \beta_\lambda\frac{\partial}{\partial\lambda} + p_i\frac{\partial}{\partial p_i} + q_j\frac{\partial}{\partial q_j} + \gamma_\mu\delta\mu\frac{\partial}{\partial\delta\mu} - d + \frac{n}{2}(\eta_\chi + d - 1) + \frac{l}{2}(\eta_\phi + d - 2)\right]\Gamma^{(n,l)}(p_i, q_j, \delta\mu, g, \lambda, \Lambda) = 0. \tag{A.72}$$

The solutions to Eq. (A.72) can be found using the method of characteristics. These solutions propagate along specific lines in the space of p_i, q_j, $\delta\mu$, g and λ called the characteristics. The characteristics are parametrized by an auxiliary parameter L, which can be identified with a length scale; they are determined by the following set of RG flow equations:

$$\frac{dp_i(L)}{d\ln L} = p_i(L), \tag{A.73a}$$

$$\frac{dq_i(L)}{d\ln L} = q_i(L), \tag{A.73b}$$

$$\frac{d\delta\mu(L)}{d\ln L} = \gamma_\mu\delta\mu(L), \tag{A.73c}$$

$$\frac{dg(L)}{d\ln L} = \beta_g(g(L)), \tag{A.73d}$$

$$\frac{d\lambda(L)}{d\ln L} = \beta_\lambda(\lambda(L)), \tag{A.73e}$$

with initial conditions $p_i(1) = p_i$, $q_j(1) = q_j$, $\delta\mu(1) = \delta\mu$, $g(1) = g$, $\lambda(1) = \lambda$. Thus the solutions of (A.72) satisfy

$$\Gamma^{(n,l)}(p_i, q_i, \delta\mu, g, \lambda) = \mathcal{M}(L)\Gamma^{(n,l)}(p_i(L), q_i(L), \delta\mu(L), g(L), \lambda(L)). \tag{A.74}$$

with

$$\frac{d\ln\mathcal{M}_{n,l}(L)}{d\ln L} = \frac{n}{2}(\eta_\chi + d - 1) + \frac{l}{2}(\eta_\phi + d - 2) - d. \tag{A.75}$$

In the vicinity of the critical point the RG flow parameter L can be identified with the correlation length ξ in (A.73), allowing one to calculate the critical exponents from the RG equations.

A.2.3 Critical exponents

Calculation of the one-loop diagrams shown in Fig. A.3 in the limit $N \to 0$ gives [Zinn-Justin, 2002]:

$$\Gamma^{(2,0)} = \langle \bar{\chi}(\mathbf{k})\chi(-\mathbf{k})\rangle^{-1} = i\boldsymbol{\gamma p} Z_\chi + i\boldsymbol{\gamma p}\frac{K_d}{2}\frac{g}{\varepsilon_4}, \tag{A.76a}$$

$$\Gamma^{(2,1)} = \langle \bar{\chi}(\mathbf{k}_1)\chi(\mathbf{k}_2)\phi(\mathbf{p})\rangle_{1\text{PI}} = \sqrt{gZ_g} - g^{3/2}\frac{K_d}{\varepsilon_4}, \tag{A.76b}$$

$$\Gamma^{(0,2)} = \langle \phi(\mathbf{k})\phi(-\mathbf{k})\rangle^{-1} = Z_\phi k^2 + Z_\mu \delta\mu - \frac{\lambda}{2}\delta\mu\frac{K_d}{\varepsilon_4}, \tag{A.76c}$$

$$\Gamma^{(0,4)} = \langle \phi(\mathbf{k}_1)\phi(\mathbf{k}_2)\phi(\mathbf{k}_3)\phi(\mathbf{k}_4)\rangle_{1\text{PI}} = Z_\lambda \lambda - \frac{3}{2}\lambda^2\frac{K_d}{\varepsilon_4}. \tag{A.76d}$$

To make these functions finite, we define the renormalization constants as follows:

$$Z_\chi = 1 - \frac{1}{2}g\frac{K_d}{\varepsilon_4}, \tag{A.77a}$$

$$Z_\phi = 1, \tag{A.77b}$$

$$Z_\mu = 1 + \frac{\lambda}{2}\frac{K_d}{\varepsilon_4}, \tag{A.77c}$$

$$Z_g = 1 + 2g\frac{K_d}{\varepsilon_4}, \tag{A.77d}$$

$$Z_\lambda = 1 + \frac{3}{2}\lambda\frac{K_d}{\varepsilon_4}. \tag{A.77e}$$

It is convenient to include $K_d/2$ in the redefinition of g and λ. The β-functions read

$$\beta_g(g,\lambda) = \varepsilon_4 g - 6g^2 \tag{A.78a}$$

$$\beta_\lambda(g,\lambda) = \varepsilon_4 \lambda - 3\lambda^2, \tag{A.78b}$$

The FP solution is given by

$$g_* = \frac{\varepsilon_4}{6},\ \lambda_* = \frac{\varepsilon_4}{3}. \tag{A.79}$$

The critical length exponent is defined by:

$$\xi \sim \delta\mu^{-\nu}, \tag{A.80}$$

thus from the RG equations (A.73), identifying the parameter L to the correlation length ξ in the region near the critical point we get

$$\nu^{-1} = \gamma_\mu = 2 - \lambda_* = 2 - \frac{\varepsilon_4}{3} + O(\varepsilon_4^2). \tag{A.81}$$

The anomalous dimension of the fermionic field reads

$$\begin{aligned} d_\chi &= \frac{1}{2}(d-1+\eta_\chi) = \frac{1}{2}(d-1+g_*) \\ &= \frac{3}{2} - \frac{5}{12}\varepsilon_4 + O(\varepsilon_4^2). \end{aligned} \tag{A.82}$$

When $\delta\mu$ is negative, the scalar field acquires a finite expectation values which generates in turn a fermion mass $m_\chi = \sqrt{g}\langle\phi\rangle$. This fermionic mass is analogous to a frequency and thus scales with the correlation length like $m_\chi \sim \xi^{-z}$. Besides, the correlations of the scalar field are determined by a ϕ^4 field theory; it is known that close to the transition the order parameter of this theory scales like

$$\langle\phi\rangle \sim \delta\mu^\beta \sim \xi^{-\beta/\nu}, \tag{A.83}$$

where ν is given by (A.80). Besides, from the RG analysis we have established that the dimensionful coupling constant $\sqrt{g}$ flows towards the FP as $\sqrt{g} \sim \xi^{-\varepsilon_4/2}\sqrt{g^*}$. This leads to

$$m_\chi \sim \sqrt{g}\langle\phi\rangle \sim \xi^{-\varepsilon_4/2-\beta/\nu}, \tag{A.84}$$

and therefore we get $z = \varepsilon_4/2 + \beta/\nu$. Moreover, the exponent β is related to the exponent ν through the scaling relation

$$\nu d = 2\beta + (2 - \eta_\phi)\nu. \tag{A.85}$$

From (A.77e) we know $Z_\phi = 1$, which gives $\eta_\phi = O(\varepsilon_4^2)$. Hence we get

$$\beta = \nu\frac{2 - \varepsilon_4}{2}, \tag{A.86}$$

and finally we find for the critical dynamic exponent z to one loop order:

$$z = \frac{\varepsilon_4}{2} + \frac{2 - \varepsilon_4}{2} = 1 + O(\varepsilon_4^2). \tag{A.87}$$

The two-loop order contribution can be calculated using the two loop expression of $2-\eta_\phi$ [Kärkkäinen et al., 1994]:

$$2 - \eta_\phi = 2 - \frac{\varepsilon_4^2}{54} + O(\varepsilon_4^3), \tag{A.88}$$

which gives

$$\begin{aligned} z &= \frac{\varepsilon_4}{2} + \frac{\beta}{\nu} = \frac{\varepsilon_4}{2} + \frac{1}{2}(d - 2 + \eta_\phi) \\ &= 1 + \frac{\varepsilon_4^2}{108} + O(\varepsilon_4^3). \end{aligned} \tag{A.89}$$

A.2.4 Instanton solutions

We now show the existence of localized instanton solutions to the GNY action in the limit $N \to 0$ that can give a non-zero contribution to the zero-energy DOS in the semimetallic phase, similar to that found for the GN model in [Nandkishore et al., 2014]. Following [Falco et al., 2009] we start by rewriting the average DOS at the Dirac point directly in $d = 3$ in the form:

$$\langle \rho(E = 0)\rangle_V = \frac{1}{L^3}\int D[V, \chi, \Psi, \Upsilon] \exp[-S], \tag{A.90}$$

where $\Psi(x)$ is a Lagrange multiplier field selecting solutions to the Dirac equation and Υ is a Lagrange multiplier enforcing normalization of $\Psi(x)$ and the action is given by

$$\begin{aligned} S = \int d^3x \left[(\nabla\phi)^2 + \mu\phi(x)^2 + \frac{\lambda}{4!}\phi(x)^4\right] - \int d^3x\ \Psi^\dagger(x)(\boldsymbol{\sigma}\cdot\nabla + \sqrt{g}\phi)\chi(x) \\ + \Upsilon\left[\int d^3x\ \chi^\dagger(x)\chi(x) - 1\right], \end{aligned} \tag{A.91}$$

where $\boldsymbol{\sigma} = \sigma_x, \sigma_y, \sigma_z$ are the Pauli matrices. We now look for a saddle-point solution to the classical equations of motion. To obtain the latter we vary the action (A.91) with respect to ϕ, χ, $\chi^\dagger$, $\Psi^\dagger$, and Υ. This yields

$$-\nabla^2\phi(x) + \mu\phi(x) + \frac{\lambda}{3!}\phi(x)^3 = \sqrt{g}\Psi^\dagger(x)\chi(x), \tag{A.92}$$

$$\Psi^\dagger(x)[\boldsymbol{\sigma}\cdot\nabla + \sqrt{g}\phi(x)] = 0, \tag{A.93}$$

$$[\boldsymbol{\sigma}\cdot\nabla + \sqrt{g}\phi(x)]\chi(x) = 0, \tag{A.94}$$

$$\int d^3x\ \chi^\dagger(x)\chi(x) = 1, \tag{A.95}$$

$$\Upsilon\ \chi(x) = 0. \tag{A.96}$$

From Eq. (A.96) it follows that $\Upsilon = 0$ and thus we can take $\Psi^\dagger(x) = \Psi_0\chi^\dagger(x)$ where Ψ_0 is a real number. Since the disorder distribution is isotropic it is naturally to assume that the DOS is dominated by a spherically symmetric saddle-point solution. This drastically simplifies the solution of the classical equations of motion (A.92)-(A.96) since they can be reduced to the problem of a Dirac particle in a self-consistent central potential. The solution to this problem can be factorized in the radial and angular parts according to

$$\chi = f_1(r)\varphi^- - f_2(r)\varphi^+, \tag{A.97}$$

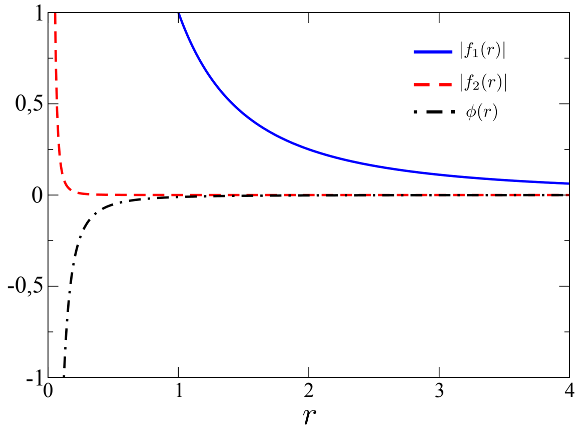

Figure A.4: The instanton wavefunction components (f_1: blue, continuous, f_2: red, dashed) (A.97) and scalar field ϕ (black, dot-dashed) solution of (A.99)-(A.101) computed numerically using the expansion (A.102)-(A.104) for $A = 1$, $\mu = -0.1$, $\lambda = 0.001$, $g = 0.001$, and $\Psi_0 = 1$.

where $\varphi^{\pm}$ are two-component spinors with total angular momentum j, angular momentum along z j_z and orbital angular momentum $l^{\pm} = j \mp 1/2$. We have:

$$\begin{aligned}\boldsymbol{\sigma}\cdot\boldsymbol{\nabla} f_i(r)\varphi^{\pm} =& \boldsymbol{\sigma}\cdot\hat{\mathbf{r}}\left(\partial_r - \frac{\boldsymbol{\sigma}\cdot\mathbf{L}}{r}\right) f_i(r)\varphi^{\pm}\\ =& \left(\partial_r + \frac{1-\kappa}{r}\right) f_i(r)\ \boldsymbol{\sigma}\cdot\hat{\mathbf{r}}\ \varphi^{\pm}\\ =& \left(\partial_r + \frac{1-\kappa}{r}\right) f_i(r)\varphi^{\mp},\end{aligned} \tag{A.98}$$

with $\kappa = \pm(j + 1/2) = \pm 1$ for the lowest level $j = 1/2$. Thus we get the following system:

$$\partial_r f_2(r) = f_1(r)\sqrt{g}\phi(r), \tag{A.99}$$

$$(\partial_r + \frac{2}{r})f_1(r) = f_2(r)\sqrt{g}\phi(r), \tag{A.100}$$

$$-(\partial_r^2 + \frac{2}{r}\partial_r - \mu)\phi + \frac{\lambda}{3!}\phi^3 = \sqrt{g}\Psi_0\left[|f_1|^2 + |f_2|^2\right]. \tag{A.101}$$

The large r expansion of the Eqs. (A.99)-(A.101) gives the following asymptotic behavior

$$\begin{aligned} f_1(r) &= \frac{A}{r^2} + \frac{A^5 g^2}{30\mu^2}\frac{1}{r^8} + O(\frac{A^9 g^4}{\mu^4 r^{14}}), && \text{(A.102)}\\ f_2(r) &= -\frac{A^3 g}{5\mu}\frac{1}{r^5} - 7\frac{A^7 g^3}{550\mu^3}\frac{1}{r^{11}} + O(\frac{A^{11} g^5}{\mu^5 r^{17}}), && \text{(A.103)}\\ \phi(r) &= \frac{A^2\sqrt{g}}{\mu}\frac{1}{r^4} + O(\frac{A^6 g^{5/2}}{\mu^3 r^{10}}), && \text{(A.104)}\end{aligned}$$

which depends on a single free parameter A. A typical solution to Eqs. (A.99)-(A.101) obtained numerically using the asymptotic behavior (A.102)-(A.104) is shown in Fig.A.4. The wave function and disorder distribution both exhibit a singular behavior at $r = 0$ and thus require a regularization [Nandkishore et al., 2014]. Moreover, to obtain the full instanton contribution to the DOS (using either GN or GNY models) one has to expand around the instanton solution and calculate the corresponding Gaussian integral which gives a prefactor to the exponential behavior. It is known that in the case of quadratic dispersion this prefactor can be expressed in the form of a ratio of two functional determinants which diverges in $d > 1$. Thus, in this case the instanton solution requires renormalization [Falco and Fedorenko, 2015]. The regularization and renormalization of the instanton solution in the case of a Dirac particles in disordered potential is an interesting open question which is left for the future.

Appendix B

Landauer and Kubo Formalism for Transport

B.1 Landauer formula

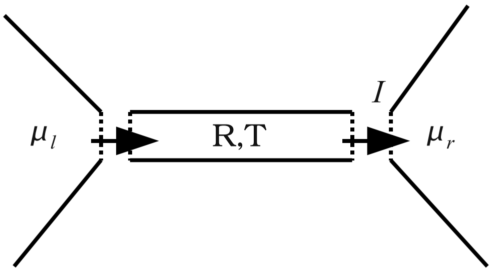

Figure B.1: Schematic view of a unidimensional conductor contacted between two reservoirs at chemical potentials μ_l and μ_r. R and T are respectively reflection and transmission probabilities for an electronic current flowing through the conductor.

The Landauer formula relates the conductance $G \equiv I/V$ of a material to the probability for transmission of an electron flow in the material [Nazarov and Blanter, 2009]. We will first give an idea of its derivation for a 1D quantum conductor contacted between two identical reservoirs with same temperature $1/\beta$ and different chemical potentials μ_l and μ_r, with corresponding difference of electric potential V defined by $\mu_r - \mu_l = eV$ (Fig. B.1). We assume that no reflection occurs at the contacts between the wire and the reservoir (for three dimensional reservoirs, there is a great number of available electronic states for electrons coming from the wire). Electrons coming from the reservoir are assumed to be at equilibrium and distributed following the Fermi-Dirac distribution at temperature $1/\beta$:

$$f_i(E) = \frac{1}{\mathrm{e}^{\beta(E-\mu_i)+1}}. \tag{B.1}$$

With $n(E)$ being the electronic density of states, T the transmission probability through the conductor (probability of being reflected is then $R = 1 - T$) and $v(E)$ the electronic group velocity, the portion of current created by electrons traveling from left to right with energy between E and $E + dE$ is given by:

$$dI_{l\to r} = \left(\frac{dn}{dE} f_l(E) dE\right) T \; ev(E). \tag{B.2}$$

Besides, we know that the density of states and velocity derive from the spectrum according to

$$v(E) = \frac{1}{\hbar}\frac{dE}{dk} \text{ and } \frac{dn}{dE} = \frac{dn}{dk}\frac{dk}{dE} = \frac{1}{2\pi\hbar}\frac{1}{v(E)}. \tag{B.3}$$

After some simplifications and taking into account the portion of current injected from the right reservoir, we get for the total current:

$$I = I_{l\to r} - I_{r\to l} = \frac{e}{h}\int (f_l(E) - f_r(E)) T dE. \tag{B.4}$$

For zero temperature the Fermi-Dirac distribution converges towards the Heaviside distribution $f_i(E) = \Theta(\mu_i - E)$. We then have, for a small enough V: $\int(f_l(E) - f_r(E))dE = (\mu_r - \mu_l)$ and the expression for the current follows:

$$I = \frac{e}{h}T(\mu_r - \mu_l), \tag{B.5}$$

which gives for the conductance G (we have $(\mu_r - \mu_l) = eV$)

$$G = \frac{e^2}{h}T. \tag{B.6}$$

Here we have considered only one channel for conduction: if spin degeneracy is present Eq. (B.6) corresponds to the conductance per spin. Notice that G is always finite, even in the ideal conductor case $T = 1$: Eq. (B.6) gives the total conductance of the ensemble made of the conductor and the two contacts. It corresponds to the conductance value read experimentally during a two-terminal measure. $G_0 = \frac{e^2}{h}$ is called the *contact conductance*: it characterizes the contacts between reservoirs and an ideal conductor ($T = 1$). The h dependence in Eq. (B.6) clearly manifests the quantum nature of this conductance, even though our derivation was semi-classical.

So far we have only considered a single propagation mode for electrons; a real wire has a finite tranverse section and therefore a great number of transverse modes. Each transverse mode corresponds to a solution of the Schrödinger equation, taking into account the confining potential $V(y, z)$. Since this potential has no dependence on the longitudinal coordinate x due to translation symmetry in this direction, tranverse modes propagate freely along the wire. The previous framework extends naturally to the multi-channel case: an electronic current in transverse mode n can either be transmitted into mode n' with probability $T_{nn'}$ or be reflected into mode n'' with probability $R_{nn''}$. Total transmission and reflection coefficients $T_n = \sum_{n'} T_{nn'}$ and $R_n = \sum_{n''} R_{nn''}$ satisfy the relation from current conservation $\sum_n T_n = \sum_n (1 - R_n)$. The Landauer formula (B.6) generalizes to:

$$G = \frac{e^2}{h}\sum_n T_n. \tag{B.7}$$

B.2 Kubo formula

Consider an electron flow $\mathbf{j}$ in a given material, created by an electric field $\mathbf{E}$. When the field is weak enough, i.e. while the system remains close to equilibrium, the linear response approximation gives the following relation between the electron current and the electric field, usually known as Ohm's law: $\mathbf{j} = \sigma\mathbf{E}$. This relation defines the conductivity tensor σ. When the medium is disordered, scattering effects will appear. In the semi-classical picture – the Drude-Boltzmann model, electrons propagate ballistically until they bounce off a scattering center. These collision processes tend to drive the system towards local equilibrium. Let us considering only elastic scattering events and define a corresponding momentum relaxation time τ. In this approximation, the frequency-dependent conductivity is given by [Akkermans and Montambaux, 2007]:

$$\sigma(\omega) = \frac{ne^2}{m}\mathrm{Re}\frac{\tau}{1 - \mathrm{i}\omega\tau}, \tag{B.8}$$

where n is the electronic density and m the electron mass. In the zero-frequency limit $\omega \to 0$, Eq. (B.8) yields the Drude formula for dc conductivity [Ashcroft and Mermin, 1976]:

$$\sigma = \frac{ne^2\tau}{m}. \tag{B.9}$$

where n and m are respectively the electronic density and mass. This model is best known as the Drude-Boltzmann model [Ashcroft and Mermin, 1976]. Note that in the limit of an ideal medium, i.e. in the absence of disorder ($\tau \to \infty$) the Drude conductivity (B.9) would diverge to infinity. It is the so-called Drude peak, corresponding to a situation where an infinitesimal electric field will induce a collective motion of electrons in the same direction. On the other hand, if the electronic density is set to zero prior to any other limit, the conductivity (B.8) vanishes. At the crossing point in graphene, the electronic density vanishes. From this classical description of transport one would predict that the conductivity at the crossing must vanish as well. However, the conductivity remains finite at the crossing. To understand this phenomena, one must include quantum effects beyond the classical Drude-Boltzmann model. Hence, let us consider the Kubo formalism which takes fully into account the wave-like nature of electrons and thus allows for an exhaustive description of quantum transport phenomena near equilibrium, based on perturbation theory.

Let us consider the local response of a system at temperature $1/\beta$ to an oscillating electric field $\mathbf{E}(\mathbf{r}',\omega)$:

$$j_\mu(\mathbf{r},\omega,\beta)=\int d\mathbf{r}'\sigma_{\mu\nu}(\mathbf{r},\mathbf{r}'\ ;\omega,\delta,\beta)E_\nu(\mathbf{r}',\omega)\ , \tag{B.10}$$

where the field $\mathbf{E}(\mathbf{r}',\omega)$ has been adiabatically switched on at time $t=-\infty$. $\delta>0$ is the characteristic adiabaticity time. For a sample of volume V, considering a spatially uniform electric field, the conductivity tensor is obtained by integrating and then averaging over spatial coordinates the bilocal conductivity:

$$\sigma_{\mu\nu}(\omega,\delta,\beta)=\int\frac{d\mathbf{r}}{V}\int d\mathbf{r}'\sigma_{\mu\nu}(\mathbf{r},\mathbf{r}'\ ;\omega,\delta,\beta)\ . \tag{B.11}$$

The Kubo formula for electrical conductivity reads [Mahan, 2013]:

$$\sigma_{\mu\nu}(\omega,\delta,\beta)=\frac{1}{\hbar\omega V}\int_0^\infty dt e^{\mathrm{i}(\omega+\mathrm{i}\delta)t}\langle[\hat{j}_\mu(t),\hat{j}_\nu(0)]\rangle_\beta\ +\mathrm{i}\frac{ne^2}{m\omega}\delta_{\mu\nu}, \tag{B.12}$$

where $\hat{j}_\mu(t)$ is the current operator in Heisenberg representation and $\langle...\rangle_\beta$ is the thermodynamic average on equilibrium density operator $\hat{\rho}_\beta$ at temperature $1/\beta$. On the right-hand side of Eq. (B.12), we note a term equivalent to the zero-disorder limit of Eq. (B.8) which diverges when $\omega\to 0$: the so-called Drude peak. We are interested in the real response function and shall therefore forget about this term in the following. Eq. (B.12) relates the conductivity to the current correlation function. It can be further simplified in the non-interacting case. Introducing fermionic creation operators $a_m^\dagger$, the Hamiltonian of the system takes the form:

$$\hat{H}=\sum_m\varepsilon_m a_m^\dagger a_m. \tag{B.13}$$

In this basis, the current operator is given by:

$$\hat{j}_\mu=\sum_{m,n}\langle n|\hat{j}_\mu|m\rangle a_n^\dagger a_m. \tag{B.14}$$

We now use the following result:

$$\mathrm{Tr}(\hat{\rho}_\beta[a_n^\dagger a_m,a_p^\dagger a_q])=\delta_{mp}\delta_{nq}(f_\beta(\varepsilon_n)-f_\beta(\varepsilon_m))\ , \tag{B.15}$$

where δ_{mp} is the Kronecker symbol and f_β the Fermi-Dirac distribution function defined in equation (B.1), and perform the integration over time in (B.12), to obtain:

$$\sigma_{\mu\nu}(\omega,\delta,\beta)=\frac{\mathrm{i}}{\omega V}\int d\varepsilon\sum_{n,m}\delta(\varepsilon-\varepsilon_n)\frac{\langle n|\hat{j}_\mu|m\rangle\langle m|\hat{j}_\nu|n\rangle}{\varepsilon-\varepsilon_m+\hbar(\omega+\mathrm{i}\delta)}[f_\beta(\varepsilon)-f_\beta(\varepsilon_m)]\ . \tag{B.16}$$

In the computations, we consider an infinite size system $L\to+\infty$ and send the adiabaticity time δ to zero in equation (B.16); by doing so, we get a second delta distribution replacing the denominator on the right hand side (keeping only the real response function) :

$$\sigma_{\mu\nu}(\omega,\beta)=\frac{\pi}{\omega L^2}\int d\varepsilon\sum_{m,n}\delta(\varepsilon-\varepsilon_n)\langle n|\hat{j}_\mu|m\rangle\langle m|\hat{j}_\nu|n\rangle(f_\beta(\varepsilon)-f_\beta(\varepsilon_m))\delta(\varepsilon-\varepsilon_m+\hbar\omega). \tag{B.17}$$

Appendix C

On the Origin of Minimal Conductivity in 3 Bands-Crossing Models

C.1 Band properties

C.1.1 Berry phase around the nodal point

Upon winding around the band touching point, electrons in the $n-$th energy band pick up a so-called Berry phase γ_n:

$$\gamma_n(\vec{K}) = \frac{-\mathrm{i}}{\pi} \oint d\vec{q}.\langle \Psi_n | \vec{\nabla}_{\vec{q}} | \Psi_n \rangle \ , \tag{C.1}$$

where Ψ_n is the corresponding Bloch eigenstate. The integrand in (C.1) is the Berry connection

$$\vec{A}_n(\vec{q}) = -\mathrm{i}\langle \Psi_n | \vec{\nabla}_{\vec{q}} | \Psi_n \rangle = \mathrm{Im}(\langle \Psi_n | \vec{\nabla}_{\vec{q}} | \Psi_n \rangle). \tag{C.2}$$

Here we compute the Berry connection and the Berry phase (C.1) for eigenstates of the general Hamiltonian of the $\mathcal{D}_I$ duality class, and for the T_3 model of the $\mathcal{D}_{II}$ duality class.

$\mathcal{D}_I$ class

The general low-energy $\mathcal{D}_I$ class Hamiltonian can be written in the following form:

$$H(\vec{q}) = \begin{pmatrix} 0 & 0 & \alpha(q_x + \lambda q_y) \\ 0 & 0 & \beta(q_x + \lambda q_y) \\ \alpha^*(q_x + \lambda^* q_y) & \beta^*(q_x + \lambda^* q_y) & 0 \end{pmatrix}. \tag{C.3}$$

The spectrum is given by: $\varepsilon_\pm(\vec{q}) = \pm\sqrt{|\alpha|^2 + |\beta|^2}|q_x + \lambda q_y|, \varepsilon_0(\vec{q}) = 0$. We may fix the total energy scale without loss of generality by setting $|\alpha|^2 + |\beta|^2 = 1$. The eigenstates of (C.3) read:

$$\Psi_\pm(\vec{q}) = \frac{1}{\sqrt{2}} \begin{pmatrix} \alpha \frac{q_x + \lambda q_y}{|q_x + \lambda q_y|} \\ \beta \frac{q_x + \lambda q_y}{|q_x + \lambda q_y|} \\ \pm 1 \end{pmatrix}, \ \varepsilon_\pm = \pm |q_x + \lambda q_y|, \tag{C.4a}$$

$$\Psi_0(\vec{q}) = \begin{pmatrix} -\beta^* \\ \alpha^* \\ 0 \end{pmatrix}, \ \varepsilon_0 = 0. \tag{C.4b}$$

We then compute the Berry connection (C.2) for the lower and upper dispersive bands Ψ_+ and Ψ_- (C.4a):

$$A_x^\pm = \mathrm{Im}(\langle \Psi_\pm | \partial_{q_x} | \Psi_\pm \rangle) = -\frac{q_y}{2|q_x + \lambda q_y|^2} \mathrm{Im}(\lambda) \tag{C.5a}$$

$$A_y^\pm = \frac{q_x}{2|q_x + \lambda q_y|^2} \mathrm{Im}(\lambda). \tag{C.5b}$$

Integrating along a loop of constant $||\vec{q}||$ yields the Berry phase:

$$\begin{aligned}\gamma_\pm &= \frac{1}{\pi}\int_0^{2\pi} qd\theta A^\pm_\theta = \int_0^{2\pi} qd\theta(\frac{q_x}{q}A^\pm_y - \frac{q_y}{q}A^\pm_x)\\ &= \left(\frac{1}{2\pi}\int_0^{2\pi}\frac{d\theta}{|\cos\theta+\lambda\sin\theta|^2}\right)\mathrm{Im}(\lambda)\\ &= \mathrm{sgn}(\mathrm{Im}(\lambda)).\end{aligned} \tag{C.6}$$

The Berry phase is quantized and in particular does not change under continuous variations of the Hamiltonian parameters, provided the duality constraint of class $\mathcal{D}_I$ is preserved. For the flat band, (C.4b) immediately gives $\vec{A}=\vec{0}$, and thus $\gamma_0 = 0$.

The H_3 model belongs to the $\mathcal{D}_I$ class; it corresponds to the case $\lambda = -\mathrm{i}$. Thus from (C.6) the invariants associated with eigenstates of the H_3 model are $\gamma_\pm = -1$, $\gamma_0 = 0$. Alternatively, one can recover these results by an explicit calculation from the eigenstates (4.41).

The T_3 model: an example from the $\mathcal{D}_{II}$ class

We now consider low-energy excitations of the T_3 model. Using expression (4.44a) for the eigenstates of the dispersive bands with $f(\vec{K}+\vec{q}) \simeq q_x - \mathrm{i}q_y = q\mathrm{e}^{-\mathrm{i}\theta}$, the Berry connection is given by:

$$\vec{A}_\pm = -\frac{1}{2}\cos 2\varphi\ \vec{\nabla}_{\vec{q}}\ \theta, \tag{C.7}$$

which yields for the Berry phase (C.1):

$$\gamma_\pm = -\cos 2\varphi. \tag{C.8}$$

Similarly, eigenstates of the flat band (4.44b) are characterized by a Berry phase:

$$\gamma_0 = 2\cos 2\varphi. \tag{C.9}$$

These phases vary continuously with the hopping parameter φ, and vanish when $\varphi = \pi/4$. The only source of Berry phases is the band crossing point itself: this manifests into the robustness of their value beyond the linear approximation. Keeping the general expression $f(\vec{k}) = |f(\vec{k})|\mathrm{e}^{\mathrm{i}\phi(\vec{k})}$ and integrating along an iso-energy contour $|f(\vec{k})| = \text{const.}$ as in Ref.[Raoux et al., 2014] still yields the windings (C.8) and (C.9).

Three-band chiral linear crossing with topological Berry phase

Here we show that for a three-band crossing described by the linearized Hamiltonian (4.49) to have a topological Berry phase, it must belong to the duality class $\mathcal{D}_I$. In particular, it thus has a finite minimal conductivity. First, consider the Λ_{ij} coefficients characterizing Hamiltonian (4.49). Through a global change of energy scale and phase of the Hamiltonian, they are cast under the form:

$$\Lambda = \begin{pmatrix}\cos\varphi\ \mathrm{e}^{\mathrm{i}b} & \cos\varphi\ \mathrm{e}^{\mathrm{i}b}\nu\\ \sin\varphi & \sin\varphi\ \mu\end{pmatrix}, \tag{C.10}$$

where φ is defined by $\tan\varphi = \frac{|\Lambda_{21}|}{|\Lambda_{11}|}$. In the context of lattice models it corresponds to the ratio of hoppings, as in (4.40) and (4.43). Eigenstates from the dispersive bands now read:

$$\psi_\pm = \frac{1}{\sqrt{2}}\begin{pmatrix}\cos\varphi\ \mathrm{e}^{\mathrm{i}b}\frac{k_x+\nu k_y}{\varepsilon_{\vec{k}}}\\ \sin\varphi\ \frac{k_x+\mu k_y}{\varepsilon_{\vec{k}}}\\ \pm 1\end{pmatrix}, \tag{C.11}$$

with energy

$$E = \pm\varepsilon_{\vec{k}} = \pm\sqrt{\cos^2\varphi\ |k_x+\nu k_y|^2 + \sin^2\varphi\ |k_x+\mu k_y|^2}. \tag{C.12}$$

From (C.11) we then obtain the Berry connection:

$$A^\pm_x = \mathrm{Im}(\langle\Psi_\pm|\partial_{q_x}|\Psi_\pm\rangle) = -\frac{q_y}{2\varepsilon^2_{\vec{k}}}(\cos^2\varphi\ \mathrm{Im}(\nu) + \sin^2\varphi\ \mathrm{Im}(\mu)) \tag{C.13a}$$

$$A^\pm_y = \frac{q_x}{2\varepsilon^2_{\vec{k}}}(\cos^2\varphi\ \mathrm{Im}(\nu) + \sin^2\varphi\ \mathrm{Im}(\mu)), \tag{C.13b}$$

from which in turn we compute the Berry phase:

$$\gamma_\pm = \frac{1}{2\pi}\int_0^{2\pi} d\theta \frac{k^2}{\varepsilon_{\vec{k}}^2}(\cos^2\varphi \ \mathrm{Im}(\nu) + \sin^2\varphi \ \mathrm{Im}(\mu)). \tag{C.14}$$

Using the following formula:

$$\begin{aligned} &\frac{1}{2\pi}\int_0^{2\pi} \frac{d\theta}{\cos^2\theta + \rho^2\sin^2\theta + 2\rho\cos\phi \ \cos\theta \ \sin\theta} \\ &\quad = \frac{1}{\rho\sqrt{1-\cos^2\phi}}, \end{aligned} \tag{C.15}$$

we can recast the last expression (C.14) into the form:

$$\gamma_\pm = \frac{\cos^2\varphi \ \mathrm{Im}(\nu) + \sin^2\varphi \ \mathrm{Im}(\mu)}{\sqrt{|\nu|^2\cos^2\varphi + |\mu|^2\sin^2\varphi - (\cos^2\varphi \ \mathrm{Re}(\nu) + \sin^2\varphi \ \mathrm{Re}(\mu))^2}}. \tag{C.16}$$

From (C.16) we recover the Berry phase expressions (C.8) and (C.6) for the different models we considered. For the Berry phase (C.16) to be topological, it must in particular be independent of φ, i.e. we must have $\partial_\varphi \gamma_\pm = 0 \ \forall \varphi$. We find that this condition is fulfilled when and only when $\nu = \mu$, i.e. when the system is in duality class $\mathcal{D}_I$, according to (4.54). Here we have thus shown that for a three-band linear crossing with chiral symmetry to have a topological Berry phase, it must necessarily belong to duality class $\mathcal{D}_I$. Reciprocally we have shown in a previous section that any model in this class has a quantized topological Berry phase.

C.2 Transport properties

C.2.1 Landauer conductivity

Matching conditions for $\vec{k}$-linear Hamiltonians

To solve the scattering problem through a tunnel junction, we want to compute the electronic wave functions in the different regions of the setup and ensure that the solutions obtained in neighbour regions satisfy the matching conditions at the interface. To this end, we want to derive matching conditions along the x direction for electronic wave packets described by a k-linear Hamiltonian $H = \vec{S}\cdot\vec{k}$. Let us consider an interface at $x = x_0$; the matching conditions at the interface derive from the continuity of the eigenvalue equation $\vec{S}\cdot\vec{k} \ \psi = (\varepsilon - V)\psi$, where $V(x < x_0) = V_1, \ V(x > x_0) = V_2$. Integrating the eigenvalue equation between $x_0 - \eta$ and $x_0 + \eta$ ($\eta > 0$) gives:

$$S_x \left[\psi(x_0+\eta) - \psi(x_0-\eta)\right] = \int_{x_0-\eta}^{x_0+\eta} (\varepsilon - V(x))\psi(x)dx, \tag{C.17}$$

where we used $\vec{k} = -\mathrm{i}\frac{\partial}{\partial \vec{x}}$ in coordinate representation. Sending η to 0, the integral in the right hand side of (C.17) vanishes, yielding the following condition:

$$S_x \cdot \psi(x_0^-) = S_x \cdot \psi(x_0^+). \tag{C.18}$$

Note that, in contrast with the usual case of the Schrödinger equation, for a k-linear Hamiltonian matching of the wavefunction does not imply continuity of the wavefunction's derivatives, but only of linear combinations of its components.

In the models we study, the presence of a chiral symmetry constrains the linearized low energy Hamiltonian to take the form (4.49) in the (A_1, A_2, B) basis. Hence, condition (C.18) enforces the continuity of ψ_B at x_0, provided Λ_{11} or Λ_{21} is non zero.

Derivation of the minimal conductivity in the $\mathcal{D}_I$ class

We now consider a given material in the $\mathcal{D}_I$ duality class: its low energy excitations are described by Hamiltonian (C.3). We now study the transmission of electronic current through a sample of dimensions $L \times W$ contacted between two electrodes, respectively at $x = 0$ and $x = L$. The chemical potential in the sample is set exactly at the band-touching point, whereas the electrodes are doped at a very large potential V_∞. Momentum in the transverse direction y is quantized in all three regions – the two electrodes and the sample. It is determined by the transverse boundary conditions: for instance, periodic boundary conditions give $q_y = \frac{2\pi n}{W}$.

The –dimensionless– dispersion relation in the electrodes writes: $V_\infty^2 = q_x^2 + q_y^2$. Since q_y is quantized and thus fixed, for a large enough potential V_∞ the normal incidence approximation $q_x/q_y \simeq 0$ becomes valid. Electronic wave functions (see eq. (C.4a)) in the left electrode then read:

$$\psi(x<0) = \frac{1}{\sqrt{2}}\begin{pmatrix}\alpha\\ \beta\\ 1\end{pmatrix} \mathrm{e}^{\mathrm{i}\vec{q}\vec{r}} + \frac{r_n}{\sqrt{2}}\begin{pmatrix}-\alpha\\ -\beta\\ 1\end{pmatrix} \mathrm{e}^{-\mathrm{i}\vec{q}\vec{r}}, \tag{C.19}$$

and in the right electrode:

$$\psi(x>L) = \frac{t_n}{\sqrt{2}}\begin{pmatrix}\alpha\\ \beta\\ 1\end{pmatrix} \mathrm{e}^{\mathrm{i}\vec{q}\vec{r}}. \tag{C.20}$$

t_n and r_n are the transmission and reflexion amplitude of mode n.

In the sample, the Fermi level lies exactly at the nodal point $E = 0$. Evanescent zero energy modes $\psi^T = (\psi_{A1}, \psi_{A2}, \psi_B)^T$ of Hamiltonian (C.3) satisfy:

$$\psi_B(0<x<L) = C\ \mathrm{e}^{-\mathrm{i}\lambda q_y x + \mathrm{i}q_y y} \tag{C.21a}$$

$$(\alpha^*\psi_{A1} + \beta^*\psi_{A2})(0<x<L) = C'\ \mathrm{e}^{-\mathrm{i}\lambda^* q_y x + \mathrm{i}q_y y}. \tag{C.21b}$$

Besides, matching conditions at the interfaces $x = 0$ and $x = L$, given by equation (C.18), correspond to the continuity of ψ_B and $(\alpha^*\psi_{A1} + \beta^*\psi_{A2})$. Enforcing this continuity at $x = 0$ and $x = L$ and solving the system of equations yields for the transmission coefficient of mode n:

$$T_n = |t_n|^2 = \frac{1}{|\cosh(\mathrm{Im}(\lambda) q_n L)|^2}, \tag{C.22}$$

where $q_y = q_n = \frac{2\pi n}{W}$. In the limit $W \gg L$, where we can neglect the impact of transverse boundary conditions, equation (C.22) leads to the following expression for Landauer conductivity:

$$\sigma = \frac{L}{W}\frac{e^2}{h}\sum_n T_n = \frac{e^2}{\pi h}\frac{1}{\mathrm{Im}(\lambda)}. \tag{C.23}$$

Note that the conductivity depends on the direction of the junction θ. The dependance can be carried out from (C.3) taking into account the dependance of λ on θ. Assuming that $\theta = 0$ corresponds to a principal axis one finds that $\lambda(\theta) := \lambda_0$ is pure imaginary and the conductivity in the direction θ is given by

$$\sigma(\theta) = \frac{e^2}{\pi h}\left(\frac{1}{|\lambda_0|}\cos^2\theta + |\lambda_0|\sin^2\theta\right). \tag{C.24}$$

The minimal conductivity takes its extrema values along the principal axes of the dispersion relation, $\sigma_1 = \frac{1}{|\lambda_0|}\frac{e^2}{\pi h}$ and $\sigma_2 = |\lambda_0|\frac{e^2}{\pi h}$. The determinant of the conductivity tensor reads straightforwardly from its expression in the principal axes basis: $\bar{\sigma} = \mathrm{diag}(\sigma_1, \sigma_2)$, which gives $\det\bar{\sigma} = (e^2/\pi h)^2$.

The H_3 model corresponds to $\lambda = -\mathrm{i}$, leading to $\sigma = \frac{e^2}{\pi h}$. Since the dispersion relation is isotropic in this case, the value of the minimal conductivity in the H_3 model is independent of the direction of the junction.

Note that reciprocally we have shown that any three-band chiral semimetal with finite minimal conductivity necessarily belongs to the $\mathcal{D}_I$ class. Indeed, a necessary condition for the existence of a minimal conductivity is given by (4.52) which, when it is fulfilled, implies in turn that the $\mathcal{D}_I$ criteria (4.54) is met.

Absence of minimal conductivity in the T_3 model

We study a strip of the T_3 material contacted between two electrodes, in a similar fashion as in the previous section. In the strip, the Fermi level is set at the band touching point $E = 0$. Let us consider the propagation of an electronic wavepacket incident from the left electrode into the sample. In the strip, the zero energy wave functions of (4.45) must satisfy $\psi_B = 0$ (for $0 < \varphi < \pi/2$, $k_y \neq 0$). In the right electrode, the wave function is $\psi(x>L) = t_n\psi^+(\vec{q})\mathrm{e}^{\mathrm{i}\vec{q}\vec{r}}$, where t_n gives the transmission coefficient of mode n: $T_n = |t_n|^2$ and ψ^+ is defined by eq. (4.44a). Thus, we have

$$\psi_B(0<x<L) = 0 \tag{C.25a}$$

$$\psi_B(x>L) = \frac{t_n}{\sqrt{2}}\mathrm{e}^{\mathrm{i}\vec{q}\vec{r}}, \tag{C.25b}$$

Matching conditions (C.18) enforce the continuity of ψ_B at the interface, leading to $t_n = 0$. This is true for all modes with non-zero transverse momentum k_y. Hence, the conductance $G = \frac{e^2}{h}\sum_n T_n$ can be zero or finite, independent of the sytem size, depending whether a mode with $k_y = 0$ is allowed or not by transverse boundary conditions. In any case, for the conductivity one finds:

$$\sigma = \frac{L}{W}\frac{e^2}{h}\sum_n T_n = 0 \tag{C.26}$$

in the limit $W \gg L$.

C.2.2 Kubo conductivity of the T$_3$ model

We now compute the Kubo conductivity at the nodal point in the T$_3$ lattice. For simplicity we only show here the calculation in the case $t_1 = t_2$: the final result remains valid for any non zero value of the hoppings. The low energy Hamiltonian writes:

$$H(\vec{K}+\vec{q}) = \hbar v_F \begin{pmatrix} 0 & 0 & q_- \\ 0 & 0 & q_+ \\ q_+ & q_- & 0 \end{pmatrix} , \tag{C.27}$$

where we denote $q_\pm = q_x \pm \mathrm{i}q_y$, and with $v_F = 3at/2$, a the honeycomb lattice spacing and t the hopping strength.

We perform the computation using Kubo formula, which gives the linear response of the system at temperature $1/\beta$ to an ac electric field with frequency ω. Here we use the scheme that was introduced in [Ryu et al., 2007] and section 4.1.1 in the case of graphene: a phenomenological scattering rate $\eta > 0$ has to be introduced, which models a finite lifetime of the electronic excitations in the presence of electrodes and allows to recover the Landauer conductivity within the Kubo formalism. The Kubo conductivity is computed in the limit of zero frequency and zero temperature, while keeping η finite. The final result for graphene is independent of η, a sign of the robustness of this material towards disorder.

The starting point is the Kubo formula (see appendix B.2) :

$$\sigma_{\mu\nu}(\omega,\eta,\beta) = \frac{\hbar}{4\pi L^2}\int d\varepsilon\ \frac{f_\beta(\varepsilon+\hbar\omega) - f_\beta(\varepsilon)}{\hbar\omega}\mathrm{Tr}[G^{A-R}_\eta(\varepsilon)\hat{j}_\mu G^{A-R}_\eta(\varepsilon+\hbar\omega)\hat{j}_\nu] , \tag{C.28}$$

where $\eta > 0$ is the imaginary part of the self-energy, f_β is the Fermi-Dirac distribution at temperature β^{-1}, G^{A-R} is the difference between advanced and retarded Green functions

$$G^{A-R}_\eta(\varepsilon) = ((\varepsilon - \mathrm{i}\hbar\eta)\mathbb{1} - H)^{-1} - ((\varepsilon + \mathrm{i}\hbar\eta)\mathbb{1} - H)^{-1} , \tag{C.29}$$

and $\hat{j}_\mu = e/\hbar\ \partial_{q_\mu}\hat{H}$ is the current operator. The trace Tr in (C.28) runs over the basis of eigenstates of the T$_3$ Hamiltonian (C.27):

$$|\mathbf{q},\pm\rangle = \frac{1}{\sqrt{2}}\begin{pmatrix} \frac{1}{\sqrt{2}}\ \mathrm{e}^{-\mathrm{i}\theta} \\ \frac{1}{\sqrt{2}}\ \mathrm{e}^{\mathrm{i}\theta} \\ \pm 1 \end{pmatrix} ,\ \varepsilon_\pm = \pm\varepsilon(q) \equiv \pm\hbar v_F q$$

$$|\mathbf{q},0\rangle = \begin{pmatrix} -\mathrm{e}^{-\mathrm{i}\theta} \\ \mathrm{e}^{\mathrm{i}\theta} \\ 0 \end{pmatrix} ,\ \varepsilon_0 = 0, \tag{C.30}$$

with $q_\pm = q\mathrm{e}^{\pm\mathrm{i}\theta}$, $t_1 = t_2$. Performing the trace over (C.30) in (C.28) and taking the limits $\omega \to 0$, $\beta \to \infty$ while keeping $\eta > 0$, one finds:

$$\sigma_{xx} = \frac{e^2}{8\pi^2 h}\int_0^\infty qdq\frac{4\pi\left(4\eta^2+2q^2\right)}{\left(\eta^2+q^2\right)^2} \tag{C.31}$$

$$= \frac{e^2}{\pi h}\left(1 + \int_0^\infty \frac{q^3 dq}{(\eta^2+q^2)^2}\right) \to \infty. \tag{C.32}$$

The integral in (C.32) is divergent. The Kubo conductivity diverges for the T_3 model with a finite electronic lifetime; in particular we do not recover the Landauer conductivity (C.26) $\sigma_{Landauer} = 0$. We note that the result for Kubo conductivity result is consistent with the value obtained in the zero disorder limit in Ref. [Vigh et al., 2013].

Appendix D

Magnetotransport Close to the Nodal Point in Weyl Junctions

In this Appendix, we provide technical details on the study of the Chiral Anomaly in Ballistic Weyl Junctions, Chapter. 5. It contains explanations on the Landau spectrum of Weyl Hamiltonians (Sec. D.1), the Lorentz (Sec. D.2) and thermal (Sec. D.3) broadenings of the quantum oscillations, the numerical study (Sec. D.4) and scalings (Sec. D.5) of Weyl semi-metal lattice models.

D.1 Landau levels

We consider the model

$$H = cp_x\sigma_x + cp_y\sigma_y + \left(\frac{p_z^2}{2m} - \Delta\right)\sigma_z, \tag{D.1}$$

with $p_i = \hbar k_i$. For $\Delta > 0$, it admits two Weyl points of opposite charge at $k_x = k_y = 0$ and $\hbar k_z = \pm\sqrt{2m\Delta}$. By minimal coupling, with a charge of carriers $q = -e$, we get $p_i = \hbar k_i \to \Pi_i = p_i - qA_i = p_i + eA_i$ in the presence of a magnetic field $\mathbf{B} = B\hat{z} = \operatorname{rot}\mathbf{A}$ along z-direction. We naturally introduce the ladder operators

$$\hat{a} = \frac{l_B}{\sqrt{2}\hbar}\left(\hat{\Pi}_x - i\hat{\Pi}_y\right) \quad ; \quad \hat{a}^\dagger = \frac{l_B}{\sqrt{2}\hbar}\left(\hat{\Pi}_x + i\hat{\Pi}_y\right) \tag{D.2}$$

which satisfy $\left[\hat{a}, \hat{a}^\dagger\right] = \eta_B\mathbb{I}$. with $\eta_B = \pm 1$ the sign of B.

- Case $B > 0$:

  The Hamiltonien then reads

  $$H = H_{xy} + \left(\frac{p_z^2}{2m} - \Delta\right)\sigma_z \ ; \ H_{xy} = \hbar\omega_0\begin{pmatrix} 0 & \hat{a} \\ \hat{a}^\dagger & 0 \end{pmatrix}, \tag{D.3}$$

  with $\hbar\omega_0 = \sqrt{2}\hbar vc/l_B = \sqrt{4\pi\hbar^2c^2|b|/a^2}$. Let us consider the quanta $|n\rangle$ defined by $\sqrt{n!}\,|n\rangle = (\hat{a}^\dagger)^n\,|0\rangle$. The spectrum of relativistic Landau levels of H_{xy} is given by $E_n = \eta\sqrt{n}\hbar\omega_0$, $\eta = \pm 1, n \in \mathbb{N}$ with the corresponding eigenstates

  $$|\psi_0\rangle = \begin{pmatrix} 0 \\ |0\rangle \end{pmatrix} \ ; \ |\psi_{\eta,n}\rangle = \frac{1}{\sqrt{2}}\begin{pmatrix} |n-1\rangle \\ \eta\,|n\rangle \end{pmatrix} \ , \ n \geq 1. \tag{D.4}$$

- Case $B < 0$:

  There the algebra of ladder is reversed,

  $$H_{xy} = \hbar\omega_0\begin{pmatrix} 0 & \hat{a}^\dagger \\ \hat{a} & 0 \end{pmatrix}, \tag{D.5}$$

  and the eigenstates take the form

  $$|\psi_0\rangle = \begin{pmatrix} |0\rangle \\ 0 \end{pmatrix} \ ; \ |\psi_{\eta,n}\rangle = \frac{1}{\sqrt{2}}\begin{pmatrix} |n\rangle \\ \eta\,|n-1\rangle \end{pmatrix} \ , \ n \geq 1. \tag{D.6}$$

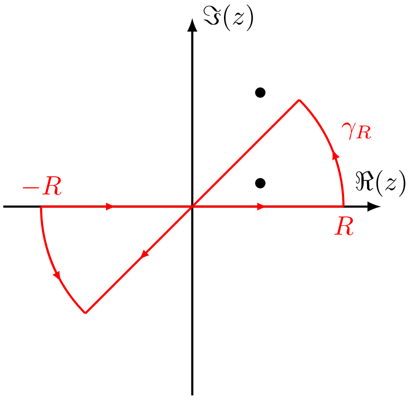

Figure D.1: Contour used for the residue theorem and poles of the Lorentzian. Angle is $\pi/4$. Pole is at $\epsilon + i$, either inside or outside the contour for $\epsilon > 1$ or $\epsilon < 1$.

We readily get the full spectrum by writing a reduced Hamiltonian in the basis $|\psi_{+,n}\rangle\,, |\psi_{-,n}\rangle$,

$$H = \sqrt{n}\hbar\omega_0\sigma_z + \left(\frac{k_z^2}{2m} - \Delta\right)\sigma_x. \tag{D.7}$$

Namely, we find

$$E_{n,\pm} = \pm\sqrt{4\pi c^2|b|n + \left(\frac{k_z^2}{2m} - \Delta\right)^2} \quad \text{with} \quad n > 0 \tag{D.8}$$

and

$$E_0 = \begin{cases} -[k_z^2/(2m) - \Delta], & \text{if} \quad B > 0, \\ k_z^2/(2m) - \Delta, & \text{if} \quad B < 0. \end{cases} \tag{D.9}$$

D.2 Lorentz broadening of the conductance

We start from Eq. (5.38) in the main text:

$$\frac{G(\mu, B)}{G_{\text{Sh}}(\mu)} = 1 + \frac{|B|}{B_c(\mu)} \int \frac{d\mu'}{\eta} f\left(\frac{\mu - \mu'}{\eta}\right) \text{sw}\left(\frac{B_c(\mu')}{|B|}\right) \tag{D.10}$$

$$= 1 + \frac{|B|}{B_c(\mu)} \int d\epsilon' f\left(\epsilon - \epsilon'\right) \text{sw}\left(\frac{\epsilon'^2}{\Lambda^2}\right) \tag{D.11}$$

with $\epsilon = \mu/\eta$, $f(x) = 1/[\pi(1 + x^2)]$, and we introduced $\Lambda^2 = (\hbar\omega_0/\eta)^2 = (\mu/\eta)^2|B|/B_c(\mu)$. Then we use the Fourier expansion of the sawtooth function

$$\text{sw}(x) = \frac{1}{\pi}\sum_{n=1}^{\infty}\frac{1}{n}\sin(2\pi n x) \tag{D.12}$$

to rewrite expression (D.11) as

$$\frac{G(\mu, B)}{G_{\text{Sh}}(\mu)} - 1 = \frac{|B|}{B_c(\mu)}\frac{1}{\pi^2}\sum_{n=1}^{\infty}\frac{1}{n}\Im\int_{-\infty}^{\infty} d\epsilon' \frac{1}{1 + (\epsilon' - \epsilon)^2}\exp i\left(2\pi n\frac{\epsilon'^2}{\Lambda^2}\right). \tag{D.13}$$

Using the contour in the complex plane of Fig. D.1 and the residue theorem gives

$$
\begin{aligned}
\int_{-\infty}^{\infty} d\epsilon' \frac{1}{1+(\epsilon'-\epsilon)^2} \exp i\left(2\pi n \frac{\epsilon'^2}{\Lambda^2}\right)& \\
= 2i\pi\Theta(\epsilon-1)\mathrm{Res}_{z\to\epsilon+i}&\left[\frac{1}{1+(z-\epsilon)^2}\exp i\left(2\pi n\frac{z^2}{\Lambda^2}\right)\right] \\
&+\int_{-\infty}^{\infty} du \frac{e^{i\frac{\pi}{4}}}{1+(e^{i\frac{\pi}{4}}u-\epsilon)^2}\exp -\left(2\pi n \frac{u^2}{\Lambda^2}\right). \qquad \text{(D.14)}
\end{aligned}
$$

Summing over n using

$$
\sum_{n=1}^{\infty}\frac{1}{n}\exp\left(-2\pi n\frac{u^2}{\Lambda^2}\right) = -\ln\left(1-\exp\left(-\frac{2\pi}{\Lambda^2}u^2\right)\right) \qquad \text{(D.15)}
$$

we obtain

$$
\begin{aligned}
\frac{G(\mu,B)}{G_{\mathrm{Sh}}(\mu)}-1 = -\frac{|B|}{B_c(\mu)}\frac{1}{\pi}\Theta\left[\epsilon-1\right]\Im&\left[\ln\left(1-\exp\left(\frac{2i\pi(\epsilon+i)^2}{\Lambda^2}\right)\right)\right] \\
-\frac{|B|}{B_c(\mu)}\frac{1}{\pi^2}\Im&\left[\int_{-\infty}^{+\infty}du\frac{e^{i\frac{\pi}{4}}}{1+(e^{i\frac{\pi}{4}}u-\epsilon)^2}\ln\left(1-\exp\left(-\frac{2\pi}{\Lambda^2}u^2\right)\right)\right]. \qquad \text{(D.16)}
\end{aligned}
$$

In the low-field limit, the first term of (D.16) leads to exponentially small correction in $|B|$, while the second term can be expanded according to

$$
\begin{aligned}
&-\frac{|B|}{B_c(\mu)}\frac{1}{\pi^2}\Im\left[\int_{-\infty}^{+\infty}du\frac{e^{i\frac{\pi}{4}}}{1+(e^{i\frac{\pi}{4}}u-\epsilon)^2}\ln\left(1-\exp\left(-\frac{2\pi}{\Lambda^2}u^2\right)\right)\right] \\
&= -\frac{|B|}{B_c(\mu)}\frac{1}{\pi^2}\Lambda\Im\left[\int_{-\infty}^{+\infty}dy\frac{e^{\frac{i\pi}{4}}}{1+(\Lambda e^{\frac{i\pi}{4}}y-\epsilon)^2}\right]\ln\left(1-e^{-2\pi y^2}\right) \\
&= -\frac{|B|}{B_c(\mu)}\frac{1}{\pi^2}\Lambda\int_{-\infty}^{+\infty}dy\Im\left[\frac{e^{\frac{i\pi}{4}}}{1+\epsilon^2}+\frac{2i\epsilon}{(1+\epsilon^2)^2}\Lambda y+\mathcal{O}\left((\Lambda y)^2\right)\right]\ln\left(1-e^{-2\pi y^2}\right) \\
&= -\frac{|B|}{B_c(\mu)}\frac{1}{\pi^2}\Lambda\int_{-\infty}^{+\infty}dy\Im\left[\frac{e^{\frac{i\pi}{4}}}{1+\epsilon^2}+\mathcal{O}\left((\Lambda y)^2\right)\right]\ln\left(1-e^{-2\pi y^2}\right) \\
&= -\frac{|B|}{B_c(\mu)}\frac{1}{\pi^2}\frac{\Lambda}{1+\epsilon^2}\int_{-\infty}^{+\infty}dy\ln\left(1-e^{-2\pi y^2}\right)+\mathcal{O}\left((\Lambda y)^2\right) \qquad \text{(D.17)}
\end{aligned}
$$

From parity arguments, the expansion will only contain terms with even powers of Λ, giving an expension in half-integer powers of B starting from $B^{\frac{3}{2}}$. At lowest order in b, we finally obtain

$$
\frac{G(\mu,B)}{G_{\mathrm{Sh}}(\mu)}-1 = \tilde{\alpha}\,\left(\frac{|B|}{B_c(\mu)}\right)^{\frac{3}{2}}\frac{\mu}{\eta}f\left(\frac{\mu}{\eta}\right)+\mathcal{O}(|B|^{\frac{5}{2}}) \qquad \text{(D.18)}
$$

with

$$
\tilde{\alpha} = -\frac{1}{\pi}\int_{-\infty}^{+\infty}dy\ln\left(1-e^{-2\pi y^2}\right)\simeq 0.59 \qquad \text{(D.19)}
$$

which is Eq. (5) in the main text.

D.3 Thermal broadening of the conductance

We use the Euler Mac Laurin formula,

$$
\sum_{n=1}^{\infty}f(n) = \int_{1}^{+\infty}dx f(x)+\frac{1}{2}f(1)+\frac{1}{12}f'(1)-\frac{1}{30\times 24}f^{(''')}(1)+..., \qquad \text{(D.20)}
$$

to express the conductance given by Eq. (4) in the main text with thermal broadening as (we assume $B,\mu>0$)

$$
2\frac{G_T}{G_{\mathrm{Sh}}} = \frac{B}{B_c}\left(1+2\sum_{n=1}^{\infty}f_F\left(\frac{\epsilon_0\sqrt{bn}}{k_BT}-\frac{\mu}{k_BT}\right)\right),\ \text{where } f_F(x)=\frac{1}{1+e^x}. \qquad \text{(D.21)}
$$

The development at low magnetic field, corresponding to $z = \hbar\omega_0/(k_BT) \ll 1$, is written, using $\epsilon = \mu/(k_BT)$, as

$$\begin{aligned}
2\frac{G_T}{G_{\text{Sh}}}\frac{B_c}{B} &= 1 + 2\int_1^{+\infty} dx f_F(z\sqrt{x}-\epsilon) + f_F(z-\epsilon) + \frac{1}{6}\frac{d}{dx}\, f_F(z\sqrt{x}-\epsilon)\big|_{x=1} + \mathcal{O}(z^3) \\
&= 1 + \frac{4}{z^2}\int_0^{+\infty} dy\frac{y}{1+e^{y-\epsilon}} - \frac{4}{z^2}\int_0^{z} dy\frac{y}{1+e^{y-\epsilon}} + f_F(z-\epsilon) + \frac{z}{12}f_F'(z-\epsilon) + \mathcal{O}(z^3) \\
&= 1 + \frac{4}{z^2}\int_0^{+\infty} dy\frac{y}{1+e^{y-\epsilon}} \\
&\quad - \frac{4}{z^2}\left[\frac{z^2}{2}(yf_F(y-\epsilon))'(0) + \frac{z^3}{6}(yf_F(y-\epsilon))^{''}(0) + \frac{z^4}{24}(yf_F(y-\epsilon))^{(''')}(0)\right] \\
&\quad + f_F(-\epsilon) + zf_F'(-\epsilon) + \frac{z^2}{2}f_F^{''}(-\epsilon) + \frac{z}{12}f_F'(-\epsilon) + \frac{z^2}{12}f_F''(-\epsilon) + \mathcal{O}(z^3) \\
&= 1 + \frac{4}{z^2}\int_0^{+\infty} dy\frac{y}{1+e^{y-\epsilon}} - \frac{4}{z^2}\left[\frac{z^2}{2}f_F(-\epsilon) + 2\frac{z^3}{6}f_F'(-\epsilon) + \frac{z^4}{8}f_F^{''}(-\epsilon)\right] \\
&\quad + f_F(-\epsilon) + zf_F'(-\epsilon) + \frac{z^2}{2}f_F^{''}(-\epsilon) + \frac{z}{12}f_F'(-\epsilon) + \frac{z^2}{12}f_F''(-\epsilon) + \mathcal{O}(z^3) \\
&= 1 + \frac{4}{z^2}\int_0^{+\infty} dy\frac{y}{1+e^{y-\epsilon}} - f_F(-\epsilon) - \frac{z}{4}f_F'(-\epsilon) + \frac{z^2}{12}{f_F}''(-\epsilon) + \mathcal{O}(z^3).
\end{aligned} \tag{D.22}$$

This expression can be rewritten

$$\frac{G_T(B)}{G_{\text{Sh}}} - \frac{G_T(0)}{G_{\text{Sh}}} = \frac{1}{2}\frac{B}{B_c}\left(1 - f_F(-\epsilon)\right) - \frac{1}{8}\left(\frac{B}{B_c}\right)^{\frac{3}{2}}\epsilon f_F'(-\epsilon) \tag{D.23}$$

which is Eq. (6) in the main text. We obtain in the limit $k_BT \ll \mu$ ($\epsilon \gg 1$) that all algebraic corrections in B vanish, while for $\mu \ll k_BT$ ($\epsilon \ll 1$)

$$\frac{G_T(B)}{G_{\text{Sh}}} - \frac{G_T(0)}{G_{\text{Sh}}} \simeq \frac{1}{4}\frac{B}{B_c} \tag{D.24}$$

D.4 Lattice models

Here we provide the explicit form of the two lattice Hamiltonians whose spectra were described – and which were studied numerically – in Sec. 5.2 in the main text.

D.4.1 8 Weyl cones model

We consider a two-band model on a cubic lattice with lattice spacing $a = 1$, whose sites are denoted by $\mathbf{r}$ below, with a nearest-neighbor Hamiltonian

$$\begin{aligned}
H = -\frac{t}{2}\sum_{\mathbf{r}} &\left[\left(i|\mathbf{r}+\mathbf{e}_x\rangle\langle\mathbf{r}| + h.c.\right)\sigma_x + \left(i|\mathbf{r}+\mathbf{e}_y\rangle\langle\mathbf{r}| + h.c.\right)\sigma_y\right] \\
&+ \sum_{\mathbf{r}}\left[\frac{-t_z}{2}\left(|\mathbf{r}+\mathbf{e}_z\rangle\langle\mathbf{r}| + h.c.\right) + (t_z - \Delta)\,|\mathbf{r}\rangle\langle\mathbf{r}|\right]\sigma_z.
\end{aligned} \tag{D.25}$$

The corresponding Bloch Hamiltonian reads

$$H(\mathbf{k}) = t\sin k_x\sigma_x + u\sin k_y\sigma_y + \left[t_z(1-\cos k_z) - \Delta\right]\sigma_z \tag{D.26}$$

and its spectrum is

$$E_{\pm} = \pm\left(t^2\sin^2 k_x\sigma_x + t^2\sin^2 k_y + \left[t_z(1-\cos k_z) - \Delta\right]^2\right)^{1/2}. \tag{D.27}$$

Hence this lattice model possess four pair of Weyl points located at $k_z = \pm\sqrt{2m\Delta}$ and $k_x, k_y = 0, \pi$. In our numerical study we use $t = m = 1$ and study transport along the z direction for various values of the saddle-point energy Δ.

D.4.2 2 Weyl cones model

We use the lattice model of [Delplace et al., 2012], whose Bloch Hamiltonian is

$$
\begin{aligned}
H = \left(2t\ \sin\frac{k_x+k_y}{2}\right)\sigma_x + \left(2t\ \sin\frac{k_x-k_y}{2}\right)\sigma_y& \\
+\ t_z\left(2m_1 + 2\cos k_z - m_2(\cos k_x + \cos k_y)\right)\sigma_z.& \qquad \text{(D.28)}
\end{aligned}
$$

The lattice spacing is set to $a = 1$ and we choose the parameters $t = 1, t_z = 0.2, m_1 = 3/4, m_2 = 1$ for which only two Weyl points exist and are located at $(0, 0, \pm K)$ with $K = \arccos(m_2 - m_1)$. Around these Weyl cones the Hamiltonian reads (up to spin rotation)

$$
H(\pm\mathbf{K} + \mathbf{q}) = 2t(q_x + q_y)\sigma_x + 2t(q_x + q_y)\sigma_y \mp c_z q_z \sigma_z \qquad \text{(D.29)}
$$

with $c_z = 2t_z\sqrt{1 - (m_2 - m_1)^2}$.

D.5 Numerical study

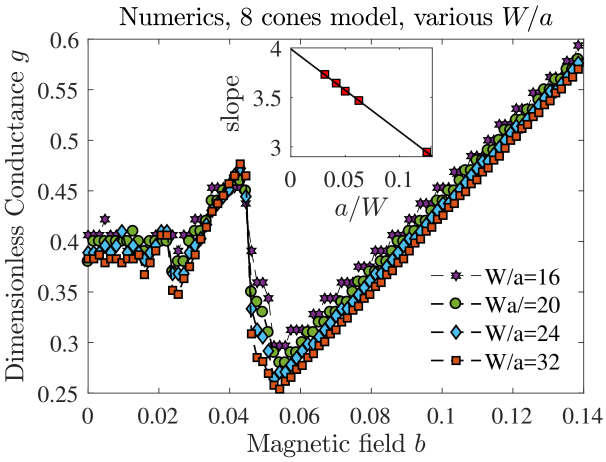

Figure D.2: Dimensionless conductance g as a function of b for $\mu = 0.7$, $\Delta = 1.$, $L/a = 4$ and various W/a. Inset shows surface corrections to the slope scaling like a/W; in the limit $W/a \to \infty$ the slope extrapolates to 4 which corresponds to $g = 4b$, 4 being the number of Weyl pairs.

We compute the conductance using a numerical implementation of the recursive Green function technique with Kwant [Groth et al., 2014]. Samples are Weyl junctions sandwiched between semi-infinite leads made out of the same lattice model. This way, we ensure a perfect ballistic transport regime with a very long lifetime for the electronic wavepackets. The usual sizes of our samples are $L/a = 4$ and $W/a = 8, 16, 24, 32$, i.e., up to 4096 unit cells. Computing the conductance for a growing transverse size allows us to discriminate between bulk and surface contributions to the conductance. The bulk-modes contribution scales like the cross-section $(W/a)^2$, whereas the surface-modes contribution only scales with transverse size as W/a. Hence, $(a/W)^2G$ flows asymptotically to the bulk conductance for growing size. In the infinite-sample limit, we expect in the high field regime

$$
g = G\left(\frac{a}{W}\right)^2 = N_{\text{pairs}} b + \mathcal{O}\left(\frac{a}{W}\right), \qquad \text{(D.30)}
$$

in units of e^2/h, where N_{pairs} counts the pairs of Weyl pairs and $b = \phi/\phi_0$. Indeed, on Fig. D.2 we show from linear fits of our results that the slope in the linear magneto-conductance regime flows toward N_{pairs}, with additional surface corrections scaling like a/W.

We have investigated the impact of reflective leads on transport, see Fig. D.3. Reflection in the leads was implemented either by replacing the leads with semi-infinite 1D chains, as in Ref. [Baireuther et al., 2014] or by changing the longitudinal velocity in the leads with respect to the junction. Both methods yielded a b^2-regime for g.

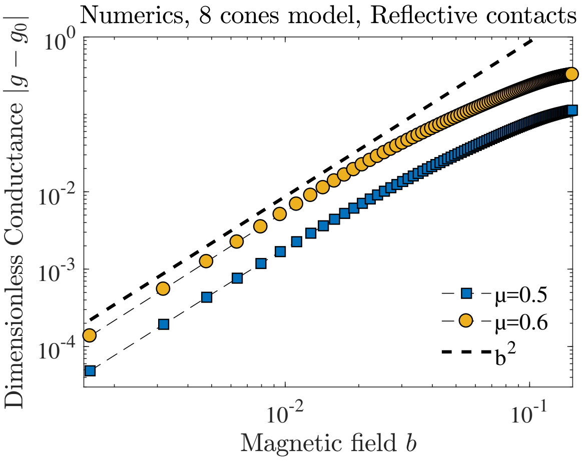

Figure D.3: Conductance of a short junction with partially reflective contacts with the leads. The conductance is no longer ballistic and a b^2-behavior is recovered at small magnetic fields. Parameters are $\Delta = 1., W/a = 24$.

Bibliography

[Abrikosov, 1998] Abrikosov, A. A. (1998). Quantum magnetoresistance. *Physical Review B*, 58(5):2788–2794.

[Abrikosov, 2000] Abrikosov, A. A. (2000). Quantum linear magnetoresistance. *EPL (Europhysics Letters)*, 49(6):789.

[Adam et al., 2009] Adam, S., Brouwer, P. W., and Das Sarma, S. (2009). Crossover from quantum to Boltzmann transport in graphene. *Physical Review B*, 79(20):201404.

[Adam et al., 2007] Adam, S., Hwang, E. H., Galitski, V. M., and Sarma, S. D. (2007). A self-consistent theory for graphene transport. *Proceedings of the National Academy of Sciences*, 104(47):18392–18397.

[Adler, 1969] Adler, S. L. (1969). Axial-Vector Vertex in Spinor Electrodynamics. *Physical Review*, 177(5):2426–2438.

[Aharonov and Bohm, 1959] Aharonov, Y. and Bohm, D. (1959). Significance of Electromagnetic Potentials in the Quantum Theory. *Physical Review*, 115(3):485–491.

[Aji, 2012] Aji, V. (2012). Adler-Bell-Jackiw anomaly in Weyl semimetals: Application to pyrochlore iridates. *Physical Review B*, 85(24):241101.

[Akkermans and Montambaux, 2007] Akkermans, E. and Montambaux, G. (2007). *Mesoscopic Physics of Electrons and Photons*. Cambridge University Press.

[Akrap et al., 2016] Akrap, A., Hakl, M., Tchoumakov, S., Crassee, I., Kuba, J., Goerbig, M. O., Homes, C. C., Caha, O., Novák, J., Teppe, F., Desrat, W., Koohpayeh, S., Wu, L., Armitage, N. P., Nateprov, A., Arushanov, E., Gibson, Q. D., Cava, R. J., van der Marel, D., Piot, B. A., Faugeras, C., Martinez, G., Potemski, M., and Orlita, M. (2016). Magneto-Optical Signature of Massless Kane Electrons in Cd_3As_2. *Physical Review Letters*, 117(13):136401.

[Aleiner and Efetov, 2006] Aleiner, I. L. and Efetov, K. B. (2006). Effect of Disorder on Transport in Graphene. *Physical Review Letters*, 97(23):236801.

[Alloul, 2010] Alloul, H. (2010). *Introduction to the Physics of Electrons in Solids*. Springer Science & Business Media.

[Altland, 2006] Altland, A. (2006). Low-Energy Theory of Disordered Graphene. *Physical Review Letters*, 97(23):236802.

[Altland and Bagrets, 2016] Altland, A. and Bagrets, D. (2016). Theory of the strongly disordered Weyl semimetal. *Physical Review B*, 93(7):075113.

[Anderson, 1958] Anderson, P. W. (1958). Absence of Diffusion in Certain Random Lattices. *Physical Review*, 109(5):1492–1505.

[Armitage et al., 2018] Armitage, N. P., Mele, E. J., and Vishwanath, A. (2018). Weyl and Dirac semimetals in three-dimensional solids. *Reviews of Modern Physics*, 90(1):015001.

[Ashby and Carbotte, 2014] Ashby, P. E. C. and Carbotte, J. P. (2014). Theory of magnetic oscillations in Weyl semimetals. *The European Physical Journal B*, 87(4):92.

[Ashcroft and Mermin, 1976] Ashcroft, N. W. and Mermin, N. D. (1976). *Solid State Physics*. Holt, Rinehart and Winston.

[Baireuther et al., 2014] Baireuther, P., Edge, J. M., Fulga, I. C., Beenakker, C. W. J., and Tworzydło, J. (2014). Quantum phase transitions of a disordered antiferromagnetic topological insulator. *Physical Review B*, 89(3):035410.

[Balog et al., 2017] Balog, I., Carpentier, D., and Fedorenko, A. A. (2017). Disorder-driven quantum transition in relativistic semimetals: Functional renormalization via the porous medium equation. *arXiv:1710.07932 [cond-mat, physics:hep-th, physics:math-ph]*.

[Bardarson et al., 2007] Bardarson, J. H., Tworzydło, J., Brouwer, P. W., and Beenakker, C. W. J. (2007). One-Parameter Scaling at the Dirac Point in Graphene. *Physical Review Letters*, 99(10):106801.

[Beenakker, 1997] Beenakker, C. W. J. (1997). Random-matrix theory of quantum transport. *Reviews of Modern Physics*, 69(3):731–808.

[Bell and Jackiw, 1969] Bell, J. S. and Jackiw, R. (1969). A PCAC puzzle: $\pi^0 \to \gamma\gamma$ in the σ-model. *Il Nuovo Cimento A (1965-1970)*, 60(1):47–61.

[Bercioux et al., 2009] Bercioux, D., Urban, D. F., Grabert, H., and Häusler, W. (2009). Massless Dirac-Weyl fermions in a $\mathcal{T}_3$ optical lattice. *Physical Review A*, 80(6):063603.

[Bernevig and Hughes, 2013] Bernevig, B. A. and Hughes, T. L. (2013). *Topological Insulators and Topological Superconductors*. Princeton University Press.

[Bernevig et al., 2006] Bernevig, B. A., Hughes, T. L., and Zhang, S.-C. (2006). Quantum Spin Hall Effect and Topological Phase Transition in HgTe Quantum Wells. *Science*, 314(5806):1757–1761.

[Berry, 1985] Berry, M. V. (1985). Aspects of Degeneracy. In *Chaotic Behavior in Quantum Systems*, NATO ASI Series, pages 123–140. Springer, Boston, MA.

[Bradlyn et al., 2016] Bradlyn, B., Cano, J., Wang, Z., Vergniory, M. G., Felser, C., Cava, R. J., and Bernevig, B. A. (2016). Beyond Dirac and Weyl fermions: Unconventional quasiparticles in conventional crystals. *Science*, 353(6299):aaf5037.

[Burkov, 2014] Burkov, A. A. (2014). Chiral Anomaly and Diffusive Magnetotransport in Weyl Metals. *Physical Review Letters*, 113(24):247203.

[Burkov, 2015] Burkov, A. A. (2015). Chiral anomaly and transport in Weyl metals. *Journal of Physics: Condensed Matter*, 27(11):113201.

[Burkov and Balents, 2011] Burkov, A. A. and Balents, L. (2011). Weyl Semimetal in a Topological Insulator Multilayer. *Physical Review Letters*, 107(12):127205.

[Burkov et al., 2011] Burkov, A. A., Hook, M. D., and Balents, L. (2011). Topological nodal semimetals. *Physical Review B*, 84(23):235126.

[Burns, 2016] Burns, G. (2016). *Solid State Physics*. Academic Press.

[Castro Neto et al., 2009] Castro Neto, A. H., Guinea, F., Peres, N. M. R., Novoselov, K. S., and Geim, A. K. (2009). The electronic properties of graphene. *Reviews of Modern Physics*, 81(1):109–162.

[Chayes et al., 1986] Chayes, J. T., Chayes, L., Fisher, D. S., and Spencer, T. (1986). Finite-Size Scaling and Correlation Lengths for Disordered Systems. *Physical Review Letters*, 57(24):2999–3002.

[Chiu et al., 2016] Chiu, C.-K., Teo, J. C. Y., Schnyder, A. P., and Ryu, S. (2016). Classification of topological quantum matter with symmetries. *Reviews of Modern Physics*, 88(3):035005.

[Cortijo, 2016] Cortijo, A. (2016). Linear magnetochiral effect in Weyl semimetals. *Physical Review B*, 94(24):241105.

[Croy et al., 2011] Croy, A., Cain, P., and Schreiber, M. (2011). Anderson localization in 1D systems with correlated disorder. *Eur. Phys. J. B*, 82(2):107.

[Danneau et al., 2008] Danneau, R., Wu, F., Craciun, M. F., Russo, S., Tomi, M. Y., Salmilehto, J., Morpurgo, A. F., and Hakonen, P. J. (2008). Shot noise in ballistic graphene. *Phys. Rev. Lett.*, 100:196802.

[Datta, 1997] Datta, S. (1997). *Electronic Transport in Mesoscopic Systems.* Cambridge University Press.

[de Jong, 1994] de Jong, M. J. M. (1994). Transition from Sharvin to Drude resistance in high-mobility wires. *Physical Review B*, 49(11):7778–7781.

[Delplace et al., 2012] Delplace, P., Li, J., and Carpentier, D. (2012). Topological Weyl semi-metal from a lattice model. *EPL (Europhysics Letters)*, 97(6):67004.

[Delplace et al., 2011] Delplace, P., Ullmo, D., and Montambaux, G. (2011). Zak phase and the existence of edge states in graphene. *Physical Review B*, 84(19):195452.

[Dietl et al., 2008] Dietl, P., Piéchon, F., and Montambaux, G. (2008). New Magnetic Field Dependence of Landau Levels in a Graphenelike Structure. *Physical Review Letters*, 100(23):236405.

[Dirac, 1928] Dirac, P. a. M. (1928). The quantum theory of the electron. *Proc. R. Soc. Lond. A*, 117(778):610–624.

[Dirac, 1931] Dirac, P. a. M. (1931). Quantised singularities in the electromagnetic field,. *Proc. R. Soc. Lond. A*, 133(821):60–72.

[Dóra et al., 2011] Dóra, B., Kailasvuori, J., and Moessner, R. (2011). Lattice generalization of the Dirac equation to general spin and the role of the flat band. *Physical Review B*, 84(19):195422.

[Dresselhaus et al., 2008] Dresselhaus, M. S., Dresselhaus, G., and Jorio, A. (2008). *Group Theory: Application to the Physics of Condensed Matter.* Springer-Verlag, Berlin Heidelberg.

[Dudka et al., 2016] Dudka, M., Fedorenko, A. A., Blavatska, V., and Holovatch, Y. (2016). Critical behavior of the two-dimensional Ising model with long-range correlated disorder. *Phys. Rev. B*, 93:224422.

[Duplantier and Ludwig, 1991] Duplantier, B. and Ludwig, A. W. W. (1991). Multifractals, operator-product expansion, and field theory. *Physical Review Letters*, 66(3):247–251.

[Evers and Mirlin, 2008] Evers, F. and Mirlin, A. D. (2008). Anderson transitions. *Reviews of Modern Physics*, 80(4):1355–1417.

[Falco and Fedorenko, 2015] Falco, G. M. and Fedorenko, A. A. (2015). Instanton theory for bosons in a disordered speckle potential. *Physical Review A*, 92(2):023412.

[Falco et al., 2009] Falco, G. M., Nattermann, T., and Pokrovsky, V. L. (2009). Weakly interacting Bose gas in a random environment. *Physical Review B*, 80(10):104515.

[Fang et al., 2012] Fang, C., Gilbert, M. J., Dai, X., and Bernevig, B. A. (2012). Multi-Weyl Topological Semimetals Stabilized by Point Group Symmetry. *Physical Review Letters*, 108(26):266802.

[Fedorenko et al., 2012] Fedorenko, A. A., Carpentier, D., and Orignac, E. (2012). Two-dimensional Dirac fermions in the presence of long-range correlated disorder. *Physical Review B*, 85(12):125437.

[Feng et al., 2017] Feng, B., Fu, B., Kasamatsu, S., Ito, S., Cheng, P., Liu, C.-C., Feng, Y., Wu, S., Mahatha, S. K., Sheverdyaeva, P., Moras, P., Arita, M., Sugino, O., Chiang, T.-C., Shimada, K., Miyamoto, K., Okuda, T., Wu, K., Chen, L., Yao, Y., and Matsuda, I. (2017). Experimental realization of two-dimensional Dirac nodal line fermions in monolayer Cu_2Si. *Nature Communications*, 8(1):1007.

[Foster, 2012] Foster, M. S. (2012). Multifractal nature of the surface local density of states in three-dimensional topological insulators with magnetic and nonmagnetic disorder. *Physical Review B*, 85(8):085122.

[Fradkin, 1986a] Fradkin, E. (1986a). Critical behavior of disordered degenerate semiconductors. I. Models, symmetries, and formalism. *Physical Review B*, 33(5):3257–3262.

[Fradkin, 1986b] Fradkin, E. (1986b). Critical behavior of disordered degenerate semiconductors. II. Spectrum and transport properties in mean-field theory. *Physical Review B*, 33(5):3263–3268.

[Fruchart and Carpentier, 2013] Fruchart, M. and Carpentier, D. (2013). An introduction to topological insulators. *Comptes Rendus Physique*, 14(9):779–815.

[Fu, 2011] Fu, L. (2011). Topological Crystalline Insulators. *Physical Review Letters*, 106(10):106802.

[Fu and Kane, 2007] Fu, L. and Kane, C. L. (2007). Topological insulators with inversion symmetry. *Physical Review B*, 76(4):045302.

[Fu et al., 2007] Fu, L., Kane, C. L., and Mele, E. J. (2007). Topological Insulators in Three Dimensions. *Physical Review Letters*, 98(10):106803.

[Ghosh et al., 2016] Ghosh, S., Gupta, R. K., Jaswin, K., and Nizami, A. A. (2016). ε-Expansion in the Gross-Neveu model from conformal field theory. *Journal of High Energy Physics*, 2016(3):174.

[Goerbig, 2011] Goerbig, M. O. (2011). Electronic properties of graphene in a strong magnetic field. *Reviews of Modern Physics*, 83(4):1193–1243.

[Goldenfeld, 1992] Goldenfeld, N. (1992). *Lectures on Phase Transitions and the Renormalization Group.* Addison-Wesley, Advanced Book Program.

[Gorbar et al., 2014] Gorbar, E. V., Miransky, V. A., and Shovkovy, I. A. (2014). Chiral anomaly, dimensional reduction, and magnetoresistivity of Weyl and Dirac semimetals. *Physical Review B*, 89(8):085126.

[Gosálbez-Martínez et al., 2015] Gosálbez-Martínez, D., Souza, I., and Vanderbilt, D. (2015). Chiral degeneracies and Fermi-surface Chern numbers in bcc Fe. *Physical Review B*, 92(8):085138.

[Goswami and Chakravarty, 2011] Goswami, P. and Chakravarty, S. (2011). Quantum Criticality between Topological and Band Insulators in $3+1$ Dimensions. *Physical Review Letters*, 107(19):196803.

[Gracey, 2008] Gracey, J. A. (2008). Four loop $\overline{MS}$ mass anomalous dimension in the Gross–Neveu model. *Nuclear Physics B*, 802(3):330–350.

[Groth et al., 2014] Groth, C. W., Wimmer, M., Akhmerov, A. R., and Waintal, X. (2014). Kwant: A software package for quantum transport. *New Journal of Physics*, 16(6):063065.

[Haldane, 1988] Haldane, F. D. M. (1988). Model for a Quantum Hall Effect without Landau Levels: Condensed-Matter Realization of the "Parity Anomaly". *Physical Review Letters*, 61(18):2015–2018.

[Hasan and Kane, 2010] Hasan, M. Z. and Kane, C. L. (2010). Colloquium: Topological insulators. *Reviews of Modern Physics*, 82(4):3045–3067.

[Hasegawa et al., 2006] Hasegawa, Y., Konno, R., Nakano, H., and Kohmoto, M. (2006). Zero modes of tight-binding electrons on the honeycomb lattice. *Physical Review B*, 74(3):033413.

[Häusler, 2015] Häusler, W. (2015). Flat-band conductivity properties at long-range Coulomb interactions. *Physical Review B*, 91(4):041102.

[Hernández-Rodríguez et al., 2015] Hernández-Rodríguez, I., García, J. M., Martín-Gago, J. A., de Andrés, P. L., and Méndez, J. (2015). Graphene growth on Pt(111) and Au(111) using a MBE carbon solid-source. *Diamond and Related Materials*, 57(Supplement C):58–62.

[Herring, 1937] Herring, C. (1937). Accidental Degeneracy in the Energy Bands of Crystals. *Physical Review*, 52(4):365–373.

[Hirschberger et al., 2016] Hirschberger, M., Kushwaha, S., Wang, Z., Gibson, Q., Liang, S., Belvin, C. A., Bernevig, B. A., Cava, R. J., and Ong, N. P. (2016). The chiral anomaly and thermopower of Weyl fermions in the half-Heusler GdPtBi. *Nature Materials*, 15(11):1161.

[Honkonen and Nalimov, 1989] Honkonen, J. and Nalimov, M. Y. (1989). *J. Phys. A: Math. Gen.*, 22:751.

[Hosur et al., 2012] Hosur, P., Parameswaran, S. A., and Vishwanath, A. (2012). Charge Transport in Weyl Semimetals. *Phys. Rev. Lett.*, 108:046602.

[Hsieh et al., 2009] Hsieh, D., Xia, Y., Wray, L., Qian, D., Pal, A., Dil, J. H., Osterwalder, J., Meier, F., Bihlmayer, G., Kane, C. L., Hor, Y. S., Cava, R. J., and Hasan, M. Z. (2009). Observation of Unconventional Quantum Spin Textures in Topological Insulators. *Science*, 323(5916):919–922.

[Huang et al., 2015] Huang, X., Zhao, L., Long, Y., Wang, P., Chen, D., Yang, Z., Liang, H., Xue, M., Weng, H., Fang, Z., Dai, X., and Chen, G. (2015). Observation of the Chiral-Anomaly-Induced Negative Magnetoresistance in 3D Weyl Semimetal TaAs. *Physical Review X*, 5(3):031023.

[Huckestein, 1995] Huckestein, B. (1995). Scaling theory of the integer quantum Hall effect. *Reviews of Modern Physics*, 67(2):357–396.

[Johansson et al., 1990] Johansson, L. S. O., Persson, P. E. S., Karlsson, U. O., and Uhrberg, R. I. G. (1990). Bulk electronic structure of silicon studied with angle-resolved photoemission from the Si(100)2×1 surface. *Physical Review B*, 42(14):8991–8999.

[Kane and Mele, 2005a] Kane, C. L. and Mele, E. J. (2005a). Quantum Spin Hall Effect in Graphene. *Physical Review Letters*, 95(22):226801.

[Kane and Mele, 2005b] Kane, C. L. and Mele, E. J. (2005b). Z_2 topological order and the quantum spin hall effect. *Physical Review Letters*, 95(14):146802.

[Kärkkäinen et al., 1994] Kärkkäinen, L., Lacaze, R., Lacock, P., and Petersson, B. (1994). Critical behaviour of the three-dimensional Gross-Neveu and Higgs-Yukawa models. *Nuclear Physics B*, 415(3):781–796.

[Katsnelson, 2012] Katsnelson, M. I. (2012). *Graphene: Carbon in Two Dimensions*. Cambridge University Press.

[Katsnelson et al., 2006] Katsnelson, M. I., Novoselov, K. S., and Geim, A. K. (2006). Chiral tunnelling and the Klein paradox in graphene. *Nature Physics*, 2(9):620.

[Kharzeev, 2014] Kharzeev, D. E. (2014). The Chiral Magnetic Effect and anomaly-induced transport. *Progress in Particle and Nuclear Physics*, 75:133–151.

[Kitaev, 2009] Kitaev, A. (2009). Periodic table for topological insulators and superconductors. *AIP Conference Proceedings*, 1134(1):22–30.

[Kittel, 2004] Kittel (2004). *Introduction to Solid State Physics, 7th Ed.* Wiley.

[Kobayashi et al., 2014] Kobayashi, K., Ohtsuki, T., Imura, K.-I., and Herbut, I. F. (2014). Density of States Scaling at the Semimetal to Metal Transition in Three Dimensional Topological Insulators. *Physical Review Letters*, 112(1):016402.

[König et al., 2007] König, M., Wiedmann, S., Brüne, C., Roth, A., Buhmann, H., Molenkamp, L. W., Qi, X.-L., and Zhang, S.-C. (2007). Quantum Spin Hall Insulator State in HgTe Quantum Wells. *Science*, 318(5851):766–770.

[Kramer and MacKinnon, 1993] Kramer, B. and MacKinnon, A. (1993). Localization: Theory and experiment. *Reports on Progress in Physics*, 56(12):1469.

[Kramers and Wannier, 1941] Kramers, H. A. and Wannier, G. H. (1941). Statistics of the Two-Dimensional Ferromagnet. Part I. *Physical Review*, 60(3):252–262.

[Lee and Ramakrishnan, 1985] Lee, P. A. and Ramakrishnan, T. V. (1985). Disordered electronic systems. *Reviews of Modern Physics*, 57(2):287–337.

[Li et al., 2016] Li, H., He, H., Lu, H.-Z., Zhang, H., Liu, H., Ma, R., Fan, Z., Shen, S.-Q., and Wang, J. (2016). Negative magnetoresistance in Dirac semimetal Cd_3As_2. *Nature Communications*, 7:10301.

[Li et al., 2014] Li, W., Guo, M., Zhang, G., and Zhang, Y.-W. (2014). Gapless MoS_2 allotrope possessing both massless Dirac and heavy fermions. *Physical Review B*, 89(20):205402.

[Lieb, 1989] Lieb, E. H. (1989). Two theorems on the Hubbard model. *Physical Review Letters*, 62(10):1201–1204.

[Liu et al., 2014] Liu, Z. K., Zhou, B., Zhang, Y., Wang, Z. J., Weng, H. M., Prabhakaran, D., Mo, S.-K., Shen, Z. X., Fang, Z., Dai, X., Hussain, Z., and Chen, Y. L. (2014). Discovery of a Three-Dimensional Topological Dirac Semimetal, Na_3Bi. *Science*, 343(6173):864–867.

[Louvet et al., 2016] Louvet, T., Carpentier, D., and Fedorenko, A. A. (2016). On the disorder-driven quantum transition in three-dimensional relativistic metals. *Physical Review B*, 94(22):220201.

[Louvet et al., 2017a] Louvet, T., Carpentier, D., and Fedorenko, A. A. (2017a). New quantum transition in Weyl semimetals with correlated disorder. *Physical Review B*, 95(1):014204.

[Louvet et al., 2015] Louvet, T., Delplace, P., Fedorenko, A. A., and Carpentier, D. (2015). On the origin of minimal conductivity at a band crossing. *Physical Review B*, 92(15):155116.

[Louvet et al., 2017b] Louvet, T., Houzet, M., and Carpentier, D. (2017b). Signature of the Chiral Anomaly in Ballistic Magneto-Transport. *arXiv:1711.06657 [cond-mat]*.

[Lu et al., 2015a] Lu, H.-Z., Zhang, S.-B., and Shen, S.-Q. (2015a). High-field magnetoconductivity of topological semimetals with short-range potential. *Physical Review B*, 92(4):045203.

[Lu et al., 2015b] Lu, L., Wang, Z., Ye, D., Ran, L., Fu, L., Joannopoulos, J. D., and Soljačić, M. (2015b). Experimental observation of Weyl points. *Science*, 349(6248):622–624.

[Lv et al., 2015] Lv, B. Q., Weng, H. M., Fu, B. B., Wang, X. P., Miao, H., Ma, J., Richard, P., Huang, X. C., Zhao, L. X., Chen, G. F., Fang, Z., Dai, X., Qian, T., and Ding, H. (2015). Experimental Discovery of Weyl Semimetal TaAs. *Physical Review X*, 5(3):031013.

[Mahan, 2013] Mahan, G. D. (2013). *Many-Particle Physics*. Springer Science & Business Media.

[Malcolm and Nicol, 2015] Malcolm, J. D. and Nicol, E. J. (2015). Magneto-optics of massless Kane fermions: Role of the flat band and unusual Berry phase. *Physical Review B*, 92(3):035118.

[McCann and Fal'ko, 2006] McCann, E. and Fal'ko, V. I. (2006). Landau-Level Degeneracy and Quantum Hall Effect in a Graphite Bilayer. *Physical Review Letters*, 96(8):086805.

[McCann et al., 2006] McCann, E., Kechedzhi, K., Fal'ko, V. I., Suzuura, H., Ando, T., and Altshuler, B. L. (2006). Weak-Localization Magnetoresistance and Valley Symmetry in Graphene. *Physical Review Letters*, 97(14):146805.

[Mezard et al., 1987] Mezard, M., Parisi, G., and Virasoro, M. A. (1987). *Spin Glass Theory and Beyond*. World Scientific.

[Mirlin et al., 2006] Mirlin, A. D., Fyodorov, Y. V., Mildenberger, A., and Evers, F. (2006). Exact Relations between Multifractal Exponents at the Anderson Transition. *Physical Review Letters*, 97(4):046803.

[Moore and Balents, 2007] Moore, J. E. and Balents, L. (2007). Topological invariants of time-reversal-invariant band structures. *Physical Review B*, 75(12):121306.

[Morimoto and Furusaki, 2014] Morimoto, T. and Furusaki, A. (2014). Weyl and Dirac semimetals with $\mathbb{Z}_2$ topological charge. *Physical Review B*, 89(23):235127.

[Murakami, 2007] Murakami, S. (2007). Phase transition between the quantum spin Hall and insulator phases in 3D: Emergence of a topological gapless phase. *New Journal of Physics*, 9(9):356.

[Murakami et al., 2017] Murakami, S., Hirayama, M., Okugawa, R., and Miyake, T. (2017). Emergence of topological semimetals in gap closing in semiconductors without inversion symmetry. *Science Advances*, 3(5).

[Nandkishore et al., 2014] Nandkishore, R., Huse, D. A., and Sondhi, S. L. (2014). Rare region effects dominate weakly disordered three-dimensional Dirac points. *Physical Review B*, 89(24):245110.

[Nazarov and Blanter, 2009] Nazarov, Y. V. and Blanter, Y. M. (2009). *Quantum Transport: Introduction to Nanoscience*. Cambridge University Press.

[Neupane et al., 2014] Neupane, M., Xu, S.-Y., Sankar, R., Alidoust, N., Bian, G., Liu, C., Belopolski, I., Chang, T.-R., Jeng, H.-T., Lin, H., Bansil, A., Chou, F., and Hasan, M. Z. (2014). Observation of a three-dimensional topological Dirac semimetal phase in high-mobility Cd_3As_2. *Nature Communications*, 5:3786.

[Nielsen and Ninomiya, 1983] Nielsen, H. B. and Ninomiya, M. (1983). The Adler-Bell-Jackiw anomaly and Weyl fermions in a crystal. *Physics Letters B*, 130(6):389–396.

[Niemann et al., 2016] Niemann, A. C., Gooth, J., Wu, S.-C., Bäßler, S., Sergelius, P., Hühne, R., Rellinghaus, B., Shekhar, C., Süß, V., Schmidt, M., Felser, C., Yan, B., and Nielsch, K. (2016). Chiral magnetoresistance in the Weyl semimetal NbP. *arXiv:1610.01413 [cond-mat]*.

[Nomura et al., 2007] Nomura, K., Koshino, M., and Ryu, S. (2007). Topological Delocalization of Two-Dimensional Massless Dirac Fermions. *Physical Review Letters*, 99(14):146806.

[Novoselov et al., 2005] Novoselov, K. S., Geim, A. K., Morozov, S. V., Jiang, D., Katsnelson, M. I., Grigorieva, I. V., Dubonos, S. V., and Firsov, A. A. (2005). Two-dimensional gas of massless Dirac fermions in graphene. *Nature*, 438(7065):197.

[Novoselov et al., 2004] Novoselov, K. S., Geim, A. K., Morozov, S. V., Jiang, D., Zhang, Y., Dubonos, S. V., Grigorieva, I. V., and Firsov, A. A. (2004). Electric Field Effect in Atomically Thin Carbon Films. *Science*, 306(5696):666–669.

[Ominato and Koshino, 2014] Ominato, Y. and Koshino, M. (2014). Quantum transport in a three-dimensional Weyl electron system. *Physical Review B*, 89(5):054202.

[Orlita et al., 2014] Orlita, M., Basko, D. M., Zholudev, M. S., Teppe, F., Knap, W., Gavrilenko, V. I., Mikhailov, N. N., Dvoretskii, S. A., Neugebauer, P., Faugeras, C., Barra, A.-L., Martinez, G., and Potemski, M. (2014). Observation of three-dimensional massless Kane fermions in a zinc-blende crystal. *Nature Physics*, 10(3):233.

[Ostrovsky et al., 2006] Ostrovsky, P. M., Gornyi, I. V., and Mirlin, A. D. (2006). Electron transport in disordered graphene. *Physical Review B*, 74(23):235443.

[Pázmándi et al., 1997] Pázmándi, F., Scalettar, R. T., and Zimányi, G. T. (1997). Revisiting the Theory of Finite Size Scaling in Disordered Systems: ν Can Be Less than $2/d$. *Physical Review Letters*, 79(25):5130–5133.

[Pixley et al., 2015] Pixley, J. H., Goswami, P., and Das Sarma, S. (2015). Anderson Localization and the Quantum Phase Diagram of Three Dimensional Disordered Dirac Semimetals. *Physical Review Letters*, 115(7):076601.

[Pixley et al., 2016] Pixley, J. H., Huse, D. A., and Das Sarma, S. (2016). Rare-Region-Induced Avoided Quantum Criticality in Disordered Three-Dimensional Dirac and Weyl Semimetals. *Physical Review X*, 6(2):021042.

[Prudnikov et al., 2000] Prudnikov, V. V., Prudnikov, P. V., and Fedorenko, A. A. (2000). Field-theory approach to critical behavior of systems with long-range correlated defects. *Phys. Rev. B*, 62:8777–8786.

[Raoux et al., 2014] Raoux, A., Morigi, M., Fuchs, J.-N., Piéchon, F., and Montambaux, G. (2014). From Dia- to Paramagnetic Orbital Susceptibility of Massless Fermions. *Physical Review Letters*, 112(2):026402.

[Roy and Das Sarma, 2014] Roy, B. and Das Sarma, S. (2014). Diffusive quantum criticality in three-dimensional disordered Dirac semimetals. *Physical Review B*, 90(24):241112.

[Roy and Das Sarma, 2016] Roy, B. and Das Sarma, S. (2016). Erratum: Diffusive quantum criticality in three-dimensional disordered Dirac semimetals [Phys. Rev. B 90, 241112(R) (2014)]. *Physical Review B*, 93(11):119911.

[Roy et al., 2016] Roy, B., Juričić, V., and Das Sarma, S. (2016). Universal optical conductivity of a disordered Weyl semimetal. *Scientific Reports*, 6:32446.

[Roy, 2009] Roy, R. (2009). Topological phases and the quantum spin Hall effect in three dimensions. *Physical Review B*, 79(19):195322.

[Ryder, 1996] Ryder, L. H. (1996). *Quantum Field Theory.* Cambridge University Press.

[Ryu et al., 2007] Ryu, S., Mudry, C., Furusaki, A., and Ludwig, A. W. W. (2007). Landauer conductance and twisted boundary conditions for Dirac fermions in two space dimensions. *Physical Review B*, 75(20):205344.

[Sbierski et al., 2015] Sbierski, B., Bergholtz, E. J., and Brouwer, P. W. (2015). Quantum critical exponents for a disordered three-dimensional Weyl node. *Physical Review B*, 92(11):115145.

[Sbierski et al., 2017] Sbierski, B., Madsen, K. A., Brouwer, P. W., and Karrasch, C. (2017). Quantitative analytical theory for disordered nodal points. *Physical Review B*, 96(6):064203.

[Sbierski et al., 2014] Sbierski, B., Pohl, G., Bergholtz, E. J., and Brouwer, P. W. (2014). Quantum Transport of Disordered Weyl Semimetals at the Nodal Point. *Physical Review Letters*, 113(2):026602.

[Schnyder et al., 2008] Schnyder, A. P., Ryu, S., Furusaki, A., and Ludwig, A. W. W. (2008). Classification of topological insulators and superconductors in three spatial dimensions. *Physical Review B*, 78(19):195125.

[Schuessler et al., 2009] Schuessler, A., Ostrovsky, P. M., Gornyi, I. V., and Mirlin, A. D. (2009). Analytic theory of ballistic transport in disordered graphene. *Physical Review B*, 79(7):075405.

[Shalaev et al., 1997] Shalaev, B. N., Antonenko, S. A., and Sokolov, A. I. (1997). Five-loop ϵ for random Ising model and marginal spin dimensionality for cubic systems. *Physics Letters A*, 230(1):105–110.

[Shekhar et al., 2016] Shekhar, C., Nayak, A. K., Singh, S., Kumar, N., Wu, S.-C., Zhang, Y., Komarek, A. C., Kampert, E., Skourski, Y., Wosnitza, J., Schnelle, W., McCollam, A., Zeitler, U., Kubler, J., Parkin, S. S. P., Yan, B., and Felser, C. (2016). Observation of chiral magneto-transport in RPtBi topological Heusler compounds. *arXiv:1604.01641 [cond-mat]*.

[Shon and Ando, 1998] Shon, N. H. and Ando, T. (1998). Quantum Transport in Two-Dimensional Graphite System. *Journal of the Physical Society of Japan*, 67(7):2421–2429.

[Simon, 2013] Simon, S. H. (2013). *The Oxford Solid State Basics*. OUP Oxford.

[Singleton, 2001] Singleton, J. (2001). *Band Theory and Electronic Properties of Solids*. OUP Oxford.

[Slot et al., 2017] Slot, M. R., Gardenier, T. S., Jacobse, P. H., van Miert, G. C. P., Kempkes, S. N., Zevenhuizen, S. J. M., Smith, C. M., Vanmaekelbergh, D., and Swart, I. (2017). Experimental realization and characterization of an electronic Lieb lattice. *Nature Physics*, 13(7):672.

[Soluyanov et al., 2015] Soluyanov, A. A., Gresch, D., Wang, Z., Wu, Q., Troyer, M., Dai, X., and Bernevig, B. A. (2015). Type-II Weyl semimetals. *Nature*, 527(7579):495.

[Son and Spivak, 2013] Son, D. T. and Spivak, B. Z. (2013). Chiral anomaly and classical negative magnetoresistance of Weyl metals. *Physical Review B*, 88(10):104412.

[Sun et al., 2015] Sun, Y., Wu, S.-C., Ali, M. N., Felser, C., and Yan, B. (2015). Prediction of Weyl semimetal in orthorhombic $\mathrm{MoTe_2}$. *Physical Review B*, 92(16):161107.

[Suzuki et al., 2016] Suzuki, T., Chisnell, R., Devarakonda, A., Liu, Y.-T., Feng, W., Xiao, D., Lynn, J. W., and Checkelsky, J. G. (2016). Large anomalous Hall effect in a half-Heusler antiferromagnet. *Nature Physics*, 12(12):1119.

[Syzranov et al., 2016] Syzranov, S. V., Ostrovsky, P. M., Gurarie, V., and Radzihovsky, L. (2016). Critical exponents at the unconventional disorder-driven transition in a Weyl semimetal. *Physical Review B*, 93(15):155113.

[Syzranov and Radzihovsky, 2018] Syzranov, S. V. and Radzihovsky, L. (2018). High-Dimensional Disorder-Driven Phenomena in Weyl Semimetals, Semiconductors, and Related Systems. *Annual Review of Condensed Matter Physics*, 9(1):35–58.

[Syzranov et al., 2015] Syzranov, S. V., Radzihovsky, L., and Gurarie, V. (2015). Critical Transport in Weakly Disordered Semiconductors and Semimetals. *Physical Review Letters*, 114(16):166601.

[Tarruell et al., 2012] Tarruell, L., Greif, D., Uehlinger, T., Jotzu, G., and Esslinger, T. (2012). Creating, moving and merging Dirac points with a Fermi gas in a tunable honeycomb lattice. *Nature*, 483(7389):302.

[Thouless et al., 1982] Thouless, D. J., Kohmoto, M., Nightingale, M. P., and den Nijs, M. (1982). Quantized Hall Conductance in a Two-Dimensional Periodic Potential. *Physical Review Letters*, 49(6):405–408.

[Trescher et al., 2015] Trescher, M., Sbierski, B., Brouwer, P. W., and Bergholtz, E. J. (2015). Quantum transport in Dirac materials: Signatures of tilted and anisotropic Dirac and Weyl cones. *Physical Review B*, 91(11):115135.

[Tworzydło et al., 2006] Tworzydło, J., Trauzettel, B., Titov, M., Rycerz, A., and Beenakker, C. W. J. (2006). Sub-Poissonian Shot Noise in Graphene. *Physical Review Letters*, 96(24):246802.

[v. Klitzing et al., 1980] v. Klitzing, K., Dorda, G., and Pepper, M. (1980). New Method for High-Accuracy Determination of the Fine-Structure Constant Based on Quantized Hall Resistance. *Physical Review Letters*, 45(6):494–497.

[Vasiliev and Vyazovsky, 1997] Vasiliev, A. N. and Vyazovsky, M. I. (1997). Proof of the absence of multiplicative renormalizability of the Gross-Neveu model in the dimensional regularization $d = 2 + \epsilon$. *Theor. Math. Phys.*, 113:1277.

[Vigh et al., 2013] Vigh, M., Oroszlány, L., Vajna, S., San-Jose, P., Dávid, G., Cserti, J., and Dóra, B. (2013). Diverging dc conductivity due to a flat band in a disordered system of pseudospin-1 Dirac-Weyl fermions. *Physical Review B*, 88(16):161413.

[Wallace, 1947] Wallace, P. R. (1947). The Band Theory of Graphite. *Physical Review*, 71(9):622–634.

[Wan et al., 2011] Wan, X., Turner, A. M., Vishwanath, A., and Savrasov, S. Y. (2011). Topological semimetal and Fermi-arc surface states in the electronic structure of pyrochlore iridates. *Physical Review B*, 83(20):205101.

[Wang et al., 2013a] Wang, J., Huang, H., Duan, W., and Liu, Z. (2013a). Identifying Dirac cones in carbon allotropes with square symmetry. *J. Chem Phys*, 139:184701–184701.

[Wang et al., 2012] Wang, Z., Sun, Y., Chen, X.-Q., Franchini, C., Xu, G., Weng, H., Dai, X., and Fang, Z. (2012). Dirac semimetal and topological phase transitions in A_3Bi (A=Na, K, Rb). *Physical Review B*, 85(19):195320.

[Wang et al., 2013b] Wang, Z., Weng, H., Wu, Q., Dai, X., and Fang, Z. (2013b). Three-dimensional Dirac semimetal and quantum transport in Cd_3As_2. *Physical Review B*, 88(12):125427.

[Webb et al., 1985] Webb, R. A., Washburn, S., Umbach, C. P., and Laibowitz, R. B. (1985). Observation of $\frac{h}{e}$ Aharonov-Bohm Oscillations in Normal-Metal Rings. *Physical Review Letters*, 54(25):2696–2699.

[Weinrib and Halperin, 1983] Weinrib, A. and Halperin, B. I. (1983). Critical phenomena in systems with long-range-correlated quenched disorder. *Phys. Rev. B*, 27:413–427.

[Weyl, 1929] Weyl, H. (1929). Elektron und Gravitation. I. *Zeitschrift für Physik*, 56(5-6):330–352.

[Xia et al., 2009] Xia, Y., Qian, D., Hsieh, D., Wray, L., Pal, A., Lin, H., Bansil, A., Grauer, D., Hor, Y. S., Cava, R. J., and Hasan, M. Z. (2009). Observation of a large-gap topological-insulator class with a single Dirac cone on the surface. *Nature Physics*, 5(6):398–402.

[Xiao et al., 2010] Xiao, D., Chang, M.-C., and Niu, Q. (2010). Berry phase effects on electronic properties. *Reviews of Modern Physics*, 82(3):1959–2007.

[Xiong et al., 2015] Xiong, J., Kushwaha, S. K., Liang, T., Krizan, J. W., Hirschberger, M., Wang, W., Cava, R. J., and Ong, N. P. (2015). Evidence for the chiral anomaly in the Dirac semimetal Na_3Bi. *Science*, 350(6259):413–416.

[Xu et al., 2011] Xu, G., Weng, H., Wang, Z., Dai, X., and Fang, Z. (2011). Chern Semimetal and the Quantized Anomalous Hall Effect in $HgCr_2Se_4$. *Physical Review Letters*, 107(18):186806.

[Xu et al., 2015] Xu, S.-Y., Belopolski, I., Alidoust, N., Neupane, M., Bian, G., Zhang, C., Sankar, R., Chang, G., Yuan, Z., Lee, C.-C., Huang, S.-M., Zheng, H., Ma, J., Sanchez, D. S., Wang, B., Bansil, A., Chou, F., Shibayev, P. P., Lin, H., Jia, S., and Hasan, M. Z. (2015). Discovery of a Weyl fermion semimetal and topological Fermi arcs. *Science*, 349(6248):613–617.

[Yan and Felser, 2017] Yan, B. and Felser, C. (2017). Topological Materials: Weyl Semimetals. *Annual Review of Condensed Matter Physics*, 8(1):337–354.

[Yang et al., 2015] Yang, B.-J., Morimoto, T., and Furusaki, A. (2015). Topological charges of three-dimensional Dirac semimetals with rotation symmetry. *Physical Review B*, 92(16):165120.

[Yang and Nagaosa, 2014] Yang, B.-J. and Nagaosa, N. (2014). Classification of stable three-dimensional Dirac semimetals with nontrivial topology. *Nature Communications*, 5:4898.

[Young et al., 2012] Young, S. M., Zaheer, S., Teo, J. C. Y., Kane, C. L., Mele, E. J., and Rappe, A. M. (2012). Dirac Semimetal in Three Dimensions. *Physical Review Letters*, 108(14):140405.

[Zee, 2003] Zee, A. (2003). *Quantum Field Theory in a Nutshell.* Princeton University Press.

[Zhang et al., 2005] Zhang, Y., Tan, Y.-W., Stormer, H. L., and Kim, P. (2005). Experimental observation of the quantum Hall effect and Berry's phase in graphene. *Nature*, 438(7065):201.

[Zinn-Justin, 2002] Zinn-Justin, J. (2002). *Quantum Field Theory and Critical Phenomena.* Clarendon Press.